UNIVERSITY OF CALIFORNIA SAN DIEGO

Asymptotic studies of unsteady non-premixed flamelets and buoyancy-induced swirling flows

A dissertation submitted in partial satisfaction of the
requirements for the degree
Doctor of Philosophy

in

Engineering Sciences (Mechanical Engineering)

by

Adam D. Weiss

Committee in charge:

Professor Antonio L. Sánchez, Chair
Professor Forman A. Williams, Co-Chair
Professor Eugene R. Pawlak
Professor Kalyanasundaram Seshadri
Professor William R. Young

2020

The dissertation of Adam D. Weiss is approved, and it is acceptable in quality and form for publication on microfilm and electronically:

_____

_____

_____

_____
Co-Chair

_____
Chair

University of California San Diego

2020

DEDICATION

To my family and friends.

TABLE OF CONTENTS

LIST OF FIGURES

ACKNOWLEDGEMENTS

The author is indebted to Professors Antonio L. Sánchez and Forman A. Williams for their valuable help and encouragement as his advisors. They suggested the topics explored in this thesis and have given their time and advice very generously. The author would also like to thank his labmates for interesting and stimulating conversations and especially Prabakaran Rajamanickam, whom he has learned a great deal from.

Chapter 1, in full, has been published in the *Journal of Fluid Mechanics*, titled "Aerodynamics of planar counterflowing jets", by A. D. Weiss, W. Coenen and A. L. Sánchez (2017) 821, 1-30. The dissertation author was the primary investigator in this publication.

Chapter 2, in full, has been published in *Combustion Theory and Modelling* titled " A novel formulation for unsteady counterflow flames using a thermal-conductivity-weighted coordinate", by A. D. Weiss, M. Vera, A. Liñán, A. L. Sánchez and F. A. Williams (2018) 22, 185-201. The dissertation author was the primary investigator in this publication.

Chapter 3, in full, has been published in *Combustion and Flame* titled "The acoustic response of Burke-Schumann counterflow flames", by A. D. Weiss, W. Coenen, A. L. Sánchez and F. A. Williams (2018) 192, 25-34. The dissertation author was the primary investigator in this publication.

Chapter 4, in full, has been published in *AIAA Journal* titled "Acoustic response of near-equilibrium diffusion flames with large activation energies", by A. D. Weiss, A. L. Sánchez and F. A. Williams (2019) 57, 2933-2945. The dissertation author was the primary investigator in this publication.

Chapter 5, in full, has been published in *Combustion and Flame* titled "Accuracies of reduced mechanisms for predicting acoustic combustion instabilities", by A. D. Weiss, A. L. Sánchez and F. A. Williams (2019) 209, 405-407. The dissertation author was the primary investigator in this publication.

Chapter 6, in full, has been submitted for publication in the *Journal of Fluid Mechanics*,

"A model for the boundary layer surrounding fire whirls", by A. D. Weiss, P. Rajamanickam, W. Coenen, A. L. Sánchez, and F. A. Williams. The dissertation author is the primary investigator in this publication.

The work reported in Part I, encompassing chapters 1 through 5, was funded by the US Air Force Office of Scientific Research through grant no. FA9550-16-1- 0321, while the work reported in Part II, consisting of chapter 6, was funded by the US National Science Foundation through grant no. 1916979

La Jolla, California. May, 2020

VITA

2013	B. S. in Mechanical Engineering, *summa cum laude* Dept. of Mechanical and Aerospace Engineering University of California San Diego
2017	M. S. in Engineering Sciences (Mechanical Engineering) Dept. of Mechanical and Aerospace Engineering University of California San Diego
2018	Advancement to Ph. D. Candidacy Dept. of Mechanical and Aerospace Engineering University of California San Diego
2020	Ph. D. in Engineering Sciences (Mechanical Engineering) Dept. of Mechanical and Aerospace Engineering University of California San Diego

PUBLICATIONS

A. D. Weiss, W. Coenen, and A. L. Sánchez, "Aerodynamics of planar counterflowing jets", *J. Fluid Mech.*, 314, 1-30, 2017.

A. D. Weiss, M. Vera, A. Liñán, A. L. Sánchez and F. A. Williams, "A novel formulation for unsteady counterflow flames using a thermal-conductivity-weighted coordinate", *Combust. Theor Model.*, 22, 185-201, 2018.

A. D. Weiss, W. Coenen, A. L. Sánchez and F. A. Williams, "The acoustic response of Burke-Schumann counterflow flames", *Combust. Flame*, 192, 25-34, 2018

A. D. Weiss, A. L. Sánchez and F. A. Williams, "Acoustic response of near-equilibrium diffusion flames with large activation energies", *AIAA J.*, 57, 2933-2945, 2019

W. Coenen, P. Rajamanickam, **A. D. Weiss**, A. L. Sánchez and F. A. Williams, "Swirling flow induced by jets and plumes", *Acta Mechanica*, 230, 2221-2231, 2019

D. Fernández-Galisteo, **A. D. Weiss**, A. L. Sánchez and F. A. Williams, "A one-step reduced mechanism for near-limit hydrogen combustion with general stoichiometry", *Combust. Flame*, 208, 1-4, 2019

A. D. Weiss, A. L. Sánchez and F. A. Williams, "Accuracies of reduced mechanisms for predicting acoustic combustion instabilities", *Combust. Flame*, 209, 405-407, 2019

P. Rajamanickam and **A. D. Weiss**, "A note on viscous flow induced by half-line sources bounded by conical surfaces", *Q. J. Mech. Appl. Math.* , 73, 24-35, 2020

A. D. Weiss, P. Rajamanickam, W. Coenen, A. L. Sánchez and F. A. Williams, "A model for the boundary layer surrounding fire whirls", *J. Fluid Mech.*, (in revision), 2020

ABSTRACT OF THE DISSERTATION

Asymptotic studies of unsteady non-premixed flamelets and buoyancy-induced swirling flows

by

Adam D. Weiss

Doctor of Philosophy in Engineering Sciences (Mechanical Engineering)

University of California San Diego, 2020

Professor Antonio L. Sánchez, Chair
Professor Forman A. Williams, Co-Chair

Asymptotic techniques are used to investigate two different phenomena, namely, acoustically driven counterflows and the flow field surrounding fire whirls.

In Part I of the dissertation, the interaction of non-premixed flamelets with acoustic waves of large characteristic wavelength, central to the development of acoustic instabilities in liquid-propellant rocket engines, is investigated using as model the counterflow diffusion flame subject to harmonic pressure and strain variations, with the presentation given in this work proceeding with increasing levels of complexity, outlined below.

In order to relate to typical experimental realizations of counterflow diffusion flames, the presentation begins with the investigation of the high-Reynolds and low-Mach number collision of two chemically frozen gaseous streams of different density. The self-similarity of the stagnation-point region is analyzed, with the strain-rate and stagnation point location, amongst other properties relevant for counterflow-flame studies, given as functions of the macroscopic properties of the experimental setup, including the nozzle-separation to semi-width ratio, for irrotational and rotational flows, with explicit formulas given for the former.

A general formulation is then provided for reacting mixing layers in counterflows subject to both time-varying strain and pressure using an inverse-thermal-conductivity-weighted coordinate which is shown to have benefits when compared to the classic Howarth-Dorodnitzyn variable. The formulation is applied to the interaction of acoustic waves with non-premixed flamelets by consideration of small amplitude harmonic oscillations of the pressure or strain-rate, with the amplitude serving as small parameter in the perturbative analysis for model one-step Arrhenius chemistry. First, the limit of infinitely fast reaction for non-unity Lewis numbers is considered. It is shown that differential-diffusion effects promote fluctuations of the flame location and reactant consumption rates. In connection with acoustic instabilities characterized by the Rayleigh index, the analysis predicts acoustic amplification for all frequencies in the pressure response, whereas a critical crossover frequency is identified in the strain response demarcating a transition between amplification and attenuation. Next, finite-rate effects are considered for systems with large activation energies. The results indicate the response for typical propellant combinations leads to acoustic amplification, not attenuation, the amplification being larger at higher strain rates.

These results, drawn on the basis of one-step model chemistry, are supplemented with numerical computations of hydrogen-air systems employing realistic chemical-kinetic mechanisms. The Rayleigh index is employed as a vehicle for quantifying inaccuracies of predictions caused by the introduction of reduced chemistry to decrease computation times. The computations indicate that inaccuracies of a systematically reduced 2-step mechanism, derived from a detailed 12-step

mechanism for hydrogen-air systems, are small at low strain rates but become appreciable as extinction is approached.

Part II of the dissertation describes the steady axisymmetric structure of the cold boundary-layer flow surrounding fire whirls developing over localized fuel sources lying on a horizontal surface. The structure is shown to consist of three separate regions, including an outer inviscid swirling region, a near-wall boundary layer and a near-axis non-slender collision region, each described sequentially. Particular attention is given to the terminal shape of the boundary-layer velocity near the axis, displaying a three-layered structure described by matched asymptotic expansions. The resulting composite expansion, dependent on the level of ambient swirl, is useful in mathematical formulations of localized fire-whirl flows, providing consistent boundary conditions for further numerical investigations.

Part I

Acoustic response of non-premixed flamelets

Brief overview of Part I

A brief overview of each chapter of Part I is given in the following five paragraphs, respectively.

In chapter 1, the planar laminar flow resulting from the impingement of two gaseous jets of different density issuing into an open space from aligned steadily fed slot nozzles of semi-width H separated a distance $2L$ is investigated by numerical and analytical methods, with specific consideration given to the high-Reynolds and low-Mach number conditions typically present in counterflow-flame experiments, for which the flow is nearly inviscid and incompressible. It is shown that introduction of a density-weighted vorticity-stream function formulation effectively reduces the problem to one involving two jets of equal density, thereby removing the vortex-sheet character of the interface separating the two jet streams. Besides the geometric parameter L/H, the solution depends only on the shape of the velocity profiles in the feed streams and on the jet momentum-flux ratio. While conformal mapping can be used to determine the potential solution corresponding to uniform velocity profiles, numerical integration is required in general to compute rotational flows, including those arising with Poiseuille velocity profiles, with simplified solutions found in the limits $L/H \ll 1$ and $L/H \gg 1$. The results are used to quantify the near-stagnation-point region, of interest in counterflow-flame studies, including the local value of the strain rate as well as the curvature of the separating interface and the variations of the strain rate away from the stagnation point.

A general formulation is given in chapter 2 for the description of reacting mixing layers in stagnation-type flows subject to both time-varying strain and pressure. The salient feature of the formulation is the introduction of a thermal-conductivity-weighted transverse coordinate that leads to a compact transport operator that facilitates numerical integration and theoretical analysis. For steady counterflow mixing layers the associated transverse mass flux is shown to be effectively linear in terms of the new coordinate, so that the conservation equations for energy and

chemical species uncouple from the mass and momentum conservation equations, thereby greatly simplifying the solution. Comparisons are shown with computations of diffusion flames with infinitely fast reaction using both the classic Howarth-Dorodnitzyn density-weighted coordinate and the new thermal-conductivity-weighted coordinate, illustrating the advantages of the latter. Also, as an illustrative application of the formulation to the computation of unsteady counterflows, the flame response to harmonically varying strain is examined in the linear limit.

In chapter 3, the acoustic response of strained nonpremixed flames is investigated using as a canonical model problem the planar counterflow configuration subject to small harmonic fluctuations of the stagnation-point pressure and strain rate. To focus on effects of modified transport rates the analysis employs the limit of infinitely fast reaction for a general non-unity Lewis number of the fuel, including values of interest in hydrogen-oxygen and hydrocarbon-oxygen systems. For both acoustic-pressure and acoustic-velocity response, differential–diffusion effects are shown to promote the fluctuations of the flame location and reactant consumption rates (while in the pressure response, distinct behaviors of the flame temperature were observed depending on stoichiometry). The results are used, together with the Rayleigh criterion, to investigate the frequency dependence of the amplification/attenuation rate relevant in computations of acoustic instabilities. The analysis predicts acoustic amplification for all frequencies in the pressure response, whereas a critical crossover frequency is identified in the strain response demarcating the transition from attenuation to amplification of acoustic energy.

Chapter 4 extends the work in chapter 3 by investigating the effects of finite-rate kinetics whereby an irreversible step with an Arrhenius rate having a large activation energy is used to model the exothermic reaction between the fuel and the oxidizer. The interactions of the chemistry with the prescribed time-dependent pressure variations are analyzed by numerical and asymptotic methods for large values of the Zel'dovich number $\beta \gg 1$ measuring the temperature dependence of the heat-release rate and small values of the relative amplitude $\varepsilon \ll 1$ of the pressure fluctuation, with the the product $\beta\varepsilon$ assumed to be of order unity in the distinguished

limit addressed. Evaluations of the local Rayleigh index for $\beta\varepsilon \ll 1$ indicate that finite-rate chemical-kinetic effects dominate the acoustic pressure response of strained flamelets under conditions near diffusion-flame extinction. For robust, diffusion-controlled flames, on the other hand, unsteady modifications to the outer chemical-equilibrium transport regions flanking the reaction layer are more important but produce only moderate effects on acoustic instabilities.

The results of chapters 3 and 4, drawn on the basis of one-step model chemistry, are supplemented with numerical computations of hydrogen-air systems employing realistic chemical-kinetic mechanisms in the chapter 5. The Rayleigh index is employed as a vehicle for quantifying inaccuracies of predictions caused by the introduction of reduced chemistry to decrease computation times. The computations indicate that inaccuracies of a systematically reduced 2-step mechanism, derived from a detailed 12-step mechanism for hydrogen-air systems, are small at low strain rates but become appreciable as extinction is approached.

Chapter 1

Aerodynamics of planar counterflowing jets

1.1 Introduction

This chapter describes the impingement of two aligned gaseous jets of different density counterflowing from opposed nozzles. Counterflow jets are ubiquitous in chemical engineering applications, including different variants with nozzle separations and feed conditions designed to optimize the specific mixing and reaction needs of the given application [1]. The closely related problem of a jet impinging on a flat surface is of utmost interest in connection with the aerodynamics of VTOL aircraft [2]. Recently, counterflow jets have found application in the field of biology for use in hydrodynamic stretching of DNA molecules [3]. The specific conditions addressed here, namely, low-Mach-number jets with moderately large Reynolds numbers and nozzle separation distances of the order of the nozzle transverse size, are of interest in laminar counterflow burners, schematically represented in figure 1.1, which are used in combustion experiments to characterize the response to strain of nonpremixed and premixed flames [4]. Both axisymmetric and planar configurations are of interest in applications, with the former

geometry analyzed in recent studies [5, 6] and the latter being investigated in the present paper by a combination of analytical and numerical methods.

Planar counterflowing jets have been subject to a number of studies, mostly for configurations with identical impinging jets, whose steady solution exhibits a symmetric structure closely related to the stagnation-point flow formed by a jet impinging on a flat wall. The latter problem has been investigated at length, to characterize both the heat transfer rate [7, 8] and the resulting wall shear stress [9]. An interesting subclass of these problems includes those in which the flow is inviscid, treated numerically for the case of a nozzle-free jet with different velocity profiles by [10] and [11]. Potential flow was analyzed using conformal mapping by [12], who examined the jet issuing from an aperture on a flat wall impacting normally on a parallel wall. The presence of a nozzle was described approximately for potential flow in the work of [2] by prescribing the condition of parallel flow at a finite distance from the wall, thereby extending the classical result of an irrotational free jet impinging on a wall (or colliding against an identical free jet). Li and collegues [13, 14] described the stability of the counterflowing jet flow with and without excitation to describe the oscillations of the stagnation plane. Effects of confinement on the oscillations were addressed in the stability analysis of [15] to characterize the dependence of the dynamics observed in experiments [16, 17] on the Reynolds number and on the geometry, defined by the ratio of nozzle spacing to nozzle radius.

Unequal counterflowing planar jets, with and without vorticity, have received considerably less attention. The previous studies have focused on colliding jets confined in channels [18–20], including the stability of the resulting configuration [15]. To the best of our knowledge, the case of two planar jets issuing into an open space from aligned nozzles, relevant for slot-jet counterflow combustors, has not been addressed in previous work.

1.2 The flow structure in counterflow combustors

Counterflow burners are widely used in experiments of premixed, partially premixed, and non-premixed flames. The planar flow sketched in figure 1.1 is relevant in connection to slot-jet burners, used for instance in studies of edge-flame propagation [21–24]. The spanwise length of these slot burners is sufficiently large to ensure that the resulting flow is locally planar away from the edges. In the figure, two opposed planar jets with volumetric flow rates $2Q_1$ and $2Q_2$ issue into a stagnant atmosphere from aligned screen-free nozzles of the same semi-width H placed at a separation distance $2L$. In typical combustion experiments the mass fractions, density, temperature, and transport coefficients are uniform upstream from the nozzle exit, although they take in general different values in each of the feed streams, denoted by the subscripts 1 and 2, including densities ρ_1^* and ρ_2^* and viscosities μ_1^* and μ_2^*. The shape of the velocity profiles in the feed streams depends on the development of the flow in the nozzle upstream from the exit plane. Sufficiently long nozzles result in Poiseuille velocity profiles, that being the case considered in figure 1.1, while short nozzles give velocity profiles that are uniform outside near-wall boundary layers.

The mean jet velocity $U_m = Q_1/H \sim Q_2/H$ used in experiments is much smaller than the speed of sound, resulting in a low-Mach-number flow with spatial pressure variations that are much smaller than the ambient pressure. For laminar flame experiments, the specific selection of the geometry and injection conditions seeks to provide steady buoyancy-free laminar conditions in the central near-stagnation-point region, of primary interest for combustion tests (see [25] for a detailed discussion of scaling criteria for counterflow burners). For instance, the jet velocity and nozzle size must be such that $U_m^2/(gH) \gg 1$ to minimize buoyancy effects, associated with density differences between the two feed streams and the surrounding ambient air or with those induced in the near-flame region.

The typical values of the Reynolds number

$$Re = \frac{\rho_1^* U_m H}{\mu_1^*} \sim \frac{\rho_2^* U_m H}{\mu_2^*} \tag{1.1}$$

range from about a hundred to about a thousand, so that the flow in the collision region is nearly inviscid. Molecular transport effects, including effects of viscous stresses, mixing, and heat conduction, are confined to thin layers, of small characteristic thickness $H/Re^{1/2} \ll 1$. As indicated in the insets of figure 1.1, one of the mixing layers is localized at the fluid surface separating the two jets, which departs from the central stagnation point, and the others at the fluid surfaces originating at the rims of the nozzles, separating the jets from the outer stagnant gas. For the moderately large values of the Reynolds number found in applications, the shear-driven instabilities affecting the mixing layers develop at a sufficiently slow rate for the central near-stagnation point region to remain virtually steady, as verified in recent direct numerical simulations [6].

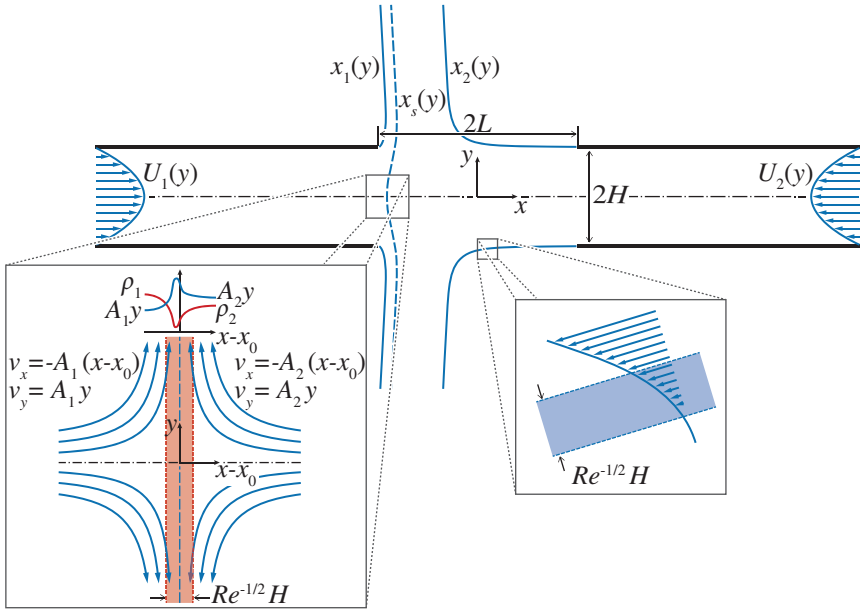

Figure 1.1: Schematic representation of the counterflow configuration considered here, including a detailed view of the self-similar region around the stagnation point. The streamlines $x_1(y)$, $x_2(y)$, and $x_s(y)$ bounding the jets correspond to numerical integrations with $L/H = 2$, $\rho_2^*/\rho_1^* = 4$, $Q_2/Q_1 = 1.5$, $Re = 500$, and Poiseuille velocity profiles in the feed streams.

In combustion applications the flame is embedded in the mixing layer localized between the two opposing streams, where molecular transport and chemical reaction occur. The changes in temperature and density associated with the chemical heat release are confined to the interior of this thin separating mixing layer, whereas the temperature and density (and also the composition) remain uniform outside, and take in general different values on either side of the mixing layer, equal to those in the corresponding feed streams. Therefore, at leading order in the limit $Re \gg 1$ the outer flow reduces to the inviscid collision of two jet streams of different density ρ_1^* and ρ_2^* bounded by sharp interfaces, whose location is to be calculated in a complicated free-boundary problem by using the condition of negligible pressure jump across the boundary interfaces [26]. The solution for the inviscid outer flow provides in particular the tangential velocity found on both sides of the interface separating the two jets, with a velocity jump occurring when the colliding jets have dissimilar density $\rho_1^* \neq \rho_2^*$, as follows from the condition of equal pressure. This vortex-sheet character is not present in opposed jets with $\rho_1^* = \rho_2^*$, for which the resulting inviscid velocity field remains continuous at the separating interface, thereby simplifying the solution.

The solution for the flow inside the slender mixing layer separating the two jets requires consideration of molecular-transport effects and, in combustion applications, also of chemical reactions. The problem, which can be formulated in the boundary-layer approximation, depends on the outer inviscid flow through the streamwise distribution of tangential velocity found on both sides of the mixing layer. The solution provides the transverse distributions of temperature, density, and composition, with boundary values given by the uniform properties of the bounding inviscid streams, different in general on both sides. As a result of the chemical heat release, the temperature is found to reach a maximum at the flame. Correspondingly, the density profile across the mixing layer, with boundary values ρ_1^* and ρ_2^*, exhibits a minimum at the flame, as indicated in the inset of figure 1.1, whereas the radial velocity has an overshoot there, resulting from the action of the pressure gradient imposed on the heated gas by the outer flow. The solution

for the inner structure of the mixing layer provides in particular the small values of the transverse velocity, of order $U_m/Re^{1/2}$, found at the outer edges of the mixing layer, resulting from the thermal expansion associated with the chemical heat released at the flame. As shown by [27], these displacement velocities determine the first-order corrections to the outer inviscid flow, of order $Re^{-1/2}$, which could be computed to increase the accuracy of the description, following a rigorous matched-asymptotic analysis for $Re \gg 1$.

The description of the counterflow is simplified at distances from the stagnation point small compared with H, in a central region where the flow is self-similar, both outside and inside the mixing layer. The local velocity in the inviscid streams is given by the stagnation-point potential solution, including a radial velocity along the interface separating the two jets that increases linearly with the distance to the centreline y^* according to $A_1^* y^*$ in the inviscid stream 1 and $A_2^* y^*$ in the inviscid stream 2. The stagnation-point strain rates A_1^* and A_2^*, of order U_m/H, are related by $\rho_1^* A_1^{*2} = \rho_2^* A_2^{*2}$, as follows from the condition of equal pressure on both sides of the mixing layer. The flow in the reactive mixing layer in this near-stagnation-point region is also self-similar, with the temperature and composition varying with the distance to the stagnation plane. The resulting one-dimensional counterflow problem, which has been the basis for studies of flame-flow interactions in nonpremixed and premixed combustion [4], is amenable to numerical integration by standard commercial codes. The solution depends on the outer flow only through the value of the strain rate at the stagnation point $A_1^* = (\rho_2^*/\rho_1^*)^{1/2} A_2^*$, the reciprocal of which being the relevant local stretch time [28]. As mentioned above, at leading order in the limit $Re \gg 1$ the value of $A_1^* = (\rho_2^*/\rho_1^*)^{1/2} A_2^*$ can be determined, with small relative errors of order $Re^{-1/2} \ll 1$, from the analysis of the inviscid collision of two jets of different density, as done earlier in connection with axisymmetric counterflows [6]. The corresponding analysis for the case of planar jets, of direct interest for slot-jet counterflow burners, is to be presented below.

The description of inviscid counterflowing jets requires in general numerical integration of the Euler equations. It will be seen below in §1.3 that the problem can be reduced by introducing

density-weighted variables to one involving equal densities in both streams, resulting in a continuous velocity across the surface separating both jets. Feed streams with uniform and Poiseuille velocity profiles will be considered in the analysis. The potential-flow solution associated with feed streams with uniform velocity profiles will be analyzed in §1.4 by conformal–mapping techniques based on Kirchhoff's method [29–31], with details of the needed mathematical development presented in an appendix. Numerical integrations of the Euler and Navier–Stokes equations will be used in §1.5 to quantify rotational flows for the case of Poiseuille velocity profiles in the feed streams. The analytical and numerical results are used to quantify many different relevant aspects of the flow, including the shape of the jet boundaries and the location and morphology of the near-stagnation-point region, the latter of direct interest in combustion applications. Finally, concluding remarks are given in §6.5.

1.3 Formulation

The problem to be analyzed below is the buoyancy-free low-Mach-number planar flow, symmetric about the centreline, resulting from the collision of two steadily fed gaseous jets of different density. Cartesian coordinates $\boldsymbol{x} = (x, y)$ centred at the middle point will be used in the description, with x and y denoting the longitudinal and transverse distances scaled with H. The mean velocity $U_m = Q_1/H$ in stream 1 will be used as characteristic scale for the dimensionless velocity $\boldsymbol{v} = (v_x, v_y)$, resulting in the nondimensional conservation equations

$$\boldsymbol{\nabla} \cdot (\rho \boldsymbol{v}) = 0, \tag{1.2}$$

$$\rho \boldsymbol{v} \cdot \boldsymbol{\nabla} \boldsymbol{v} = -\boldsymbol{\nabla} p' + \frac{1}{Re} \boldsymbol{\nabla} \cdot [\mu (\boldsymbol{\nabla} \boldsymbol{v} + \boldsymbol{\nabla} \boldsymbol{v}^T)], \tag{1.3}$$

$$\rho \boldsymbol{v} \cdot \boldsymbol{\nabla} T = \frac{1}{PrRe} \boldsymbol{\nabla} \cdot (k \boldsymbol{\nabla} T), \tag{1.4}$$

$$\rho \boldsymbol{v} \cdot \boldsymbol{\nabla} Y_i = \frac{1}{Sc_i Re} \boldsymbol{\nabla} \cdot (\rho D_i \boldsymbol{\nabla} Y_i), \tag{1.5}$$

with the equation of state taking the simplified form

$$\rho T \sum_i \frac{W_1}{W_i} Y_i = 1. \tag{1.6}$$

These equations must be complemented with expressions for the variation of the transport parameters μ, k, and D_i with the temperature and composition. The properties of stream 1 have been used to define dimensionless quantities, including the temperature T, density ρ, viscosity μ, thermal conductivity k, and diffusion coefficient D_i of chemical species i. The composition is described in terms of the mass fractions Y_i of species i, with W_i representing in (1.6) its molecular mass and $W_1 = 1/(\sum_i Y_{i1}/W_i)$ being the mean molecular mass in stream 1. In the momentum equation, p' represents the pressure difference from the ambient value scaled with $\rho_1^* U_m^2$. The parameters appearing in the above equations include the Prandtl and Schmidt numbers Pr and Sc_i, and the Reynolds number Re defined in (1.1), the latter taking moderately large values in typical combustion applications.

1.3.1 Nearly inviscid flow

In the limit $Re \gg 1$, the shear layers bounding the jets, of characteristic thickness $Re^{-1/2}H$ at distances of order H, appear as infinitesimally thin surfaces. As indicated in figure 1.1, the two impinging streams are separated by the streamline $x = x_s(y)$ departing from the stagnation point $\boldsymbol{x}_o = (x_o, 0)$. In addition, each jet is separated from the outer stagnant gas by the streamline $x = x_1(y)$ and $x = x_2(y)$, respectively, each originating from their respective nozzle rim $(x,y) = (-L/H, 1)$ and $(x,y) = (L/H, 1)$. These bounding surfaces are unknowns to be determined as part of the solution of a free-boundary problem, to be formulated below.

Consideration of the limit $Re \gg 1$ in (1.4) and (1.5) leads to $\boldsymbol{v} \cdot \boldsymbol{\nabla} T = \boldsymbol{v} \cdot \boldsymbol{\nabla} Y_i = 0$, indicating that the temperature and composition remain constant along any given streamline in

the nearly inviscid jets outside the bounding mixing layers. Using these equations in (1.6) yields

$$\boldsymbol{v} \cdot \boldsymbol{\nabla} \rho = 0, \tag{1.7}$$

a result that can be used in (1.2) to give

$$\boldsymbol{\nabla} \cdot \boldsymbol{v} = 0 \tag{1.8}$$

and in (1.3) to give $\boldsymbol{v} \cdot \boldsymbol{\nabla}(p' + \rho \boldsymbol{v}^2/2) = 0$. The latter corresponds to the familiar condition of constant stagnation pressure $p' + \rho \boldsymbol{v}^2/2$ along streamlines, yielding in particular

$$p' + \rho \boldsymbol{v}^2/2 = p'_o \tag{1.9}$$

along the centreline, where p'_o is the pressure at the stagnation point $\boldsymbol{x}_o$, and

$$|\boldsymbol{v}| = \text{constant at } x = x_1(y) \text{ and at } x = x_2(y) \tag{1.10}$$

along the streamlines separating the jets from the stagnant air, where $p' = 0$, with the constant taking in general different values on the surface of each jet.

According to (1.7), for inviscid incompressible flow each streamline carries the value of the density, so that the density field in the jet collision region is linked to the upstream boundary distributions of density in the feed streams. In configurations in which the density of the feed streams is nonuniform, the resulting density is different along different streamlines. In that case, vorticity is generated in the jet collision region as a result of the interaction of misaligned pressure and density gradients. This additional vorticity production supplements the vorticity already carried by the feed streams. The analysis below is restricted to configurations involving feed streams with uniform temperature and uniform composition, typically encountered in experiments,

for which the density in each one of the jets is uniform, given by $\rho = 1$ in jet 1 and $\rho = \rho_2^*/\rho_1^*$ in jet 2. Correspondingly, the baroclinic torque is negligible everywhere, except at the vortex sheet $x = x_s(y)$, where it generates a velocity jump according to

$$|\boldsymbol{v}|_1^2 = (\rho_2^*/\rho_1^*)|\boldsymbol{v}|_2^2 \text{ along } x = x_s(y), \tag{1.11}$$

with the subscripts 1 and 2 denoting the velocities on the left and right sides of the interface. The above equation follows from the condition of zero pressure jump across the interface separating the two jets, with the pressure evaluated with use made of $p' + \rho \boldsymbol{v}^2/2 =$ constant on both sides of $x = x_s(y)$. Along all other streamlines the vorticity magnitude $\omega = \partial v_y/\partial x - \partial v_x/\partial y$ remains constant, with a value equal to that found in the feed streams, to be determined from the boundary velocity distributions

$$\begin{cases} \boldsymbol{v} = u_1(y)\boldsymbol{e}_x & \text{as} \quad x \to -\infty, \\ \boldsymbol{v} = -(Q_2/Q_1)u_2(y)\boldsymbol{e}_x & \text{as} \quad x \to \infty, \end{cases} \tag{1.12}$$

where $u_1(y)$ and $u_2(y)$ represent nondimensional shape functions satisfying $\int_0^1 u_1 \mathrm{d}y = \int_0^1 u_2 \mathrm{d}y = 1$. For example $u_1 = u_2 = 1$ and $u_1 = u_2 = (3/2)(1-y^2)$ for uniform and parabolic Poiseuille distributions, respectively.

In the vicinity of $\boldsymbol{x}_o = (x_o, 0)$, the velocity is given by the well-known stagnation-point distribution

$$\begin{cases} -v_x/(x-x_o) = v_y/y = A_1 & \text{in stream 1}, \\ -v_x/(x-x_o) = v_y/y = A_2 & \text{in stream 2}, \end{cases} \tag{1.13}$$

where the dimensionless strain rates $A_1 = A_1^*/(Q_1/H^2)$ and $A_2 = A_2^*/(Q_1/H^2)$ are related by

$$A_1 = (\rho_2^*/\rho_1^*)^{1/2} A_2, \tag{1.14}$$

consistent with (1.11). As previously mentioned, this inviscid value of the strain rate, to be

quantified below in terms of the parameters defining the opposed-nozzle flow (i.e. L/H, ρ_2^*/ρ_1^*, and Q_2/Q_1), determines the near-stagnation-point solution for the thin reactive mixing layer separating the two jet streams. The accuracy of the selfsimilar mixing-layer solution, which applies strictly at the centreline, can be expected to degrade with increasing distances from the stagnation point as a result of curvature effects and of departures of the outer velocity from the linear distributions $v_y = A_1 y$ and $v_y = A_2 y$. Curvature effects can be quantified by computing the shape of the separating streamline $x = x_s(y)$ away from the centreline, given by

$$x_s = x_o + y^2/(2r_c), \tag{1.15}$$

with r_c representing the local radius of curvature. On the other hand, the variations of the velocity on both sides of the separating vortex sheet are of the form

$$|\boldsymbol{v}|_1 = (v_y)_1 = A_1 y + A_1'' y^3/6 \text{ and } |\boldsymbol{v}|_2 = (v_y)_2 = A_2 y + A_2'' y^3/6, \tag{1.16}$$

written with account taken of the result $\partial^2 v_y/\partial y^2 = 0$ at $y = 0$, stemming from the symmetry condition $\partial v_x/\partial y = 0$ at $y = 0$ and the solenoidal character of the velocity field. Clearly, configurations with smaller values of r_c^{-1} and $A_1'' = (\rho_2^*/\rho_1^*)^{1/2} A_2''$ can be expected to exhibit an extended domain where the mixing layer is planar and is subject to a constant strain rate. In that respect, quantifications of the near-stagnation-point region based on the inviscid solution can be useful in assessing the range of validity of the one-dimensional selfsimilar description for the reactive mixing layer.

1.3.2 Vorticity-stream function formulation

In view of (1.8) the problem can be formulated in terms of the standard stream function ψ, related to the vorticity by

$$\frac{\partial^2\psi}{\partial x^2}+\frac{\partial^2\psi}{\partial y^2}=-\omega. \tag{1.17}$$

The vorticity is constant along the streamlines, so that $\omega=\Omega(\psi)$, with the function $\Omega(\psi)$ determined implicitly through the expressions

$$\begin{cases}\Omega=-\dfrac{\mathrm{d}u_1}{\mathrm{d}y}, \quad \psi=\displaystyle\int_0^y u_1\mathrm{d}y, \quad \text{for} \quad 0\le\psi\le 1\\ \Omega=\left(\dfrac{Q_2}{Q_1}\right)\dfrac{\mathrm{d}u_2}{\mathrm{d}y}, \quad \psi=-\left(\dfrac{Q_2}{Q_1}\right)\displaystyle\int_0^y u_1\mathrm{d}y, \quad \text{for} \quad -Q_2/Q_1\le\psi\le 0\end{cases} \tag{1.18}$$

derived with use of the boundary distributions (1.12). The problem reduces to the integration of

$$\frac{\partial^2\psi}{\partial x^2}+\frac{\partial^2\psi}{\partial y^2}=-\Omega(\psi), \tag{1.19}$$

supplemented with the implicit definition of $\Omega(\psi)$ given in (1.18) and subject to the boundary conditions

$$\psi=0 \begin{cases}\text{at } y=0 \text{ for } -\infty<x<+\infty\\ \text{and at } x=x_s(y) \text{ for } y\ge 0,\end{cases} \tag{1.20}$$

$$\psi=1 \begin{cases}\text{at } y=1 \text{ for } -\infty<x<-L/H\\ \text{and at } x=x_1(y) \text{ for } y\ge 1,\end{cases} \tag{1.21}$$

$$\psi=-Q_2/Q_1 \begin{cases}\text{at } y=1 \text{ for } L/H<x<\infty\\ \text{and at } x=x_2(y) \text{ for } y\ge 1.\end{cases} \tag{1.22}$$

The surfaces $x_s(y)$, $x_1(y)$, and $x_2(y)$ are unknown free boundaries to be determined with use made of the additional boundary conditions (1.10) and (1.11), written in the form

$$\begin{cases} \frac{1}{2}|\nabla\psi|^2 = p'_o - \frac{1}{2}[u_1^2(0) - u_1^2(1)] & \text{at} \quad x = x_1(y), \\ \frac{1}{2}(\rho_2^*/\rho_1^*)|\nabla\psi|^2 = p'_o - \frac{1}{2}(\rho_2^*/\rho_1^*)(Q_2/Q_1)^2[u_2^2(0) - u_2^2(1)] & \text{at} \quad x = x_2(y), \end{cases} \tag{1.23}$$

and

$$|\nabla\psi|_1^2 = (\rho_2^*/\rho_1^*)|\nabla\psi|_2^2 \quad \text{at} \quad x = x_s(y), \tag{1.24}$$

respectively. In writing (1.23) from (1.10) we have used (1.9) to express the pressure for the parallel flow in the nozzles far upstream from the exit in terms of the stagnation-point pressure p'_o.

1.3.3 Reduction to the case of equal densities

The problem defined in (1.18)–(1.24) determines the stream function $\psi(x,y)$ along with the jet boundaries $x_1(y)$, $x_2(y)$, and $x_s(y)$, and the stagnation-point pressure p'_o. Besides the shapes of the velocity profiles in the feed streams, defined by the functions $u_1(y)$ and $u_2(y)$, the solution depends on three parameters, namely, L/H, Q_2/Q_1, and ρ_2^*/ρ_1^*. As noted earlier in connection with axisymmetric jets [6], the solution can be simplified by incorporating a renormalization factor $(\rho_2^*/\rho_1^*)^{1/2}$ in the definition of the kinematic variables for the fluid of density ρ_2^*. Specifically, we introduce new density-weighted functions $\hat{\psi}$ and $\hat{\Omega}$, defined by

$$\hat{\psi} = \begin{cases} \psi, & \\ (\rho_2^*/\rho_1^*)^{1/2}\psi, & \end{cases} \quad \text{and} \quad \hat{\Omega} = \begin{cases} \Omega, & \text{for} \quad \psi > 0 \\ (\rho_2^*/\rho_1^*)^{1/2}\Omega, & \text{for} \quad \psi < 0, \end{cases} \tag{1.25}$$

to write (1.19) as

$$\frac{\partial^2\hat{\psi}}{\partial x^2} + \frac{\partial^2\hat{\psi}}{\partial y^2} = -\hat{\Omega}(\hat{\psi}), \tag{1.26}$$

to be integrated with the boundary conditions

$$\begin{cases} \hat{\psi} = 0 & \text{at} \quad y = 0 \quad \text{for} \quad -\infty < x < +\infty \\ \hat{\psi} = 1 & \text{at} \quad y = 1 \quad \text{for} \quad -\infty < x < -L/H \\ \hat{\psi} = -\Lambda & \text{at} \quad y = 1 \quad \text{for} \quad L/H < x < +\infty \end{cases} \tag{1.27}$$

and

$$\begin{cases} \hat{\psi} = 1, \qquad \frac{1}{2}|\nabla\hat{\psi}|^2 = p_o' - \frac{1}{2}[u_1^2(0) - u_1^2(1)], \quad \text{at } x = x_1(y) \\ \hat{\psi} = -\Lambda, \quad \frac{1}{2}|\nabla\hat{\psi}|^2 = p_o' - \frac{1}{2}\Lambda^2[u_2^2(0) - u_2^2(1)] \quad \text{at } x = x_2(y), \end{cases} \tag{1.28}$$

which follow from (1.20)–(1.23), respectively, whereas the dynamic condition (1.24) is automatically satisfied provided that $\nabla\hat{\psi}$ is continuous, thereby removing the need to consider the separating surface $x_s(y)$ as a free boundary. In the reduced formulation the ratios Q_2/Q_1 and ρ_2^*/ρ_1^* appear jointly in the new parameter

$$\Lambda = \left(\frac{\rho_2^*}{\rho_1^*}\right)^{1/2}\left(\frac{Q_2}{Q_1}\right), \tag{1.29}$$

with Λ^2 representing a measure of the ratio of jet momentum fluxes. The function $\hat{\Omega}(\hat{\psi})$, identically zero for uniform velocity in the feed streams, can be determined in general from (1.18) written in the form

$$\begin{cases} \hat{\Omega} = -\dfrac{\mathrm{d}u_1}{\mathrm{d}y}, \quad \hat{\psi} = \displaystyle\int_0^y u_1 \mathrm{d}y, \quad \text{as} \quad x \to -\infty, \\ \hat{\Omega} = \Lambda\dfrac{\mathrm{d}u_1}{\mathrm{d}y}, \quad \hat{\psi} = -\Lambda\displaystyle\int_0^y u_2 \mathrm{d}y, \quad \text{as} \quad x \to \infty. \end{cases} \tag{1.30}$$

Inspection of (1.26)–(1.28) reveals that the transformation (1.25) effectively simplifies the problem to one involving constant density, removing the vortex-sheet character of the separating surface $x_s(y)$, and concurrently reduces the number of controlling parameters from three to only two, namely, L/H and Λ. Since the streamline pattern found with Λ is a mirror image about the

plane $x = 0$ of that found with $1/\Lambda$, only flows with $\Lambda \geq 1$ need to be considered in the following.

The jet outer interfaces $x_1(y)$ and $x_2(y)$ remain as unknown free boundaries, to be determined along with the unknown value of the stagnation pressure p'_o as part of the computation of $\hat{\psi}(x,y)$ for given values of $u_1(y)$, $u_2(y)$, Λ, and L/H. The solution provides the location of the stagnation point $\boldsymbol{x}_o = (x_o, 0)$ and also the associated local values of

$$A_o = -\left.\frac{\partial^2 \hat{\psi}}{\partial x \partial y}\right|_{\boldsymbol{x}=\boldsymbol{x}_o}, \quad \frac{1}{r_c} = \frac{1}{3A_o}\left.\frac{\partial^3 \hat{\psi}}{\partial y^3}\right|_{\boldsymbol{x}=\boldsymbol{x}_o}, \text{ and } A''_o = -\left.\frac{\partial^4 \hat{\psi}}{\partial x \partial y^3}\right|_{\boldsymbol{x}=\boldsymbol{x}_o}, \tag{1.31}$$

with $A_o = A_1 = (\rho_2^*/\rho_1^*)^{1/2} A_2$ and $A''_o = A''_1 = (\rho_2^*/\rho_1^*)^{1/2} A''_2$. The free-boundary problem formulated above has analytical solutions only for configurations with uniform velocity distributions in the feed streams, such that $\hat{\Omega}$ is identically zero, that being the case considered in the following section, with rotational solutions addressed in §1.5.

1.4 Irrotational counterflow jets

1.4.1 General considerations

When the velocity profiles in the feed streams are uniform, the vorticity function $\hat{\Omega}$ in (1.26) is identically zero, so that the inviscid flow is irrotational. With $u_1 = u_2 = 1$, the stagnation pressure in both feed streams is uniform, equal to the stagnation-point pressure p'_o. The presence of the collision region generates an overpressure in the feed streams upstream from the nozzle exit, given by $p'_1 = p'_o - 1/2 \geq 0$ and $p'_2 = p'_o - \Lambda^2/2 \geq 0$, respectively. The boundary condition (1.28) on the jet surface reduces to

$$\begin{cases} \hat{\psi} = 1, & \frac{1}{2}|\boldsymbol{\nabla}\hat{\psi}|^2 = p'_o, \quad \text{at } x = x_1(y), \\ \hat{\psi} = -\Lambda, & \frac{1}{2}|\boldsymbol{\nabla}\hat{\psi}|^2 = p'_o, \quad \text{at } x = x_2(y), \end{cases} \tag{1.32}$$

revealing in particular that the speed $|\nabla\hat{\psi}|$ remains constant along these free surfaces, with a value given by $U=\sqrt{2p'_o}$, to be determined as part of the analysis.

The configuration depicted in figure 1.2 corresponds to $L\sim H$, the case typically encountered in counterflow burners. Large and small values of L/H, also considered below, are of interest in chemical engineering applications [1]. For large separation distances, in the symmetric case $\Lambda=1$ the problem reduces to the classical problem of collision of two free jets [29–31], with the stagnation plane $x=0$ located far from both nozzle exits. This symmetric configuration is known to be prone to oscillatory instabilities [13] that cause the stagnation plane to shift alternatively between both nozzle exits. Configurations with unbalanced momentum flux (i.e. $\Lambda\neq 1$) result in the collision region migrating to the vicinity of the nozzle carrying less momentum (the left nozzle in the cases $\Lambda>1$ considered here). In that case, the presence of a collision region has little effect on the flow at the outlet of nozzle 2, where the overpressure is $p'_2=0$ and the velocity profile remains uniform with magnitude Λ, so that for $L/H\gg 1$ and $\Lambda>1$ the constant free streamline speed U is simply equal to Λ.

The collision of the opposed jets results in two symmetric jets that emerge laterally, as shown in figure 1.2. At transverse distances large compared with H the streamlines in these lateral jets become aligned as the pressure approaches the ambient pressure $p'=0$, with the velocity correspondingly approaching the unknown uniform value $U=\sqrt{2p'_o}$ across the jet, as follows from conservation of stagnation pressure along the streamlines. Conservation of mass and of longitudinal momentum provides the two relationships

$$\frac{h}{H}U=1+\Lambda \quad \text{and} \quad \frac{h}{H}U^2\sin\alpha=(\Lambda^2-1)/2, \tag{1.33}$$

respectively, involving the thickness h/H and deflection angle α of the lateral jet far from the opening, the latter measured relative from the y-axis. These two expressions can be combined

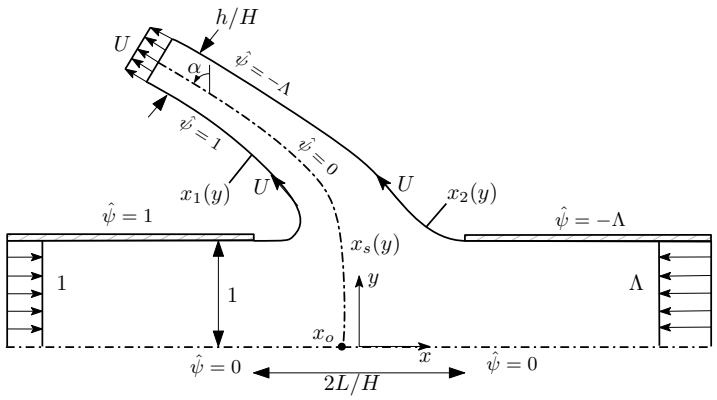

Figure 1.2: Schematic view of the collision region for $L/H \sim 1$ and uniform velocity profiles in the feed streams.

with $U = \sqrt{2p'_o} = \sqrt{\Lambda^2 + 2p'_2}$ to give

$$\sin\alpha = \frac{\Lambda - 1}{2U} = \frac{1}{2}\frac{1 - 1/\Lambda}{(1 + 2p'_2/\Lambda^2)^{1/2}}, \tag{1.34}$$

involving the unknown overpressure $p'_2 \geq 0$ in the feed stream 2. As can be seen, the value of α, identically zero in the symmetric case $\Lambda = 1$, increases for increasing values of Λ. An interesting conclusion stemming from (1.34) is that for the opposed-jet arrangement investigated here (i.e. aligned jets issuing from nozzles of equal radius) the lateral-jet deflection is limited to a maximum value $\alpha = \pi/6$, achieved for $\Lambda \gg 1$ when the nozzles are placed far apart, so that the pressure in nozzle 2 equals the ambient value $p'_2 = 0$.

The thickness of the shear layers at the periphery of the lateral jets, small in the collision region, grow with distance, so that the potential description given here fails at distances of the order of *Re* times the jet width *h*. Consideration of viscous effects, which are significant all across the jet in this far-field region, would be needed to describe the transition of the jet velocity profile from the uniform value U to the far-field Bickley profile, as done by [32].

1.4.2 Selected potential-flow formulae

The solution simplifies for $L/H \ll 1$, in that the flow in the nozzles away from the small opening, including the central region near the stagnation point, is independent of the lateral emerging jets, with the opening acting as an apparent point sink of strength $(1+\Lambda)$ for the flow in the nozzles. The solution can be determined using superposition of a uniform flow and a sink in a channel [see 31] to give

$$\hat{\psi} = y - \frac{1+\Lambda}{\pi} \arctan\left[\frac{e^{\pi x}\sin(\pi y)}{e^{\pi x}\cos(\pi y)+1}\right]. \tag{1.35}$$

The above expression can be used to determine the stagnation–point axial location from the condition $\partial\hat{\psi}/\partial y = 0$ at $y = 0$ as well as the values of A_o, r_c^{-1}, and A_o'' from (1.31), yielding

$$x_o = \frac{1}{\pi}\ln(1/\Lambda), \quad A_o = \frac{\pi\Lambda}{\Lambda+1}, \quad r_c = \frac{3(\Lambda+1)}{\pi(\Lambda-1)}, \text{ and } A_o'' = -\frac{\pi^3\Lambda(\Lambda^2-4\Lambda+1)}{(\Lambda+1)^3}, \tag{1.36}$$

independent of L/H. The high-speed flow at distances of order $L \ll H$ from the opening corresponds to the potential solution for the discharge of a pressurized container through an aperture, described for instance on pp. 310–311 of [31], including an emerging jet with

$$\frac{h}{H} = \frac{2\pi}{2+\pi}\frac{L}{H} \quad \text{and} \quad U = \frac{2+\pi}{2\pi}\frac{1+\Lambda}{L/H}, \tag{1.37}$$

with the associated value of $h/(2L) = \pi/(2+\pi) \simeq 0.61$ being the well-known coefficient of contraction of a planar jet. Because of its large velocity, the deflection of the emerging jet, required to accommodate the unbalanced momentum flux of the opposed streams, is very small, as can be seen by using (1.33) and (1.37) to write

$$\sin\alpha = \frac{\pi}{2+\pi}\frac{\Lambda-1}{\Lambda+1}\frac{L}{H}. \tag{1.38}$$

The derivation of the corresponding analytic solution for the potential flow in the general case $L/H \sim 1$ requires use of conformal mapping techniques. A full and systematic discussion of the needed analysis is presented in § 1.6. The development provides, in particular, the equation

$$h/H = \cos\alpha\left\{2L/H + \frac{1}{\pi U^2}\left[(U^2+1)\ln\left(\frac{U-1}{U+1}\right) + (U^2+\Lambda^2)\ln\left(\frac{U-\Lambda}{U+\Lambda}\right) + \frac{\Lambda^2-1}{2}\ln\left(\frac{2U+\Lambda-1}{2U-\Lambda+1}\right)\right]\right\}, \tag{1.39}$$

relating the three unknowns α, h/H, and U with the parameters Λ and L/H, as well as the expressions

$$A_o = \frac{\pi\Lambda U^4}{(U^2+\Lambda)^2(\Lambda+1)},\ \frac{1}{r_c} = \frac{\pi U^2(U^2-2\Lambda)(\Lambda-1)}{3(\Lambda+1)(U^2+\Lambda)^2},\ A_o'' = \frac{\pi^3 U^8\Lambda}{(\Lambda+1)^3(U^2+\Lambda)^6} \times [4U^2\Lambda(\Lambda-2)(2\Lambda-1) - U^4(\Lambda^2-4\Lambda+1) - 2\Lambda^2(3\Lambda^2-7\Lambda+3)] \tag{1.40}$$

for the stagnation–point properties in terms of U and Λ. Also, the conformal transformation provides integral expressions for the boundary surfaces $x_1(y)$ and $x_2(y)$, given in (1.67) and (1.68), and for the separating streamline $x_s(y)$ departing from the stagnation point $\boldsymbol{x}_o = (x_o, 0)$, obtained by integrating (1.65) along the contour Γ defined by (1.73), with x_o determined from (1.72).

Equations (1.40), valid in general for configurations with $L/H \sim 1$, enable quantification of stagnation-point properties in the limiting cases $L/H \ll 1$ and $L/H \gg 1$. For instance, the expressions given in (1.36) for A_o, r_c^{-1}, and A_o'' when $L/H \ll 1$ may be recovered by letting $U \to \infty$ in (1.40), the appropriate limit as $L/H \to 0$. In the opposite limit $L/H \gg 1$ the free–stream velocity reduces to $U = \Lambda$, as discussed above, so that (1.40) gives

$$A_o = \frac{\pi\Lambda^3}{(\Lambda+1)^3},\quad \frac{1}{r_c} = \frac{\pi\Lambda(\Lambda-2)(\Lambda-1)}{3(1+\Lambda)^3},\quad A_o'' = -\frac{\pi^3(\Lambda-1)^2\Lambda^5(\Lambda^2-10\Lambda+6)}{(1+\Lambda)^9} \tag{1.41}$$

as the limiting values characterizing the stagnation point for distant nozzles with $L/H \gg 1$.

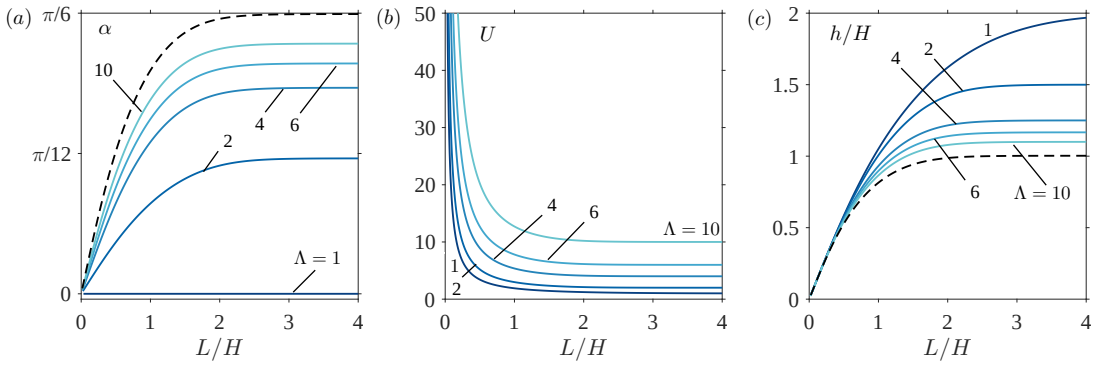

Figure 1.3: The variation with nozzle spacing L/H of the deflection α of the emerging jet (a), surface speed U (b), and emerging-jet width h/H (c) for selected values of the momentum-flux ratio Λ. The dashed line in panels (a) and (c) correspond to $\Lambda \to \infty$.

1.4.3 General dependences on L/H and Λ

The formulas developed above can be employed to determine the dependence of different flow features on the inter–nozzle spacing L/H and on the momentum-flux ratio Λ. The free-surface velocity U and the deflection angle α and dimensionless width h/H of the emerging jet are computed by solving the mass and momentum conservation equations given in (1.33) together with (1.39). For ease of calculation, it is convenient to select the values of Λ and U and then use (1.33) to determine α and h/H, with the corresponding value of L/H finally computed from (1.39). Results are shown in figure 1.3 in the extended parametric ranges $0 < L/H \leq 4$ and $1 \leq \Lambda \leq 10$.

The curves in figure 1.3 help to quantify the effect of the inter–nozzle spacing L/H on the resulting emerging jet. For small values of L/H the inter–nozzle opening appears as a small gap, so that a large stagnation pressure p'_o is needed to maintain the finite outflow rate $1+\Lambda$. This results in emerging jets with larger speeds U and smaller thicknesses h/H, as described by the asymptotic behaviors given in (1.37) and (1.38), corresponding to a jet discharging from a pressurized container through an aperture of width $2L$ on a flat wall. The opposite limit $L/H \gg 1$ corresponds to two nozzles placed at large distances. In the symmetric case $\Lambda = 1$, the two jets collide at the midpoint between the two distant nozzles, giving rise to two identical transverse jets

of width $h = 2H$ and velocity $U = 1$. When $\Lambda > 1$, the collision region migrates to the vicinity of nozzle 1, where the outgoing stream encounters the opposed jet of stream 2, which effectively behaves as a free jet with speed $U = \Lambda$. This is also the speed of the emerging jet for $L/H \gg 1$, whereas its thickness approaches $h/H = (1+\Lambda)/U = (1+\Lambda)/\Lambda$ in this same limit, as follows from continuity. The jet deflection, identically zero in the symmetric case $\Lambda = 1$, is seen to increase with increasing L/H for $\Lambda \neq 1$ to reach a maximum value $\alpha = \arcsin[(\Lambda-1)/(2\Lambda)]$ for $L/H \gg 1$, as can be obtained from (1.34) with $U = \Lambda$. As pointed out earlier, the deflection is limited to a maximum value $\alpha = \pi/6$, reached as $\Lambda \to \infty$.

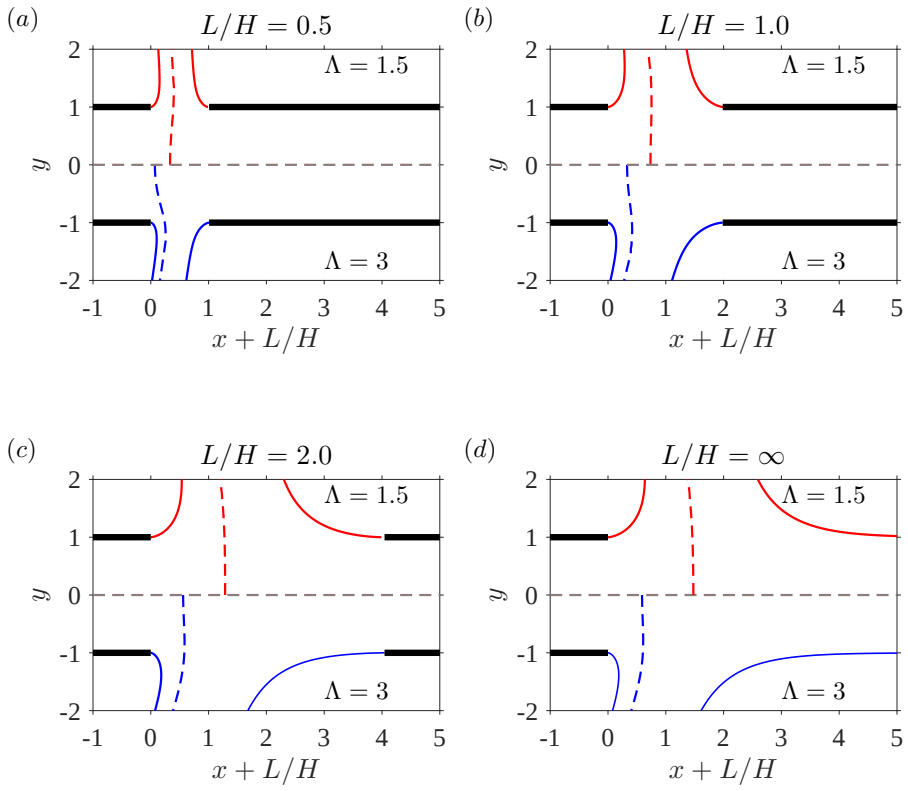

Figure 1.4: Free–streamline patterns for different values of Λ and L/H, including the outer interfaces $\hat{\psi} = 1$ and $\hat{\psi} = \Lambda$ (solid curves) and the separating interface $\hat{\psi} = 0$ (dashed curves).

The interfaces $x = x_1(y)$, $x = x_2(y)$, and $x = x_s(y)$ are shown in figure 1.4 for configurations with unbalanced momentum flux and different nozzle separation distances. As expected, a larger value of Λ results in a displacement of the stagnation point towards the jet with smaller momentum

and in a larger deflection of the emerging jet, the latter feature quantified in figure 1.3*a*. The variation with L/H of the distance $x_o + L/H$ between the stagnation point and the left nozzle is shown in figure 1.5*a*, with negative values of $x_o + L/H$ corresponding to stagnation points lying inside the left nozzle. As can be seen, for a given momentum-flux ratio the stagnation point moves for increasing L/H from the location $-\ln(\Lambda)/\pi$ corresponding to $L/H = 0$ to reach a finite distance from the nozzle as $L/H \to \infty$, the only exception being the symmetric case $\Lambda = 1$, for which the stagnation point keeps getting farther according to $x_o + L/H = L/H$. It is worth noting that for $\Lambda \gtrsim 8.4$ the stagnation point remains inside the nozzle regardless of the value of L/H.

As previously mentioned, the flame in combustion experiments is embedded in the mixing layer separating the two jets, centred about the inviscid interface $x = x_s(y)$. Interest is focused on the near-stagnation-point region, where the solution for the inner structure of the reactive mixing layer is selfsimilar in the first approximation, determined by stagnation-point values of the strain rate A_1 and A_2 found in both colliding streams outside the mixing layer, related by $A_o = A_1 = (\rho_2^*/\rho_1^*)^{1/2} A_2$. For slot nozzles with upstream uniform velocity profiles in the feed streams the analytic expression given in (1.40) can be employed to determine A_o, with Λ and L/H entering as the only controlling parameters. The value of A_o evaluated from (1.40) with the surface velocity U obtained from solving (1.33) and (1.39) is shown in figure 1.5*b* as a function of L/H for different Λ. The results indicate that A_o increases with increasing Λ and with decreasing L/H, so that the resulting values range between the minimum $A_o = \pi/8$, corresponding to symmetric configurations with distant nozzles, to the maximum $A_o = \pi$, found irrespective of the nozzle spacing when the momentum flux is severely unbalanced.

The selfsimilar solution for the counterflow mixing layer assumes a locally planar structure, with negligible curvature. In reality, however, the separating interface is curved, and there is interest in quantifying this curvature to assess departures from locally planar selfsimilar structures. This is done in figure 1.5*c* with use made of (1.40). The plots reveal that the curvature is always

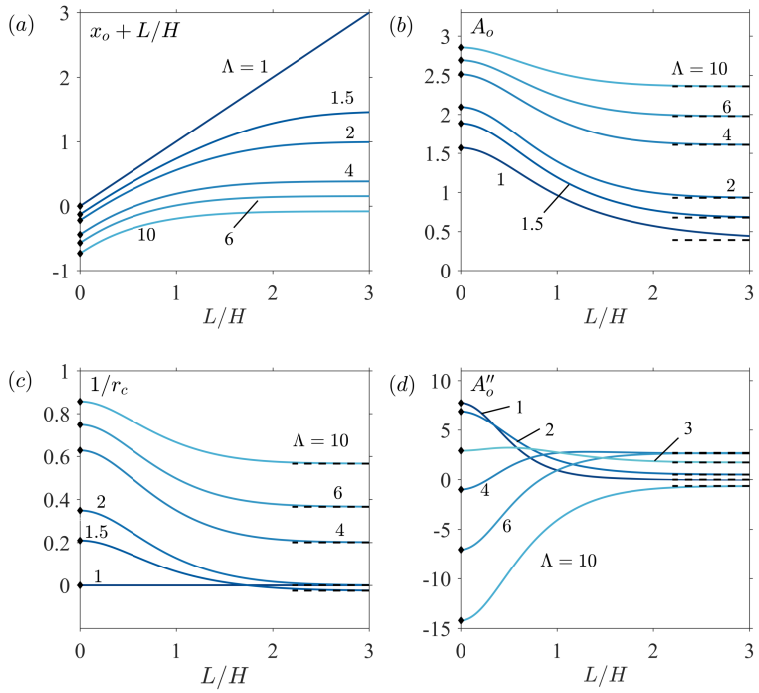

Figure 1.5: The variation with L/H of the distance of the stagnation point from the exit plane of the left nozzle $x_o + L/H$ (a), the stagnation-point strain rate A_o (b), the local curvature of the separating interface at the stagnation point $1/r_c$ (c), and the parameter A_o'' measuring the departures of the velocity from the stagnation-point solution (d) for selected values of Λ; the dots along the vertical axes represent the limiting values given in (1.36) for $L/H = 0$ whereas the dashed lines are the asymptotic values given in (1.41) for $L/H \gg 1$.

positive for $\Lambda > 2$, corresponding to convex interfaces. For values of the momentum-flux ratio in the range $1 < \Lambda < 2$, however, the curvature becomes negative for sufficiently large values of L/H, with a minimum value, reached as $L/H \to \infty$, given in (1.41). This change of sign of the curvature from convex to concave as the inter-nozzle distance is increased is apparent in the separating interfaces shown in figure 1.4 for $\Lambda = 1.5$. The results indicate that for configurations with $L/H \sim 1$ and $\Lambda \lesssim 2$, most often found in typical experimental arrangements, the separating streamline remains fairly flat, a finding that supports the neglect of curvature effects in analyzing the structure of the reactive mixing layer.

Also central to the selfsimilar character of the counterflow mixing layer is the assumption

that the velocity in the outer inviscid stream increases linearly with the streamwise distance, as occurs sufficiently close to the stagnation point. With increasing distances, however, the deviations from the linear acceleration become more noticeable, with the nondimensional parameters A_1'' and A_2'' measuring the extent of the departures, as indicated in (1.16). The value of $A_o'' = A_1'' = (\rho_2^*/\rho_1^*)^{1/2} A_2''$ evaluated from (1.40) is shown in figure 1.5*d*. For $L/H \lesssim 1$, the differences in values of A_o'' for different Λ can be fairly large, with small values of Λ resulting in accelerating flows with $A_o'' > 0$ whereas sufficiently large values yield decelerating velocities with negative A_o''. The differences diminish as the nozzle spacing increases. As seen in figures 1.5*c* and 1.5*d*, configurations with $1 \leq \Lambda \leq 2$ tend to produce relatively small values of A_o'' and $1/r_c$ for $L/H \gtrsim 1.5$, delineating an attractive parametric range for experimental designs aimed at minimizing departures of the mixing-layer structure from one-dimensional solutions.

1.5 Counterflowing jets with distributed vorticity

We now investigate flows in which $\hat{\Omega} \neq 0$, specifically considering the case of long nozzles with Poiseuille flow in each feed stream, for which $\hat{\Omega}(\hat{\psi})$ is given by the implicit representation

$$\hat{\psi} = \begin{cases} (\hat{\Omega}/6)\{3 - (\hat{\Omega}/3)^2\} & \text{for} \quad \hat{\psi} > 0 \\ (\hat{\Omega}/6)\{3 - [\hat{\Omega}/(3\Lambda)]^2\} & \text{for} \quad \hat{\psi} < 0 \end{cases} \tag{1.42}$$

as follows from (1.30) with $u_1 = u_2 = (3/2)(1-y^2)$. The description of the inviscid flow requires numerical integration of (1.26)–(1.28), with the interfaces $x = x_1(y)$ and $x = x_2(y)$ entering as free boundaries. The constant speeds along these interfaces are given from (1.28) by $U_1 = [2p_o' - (3/2)^2]^{1/2}$ and $U_2 = [2p_o' - (3/2)^2\Lambda^2]^{1/2}$, respectively, where p_o' is the stagnation-point pressure. The boundary distribution of stagnation pressure $p' + \frac{1}{2}|\nabla\hat{\psi}|^2$ is given by $p_o' + \frac{1}{2}(3/2)^2[(1-y^2)^2 - 1]$ in stream 1 and by $p_o' + \frac{1}{2}(3/2)^2\Lambda^2[(1-y^2)^2 - 1]$ in stream 2, respectively. Since the stagnation pressure is different for different streamlines, the velocity across the emerging

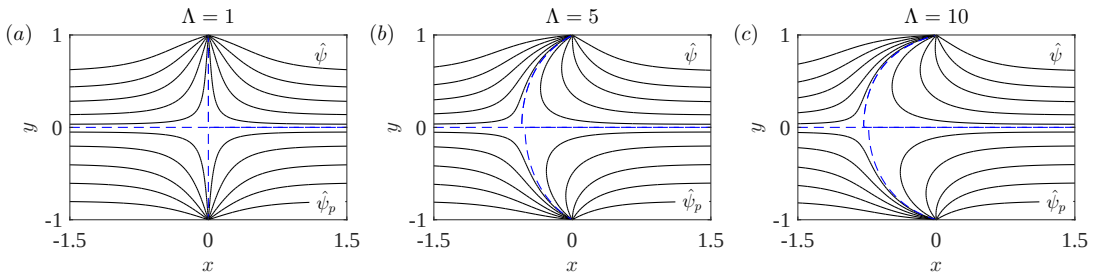

Figure 1.6: Streamlines corresponding to $L/H = 0$ for feed streams with Poiseuille velocity profiles (upper half of the plots) and with uniform velocity profiles (lower half of the plots). Besides the separating streamline $\hat{\psi} = 0$, denoted with a dashed curve, the plots show the streamlines $\hat{\psi} = (0.05, 0.2, 0.4, 0.6, 0.8)$ for stream 1 and the streamlines $\hat{\psi} = -\Lambda \times (0.05, 0.2, 0.4, 0.6, 0.8)$ for stream 2.

jet exhibits a nonuniform distribution in the far field, where $p' = 0$, with the maximum velocity, equal to $\sqrt{2p'_o}$, found along the separating streamline $x = x_s(y)$.

The solution simplifies for $L/H \ll 1$ when the description of the flow in the nozzles away from the openings does not require consideration of the separating interfaces. This case is considered in §1.5.1, which includes comparisons with the irrotational results derived earlier in §1.4.2 to investigate influences of boundary velocity distributions. Next, we shall consider configurations with $L/H \sim 1$. Instead of solving the complicated free-boundary problem (1.26)–(1.28) arising in the inviscid limit, the large-Reynolds-number flow will be described through integrations of the complete Navier–Stokes equations for $100 \leq Re \leq 500$. Results of a selected group of computations with uniform feed streams will be compared with the exact potential solution to validate the numerical description and also to test the reduced parametric dependence identified above.

1.5.1 Rotational flow with $L/H \ll 1$

For cases with $L \ll H$, the velocity at distances of order L from the opening becomes a factor H/L larger than that found in the feed streams, as follows from a straightforward continuity balance. The associated point–sink singularities arising in the limit $L/H \to 0$ at the apparent opening locations $(x, y) = (0, \pm 1)$ can be effectively handled in the numerical description by

expressing $\hat{\psi}$ as the sum of a potential stream function $\hat{\psi}_p$ carrying the volume flux of the two streams and a rotational stream function $\hat{\psi}_r$ with associated zero volume flux. The rotational stream function satisfies

$$\frac{\partial^2 \hat{\psi}_r}{\partial x^2} + \frac{\partial^2 \hat{\psi}_r}{\partial y^2} = -\hat{\Omega}(\hat{\psi}), \tag{1.43}$$

where $\hat{\Omega}(\hat{\psi})$ must be evaluated from (1.42) in terms of $\hat{\psi} = \hat{\psi}_p + \hat{\psi}_r$ with $\hat{\psi}_p$ given in (1.35). The boundary conditions for $\hat{\psi}_r$ reduce to

$$\hat{\psi}_r = 0 \quad \text{at} \quad y = 0, 1 \quad \text{for} \quad -\infty < x < \infty \tag{1.44}$$

and

$$\hat{\psi}_r = \frac{y}{2}(1-y^2) \quad \text{as} \quad x \to -\infty \qquad \text{and} \qquad \hat{\psi}_r = -\Lambda\frac{y}{2}(1-y^2) \quad \text{as} \quad x \to \infty, \tag{1.45}$$

for $0 \leq y \leq 1$. The stream function approaches the Poiseuille distributions according to

$$\begin{cases} \hat{\psi}_r = \dfrac{y}{2}(1-y^2) + C_{-\infty} e^{\lambda_1 x} F_1(y) & \text{as } x \to -\infty, \\ \hat{\psi}_r = -\Lambda\dfrac{y}{2}(1-y^2) + C_{+\infty} e^{-\lambda_1 x} F_1(y) & \text{as } x \to +\infty, \end{cases} \tag{1.46}$$

where $\lambda_1 = 2.59$ and F_1 are the smallest eigenvalue and corresponding eigenfunction of the homogeneous problem

$$F_n'' + \left[\frac{2}{1-y^2} + \lambda_n\right] F_n = 0; \quad F(0) = F(1) = 0, \tag{1.47}$$

obtained by linearizing (1.43) about the Poiseuille velocity distribution. The constant factors $C_{\pm\infty}$ in (1.46) are to be determined as part of the numerical integration of (1.43).

Equation (1.43) was solved iteratively on a fixed rectangular domain until convergence was achieved, determined by the condition $||\hat{\psi}_r^{k+1} - \hat{\psi}_r^k||_{\max} < 10^{-6}$. A second-order central-difference

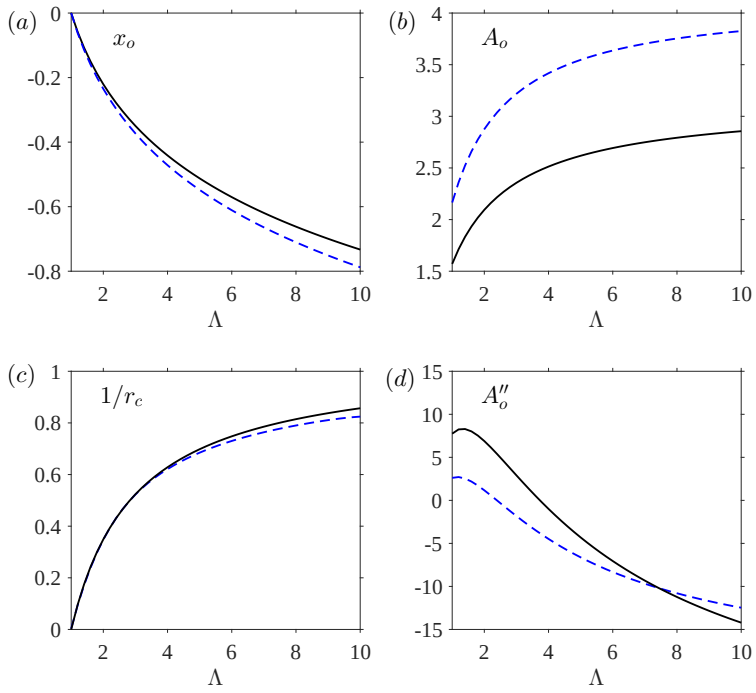

Figure 1.7: The variation with Λ for $L/H = 0$ of the distance of the stagnation point from the exit plane of the left nozzle x_o (a), the stagnation-point strain rate A_o (b), the local curvature of the separating interface at the stagnation point $1/r_c$ (c), and the parameter A_o'' measuring the departures of the velocity from the stagnation-point solution (d) as obtained numerically for selected values of Λ with boundary Poiseuille velocity profiles (dashed curves) and evaluated from (1.36) for uniform velocity profiles (solid curves).

scheme was used to discretize (1.43) written at each iteration k in the form $\nabla^2\hat{\psi}_r^{k+1} = \hat{\Omega}(\hat{\psi}^k)$, which includes a nonlinear solve for $\hat{\Omega}(\hat{\psi}^k)$ as defined by the implicit representation (1.42). To facilitate convergence of the integrations in the finite domain $x_{-\infty} \le x \le x_{+\infty}$, the boundary conditions (1.45) as $x \to \pm\infty$ were replaced by

$$\begin{cases} \hat{\psi}_r - \dfrac{1}{\lambda_1}\dfrac{\partial\hat{\psi}_r}{\partial x} = \dfrac{y}{2}(1-y^2) & \text{at } x = x_{-\infty}, \\ \hat{\psi}_r + \dfrac{1}{\lambda_1}\dfrac{\partial\hat{\psi}_r}{\partial x} = -\Lambda\dfrac{y}{2}(1-y^2) & \text{at } x = x_{+\infty}, \end{cases} \tag{1.48}$$

derived with account taken of the asymptotic behaviors (1.46). The solution was found to be independent of the longitudinal extent of the integration domain for sufficiently large values of $-x_{-\infty}$ and $x_{+\infty}$, with the results shown in figures 1.6 and 1.7 corresponding to $-x_{-\infty} = x_{+\infty} = 5$.

The streamlines $\hat{\psi} = \hat{\psi}_p + \hat{\psi}_r =$ constant are shown in figure 1.6 for different values of Λ along with the corresponding potential-flow results, evaluated with use made of (1.35). As can be seen, the general morphology of the flow is not critically affected by the shape of the boundary velocity distribution. The resulting changes in connection with the stagnation point are further quantified in figure 1.7. In the range $1 \leq \Lambda \leq 10$, the relative changes in axial location x_o and in the local curvature $1/r_c$ of the separating streamline $x = x_o + y^2/(2r_c)$ are of the order of 5 %. By way of contrast, the local velocity field in the vicinity of $\boldsymbol{x}_o = (x_o, 0)$ is much more sensitive to the shape of the velocity in the feed streams, as seen in figures 1.7*b* and 1.7*d*. The higher velocity of the Poiseuille distribution at the centreline produces a significantly higher value of A_o. The parameter A_o'', measuring the variation of the strain rate along the separating interface also exhibits pronounced differences. In particular, for $\Lambda \sim 1$ the rate of increase of the strain rate is considerably larger for potential flow.

1.5.2 Vortical flow with $L/H \simeq \boldsymbol{O}(1)$

The computation of inviscid flows with free boundaries is in general a difficult task, especially with vorticity present. As shown by [26] when examining the related problem of an axisymmetric constant-density jet impinging on a perpendicular wall, the inviscid description can be approached by considering integrations of the Navier–Stokes equations for moderately large values of the Reynolds number, with associated departures from inviscid flow of order $Re^{-1/2}$. This is the procedure followed below.

The previous results concerning the parametric dependence of the problem in the limit $Re \gg 1$ indicate that the specific selection of composition and temperature in the feed streams for the Navier–Stokes computations is not critical, in that different configurations with the same value of Λ approach the same nearly inviscid flow structure in the limit $Re \gg 1$, with differences arising only in the interior of the mixing layers surrounding the jets. For simplicity, the integrations below pertain to isothermal jets of two gases of different densities ρ_2^* and ρ_1^* but identical viscosities

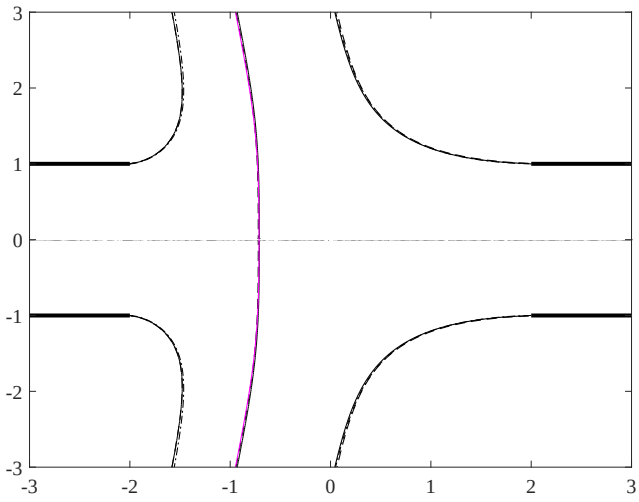

Figure 1.8: Free and separating streamlines corresponding to uniform velocity in the feed streams and $L/H = 2$ obtained from numerical integrations of the Navier–Stokes equations for $Re = 500$ with $\rho_2^*/\rho_1^* = 1$ and $Q_2/Q_1 = 3/2$ (solid curves), with $\rho_2^*/\rho_1^* = 9/4$ and $Q_2/Q_1 = 1$ (dashed curves), and from evaluation of the potential–flow results of §1.4 (dash-dotted). All three cases correspond to $\Lambda = 3/2$.

$\mu_1^* = \mu_2^*$, so that $\mu = 1$ in (1.3). The density of the ambient gas is taken to be equal to that of stream 1, so that the density at any point can be computed in terms of the mass fraction Y_2 by writing (1.6) in the form $\rho = [1 - Y_2 + Y_2(\rho_1^*/\rho_2^*)]^{-1}$, which can be used in (1.5) to give

$$\boldsymbol{v} \cdot \boldsymbol{\nabla} \rho = \frac{\rho}{ScRe} \boldsymbol{\nabla} \cdot (\frac{1}{\rho} \boldsymbol{\nabla} \rho) \tag{1.49}$$

as a conservation equation for the gas density. Here $Sc = \mu_1^*/(\rho_1^* D^*)$ is the Schmidt number based on the binary diffusion coefficient D^* of the two gases, with the value $Sc = 0.7$ used in the numerical integrations reported below. The problem reduces to the integration of (1.2), (1.3), and (1.49) with boundary conditions in the feed streams $v_x - (3/2)(1-y^2) = v_y = \rho - 1 = 0$ as $x \to -\infty$ and $v_x + (3/2)(Q_2/Q_1)(1-y^2) = v_y = \rho - (\rho_2^*/\rho_1^*) = 0$ as $x \to +\infty$. Nonpermeable walls with a nonslip flow condition are employed in the description, along with the symmetry conditions $\partial v_x/\partial y = v_y = \partial \rho/\partial y = 0$ at $y = 0$ and a condition of vanishing normal stress in the surrounding gas atmosphere, where $\rho = 1$. The equations were integrated in the rectangular domain $x_{-\infty} \le x \le x_{+\infty}$

and $0 \leq y \leq y_{+\infty}$, with $-x_{-\infty} = x_{+\infty} = 3L/H$ and $y_{+\infty} = 7$. The integrations employed a finite-element method with $P1$ elements for the pressure field and $P2$ elements for the remaining variables, combined with a Newton-Raphson root-finding algorithm; details of the discretization method, used for instance by [33], can be found in [34]. An illustration of the resulting flow is given in figure 1.1, where the boundary streamlines $x_1(y)$, $x_2(y)$, and $x_s(y)$ are obtained by integrating the above problem for $L/H = 2$, $\rho_2^*/\rho_1^* = 4$, $Q_2/Q_1 = 1.5$, $Re = 500$.

For the purpose of verification, a number of integrations were performed for uniform velocity in the feed streams, with a slip flow condition used at the wall to make the results of the integrations independent of the longitudinal extent of the integration domain. Figure 1.8 shows the separating streamlines (departing from the nozzle rims and from the stagnation point $\boldsymbol{x}_o$) obtained for $L/H = 2$ from integrations of the Navier–Stokes equations with $Re = 500$ for two different set of conditions, namely, $\rho_2^*/\rho_1^* - 1 = Q_2/Q_1 - 3/2 = 0$ and $\rho_2^*/\rho_1^* - 9/4 = Q_2/Q_1 - 1 = 0$, resulting in the same momentum-flux parameter $\Lambda = 3/2$. The associated curves are practically indistinguishable, supporting the reduced parametric dependence predicted by the density-weighted formulation presented in §1.3.3. The figure includes comparisons with the potential–flow solution derived in §1.4, whose associated jet interfaces $x = x_1(y)$, $x = x_2(y)$, and $x = x_s(y)$ are represented as dot-dashed curves. The close agreement of the potential flow with the Navier–Stokes results, expected in the limit $Re \gg 1$ [26], serves as verification for the numerical method.

To investigate the flow near the stagnation point the distribution of longitudinal velocity along the centreline obtained with Poiseuille velocity profiles in the feed streams is plotted in figure 1.9 for $Re = 500$, $L/H = 2$, and three different density ratios, with corresponding volume–flux ratios Q_2/Q_1 selected to maintain in all three cases the same value $\Lambda = (\rho_2^*/\rho_1^*)^{1/2} Q_2/Q_1 = 1.5$. The velocity on each side of the stagnation point outside the mixing layer follows a linear distribution given by $v_x = -A_1(x - x_o)$ in stream 1 and $v_x = -A_2(x - x_o)$ in stream 2, in agreement with the local potential solution (1.13). The values of A_1 and A_2, which can be obtained by

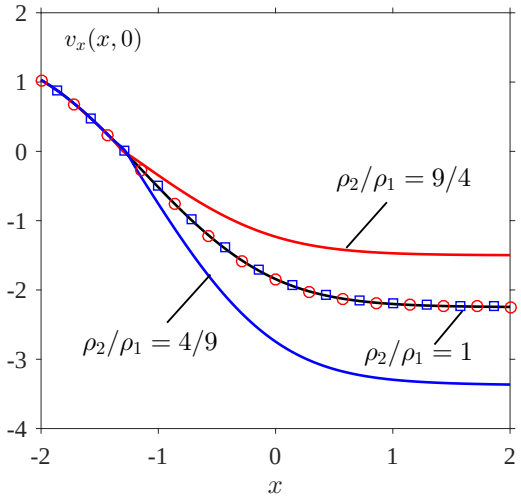

Figure 1.9: The distribution of longitudinal velocity along the centreline determined from the Navier–Stokes computations for $Re = 500$, $L/H = 2$, and $Q_2/Q_1 = 1.5/(\rho_2^*/\rho_1^*)^{1/2}$ with $\rho_2^*/\rho_1^* = (4/9, 1, 9/4)$; the symbols represent the rescaled velocity distributions $\rho^{1/2} v_x$ for $\rho_2^*/\rho_1^* = 4/9$ (squares) and for $\rho_2^*/\rho_1^* = 9/4$ (circles).

extrapolating the numerical results near the stagnation point, are seen to satisfy the relationship $A_o = A_1 = (\rho_2^*/\rho_1^*)^{1/2} A_2$ stated in (1.14). The resulting values, $A_o = (1.58, 1.59, 1.60)$ for $\rho_2^*/\rho_1^* = (4/9, 1, 9/4)$, are almost identical in all three cases, in agreement with the reduced inviscid formulation introduced earlier, which predicts that the strain rate $A_1 = (\rho_2^*/\rho_1^*)^{1/2} A_2$ depends on ρ_2^*/ρ_1^* and Q_2/Q_1 through the single parameter $\Lambda = (\rho_2^*/\rho_1^*)^{1/2}(Q_2/Q_1)$. The derivation of this reduced dependence is based on the density-weighted variables defined in (1.25), which are tested in figure 1.9 by representing with symbols the distribution of $\rho^{1/2} v_x$ for the two cases with unequal jet densities. The resulting curves fall on top of the velocity distribution of the uniform-density case, further illustrating the applicability of the reduced inviscid formulation.

The dependence of the results on the Reynolds number was found to be relatively weak for moderately large values of Re. Only small variations of a few percent were found in values of the stagnation-point location x_o and in the stagnation-point values of A_o and A_o'' for $100 \leq Re \leq 500$, with somewhat larger variations affecting the curvature of the separating streamline $1/r_c$. For instance, for $L/H = 2$, $\rho_2^*/\rho_1^* = 1$, and $Q_2/Q_1 = 1.5$ the integrations provide $x_o = (-1.27, -1.29, -1.29)$, $A_o = (1.55, 1.58, 1.59)$, $A_o'' = (1.07, 1.07, 1.07)$, and

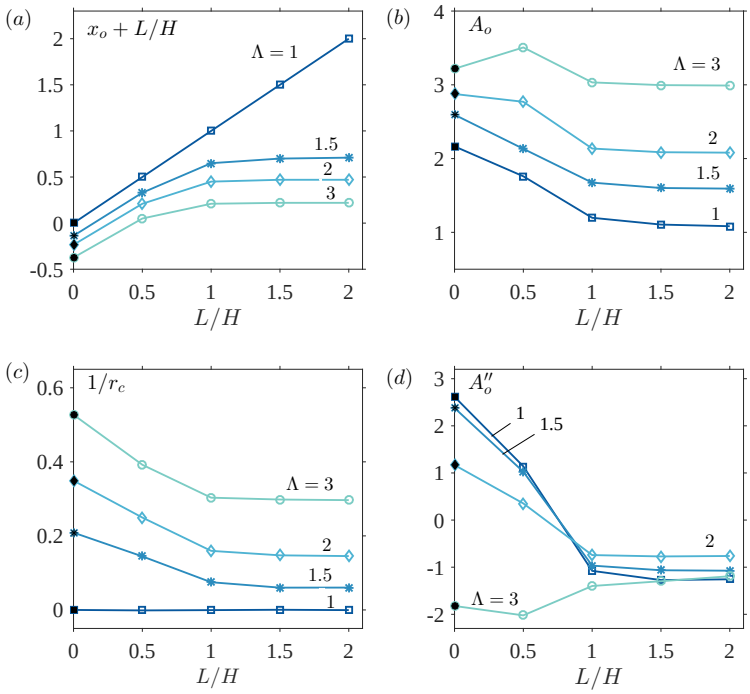

Figure 1.10: The variation with L/H of the distance of the stagnation point from the exit plane of the left nozzle $x_o + L/H$ (a), the stagnation-point strain rate A_o (b), the local curvature of the separating interface at the stagnation point $1/r_c$ (c), and the parameter A_o'' measuring the departures of the velocity from the stagnation-point solution (d) obtained from the Navier–Stokes computations for $Re = 500$ and $\rho_2^*/\rho_1^* = 1$; the solid symbols along the vertical axes represent the limiting values given in figure 1.7.

$1/r_c = (0.044, 0.0561, 0.0589)$ for $Re = (100, 300, 500)$, respectively.

The computations for $Re = 500$ and $\rho_2^*/\rho_1^* = 1$ are used in figure 1.10 as a basis to investigate the dependence of x_o, A_o, $1/r_c$, and A_o'' on L/H and Λ. The numerical evaluation of A_o involves a linear fit about $x = x_o$ of the longitudinal velocity distribution $v_x(x,0)$. Similarly, A_o'' is obtained by computing the slope of a linear fit of the longitudinal distribution of $\partial^2 v_x/\partial y^2(x,0)$ about $x = x_o$, while the computation of r_c requires a parabolic fit of the form (1.15) for the separating streamline departing from $\boldsymbol{x}_o$. The resulting curves, which include the limiting results for $L/H = 0$ computed earlier in §1.5.1, exhibit trends that are qualitatively similar to those of the irrotational results in figure 1.5.

1.6 Conformal mapping solution for uniform velocity profiles in feed streams

This section is concerned with the solution of irrotational counterflows in the general case $L/H \sim 1$, represented schematically in figure 1.11a. The resulting flow can be described in terms of a complex potential

$$w(z) = \hat{\phi} + \mathrm{i}\hat{\psi}, \tag{1.50}$$

with associated complex velocity

$$\nu(z) = \frac{\mathrm{d}w}{\mathrm{d}z} = qe^{-\mathrm{i}\theta}, \tag{1.51}$$

where q and θ are the components of the velocity in polar form. The needed conformal transformation, presented below, is based on Kirchhoff's method, delineated in section 11.50 of [31].

1.6.1 Definition of conformal planes and associated mapping

The boundary points employed in the conformal transformation are indicated in figure 1.11a, which includes four additional panels representing the different mapping planes involved in the solution. The points A_∞ and A'_∞ are considered to be at $z = \mp\infty$ respectively. The location of the stagnation point O, which generally does not coincide with the origin $z = 0$ except in the symmetric case $\Lambda = 1$, must be determined as part of the solution. The speed is constant and equal to U along the free streamlines BC_∞ and $B'C'_\infty$ bounding the resulting free jet that forms downstream from the impinging region. This lateral jet becomes uniform at $C_\infty C'_\infty$ with width h/H and direction α measured relative to the y-axis.

The objective of the following development is to determine, for given values of Λ and L/H, (i) the location of the free streamlines $x = x_1(y)$ and $x = x_2(y)$, (ii) the speed U along

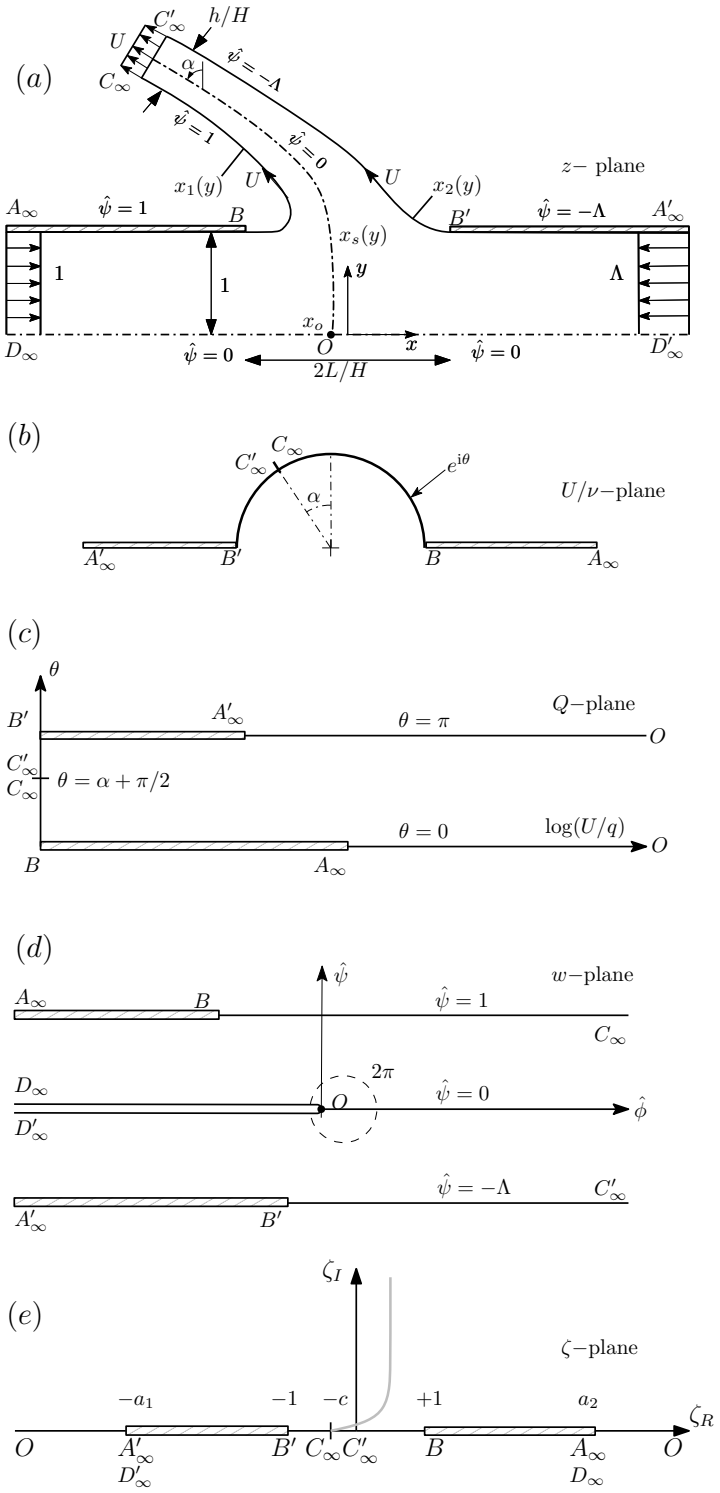

Figure 1.11: All relevant complex planes involved in the conformal transformation: (a) $z-$plane, (b) hodographic $U/\nu-$plane, (c) $Q-$plane, (d) $w-$plane, (e) upper-half $\zeta-$plane. The contour Γ in the $\zeta-$plane represents the separating streamline $\hat{\psi}=0$.

these streamlines, (iii) the width h/H and angle α of the emerging jet, (iv) the location of the stagnation point $z = x_o$, (v) the value A_o of the strain rate at the stagnation point, (vi) the shape of the separating interface $x = x_s(y)$, including its curvature $1/r_c$ at $z = x_o$, and (vii) the parameter A_o'' measuring the initial variation of the strain rate along $x = x_s(y)$.

Defining the ratio U/ν we obtain the hodographic plane shown in figure 1.11*b*. Taking the logarithm

$$Q = \ln(U/\nu) = \ln(U/q) + i\theta \tag{1.52}$$

gives a polygon whose interior may be mapped onto the upper-half $\zeta-$plane using the elementary transformation $\zeta = \cosh Q$, such that

$$\zeta = \frac{1}{2}\left(\frac{U}{q}e^{i\theta} + \frac{q}{U}e^{-i\theta}\right), \tag{1.53}$$

thus defining the location of the different points in the $\zeta-$plane in terms of the unknown parameter U. For example, the point A_∞, corresponding to $q = 1$ and $\theta = 0$, is mapped onto $\zeta = (U^2+1)/2U$. The $\zeta-$plane is shown in figure 1.11*e* where the positive constants

$$a_1 = \frac{U^2+\Lambda^2}{2\Lambda U}, \qquad a_2 = \frac{U^2+1}{2U}, \qquad c = \sin\alpha, \tag{1.54}$$

are the images of A'_∞, A_∞, and C, respectively. The points B and B' are mapped onto ± 1, while the stagnation point O is mapped to $\zeta = \infty$, as shown in the figure.

Taking $\hat{\phi} = 0$ at the stagnation point O, implies that both $A_\infty D_\infty$ and $A'_\infty D'_\infty$ correspond to $\hat{\phi} = -\infty$, while $C_\infty C'_\infty$ corresponds to $\hat{\phi} = \infty$. These selections are accounted for when plotting the w plane in figure 1.11*d*.

The next step involves mapping the $w-$plane, regarded as interior to a polygon, onto the upper half $\zeta-$plane by use of the Schwarz-Christoffel transformation. The images in the ζ-plane have already been determined from the mapping $Q \mapsto \zeta$ defined above. Hence, the required

transformation is given by

$$\frac{\mathrm{d}w}{\mathrm{d}\zeta} = K(\zeta+a_1)^{-1}(\zeta+c)^{-1}(\zeta-a2)^{-1} = K\left\{\frac{\delta}{\zeta-a_2}+\frac{\beta}{\zeta+a_1}-\frac{\gamma}{\zeta+c}\right\}, \tag{1.55}$$

where $K = K_R + \mathrm{i}K_I$ is in general a complex constant and δ, β, and γ are given by

$$\delta = \frac{1}{(a_1+a_2)(c+a_2)}, \qquad \beta = \frac{1}{(a_1+a_2)(a_1-c)}, \qquad \gamma = \frac{1}{(a_1-c)(c+a_2)}, \tag{1.56}$$

obtained from partial fraction expansion, with $\delta+\beta-\gamma=0$. Integrating (1.55) yields

$$w = K\left\{\delta\ln(\zeta-a_2)+\beta\ln(\zeta+a_1)-\gamma\ln(\zeta+c)\right\}+E, \tag{1.57}$$

where E is a complex constant of integration. Rearranging (1.57) in the form

$$w = \frac{K}{(a_1-c)(c+a_2)(a_1+a_2)}\left\{-a_1\ln\left(\frac{\zeta+c}{\zeta-a_2}\right)-a_2\ln\left(\frac{\zeta+c}{\zeta+a_1}\right) +c\ln\left(\frac{\zeta+a_1}{\zeta-a_2}\right)\right\}+E, \tag{1.58}$$

and enforcing the condition that the stagnation point O ($w=0$) is mapped to $\zeta=\infty$, immediately gives $E=0$ since the logarithms in (1.58) vanish as $\zeta\to\infty$.

On $D_\infty O$, $\hat{\psi}=0$ and hence w is real. Since in the ζ-plane the portion $D_\infty O$ corresponds to $\zeta-a_2>0$, $\zeta+a_1>0$, $\zeta+c>0$, all logarithms in (1.57) are necessarily real. Hence, evaluating (1.57) along $D_\infty O$, where $\hat{\phi}\neq 0$ and $\hat{\psi}=0$, reveals that $K_I=0$, so that $K=K_R$ is purely real.

Evaluating (1.57) along BC_∞, corresponding to the streamline $\hat{\psi}=1$, and equating real and imaginary parts yields

$$K = \frac{(a_1+a_2)(c+a_2)}{\pi}. \tag{1.59}$$

The constant K may be related to the momentum–flux parameter Λ, by evaluating (1.57) along

$B'C'_\infty$ for which $\hat{\psi} = -\Lambda$. Equating real and imaginary parts and solving for K gives

$$K = \frac{\Lambda(a_1 - c)(a_1 + a_2)}{\pi}. \tag{1.60}$$

Equating (1.59) and (1.60) yields $c = (\Lambda - 1)/2U$, relating $c = \sin\alpha$ with Λ and U. Note that this last result may be derived directly from the continuity and momentum integral balances (1.33).

In summary, we have obtained the following mappings to the upper half $\zeta-$plane

$$Q(\zeta) = \cosh^{-1}\zeta = \ln(\zeta + \sqrt{\zeta^2 - 1}), \tag{1.61}$$

$$w(\zeta) = K\Big\{\delta\ln(\zeta - a_2) + \beta\ln(\zeta + a_1) - \gamma\ln(\zeta + c)\Big\}. \tag{1.62}$$

Equation (1.61), together with the definition of Q given in (1.52) provide

$$\nu(\zeta) = \frac{U}{\zeta + \sqrt{\zeta^2 - 1}}. \tag{1.63}$$

for the complex velocity.

1.6.2 The jet outer boundaries

In order to compute streamlines, the line element

$$\mathrm{d}z = \frac{\mathrm{d}z}{\mathrm{d}w}\frac{\mathrm{d}w}{\mathrm{d}\zeta}\mathrm{d}\zeta = \frac{1}{\nu}\frac{\mathrm{d}w}{\mathrm{d}\zeta}\mathrm{d}\zeta, \tag{1.64}$$

is expressed as

$$\frac{\mathrm{d}z}{\mathrm{d}\zeta} = Z(\zeta) = \frac{K}{U}\frac{\zeta + \sqrt{\zeta^2 - 1}}{(\zeta + a_1)(\zeta + c)(\zeta - a_2)} \tag{1.65}$$

with use of (1.55) and (1.63). Since the free streamlines separating the jets from the ambient gas are mapped onto the segment $-1 < \zeta < 1$ on the real axis of the $\zeta-$ plane, we may write

$\sqrt{\zeta^2-1} = \mathrm{i}\sqrt{1-\zeta^2}$. Separating real and imaginary parts of (1.65) then gives

$$\begin{aligned} \frac{\mathrm{d}x}{\mathrm{d}\zeta} &= X(\zeta) = \frac{K}{U}\frac{\zeta}{(\zeta+a_1)(\zeta+c)(\zeta-a_2)}, \\ \frac{\mathrm{d}y}{\mathrm{d}\zeta} &= Y(\zeta) = \frac{K}{U}\frac{\sqrt{1-\zeta^2}}{(\zeta+a_1)(\zeta+c)(\zeta-a_2)}, \end{aligned} \tag{1.66}$$

which can be integrated to give

$$x_1(\zeta) = -L/H + \int_1^{\zeta} X(\zeta')\mathrm{d}\zeta' \qquad \text{and} \qquad y(\zeta) = 1 + \int_1^{\zeta} Y(\zeta')\mathrm{d}\zeta' \tag{1.67}$$

as an implicit representation for $x_1(y)$, and

$$x_2(\zeta) = L/H + \int_{-1}^{\zeta} X(\zeta')\mathrm{d}\zeta' \qquad \text{and} \qquad y(\zeta) = 1 + \int_{-1}^{\zeta} Y(\zeta')\mathrm{d}\zeta' \tag{1.68}$$

as an implicit representation for $x_2(y)$.

1.6.3 The emerging jet

The two streamlines $x_1(y)$ and $x_2(y)$ become parallel as $y \to \infty$. The thickness of the resulting jet, given by

$$h/H = \cos\alpha \lim_{y\to\infty}(x_2 - x_1), \tag{1.69}$$

can be obtained by evaluating the first equations in (1.67) and (1.68) as $\zeta \to -c$ and taking the difference to yield

$$\begin{aligned} h/H = \cos\alpha \Bigg\{ 2L/H + \frac{1}{\pi U^2}\Bigg[(U^2+1)\ln\left(\frac{U-1}{U+1}\right) + (U^2+\Lambda^2)\ln\left(\frac{U-\Lambda}{U+\Lambda}\right) \\ + \frac{\Lambda^2-1}{2}\ln\left(\frac{2U+\Lambda-1}{2U-\Lambda+1}\right)\Bigg]\Bigg\}, \end{aligned} \tag{1.70}$$

after simplification with use made of (1.54), (1.56) and (1.59). This equation together with the continuity and momentum integral balances (1.33) can be used to determine the three unknowns α, h/H, and U in terms of the parameters Λ and L/H. The value of U can then be used in (1.59) to compute the factor

$$K = \frac{(U^2+\Lambda)^2(\Lambda+1)}{4\Lambda U^2} \tag{1.71}$$

for the functions $Z(\zeta)$, $X(\zeta)$, and $Y(\zeta)$ defined in (1.65) and (1.66).

1.6.4 The interface separating the jets

The stagnation point $\boldsymbol{x}_o = (x_o, 0)$ is located at $\zeta = \infty$ in the $\zeta-$plane. Integrating (1.65) along $BA_\infty O$ on the real axis of the $\zeta-$ plane, for which $\zeta > 1$ so that $\mathrm{d}z = \mathrm{d}x$, gives

$$x_o = -L/H + \fint_1^\infty Z(\zeta')\mathrm{d}\zeta', \tag{1.72}$$

with the principal value of the integral needed to account for the singularity at $\zeta = a_2$. Equation (1.72) may be integrated numerically to obtain x_o.

The separating streamline departs from $(x,y) = (x_o, 0)$. Its shape can be computed by integrating (1.65) along the corresponding contour $\hat{\psi} = 0$ in the $\zeta-$plane. This contour, denoted by Γ in figure 1.11*e*, is obtained from the condition

$$\hat{\psi}(\zeta) = \mathrm{Im}[w(\zeta)] = 0, \tag{1.73}$$

with $w(\zeta)$ defined by the transformation given in (1.62). The constant of integration is determined by imposing the correspondence of the points $\zeta = \infty$ and $z = x_o$.

1.6.5 Flow properties near the stagnation point

As discussed in the main text, the structure of the mixing layer near the stagnation point, of particular interest in counterflow–flame studies, depends on the local strain rate $A_o = A_1 = (\rho_2/\rho_1)^{1/2}A_2$, with departures from selfsimilarity measured by the local values of the mixing-layer curvature r_c and of the parameter $A_o'' = A_1'' = (\rho_2/\rho_1)^{1/2}A_2''$, the latter entering in the velocity distributions on both sides of the mixing layer given in (1.16). These quantities can be evaluated by writing (1.31) in terms of the complex potential to give

$$A_o = -\mathrm{Re}\left[\frac{\mathrm{d}^2 w}{\mathrm{d}z^2}\right]_{z=x_o}, \quad \frac{1}{r_c} = -\frac{1}{3A_o}\mathrm{Re}\left[\frac{\mathrm{d}^3 w}{\mathrm{d}z^3}\right]_{z=x_o}, \text{ and } A_o'' = \mathrm{Re}\left[\frac{\mathrm{d}^4 w}{\mathrm{d}z^4}\right]_{z=x_o}. \tag{1.74}$$

Since an explicit expression for $w = w(z)$ is not available, in evaluating the above equations it is convenient to use the expression (1.62) for $w = w(\zeta)$ and use the chain rule to express the derivatives in (1.74) in the form $\mathrm{d}/\mathrm{d}z = Z(\zeta)^{-1}\mathrm{d}/\mathrm{d}\zeta$, where $Z(\zeta) = \mathrm{d}z/\mathrm{d}\zeta$ is defined in (1.65). Evaluating the derivatives as $\zeta \to \infty$, corresponding to the location of the stagnation point $z = x_o$ on the ζ-plane, provides

$$\begin{aligned} A_o = \frac{\pi\Lambda U^4}{(U^2+\Lambda)^2(\Lambda+1)},\ \frac{1}{r_c} = \frac{\pi U^2(U^2-2\Lambda)(\Lambda-1)}{3(\Lambda+1)(U^2+\Lambda)^2},\ A_o'' = \frac{\pi^3 U^8 \Lambda}{(\Lambda+1)^3(U^2+\Lambda)^6} \\ \times [4U^2\Lambda(\Lambda-2)(2\Lambda-1) - U^4(\Lambda^2-4\Lambda+1) - 2\Lambda^2(3\Lambda^2-7\Lambda+3)], \end{aligned} \tag{1.75}$$

after simplifying the result.

1.6.6 Extending solution to the distant nozzle limit $L/H \gg 1$

As discussed in §1.4.1, when $L/H \gg 1$ the constant free streamline speed U is simply equal to Λ and the collision region migrates to the vicinity of the nozzle with less momentum. Such a flow can best be classified as the impingement of a free jet onto a nozzle. It should be noted that the solution presented in this appendix thus far is readily extended to this limiting case.

To this end, all results derived henceforth may be applied to the distant nozzle limit $L/H \gg 1$ by simply taking $U = \Lambda$ or equivalently $a_1 = 1$ in the corresponding equation. The corresponding Q, w, and $\zeta-$planes are simply the counterparts of those shown in figure 1.11 with A'_∞ and B' coincident. In the analysis, the origin of the coordinate system in figure 1.11*a* should be placed at the outlet of nozzle 1 (i.e. the nozzle carrying less momentum), the natural selection for $L/H \gg 1$.

1.7 Conclusions

The present paper contributes to the quantitative description of the steady planar flow resulting from the impingement of opposed low-Mach-number gaseous jets of different density issuing into an open stagnant atmosphere from aligned nozzles, with specific attention given to the high-Reynolds-number conditions prevailing in most chemical reactors [1] as well as in combustion facilities used to investigate the response of flames to strain [25]. The flow is nearly inviscid in the outer streams, with effects of viscous forces, heat conduction, and species diffusion confined to thin mixing layers, one separating the two jets and the others separating each jet from the surrounding stagnant atmosphere. In combustion applications, the flame is embedded in the mixing layer separating the two jets, across which we find large density changes due to the heat released by the chemical reaction, whereas outside the density in each jet remains equal to the value found in its feed stream. The solution presented here for the inviscid collision of the two jets provides, amongst other things, the strain rate exerted by the outer flow on the separating mixing layer, a quantity of fundamental interest for studies of flame response to strain.

A formulation involving a density-weighted stream function is introduced to simplify the problem to one involving two jets of equal density. The proposed formulation is also useful in reducing the number of controlling parameters to only two, namely, the dimensionless nozzle spacing L/H and the ratio of jet momentum fluxes Λ^2. For uniform velocity in the feed streams, the resulting potential flow can be described analytically by conformal–mapping

techniques, while numerical integration is needed to describe rotational flow, which is analyzed here for the important case of Poiseuille flow in the feed streams. The theoretical and numerical analyses provide relevant quantitative information regarding the parametric dependence of the flow, including analytic expressions derived for potential flow, given for instance in (1.33), (1.39), and (1.40), which enable relevant flow characteristics to be readily evaluated for nozzle-flow types of laminar counterflows with thin near-wall boundary layers.

The variation of the shape of the interfaces bounding the jets is investigated in figure 1.4, while the far-field characteristics of the associated lateral jet is shown in figure 1.3. The jet deflection α from the perpendicular direction, small when the two nozzles are placed at a small distance, is seen to increase with increasing inter-nozzle distances. As anticipated in (1.34) on the basis of a simple jet-momentum balance, the deflection is limited to a maximum value $\alpha = \pi/6$, reached when $L/H \gg 1$ and $\Lambda \gg 1$. Because of their interest in combustion applications, specific attention has been given to the morphology and velocity field of the near-stagnation-point region, with results summarized in figures 1.5 and 1.10. The results reveal qualitative similarity in the stagnation region properties between irrotational flows and those with distributed vorticity, main differences entering in the larger values of the strain rate in the latter while in the former the flow accelerates away from the stagnation region at a faster rate. An attractive parametric range — characterized by momentum flux ratios between $1 \leq \Lambda^2 \leq 4$ and nozzle spacings $L/H \gtrsim 1.5$ — was identified aimed at minimizing departures of the mixing-layer structure from one-dimensional selfsimilar solutions.

The analysis helps to clarify the flow characteristics of planar open-duct and nozzle-flow types of counterflows, found in chemical reactors and counterflow burners. The associated quantitative information may aid in considerations of experimental designs of such devices. Corrections to the leading-order results given here arising from finite-Reynolds-number effects, near-edge departures from two-dimensional flow, shear-layer instabilities introducing unsteadiness in the flow, and buoyancy-induced motion should be considered in such designs if increased

accuracy is desired.

This chapter, in full, has been published in the *Journal of Fluid Mechanics*, titled "Aerodynamics of planar counterflowing jets" by A. D. Weiss, W. Coenen and A. L Sánchez (2017) 821, 1-30. The dissertation author is the primary investigator in this publication. The inputs of Profs. S. Llewellyn Smith, J. Carpio, J. C. Lasheras, A. Liñán, and F. A. Williams on different aspects of this research are gratefully acknowledged.

Bibliography

[1] A. Tamir. *Impinging Streams Reactors: Fundamentals and Applications*. Elsevier, 1994.

[2] T. Strand. Inviscid-incompressible-flow theory of static two-dimensional solid jets in proximity to the ground. *J. Aerospace Sciences*, 29:170–173, 1962.

[3] C. B. Renner and P. S. Doyle. Stretching self-entangled dna molecules in elongational fields. *Soft Matter*, 11:3105–3114, 2015.

[4] N. Peters. *Turbulent Combustion*. Cambridge University Press, 2000.

[5] G. Scribano and F. Bisetti. Reynolds number and geometry effects in laminar axisymmetric isothermal counterflows. *Phys. Fluids*, 28:123605, 2016.

[6] J. Carpio, A. Liñán, A. L. Sánchez, and F. A. Williams. Aerodynamics of axisymmetric counterflowing jets. *Combust. Flame*, (to appear), 2017.

[7] R. Gardon and J. C. Akfirat. Heat transfer characteristics of impinging two-dimensional air jets. *J. Heat Transfer*, 88:101–107, 1966.

[8] H. Martin. Heat and mass transfer between impinging gas jets and solid surfaces. *Adv. Heat Transfer*, 13:1–60, 1977.

[9] D. J. Phares, G. T. Smedley, and R. C. Flagan. The wall shear stress produced by the normal impingement of a jet on a flat surface. *J. Fluid Mech.*, 418:351–375, 2000.

[10] A. Rubel. Computations of jet impingement on a flat surface. *AIAA J.*, 18:168–175, 1980.

[11] D. J. Phares, G. T. Smedley, and R. C. Flagan. The inviscid impingement of a jet with arbitrary velocity profile. *Phys. Fluids*, 12:2046–2055, 2000.

[12] Harris C Levey. The back effect of a wall on a jet. *Zeitschrift für angewandte Mathematik und Physik ZAMP*, 11:152–157, 1960.

[13] W.F. Li, T.L. Yao, H.F. Liu, and F.C. Wang. Experimental investigation of flow regimes of axisymmetric and planar opposed jets. *AIChE Journal*, 57:1434–1445, 2011.

[14] W.F. Li, G.F. Huang, G.Y. Tu, H.F. Liu, and F.C. Wang. Experimental study of planar opposed jets with acoustic excitation. *Phys. Fluids*, 25:014108, 2013.

[15] R. P. Pawlowski, A. G. Salinger, J. N. Shadid, and T. J. Mountziaris. Bifurcation and stability analysis of laminar isothermal counterflowing jets. *J. Fluid Mech.*, 551:117–139, 2006.

[16] V. A. Denshchikov, V. N. Kondrat'ev, and A. N. Romashov. Interaction between two opposed jets. *Fluid Dynamics*, 13:924–926, 1978.

[17] V. A. Denshchikov, V. N. Kondrat'Ev, A. N. Romashov, and V. M. Chubarov. Auto-oscillations of planar colliding jets. *Fluid Dynamics*, 18:460–462, 1983.

[18] V. Gupta, S. A. Safvi, and T. J. Mountziaris. Gas-phase decomposition kinetics in a wall-less environment using a counterflow jet reactor: design and feasibility studies. *Ind. Eng. Chem. Res.*, 35:3248–3255, 1996.

[19] S. M. Hosseinalipour and A. S. Mujumdar. Flow and thermal characteristics of steady two dimensional confined laminar opposing jets: Part i. equal jets. *Int. Comm. Heat Mass Transfer*, 24:27–38, 1997.

[20] S. M. Hosseinalipour and A. S. Mujumdar. Flow and thermal characteristics of steady two dimensional confined laminar opposing jets: Part ii. unequal jets. *Int. Comm. Heat Mass Transfer*, 24:39–50, 1997.

[21] M.L. Shay and P.D. Ronney. Nonpremixed edge flames in spatially varying straining flows. *Combust. Flame*, 112:171–180, 1998.

[22] J.-B. Liu and P.D. Ronney. Premixed edge-flames in spatially-varying straining flows. *Combust. Sci. Technol.*, 144:21–45, 1999.

[23] M.S. Cha and P.D. Ronney. Propagation rates of nonpremixed edge flames. *Combust. Flame*, 146:312–328, 2006.

[24] H.S. Song, P. Wang, R.S. Boles, D. Matinyan, H. Prahanphap, J. Piotrowicz, and P.D. Ronney. Effects of mixture fraction on edge-flame propagation speeds. *Proc. Combust. Inst.*, page to appear, 2016.

[25] U. Niemann, K. Seshadri, and F. A. Williams. Accuracies of laminar counterflow flame experiments. *Combust. Flame*, 162:1540–1549, 2015.

[26] J.M. Bergthorson, K. Sone, T. W. Mattner, P. E. Dimotakis, D. G. Goodwin, and D. I. Meiron. Impinging laminar jets at moderate reynolds numbers and separation distances. *Phys. Rev. E.*, 72:066307, 2005.

[27] J. Kim, P.A. Libby, and F. A. Williams. On the displacement effects of laminar flames. *Combust. Sci. Technol.*, 87:1–25, 1993.

[28] A. Liñán, M. Vera, and A.L. Sánchez. Ignition, liftoff, and extinction of gaseous diffusion flames. *Annu. Rev. Fluid Mech.*, 47:293–314, 2015.

[29] Garrett Birkhoff and E. H. Zarantonello. *Jets, Wakes and Cavities*. Academic Press, 1957.

[30] M. I. Gurevich. *The Theory of Jets in an Ideal Fluid*. Pergamon Press, 1966.

[31] L. M. Milne-Thomson. *Theoretical Hydrodynamics*. Macmillan, 1968.

[32] A. Revuelta, A.L. Sánchez, and A. Liñán. The virtual origin as a first-order correction for the far-field description of laminar jets. *Phys. Fluids*, 14:1821–1824, 2002.

[33] D. Moreno-Boza, W. Coenen, A. Sevilla, J. Carpio, and A. L. Sánchez. Diffusion-flame flickering as a hydrodynamic global mode. *J. Fluid Mech.*, 798:997–1014, 2016.

[34] F. Hecht. New development in FreeFem++. *J. Numer. Math.*, 20:251–265, 2012.

Chapter 2

A novel formulation for unsteady counterflow flames using a thermal-conductivity-weighted coordinate

2.1 Introduction

Transformation methods aimed at facilitating the analysis of laminar boundary-layer type problems involving variable density were first introduced in the seminal work of Howarth and Dorodnitzyn [1–3]. These methods employ a density-weighted transverse coordinate that, when combined with assumptions regarding the variation of the transport properties (i.e. constant Prandtl and Lewis numbers and a constant value of the product of the density and viscosity), reduce the molecular–transport operators to second-order derivatives with respect to the transverse coordinate. In time-dependent flows, use of the Howarth-Dorodnitzyn transformation along with the introduction of an appropriately defined stream function simplifies the analysis in a similar fashion in what is often referred to as the Moore-Stewartson transformation [4, 5]. While these methods work very well in the one-dimensional, time-dependent problems for which they were

designed, their utility is downgraded in stagnation-point or counterflow problems of the type addressed here.

The above-mentioned transformations find application in the analysis of reactive boundary-layer flows (see [6] for a general formulation of the problem), characterized by large variations of the temperature and composition, which in turn produce significant relative changes of the density and transport coefficients. In the Howarth-Dorodnitzyn transformation these changes are embodied in the so-called Chapman-Rubesin parameter (i.e. the product of the density and viscosity expressed in dimensionless form) appearing in the reduced viscous term of the momentum equation, and also in the heat-conduction and diffusion terms of the energy and species conservation equations, when these are written with constant Prandtl and Lewis numbers. In the presence of a flame, the widely used simplifying assumption of unity Chapman-Rubesin parameter is in general not justified, thereby complicating the analysis.

As is apparent from observation of the conservation equations, an alternative to the Howarth-Dorodnitzyn transformation that readily simplifies the molecular–transport operator involves consideration of a transverse coordinate weighted with the inverse of the viscosity or thermal conductivity. While well known in the study of freely propagating premixed flames [7–9], a review of the literature reveals that such a transformation has been largely overlooked for non-premixed configurations such as those considered here, perhaps because the simplification that it offers is not immediately obvious. Only recently has this transformed variable been used in an investigation of steady diffusion flames [10], shedding light on the utility of this alternative variable for describing situations characterized by large variation in transport properties, that being the case in reactive flows of interest in combustion.

The purpose of this paper is to explore further the applicability of the thermal-conductivity-weighted coordinate, extending the treatment to the case of unsteady flows by introduction of an appropriately defined apparent transverse mass flux. The flow selected for purposes of comparison will be the mixing layer separating planar counterflowing streams, depicted in Figure 2.1, which

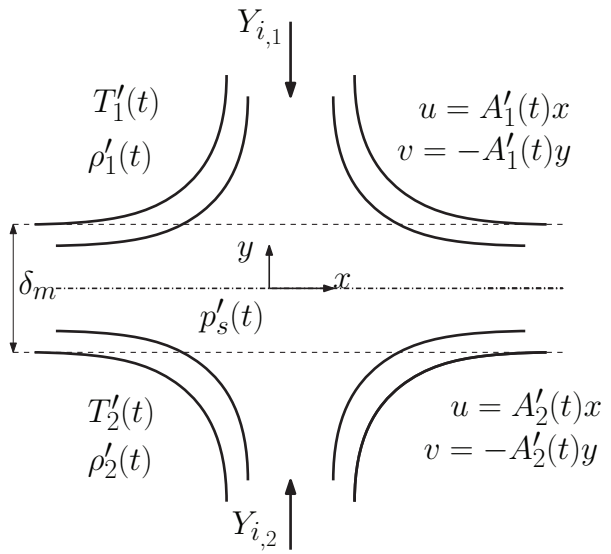

Figure 2.1: Schematic of stagnation-point mixing layer of characteristic thickness δ_m subject to variable strain $A_1'(t)$ and variable pressure $p_s'(t)$.

has been widely employed as a canonical problem to analyze effects of flow strain on premixed, partially premixed, and nonpremixed flames [11]. The strain rate imposed on the mixing layer depends on the characteristics of the outer inviscid flow, as described recently for the case of slot-jet counterflow burners [12]. The mixing-layer formulation given below includes unsteady effects through variable strain and pressure as well as a general chemistry description, thereby enabling future analyses involving time-dependent finite-rate systems. Results for steady diffusion flames will be compared to those generated with the classical Howarth-Dorodnitzyn variable. It will be shown that the new formulation is particularly advantageous in this case, because the transverse mass flux is linearly proportional to the thermal-conductivity-weighted coordinate, so that the solution effectively reduces to that corresponding to constant density and constant transport properties. To further illustrate the applicability of the model to unsteady situations, the formulation is employed to analyze the flame response to harmonic perturbations of the imposed strain rate, with results presented in an appendix.

2.2 Unsteady mixing layers subject to strain and variable pressure

Let us consider the counterflow mixing layer separating two opposed nearly inviscid planar streams. A reference system moving with the dividing streamline will be employed in the description, with x and y denoting the streamwise and transverse coordinates, as indicated in Figure 2.1. Following [13], attention is directed to the self-similar stagnation-point region, described in terms of the streamwise and transverse velocity components $u = A'(y,t)x$ and $v(y,t)$, temperature $T'(y,t)$, density $\rho'(y,t)$, and mass fractions $Y_i(y,t)$, with $A'(y,t)$ being the strain rate. A prime $'$ is introduced in the notation to differentiate between equivalent non-dimensional variables that will appear later. Subscripts 1 and 2 will be used to denote conditions in each feed stream.

In the general time-dependent formulation given below the pressure, although uniform in the first approximation because of the prevailing low-Mach-number conditions, is allowed to vary with time. The stagnation-point pressure $p'_s(t)$ will be used as a convenient reference value to describe these temporal pressure changes, which must be accounted for in the equation of state

$$p'_s(t) = \rho' T' R/M, \tag{2.1}$$

where R is the universal gas constant and $M(y,t) = [\sum_i Y_i/M_i]^{-1}$ is the mean molecular mass, with M_i denoting the molecular mass of species i. As a result of the compression work, the feed-stream values of the temperature and density vary in time and satisfy the relationships

$$\rho'_1 c_{p_1} \frac{dT'_1}{dt} = \rho'_2 c_{p_2} \frac{dT'_2}{dt} = \frac{dp'_s}{dt}, \tag{2.2}$$

obtained by writing the energy equation in the outer chemically frozen uniform streams, with c_p denoting the specific heat at constant pressure. Using $p'_s = \rho'_1 T'_1 R/M_1 = \rho'_2 T'_2 R/M_2$ in (2.2)

gives the familiar equation

$$\frac{\gamma_1}{\gamma_1-1}\frac{1}{T_1'}\frac{\mathrm{d}T_1'}{\mathrm{d}t}=\frac{\gamma_1}{\rho_1'}\frac{\mathrm{d}\rho_1'}{\mathrm{d}t}=\frac{\gamma_2}{\gamma_2-1}\frac{1}{T_2'}\frac{\mathrm{d}T_2'}{\mathrm{d}t}=\frac{\gamma_2}{\rho_2'}\frac{\mathrm{d}\rho_2'}{\mathrm{d}t}=\frac{1}{p_s'}\frac{\mathrm{d}p_s'}{\mathrm{d}t} \tag{2.3}$$

involving the specific-heat ratios $\gamma_1 = c_{p_1}/(c_{p_1}-R/M_1)$ and $\gamma_2 = c_{p_2}/(c_{p_2}-R/M_2)$. For systems such that the approximation $\gamma_1=\gamma_2$ is sufficiently accurate, the ratio of boundary temperatures and boundary densities at all times takes constant values according to

$$T_2'/T_1' = (M_2/M_1)/(\rho_2'/\rho_1') = \Theta \tag{2.4}$$

as can be obtained from integration of (2.3). This approximation is to be adopted below with $\gamma=\gamma_1=\gamma_2$ representing in the following the constant ratio of specific heats.

The spatial pressure differences from the stagnation-point value $\tilde{p}=p'-p_s'(t)$ are smaller than p_s' by a factor of the order of the Mach number squared, and they correspondingly have been neglected in writing (2.1) and (2.2). They are, however, fundamental in establishing the motion along the mixing layer. At leading order in the boundary-layer approximation $\tilde{p}(x,t)$ does not vary with the transverse coordinate. This condition of negligible pressure jump across the mixing layer can be used in evaluating the streamwise component of the momentum equation in the outer streams to yield

$$\rho_1'\left(\frac{\mathrm{d}A_1'}{\mathrm{d}t}+A_1'^2\right)x=\rho_2'\left(\frac{\mathrm{d}A_2'}{\mathrm{d}t}+A_2'^2\right)x=-\frac{\partial\tilde{p}}{\partial x}, \tag{2.5}$$

as an expression relating A_1' and A_2'. For given values of $p_s'(t)$ and $A_1'(t)$, the first equation in (2.5) together with (2.4) provide a Ricatti equation to determine $A_2'(t)$, while (2.3) determines ρ_1', ρ_2', T_1' and T_2' as functions of time. These serve as boundary conditions for the mixing–layer problem, to be formulated below, following [13].

The solution for the self-similar reactive counterflow mixing layer involves the integration

of

$$\frac{\partial \rho'}{\partial t} + \frac{\partial}{\partial y}(\rho' v) + \rho' A' = 0 \tag{2.6}$$

$$\rho' \left(\frac{\partial A'}{\partial t} + v \frac{\partial A'}{\partial y} + A'^2 \right) = \rho'_1 \left(\frac{\mathrm{d}A'_1}{\mathrm{d}t} + A'^2_1 \right) + \frac{\partial}{\partial y} \left(\mu \frac{\partial A'}{\partial y} \right) \tag{2.7}$$

$$\rho' c_p \left(\frac{\partial T'}{\partial t} + v \frac{\partial T'}{\partial y} \right) = \frac{\partial}{\partial y} \left(\lambda' \frac{\partial T'}{\partial y} \right) + \frac{\mathrm{d}p'_s}{\mathrm{d}t} - \sum_i h_i^o \dot{m}_i \tag{2.8}$$

$$\rho' \left(\frac{\partial Y_i}{\partial t} + v \frac{\partial Y_i}{\partial y} \right) = \frac{\partial}{\partial y} \left(\rho' D_i \frac{\partial Y_i}{\partial y} \right) + \dot{m}_i \tag{2.9}$$

with $v = 0$ at $y = 0$ and boundary conditions obtained by matching to outer inviscid regions

$$A' - A'_1(t) = T' - T'_1(t) = Y_i - Y_{i,1} = 0 \quad \text{as} \quad y \to \infty \tag{2.10}$$

$$A' - A'_2(t) = T' - T'_2(t) = Y_i - Y_{i,2} = 0 \quad \text{as} \quad y \to -\infty. \tag{2.11}$$

A Fickian description with Soret diffusion neglected has been adopted for the diffusion velocities, with D_i representing the diffusion coefficient of species i in the mixture. Differences of specific heat of each species from the mean value c_p have been neglected along with Dufour effects in writing the conductive heat flux, with λ' representing the thermal conductivity. In the chemical reaction terms h_i^o and $\dot{m}_i$ are the enthalpy of formation and chemical rate of production of species i. The above equations (2.6)–(2.9) must be supplemented by the equation of state (2.1) and by expressions for the variation with T' and composition of the specific heat c_p, viscosity μ, and the transport coefficients λ' and D_i.

2.3 Simplified non-dimensional formulation

The formulation given above can be used for the analysis of time-dependent combustion problems, including transient ignition events in Diesel-engine applications [13] and periodic solutions, such as those arising in studies of flame acoustic response [14, 15]. The nondimen-

sionalization of the problem begins by writing the stagnation-point pressure and the strain rate in the dimensionless form $p_s = p'_s/p'_c$ and $A = A'/A'_c$ with use made of appropriately selected scales p'_c and A'_c, the latter used also in the definition of the dimensionless time $\tau = A'_c t$. For steady problems the constant values of p'_s and A'_1 are used as scales, whereas for time-dependent systems the specific selection of p'_c and A'_c depends on the problem at hand. For instance, for transient ignition or extinction problems the natural scales are the initial values $p'_s(0)$ and $A'_1(0)$ whereas for studies of flame response to periodic oscillations the time-average values of $p'_s(t)$ and $A'_1(t)$ would be preferred. For a given value of p'_c, the accompanying characteristic values of the temperature and density T'_c and ρ'_c for the variables $T = T'/T'_c$ and $\rho = \rho'/\rho'_c$ are to be selected from the properties of stream 1 to reduce (2.3) to

$$T_1 = T_2/\Theta = p_s^{(\gamma-1)/\gamma} \quad \text{and} \quad \rho_1 = \rho_2\Theta/(M_2/M_1) = p_s^{1/\gamma}. \tag{2.12}$$

These dimensionless variables can be used to write (2.5) in the form

$$\frac{dA_2}{d\tau} + A_2^2 = \frac{\Theta}{M_2/M_1}\left(\frac{dA_1}{d\tau} + A_1^2\right), \tag{2.13}$$

whereas the equation of state (2.1) becomes

$$p_s(t) = \rho T \sum_i (M_1/M_i) Y_i. \tag{2.14}$$

The key component of the formulation is the introduction of the dimensionless inverse-thermal-conductivity-weighted coordinate

$$\eta(y,t) = (\lambda'_c/\delta_m)\int_0^y \frac{dy}{\lambda'(y,t)}, \tag{2.15}$$

involving the characteristic thermal conductivity $\lambda'_c = \lambda'(T'_c, Y_{i_1})$ of stream 1 and the characteristic

mixing layer thickness $\delta_m = (\lambda'_c/\rho'_c c_p A'_c)^{1/2}$. Introduction of the transformed coordinate η along with the modified nondimensional transverse mass flux

$$F = -\frac{\rho' v + \rho'\lambda' \int_0^y \frac{\partial}{\partial t}\left(\frac{1}{\lambda'}\right) \mathrm{d}y}{\rho'_c \delta_m A'_c} \tag{2.16}$$

reduce (2.6)–(2.9) to

$$\frac{\partial}{\partial \tau}(\rho\lambda) = \frac{\partial F}{\partial \eta} - \rho\lambda A \tag{2.17}$$

$$\rho\lambda\frac{\partial A}{\partial \tau} = F\frac{\partial A}{\partial \eta} + Pr\frac{\partial^2 A}{\partial \eta^2} + \lambda\left[p_s^{1/\gamma}\left(\frac{\mathrm{d}A_1}{\mathrm{d}\tau} + A_1^2\right) - \rho A^2\right] \tag{2.18}$$

$$\rho\lambda\frac{\partial T}{\partial \tau} = F\frac{\partial T}{\partial \eta} + \frac{\partial^2 T}{\partial \eta^2} + \frac{\gamma-1}{\gamma}\lambda\frac{\mathrm{d}p_s}{\mathrm{d}\tau} - \lambda\sum_i\left(\frac{h_i^o}{c_p T'_c}\right)\left(\frac{\dot{m}_i}{\rho'_c A'_c}\right) \tag{2.19}$$

$$\rho\lambda\frac{\partial Y_i}{\partial \tau} = F\frac{\partial Y_i}{\partial \eta} + \frac{1}{L_i}\frac{\partial^2 Y_i}{\partial \eta^2} + \lambda\frac{\dot{m}_i}{\rho'_c A'_c}. \tag{2.20}$$

where

$$\lambda(T, Y_i) = \lambda'/\lambda'_c \tag{2.21}$$

is the nondimensional thermal conductivity, a function of the temperature and composition. A constant specific heat c_p has been assumed in writing (2.19) while constant values of the Prandtl number $Pr = \mu c_p/\lambda'$ and Lewis numbers $L_i = \lambda'/(\rho' c_p D_i)$ have been used in (2.18) and (2.20), respectively. These approximations are introduced to exhibit most clearly the advantage of the transformation being investigated, since variable specific heats and Prandtl or Lewis numbers introduce distracting complications with any transformation. Comparison of (2.17)–(2.20) with (2.6)–(2.9) reveals that, in this transformed formulation, the product $\rho\lambda$, which corresponds to the Chapman-Rubesin parameter of the Howarth-Dorodnitzyn transformation, curiously plays essentially the same role as the gas density in the original dimensional formulation.

For given functions $p_s(\tau)$ and $A_1(\tau)$, the problem reduces to that of integrating (2.17)–(2.20) supplemented with (2.14) and (2.21) subject to the initial conditions $A(\eta, 0) = A_{\text{init}}(\eta)$,

$T(\eta,0) = T_{\text{init}}(\eta)$, and $Y_i(\eta,0) = Y_{i_{\text{init}}}(\eta)$ and the boundary conditions $F = 0$ at $\eta = 0$ and

$$\begin{cases} A - A_1(\tau) = T - p_s^{(\gamma-1)/\gamma} = Y_i - Y_{i,1} = 0 & \text{as} \quad \eta \to \infty \\ A - A_2(\tau) = T - \Theta p_s^{(\gamma-1)/\gamma} = Y_i - Y_{i,2} = 0 & \text{as} \quad \eta \to -\infty, \end{cases} \tag{2.22}$$

with the fuel-side strain rate $A_2(\tau)$ determined from integration of (2.13). Inspection of (2.17)–(2.20) reveals that introduction of the transverse coordinate η and the accompanying mass flux F leads to a compact convective-diffusive operator that facilitates numerical integration. As shown below, an additional advantage of the current formulation lies in the remarkable fact that in steady systems the transverse mass flux across the mixing layer can be approximated by the linear distribution $F = \eta$, so that the conservation equations for energy and species reduce to those obtained when employing the thermo-diffusive approximation (constant density and transport properties), uncoupled from continuity and momentum conservation, and resulting in the mixture-fraction profile being expressible in explicit form in terms of the error function.

2.4 An illustrative application of the formulation

2.4.1 Steady counterflow diffusion flames

As an illustrative example the counterflow formulation is applied to steady nonpremixed methane-air flames, corresponding to stationary situations in which the boundary values of the strain rate A_1 and A_2 and the stagnation-point pressure p_s remain constant. The steady profiles obtained below provide the base flow needed to analyze unsteady flame perturbations, for example in studies of flame instability or acoustic response to external forcing. To further illustrate the applicability of the formulation to these unsteady cases, we present in an appendix the results corresponding to the flame response to harmonic changes of the imposed strain rate. Extensions to other cases, including studies of acoustic pressure response, are worth pursuing in future work.

Stream 1 will be taken to be the air stream, with corresponding air-side oxygen mass fraction $Y_{\mathrm{O}_{2,1}} = 0.232$. For generality, dilution of the fuel stream with nitrogen is permitted, and results will be presented for different values $Y_{\mathrm{F},2} \leq 1$ of the methane mass fraction in its feed stream. Since the focus is on the flow structure, the oxidation of the fuel will be modeled with a one-step irreversible reaction $CH_4 + 2O_2 \rightarrow CO_2 + 2H_2O$ with infinitely fast rate. As is well known, if a unity Lewis number is assumed for both reactants, a good approximation for methane-air flames, then the associated Burke-Schumann problem [16] can be described in terms of the mixture fraction

$$Z = \frac{SY_{\mathrm{F}} - Y_{\mathrm{O}} + 1}{S+1} = \frac{T - 1 + q(Y_{\mathrm{O}} - 1)}{\Theta - 1 - q}, \tag{2.23}$$

written for the normalized reactant mass fractions $Y_{\mathrm{F}} = Y_{\mathrm{F}}/Y_{\mathrm{F},2}$ and $Y_{\mathrm{O}} = Y_{\mathrm{O}2}/Y_{\mathrm{O}_{2,1}}$. Two thermochemical parameters appear in the description, namely, the mass of air needed to burn the unit mass of fuel stream $S = 4Y_{\mathrm{F},2}/Y_{\mathrm{O}_{2,1}}$ and the dimensionless heat of reaction $q = (q' Y_{\mathrm{O}_{2,1}})/(c_p T_c')$, where $q' = (h_{\mathrm{F}}^o - 2h_{\mathrm{H_2O}}^o - h_{\mathrm{CO_2}}^o)/(2M_{\mathrm{O}_2}) \simeq 12,537$ kJ/g is the amount of heat released per unit mass of oxygen consumed in the reaction. The flame appears as a surface $\eta = \eta_f$ separating a fuel region with $Y_{\mathrm{O}} = 0$ from an oxidizer region with $Y_{\mathrm{F}} = 0$, with the reactants reaching the flame by diffusion from opposite sides in stoichiometric proportions. Both reactant mass fractions vanish at the flame sheet η_f, where

$$Z = Z_s = \frac{1}{S+1} = \frac{1}{4Y_{\mathrm{F},2}/0.232 + 1} \tag{2.24}$$

and

$$T = T_f = 1 + (\Theta - 1)Z_s + q(1 - Z_s). \tag{2.25}$$

Use of (4.53) allows for the temperature and composition to be expressed as piecewise linear

functions of Z according to

$$\begin{cases} Z > Z_s : Y_{\mathrm{O}} = 0, \quad Y_{\mathrm{F}} = (Z - Z_s)/(1 - Z_s), \quad T = (\Theta - 1 - q)Z + 1 + q, \\ Z < Z_s : Y_{\mathrm{O}} = 1 - Z/Z_s, \quad Y_{\mathrm{F}} = 0 \quad T = (\Theta - 1 - q)Z + 1 + qZ/Z_s. \end{cases} \tag{2.26}$$

The problem reduces to the integration of the continuity and momentum equations coupled with a transport equation for the mixture fraction. In terms of the thermal-conductivity-weighted coordinate η defined in (3.1) and the nondimensional transverse mass flux $F = -(\rho' v)/(\rho'_1 \delta_m A'_1)$, with

$$\delta_m = \left(\frac{\lambda'_1}{\rho'_1 c_p A'_1} \right)^{1/2} \tag{2.27}$$

representing the characteristic mixing-layer thickness, the needed conservation equations become

$$\begin{aligned} \frac{\mathrm{d}F}{\mathrm{d}\eta} - \rho\lambda A &= 0 \\ Pr\frac{\mathrm{d}^2 A}{\mathrm{d}\eta^2} + F\frac{\mathrm{d}A}{\mathrm{d}\eta} + \lambda(1 - \rho A^2) &= 0 \\ \frac{\mathrm{d}^2 Z}{\mathrm{d}\eta^2} + F\frac{\mathrm{d}Z}{\mathrm{d}\eta} &= 0 \end{aligned} \tag{2.28}$$

to be integrated with the boundary conditions $F(0) = 0$ and

$$\begin{cases} \eta \to +\infty : \quad A - 1 = Z = 0 & \text{(oxidizer side)} \\ \eta \to -\infty : \quad A - A_2 = Z - 1 = 0. & \text{(fuel side)} \end{cases} \tag{2.29}$$

As follows from (2.13), for steady counterflows the fuel-side strain rate is given by $A_2 = [\Theta(M_1/M_2)]^{1/2}$, where the molecular–mass ratio varies with the fuel-side dilution according to

$$\frac{M_1}{M_2} = \frac{1 + (M_{\mathrm{N_2}}/M_{\mathrm{CH_4}} - 1)Y_{\mathrm{F},2}}{1 + (M_{\mathrm{N_2}}/M_{\mathrm{O_2}} - 1)Y_{\mathrm{O_2},1}}, \tag{2.30}$$

with $M_{\mathrm{N_2}}/M_{\mathrm{CH_4}} = 28/16$ and $M_{\mathrm{N_2}}/M_{\mathrm{O_2}} = 28/32$. In the integration, equations (2.28) are sup-

plemented with the presumed power-law expression $\lambda = T^{0.7}$ for the thermal conductivity and the equation of state

$$1 = \rho T \left\{ \frac{M_1}{M_{N_2}} + Y_{F,2} \frac{M_1}{M_{N_2}} \left(\frac{M_{N_2}}{M_{CH_4}} - 1 \right) Y_F + \left(1 - \frac{M_1}{M_{N_2}} \right) Y_O \right\}, \tag{2.31}$$

which is written by assuming that the mean molecular mass of the combustion products M_P is equal to that of nitrogen, an excellent approximation for methane-air combustion, for which $M_P = (M_{CO_2} + 2M_{H_2O})/3 = 27 \approx M_{N_2} = 28$ g/mol.

Results obtained with (2.28) will be compared to integrations employing the alternative conservation equations

$$\begin{aligned} \frac{dF}{d\zeta} - A &= 0 \\ Pr \frac{d}{d\zeta} \left(C \frac{dA}{d\zeta} \right) + F \frac{dA}{d\zeta} + \frac{1}{\rho} - A^2 &= 0 \\ \frac{d}{d\zeta} \left(C \frac{dZ}{d\zeta} \right) + F \frac{dZ}{d\zeta} &= 0 \end{aligned} \tag{2.32}$$

employing the standard Howarth-Dorodnitzyn coordinate

$$\zeta = (\rho_1' \delta_m)^{-1} \int_0^y \rho'(y) dy. \tag{2.33}$$

The corresponding boundary conditions are identical to those written above for (2.28). Appearing as a factor in the viscous stress and in the diffusive flux of (2.32) is the Chapman-Rubesin function $C = \rho\lambda$ which describes the relation between ζ and η according to $d\zeta/d\eta = C$ as follows from the respective definition of each coordinate. In general, $C \neq 1$ and the resulting transport operators in (2.32) are more complicated than those obtained with the coordinate η, as can be seen by comparing (2.28) and (2.32).

2.4.2 Sample numerical results

Integrations were performed for $Pr = 0.7$, $\Theta = 1$, and $q = 7$, as corresponds to methane-air combustion with equal feed-stream temperatures. Solutions are given for different extents of dilution of the fuel stream, measured by $Y_{\mathrm{F},2}$, which enters in the equation of state (2.31), in the boundary value of the strain rate $A_2 = [\Theta(M_1/M_2)]^{1/2}$ through the molecular-mass-ratio (2.30), and in the definition of the stoichiometric mixture fraction Z_s defined in (2.24). In particular, Figure 2.2 shows the mixing-layer structure in terms of the density-weighted coordinate ζ for methane-air ($Y_{\mathrm{F},2} = 1$) and diluted methane-air ($Y_{\mathrm{F},2} = 0.1$), with corresponding results plotted in terms of the thermal-conductivity-weighted coordinate η in Figure 2.3. Besides profiles of mixture fraction Z and transverse momentum flux F, the plots include profiles of reactant mass fractions and normalized temperature increment evaluated using the piecewise relations (4.55).

The right plots in Figure 2.2 display also the variation of the Chapman-Rubesin parameter $C = \rho\lambda$ across the mixing layer, which shows a discontinuous slope at the flame, with an associated value there given by

$$C_f = T_f^{-0.3} M_{\mathrm{N}_2}/M_1, \tag{2.34}$$

with $T_f = 1 + q(1 - Z_s)$, as follows from (3.21). In addition, the graphs show the results obtained by writing (2.32) with the commonly used approximation $C = 1$, with associated profiles represented by the light curves. The departures from unity of C are seen to be substantial, especially for undiluted fuel feed. Correspondingly, the mixing-layer structures computed with $C = 1$, including the resulting flame location in the transformed coordinate, differ significantly from the exact results.

For completeness, dashed curves are included in Figure 2.2 to illustrate the applicability of the approximation $F = \zeta$, which when combined with the assumption $C = 1$ leads to the analytic result $Z = (1/2)\mathrm{erfc}(\zeta/\sqrt{2})$, quoted in early flamelet studies [17], where erfc is the complementary error function. As can be seen, the resulting accuracy is far from satisfactory,

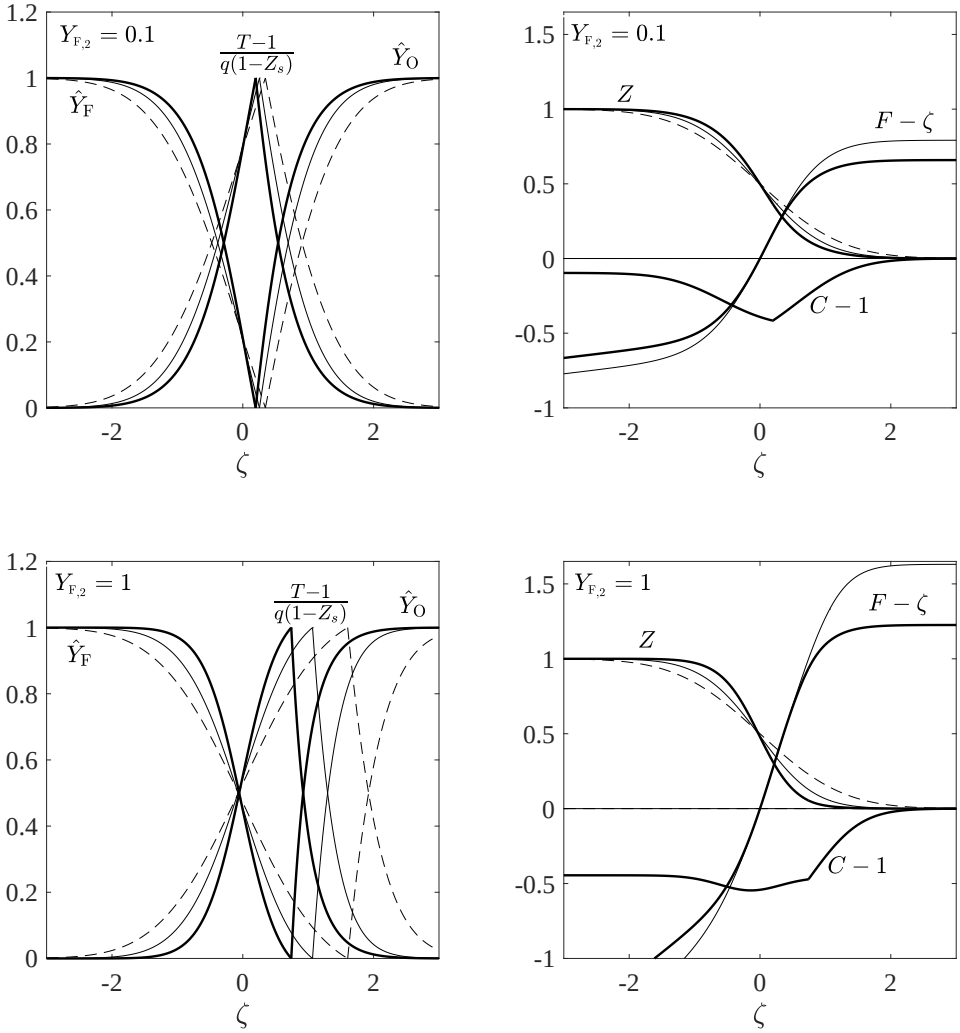

Figure 2.2: Results of integrations (dark solid curves) using the density-weighted Howarth-Dorodnitzyn variable ζ for diluted $Y_{\mathrm{F},2} = 0.1$ (top) and pure $Y_{\mathrm{F},2} = 1$ (bottom) methane-air counterflow respectively. Shown in light curves are integrations employing $C = 1$ in (2.32), with the dashed curves corresponding to results with the additional approximation $F = \zeta$, for which $Z = (1/2)\mathrm{erfc}(\zeta/\sqrt{2})$.

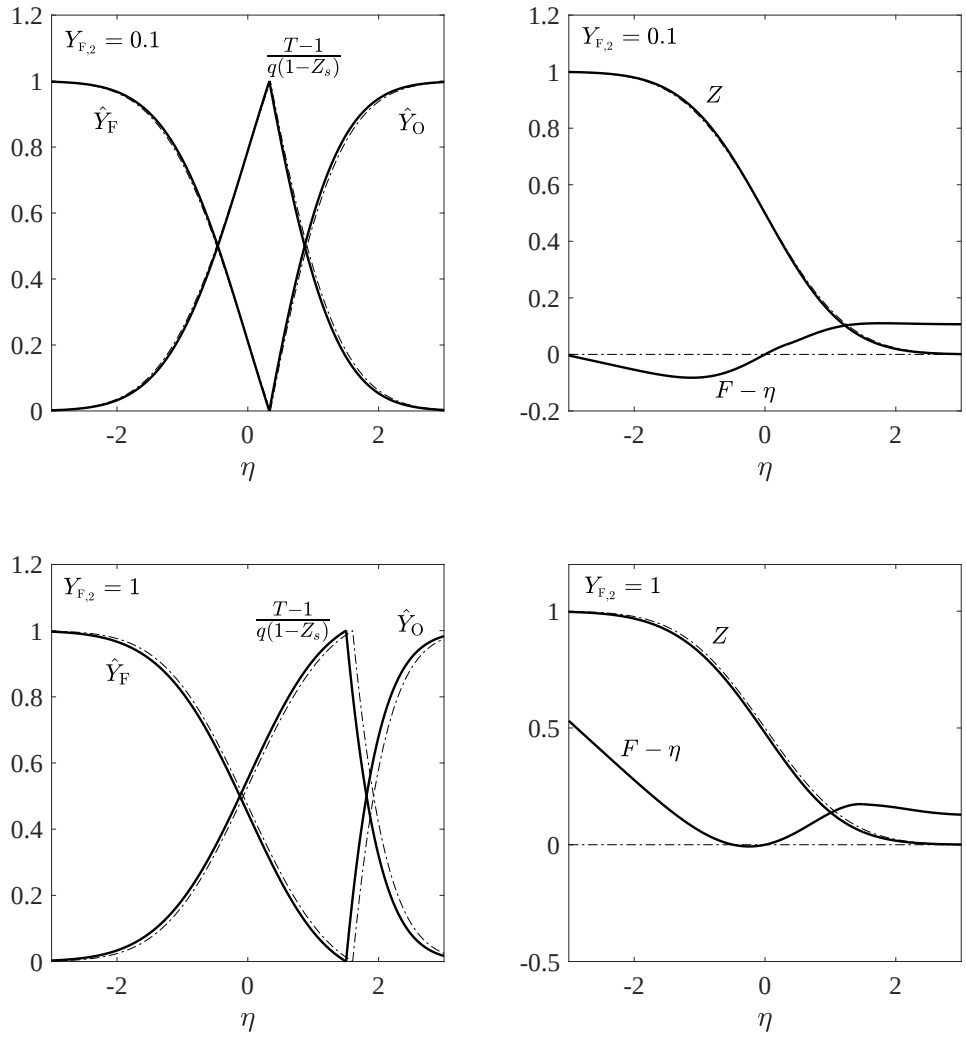

Figure 2.3: Integrations (solid lines) using the thermal-conductivity variable η for diluted $Y_{\mathrm{F},2} = 0.1$ (top) and pure $Y_{\mathrm{F},2} = 1$ (bottom) methane-air counterflow respectively. Shown in dot-dashed lines are analytic results obtained using the approximation $F = \eta$, including $Z = (1/2)\mathrm{erfc}(\eta/\sqrt{2})$ from which T, Y_{F} and Y_{O} may be found using the piecewise relation (4.55).

as would be expected, in view of the profiles of $F-\zeta$ shown in the right-hand-side plots of Figure 2.2.

By way of contrast, the profiles shown on the right-hand-side plots of Figure 2.3 indicate that the departures of the transverse mass flux from the linear distribution are moderately small when expressed in terms of the thermal-conductivity-weighted coordinate η. Correspondingly, the solution for the mixture fraction $Z=(1/2)\mathrm{erfc}(\eta/\sqrt{2})$, obtained with the approximation $F=\eta$ by integrating the third equation in (2.28), and the accompanying profiles of temperature and reactant mass fraction, evaluated from (4.55), give excellent predictions for the mixing-layer structure, as can be seen in the comparisons of Figure 2.3. The differences of the analytic predictions, represented by the dot-dashed curves, from the results of numerical integrations of (2.28) are almost imperceptible for $Y_{\mathrm{F},2}=0.1$ and remain remarkably small even for $Y_{\mathrm{F},2}=1$. Use of these analytic expressions for the temperature and composition within the middle equation of (2.28) together with $F=\eta$ provides a simplified equation for computing the strain rate. The resulting profiles $A(\eta)$, not shown here, compare well with those of the full numerical solution, with relative departures of the same order as those seen in Figure 2.3 for the corresponding profiles of composition and temperature.

For completeness, Figure 2.4 shows the variation with fuel-feed dilution of the flame location y_f, defined in the Burke-Schumann limit by the condition $Z=Z_s$. Naturally, when no simplifications are introduced, both formulations (2.28) and (2.32) provide the same value, which can be expressed in the dimensionless form

$$\frac{y_f}{\delta_m}=\int_0^{\eta_f}\lambda\,\mathrm{d}\eta=\int_0^{\zeta_f}\frac{\mathrm{d}\zeta}{\rho} \tag{2.35}$$

in terms of the dimensionless flame locations η_f and ζ_f, with δ_m given for the steady counterflow in (2.27). For the range of $Y_{\mathrm{F},2}$ investigated, the resulting flame always lies on the air side of the mixing layer. Consequently, since $Y_{\mathrm{O}}=0$ between the stagnation plane and the flame, the

first expression in (4.55) must be used in evaluating the integrals in (2.35). The exact numerical results, shown as a dark solid curve, are compared with those obtained by employing in (2.32) the approximation $C = 1$ (light solid curve) and also with those obtained with $Z = (1/2)\mathrm{erfc}(\zeta/\sqrt{2})$ (dashed curve). Clearly, the predictions of flame location resulting from these approximations are far from satisfactory, with both approximations significantly overpredicting the flame distance to the stagnation plane, in agreement with the profiles shown in Figure 2.2. The figure also tests the approximation $F = \eta$ and associated prediction $y_f/\delta_m = \int_0^{\eta_f}[1+q(1-Z)]^{0.7}\mathrm{d}\eta$, where $\eta_f = \sqrt{2}\mathrm{erfc}^{-1}(2Z_s)$ and $Z = (1/2)\mathrm{erfc}(\eta/\sqrt{2})$, with erfc^{-1} denoting the inverse (not the reciprocal) of the complementary error function. As can be seen, over the entire range of dilution considered the accuracy of this approximation is remarkably good.

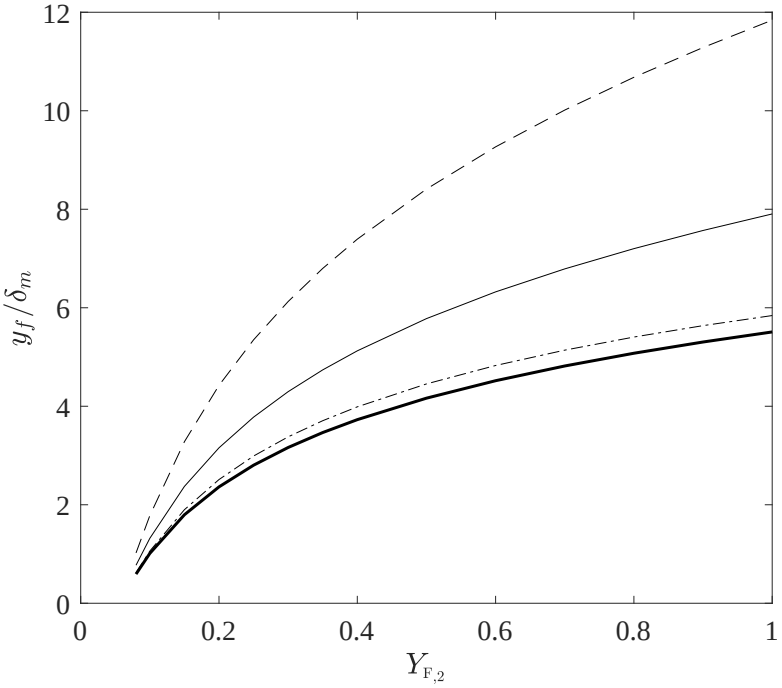

Figure 2.4: The variation with the fuel-stream dilution of the flame location (2.35) obtained from numerical integration of (2.28) or (2.32) (dark solid curve), with the approximation $C = 1$ used in integrating (2.32) (light solid curve), with the presumed profile $Z = (1/2)\mathrm{erfc}(\zeta/\sqrt{2})$ used to evaluate the density in the last expression of (2.35) (dashed curve), and with the approximation $y_f/\delta_m = \int_0^{\eta_f}[1+q(1-Z)]^{0.7}\mathrm{d}\eta$ with $\eta_f = \sqrt{2}\mathrm{erfc}^{-1}(2Z_s)$ and $Z = (1/2)\mathrm{erfc}(\eta/\sqrt{2})$ (dot-dashed curve).

In summary, the results in Figures 2.2 and 2.4 indicate that departures from unity of the Chapman-Rubesin parameter cannot be neglected in computations of counterflow flames using a density-weighted coordinate, and that the analytic solutions stemming from using the approximations $C = 1$ and $F = \zeta$ are not capable of giving acceptable accuracy under most conditions. In contrast, the alternative coordinate η results in a simpler transport operator and, for the steady flames shown in Figure 2.3, effectively reduces the solution to one involving a linearly varying transverse mass flux. Therefore, somewhat unexpectedly, the resulting solution is analogous to that obtained in the thermo-diffusive approximation of constant density and constant transport properties, a drastic simplification worthy of being considered in future work.

2.4.3 Scalar dissipation rate

The above counterflow results can be used to evaluate the scalar dissipation rate $\chi = 2[\lambda'/(\rho' c_p)]|\nabla Z|^2$, a quantity of utmost importance in nonpremixed combustion [11]. For the two formulations considered above the value χ_f of χ at the flame, scaled with the air-side strain rate A_1', can be expressed as

$$\frac{\chi_f}{A_1'} = \frac{2}{C_f}\left(\left.\frac{\mathrm{d}Z}{\mathrm{d}\eta}\right|_f\right)^2 = 2C_f\left(\left.\frac{\mathrm{d}Z}{\mathrm{d}\zeta}\right|_f\right)^2, \tag{2.36}$$

where the mixture-fraction derivatives are to be evaluated at $\eta = \eta_f$ or $\zeta = \zeta_f$, with C_f correspondingly representing the flame value of the Chapman-Rubesin parameter, given in (2.34) in terms of the flame temperature (3.21). The corresponding value of χ_f/A_1' is represented by a dark solid curve in Figure 2.5 as a function of the fuel-feed dilution.

The different approximations discussed above are also tested in Figure 2.5. The curve styles have been selected to match those employed in the corresponding curves of Figures 2.2–2.4. Thus, consistent with the results in Figures 2.2 and 2.4, the light curve represents results obtained from the last expression in (2.36) with $C_f = 1$ and with $\mathrm{d}Z/\mathrm{d}\zeta|_f$ computed from (2.32) with

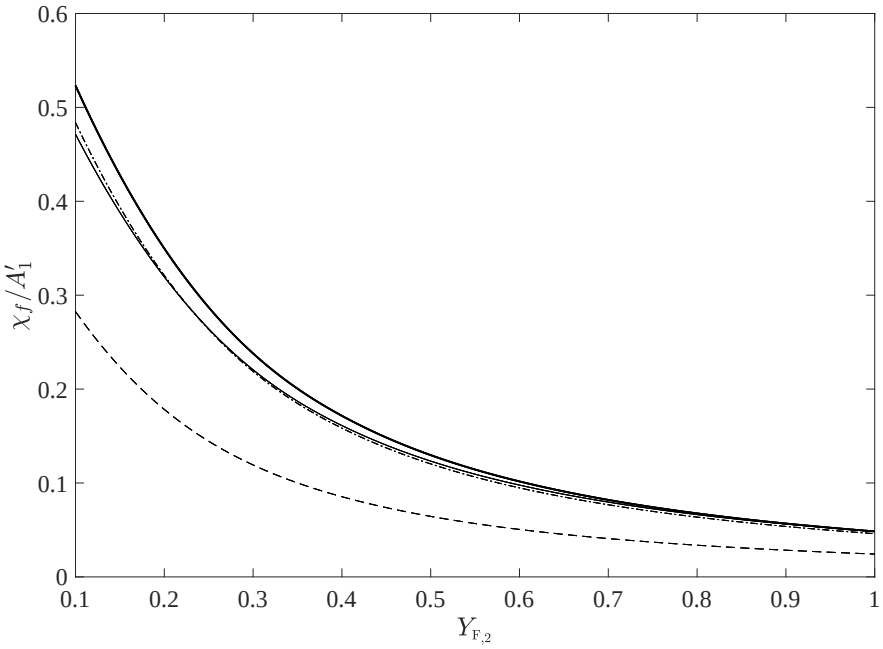

Figure 2.5: The variation with the fuel-stream dilution of the scalar dissipation rate at the flame (2.36) with the mixture-fraction gradient computed by numerical integration of (2.28) or (2.32). The dark solid curve represents exact numerical results; the light curve is the prediction obtained by employing $C = 1$ in computing $\mathrm{d}Z/\mathrm{d}\zeta|_f$ along with $C_f = 1$; the dashed curve is obtained with $C_f = 1$ and (2.37); and the dot-dashed curve is obtained from (2.38).

$C = 1$, whereas the dashed curve is the prediction obtained by using simultaneously $C_f = 1$ together with

$$\left(\left. \frac{\mathrm{d}Z}{\mathrm{d}\zeta} \right|_f \right)^2 = \frac{1}{2\pi} \exp[-\{\sqrt{2}\mathrm{erfc}^{-1}(2Z_s)\}^2] \tag{2.37}$$

the latter stemming from the commonly used approximation $Z = (1/2)\mathrm{erfc}(\zeta/\sqrt{2})$ [11]. Also tested in the figure is the approximation $F = \eta$, leading to $Z = (1/2)\mathrm{erfc}(\eta/\sqrt{2})$ and to

$$\frac{\chi_f}{A_1'} = \frac{1}{\pi C_f} \exp[-\{\sqrt{2}\mathrm{erfc}^{-1}(2Z_s)\}^2], \tag{2.38}$$

with corresponding predictions, obtained with use made of (2.24), (3.21), and (2.34), shown as a dot-dashed curve, that being the curve style used for this approximation in Figures 2.3 and 2.4.

Consistent with the degree of accuracy exhibited by the dot-dashed curves in Figures 2.3

and 2.4, the comparisons indicate that the analytical prediction (2.38) is remarkably good, with relative errors that remain smaller than 5% over the whole range of dilutions considered in the figure. Somewhat unexpectedly, the prediction obtained by using the Howarth-Dorodnitzyn transformation together with the approximation $C = 1$ yields similar accuracy. This is the result of a fortuitous cancellation of errors in (2.36), as can be inferred from the profiles shown in Figure 2.3. Thus, the approximation $C = 1$ yields flames that are too far from the stagnation plane, thereby leading to severe underpredictions of $\mathrm{d}Z/\mathrm{d}\zeta$, but these are almost exactly corrected when the value of $C_f \simeq 0.5 - 0.6$ is replaced by $C_f = 1$ in (2.36). As can be seen in Figure 2.5, this fortuitous accuracy degrades significantly when the gradient of mixture fraction is evaluated with use of (2.37).

2.5 Diffusion-flame response to harmonic variations of the strain rate

As an illustrative example of the applicability of the formulation to unsteady situations, this section investigates perturbations to the flame arising from variation of the imposed strain rate. For simplicity, variations of the molecular weight will be neglected and the two feed streams will be assumed to be at the same temperature (i.e. $\Theta = 1$). Attention is directed to small harmonic perturbations of the strain rate of the form $A_1(\tau) = A_2(\tau) = 1 + \varepsilon e^{\mathrm{i}\omega\tau}$, where the angular frequency ω has been scaled with the mean strain rate. In the Burke-Schumann limit, the analysis reduces to the integration of the continuity and momentum equations (2.17) and (2.18) together with the unsteady form of the mixture-fraction equation

$$\rho\lambda\frac{\partial Z}{\partial\tau} = F\frac{\partial Z}{\partial\eta} + \frac{\partial^2 Z}{\partial\eta^2} \tag{2.39}$$

with boundary conditions $F = 0$ at $\eta = 0$, $Z = A - A_1(\tau) = 0$ as $\eta \to \infty$, and $Z - 1 = A - A_2(\tau) = 0$ as $\eta \to -\infty$. In the integration, the temperature must be evaluated in terms of the mixture fraction with use made of (4.55), with the simplified equation of state $\rho = 1/T$ and the presumed power law $\lambda = T^{0.7}$ used to evaluate the density and the thermal conductivity.

For $\varepsilon \ll 1$ the unsteady perturbations to the different flow variables remain small, so that expressions of the form $F = \bar{F}(\eta) + \varepsilon e^{i\omega\tau}\hat{F}(\eta)$, $A = \bar{A}(\eta) + \varepsilon e^{i\omega\tau}\hat{A}(\eta)$, $Z = \bar{Z}(\eta) + \varepsilon e^{i\omega\tau}\hat{Z}(\eta)$, and $T = \bar{T}(\eta) + \varepsilon e^{i\omega\tau}\hat{T}(\eta)$ may be introduced. The bar is employed to denote the unperturbed steady solution, whereas the hat denotes the complex functions that describe the unsteady response of the flame. The solution for the steady functions $\bar{F}(\eta)$, $\bar{A}(\eta)$, and $\bar{Z}(\eta)$, presented in the paper in section 2.4, determines the basic properties of the unperturbed flame, including the flame location $\bar{\eta}_f$. The functions $\hat{F}$, $\hat{A}$, and $\hat{Z}$, which must satisfy the boundary conditions $\hat{F}(0) = 0$; $\hat{Z}(\pm\infty) = 0$; $\hat{A}(\pm\infty) = 1$, are governed by the conservation equations

$$\begin{aligned} -\bar{T}\hat{F}' + \bar{T}^{\sigma}\hat{A} + (\sigma - 1)\bar{T}^{\sigma-1}(i\omega + \bar{A})\hat{T} &= 0, \\ -\bar{A}'\hat{F} + (i\omega + 2\bar{A})\bar{T}^{\sigma-1}\hat{A} - \bar{F}\hat{A}' - Pr\hat{A}'' & \\ + \left[\bar{A}^2(\sigma - 1)/\bar{T} - \sigma\right]\bar{T}^{\sigma-1}\hat{T} &= \bar{T}^{\sigma}(i\omega + 2), \\ -\bar{Z}'\hat{F} + i\omega\bar{T}^{\sigma-1}\hat{Z} - \bar{F}\hat{Z}' - \hat{Z}'' &= 0, \end{aligned} \tag{2.40}$$

obtained by linearizing (2.17), (2.18), and (2.39), with the prime denoting differentiation with respect to η. The integration must employ the expressions $\hat{T} = -q\hat{Z}$ for $\eta < \bar{\eta}_f$ and $\hat{T} = q(1/Z_s - 1)\hat{Z}$ for $\eta > \bar{\eta}_f$, obtained from linearizing the piecewise-relation (4.55).

The functions $\hat{F}$, $\hat{A}$, and $\hat{Z}$ obtained by integration of the above problem can be used to evaluate the flame response to the outer perturbations. For instance, as a result of the harmonic forcing the flame location η_f oscillates about its unperturbed value $\bar{\eta}_f$ according to $\eta_f = \bar{\eta}_f + \varepsilon e^{i\omega\tau}\hat{\eta}_f$, where the perturbation $\hat{\eta}_f$ can be evaluated in terms of the value of $\hat{Z}$ at $\bar{\eta}_f$ from $\hat{\eta}_f\bar{Z}'(\bar{\eta}_f) + \hat{Z}(\bar{\eta}_f) = 0$, obtained by linearizing the equation $Z(\eta_f) = Z_s$. It is worth mentioning

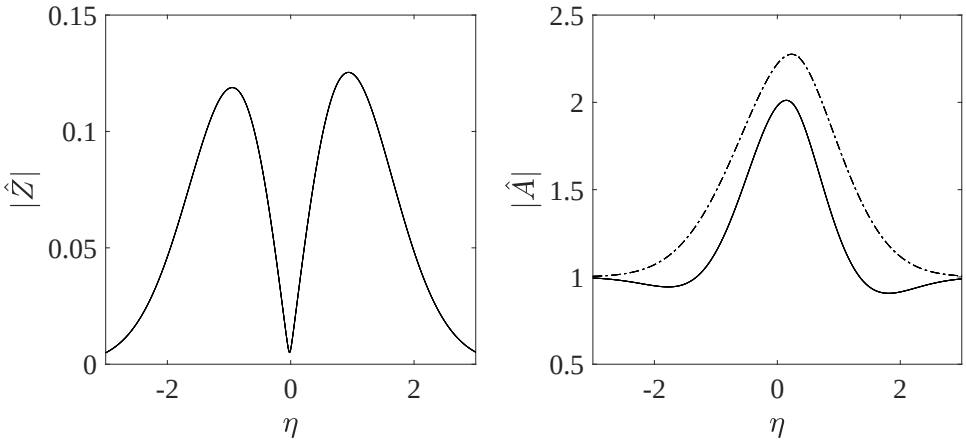

Figure 2.6: The mixture fraction and strain-rate perturbations obtained for $\omega = 1$. Solid lines correspond to full integration of (2.40) whereas dash-dotted line corresponds to the $F = \eta$ approximation

that, as can be easily verified by the reader, the linearized equations obtained when using the conventional density-weighted coordinate are significantly more complicated than those presented above, the inherent simplification of the thermal-conductivity-weighted coordinate being a consequence of the associated compact transport operator.

Representative profiles of perturbation amplitudes are shown in Figure 2.6 for $\omega = 1$. The integration considers the parametric values $Pr = 0.7$, $q = 7$, and $Z_s = 0.367$ corresponding to the flame displayed in the top plots of Figure 2.3. As can be seen, the perturbations to the mixture fraction are very small, while the perturbations to the streamwise velocity, measured by the function $|\hat{A}|$, are much larger. Since $|\hat{Z}|$ is everywhere small, the associated flame displacement $\hat{\eta}_f$, and also the variations of the temperature $\hat{T}$ and of the scalar dissipation rate, can be expected to be very limited, indicating that Burke-Schumann flames are rather insensitive to temporal variations of the outer strain rate, despite significant variations of the streamwise velocity.

It is worth mentioning that the extremely small value of $\hat{Z}$ shown in Figure 2.6 is consistent with our previous observation that the departures of the transverse mass flux F from the linear distribution $F = \eta$ are small. To see this, note that the approximation $F = \eta$ leads to mixture-fraction perturbations $\hat{Z}$ that are identically zero, as follows from integration of the last equation

in (2.40) with $\hat{F} = 0$. To further explore the accuracy of the approximation $F = \eta$ the value of $|\hat{A}|$ obtained from integrating the middle equation in (2.40) with $\bar{F} = \eta$ and $\hat{F} = \hat{T} = 0$ is shown as a dashed curve in Figure 2.6. The resulting strain-rate distribution is seen to be reasonably accurate, further suggesting that use of of the thermal-conductivity-weighted coordinate η together with the approximation $F = \eta$, shown to give excellent results in steady systems, can also provide a sufficiently accurate description in future computations of unsteady counterflow flames.

2.6 Concluding remarks

A compact formulation has been presented based on introduction of a new inverse-thermal-conductivity-weighted variable and associated transformed mass flux which may be applied towards the description of reacting counterflow mixing layers subject to variable strain rates and pressures. When compared to classical methods for dealing with boundary-layer-type problems, namely that of Howarth and Dorodnitzyn, the resulting equations posses a simpler convective-diffusive operator stemming from the fact that the variation with temperature of the transport coefficients is removed from the diffusive terms, thereby facilitating numerical integration and theoretical analyses of these flows, of direct interest in flamelet modeling. The advantage of the new transformation for combustion problems must be related to the effect of an increasing thermal conductivity tending to increase the distances over which variables change, thereby approaching constant-density conditions in the transformed coordinate. The formulation given can be extended readily, with minor modifications, to other stagnation-point flows of practical interest, including axisymmetric counterflow mixing layers separating opposed round jets, as well as stagnation-point boundary-layer flows generated by a jet impinging normally on a wall. The results presented in the appendix for the response of the counterflow flame to variations of the strain rate illustrate the potential advantages of the inverse-thermal-conductivity-weighted coordinate in analyses of unsteady flames, indicating the utility of the formulation in future

studies of acoustic response or flame stability, for instance. The use of the transformation to describe flames subject to nonuniform strain rates, such as those arising in problems involving interaction of vortices with mixing layers [18], is also worth further investigation, although the applicability of the reduced variables employed here to these non-selfsimilar configurations does not appear to be straightforward.

Numerical integrations reveal that, for steady situations, the transformed transverse mass flux F varies linearly with the rescaled coordinate η, a simplification that does not arise with the classical density-weighted coordinate ζ. This remarkable fact may be used to uncouple species and energy conservation from the continuity and momentum equations which then no longer need to be considered in the analysis. This simplification, akin to the thermo-diffusive approximation of constant density and constant transport properties, illustrates an additional advantage of the inverse-thermal-conductivity-weighted coordinate η in the description of stagnation-type flows.

This chapter, in full, has been published in *Combustion Theory and Modelling* titled " A novel formulation for unsteady counterflow flames using a thermal-conductivity-weighted coordinate", by A. D. Weiss, M. Vera, A. Liñán, A. L. Sánchez and F. A. Williams (2018) 22, 185-201. The dissertation author is the primary investigator in this publication.

Bibliography

[1] L. Howarth. On the solution of the laminar boundary layer equations. *Proc. R. Soc. Lond. A. Math Phys. Sci.*, 164.

[2] L. Howarth. Concerning the effect of compressibility on lam inar boundary layers and their separation. *Proc. R. Soc. Lond. A. Math Phys. Sci.*, 194:16–42, 1948.

[3] A Dorodnitsyn. Laminar boundary layer in compressible fluid. *Dokl. Akad. Nauk SSSR*, 34:213–219, 1942.

[4] F. K. Moore. Unsteady laminar boundary-layer flow. Technical report, 1951. Report No. NACA-TN-2471.

[5] K T Stewartson. On the impulsive motion of a flat plate in a viscous fluid. *Q. J. Mech. Appl. Math.*, 4:182–198, 1951.

[6] F. A. Williams. *Combustion Theory*. 2nd Edn., Addison-Wesley Publ. Co., 1985. pp.485-495.

[7] S. S Penner and F. A. Williams. The theory of steady, one-dimensional, laminar flame propagation for one-step chemical reactions. *Acta Astronaut.*, 7:171–189, 1961.

[8] N. Peters and B. Rogg. *Reduced kinetic mechanisms for applications in combustion systems*. Springer-Verlag, 1993. Ch.3, pp. 31.

[9] M. Matalon, C. Cui, and J. K. Bechtold. Hydrodynamic theory of premixed flames: effects of stoichiometry, variable transport coefficients and arbitrary reaction orders. *J. Fluid Mech.*, 487:179–210, 2003.

[10] A. Liñán, D. Martínez-Ruiz, M. Vera, and A. L. Sánchez. The large-activation-energy analysis of extinction of counterflow diffusion flames with non-unity lewis numbers of the fuel. *Combust. Flame*, 175:91–106, 2017.

[11] N. Peters. *Turbulent combustion*. Cambridge University Press, 2000.

[12] A. D. Weiss, W. Coenen, and A. L. Sánchez. Aerodynamics of planar counterflowing jets. *J. Fluid Mech.*, 821:1–30, 2017.

[13] A. Liñán and F. A. Williams. Ignition in an unsteady mixing layer subject to strain and variable pressure. *Combust. Flame*, 95:31–46, 1993.

[14] J. S. Kim and F. A. Williams. Contribution of strained diffusion flames to acoustic pressure response. *Combust. Flame*, 98:279–299, 1994.

[15] H. G. Im, C. K. Law, J. S. Kim, and F. A. Williams. Response of counterflow diffusion flames to oscillating strain rates. *Combust. Flame*, 100:21–30, 1995.

[16] Amable Liñán, Marcos Vera, and Antonio L Sánchez. Ignition, liftoff, and extinction of gaseous diffusion flames. *Annu. Rev. Fluid Mech.*, 47:293–314, 2015.

[17] N. Peters. Laminar diffusion flamelet models in non-premixed turbulent combustion. *Prog. Ener. Combust. Sci.*, 10:319–339, 1984.

[18] M Vera and A. Liñán. On the interaction of vortices with mixing layers. *Phys.Fluids*, 16:2237–2254, 2004.

Chapter 3

The acoustic response of Burke-Schumann counterflow flames

3.1 Introduction

Acoustic combustion instabilities, characterized by the amplification of pressure oscillations corresponding to the acoustic eigenmodes of the combustion chamber, mainly through interactions with the exothermic combustion reactions, have been a significant concern in the development of liquid-propellant rocket engines from the beginning [1]. In an effort to minimize the potential physical manifestations of these instabilities – including excessive vibration, thermo-mechanical failure, and reduced performance – there has been considerable incentive for scientific studies that provide valuable insight into this unwanted phenomena [2]. Associated concerns about instabilities continue in recent years [3–8].

Difficulty in predicting acoustic instabilities is intrinsically linked to the complex nature of the turbulent multi-phase conditions throughout the combustor, so that in the absence of a general theory for describing such flows, insufficient knowledge of unsteady high-pressure phenomena limits predictive capabilities of acoustic instabilities. Despite this, significant progress has been

made with use of flamelet-modeling approaches, in which the turbulent flame is modeled as an ensemble of laminar flamelets that are strained and distorted by the turbulent flow [9, 10]. Computations of liquid-propellant rocket-engine instabilities using flamelet modeling require not only knowledge of the statistics regarding distributions of elementary laminar flamelets throughout the chamber but also their response functions to acoustic excitation [11]. The present paper addresses the last aspect of this challenging problem by investigating the acoustic response of planar counterflow nonpremixed flames.

The counterflow diffusion flame has been utilized in the past as a canonical problem to investigate the interplay of the pressure oscillations with the oscillations of rates of heat release by chemical reactions, which are modified as the acoustic perturbations propagate through the diffusion layers of the flames. In the linear limit, the analysis may be greatly simplified by noting that the acoustic pressure nodes and velocity antinodes coincide [12] so that the flame response to pressure perturbations and velocity perturbations may be studied independently by regarding the flamelet to be located at the appropriate node. The analysis here will be concerned with the Burke-Schuman (B-S) limit of infinitely fast reaction, a limit previously considered in the analysis of droplet burning [13] and fuel plates [14]. Unlike these early analyses, our computations account for differential diffusion effects associated with fuel Lewis numbers different from unity.

The solutions obtained here pertain to a flame sheet separating two unsteady regions in chemical equilibrium. This not only provides the basic structure for future studies accounting for finite-rate effects but also quantifies one of the two contributions that arise of finite-rate cases, namely, the direct transport-region contribution. In these respects, it is worth pointing out that some of the previous finite-rate analyses of flame acoustic response [15, 16] have investigated the so-called premixed-flame regime [17], including fuel leakage of order unity into the oxidizer side, which is chemically frozen rather than in chemical equilibrium. This basic structure, fundamentally different from the B-S structure, is favored when the stoichiometric mixture fraction Z_S is sufficiently small, as occurs in hydrocarbon-air systems, for which $Z_S \simeq 1/16$. Much

larger values $Z_S \simeq 1/5$ are found when the oxidizer is oxygen, which is much more relevant for liquid-propellant rocket-engine applications, in which burning is likely to occur predominantly in the diffusion-flame regime [17], which, at leading order, reduces to the B-S limit investigated here. This fact underscores the need to quantify accurately the response of B-S flames as a necessary step in future efforts to account for effects of realistic chemistry descriptions.

As shown recently [18], the description of stagnation-point mixing layers subject to large variations in density and transport properties resulting from chemical heat release can be facilitated by introducing a thermal-conductivity-weighted coordinate, which is adopted here in formulating the problem in Sec. 3.2. The limit of infinitely fast reaction and the perturbation strategy for its description are discussed in Sec. 3.3 and 3.4, respectively. The acoustic pressure response is discussed in Sec. 3.5. The acoustic velocity or strain response is examined in Sec. 3.6. A discussion of implications to acoustic instabilities is given in Sec. 3.7, which is followed by concluding remarks in Sec. 3.8.

3.2 Problem formulation

We consider a locally planar strained mixing layer situated in the stagnation-point flow generated by counterflowing streams of fuel and oxidizer. At moderately large Reynolds numbers the thin mixing layer separates two effectively inviscid and isentropic streams whose structure provides appropriate boundary conditions for the analysis of the unsteady chemically active mixing region [19]. A reference system moving with the dividing streamline is employed in the description, with cartesian coordinates (x, y) and the oxidizer approaching from $y = +\infty$, as indicated in Fig. 3.1. Subscripts O and F are used to denote properties in the oxidizer and fuel streams, respectively. In the outer inviscid streams the velocity field is given by the potential solutions $(v_x, v_y) = A^*_{\mathrm{O}}(x, -y)$ and $(v_x, v_y) = A^*_{\mathrm{F}}(x, -y)$ in terms of the time-dependent strain rates $A^*_{\mathrm{O}}(t)$ and $A^*_{\mathrm{F}}(t)$, an asterisk idntifying original dimensional variables throughout. The

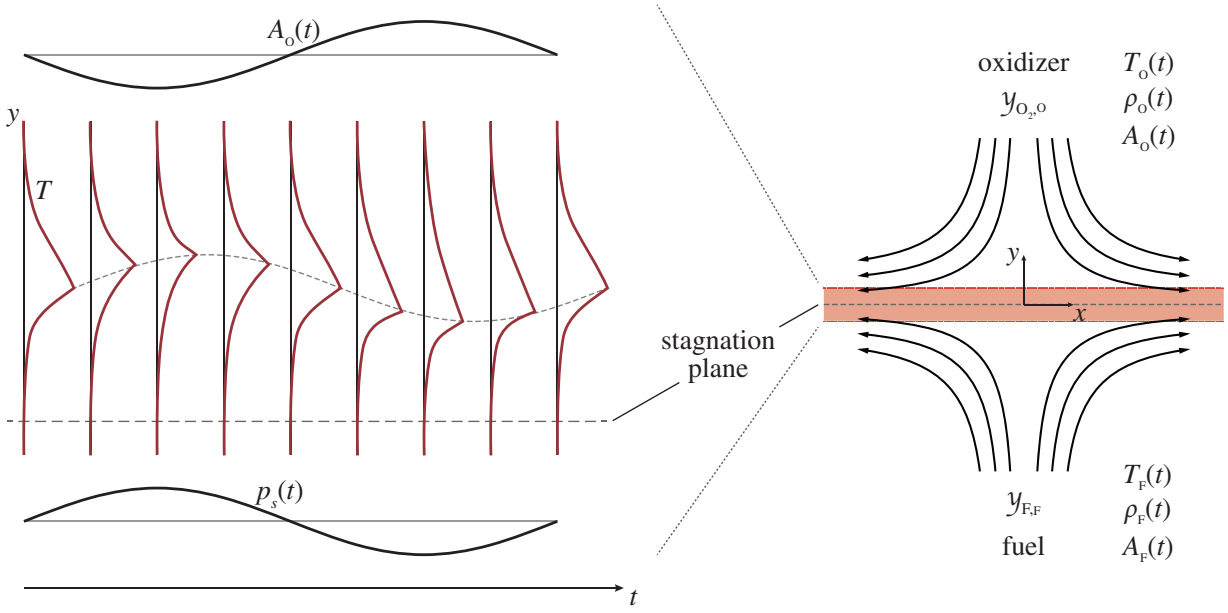

Figure 3.1: A schematic view of the planar counterflow system studied here along with a detailed view of the characteristic time evolution of the temperature profile and associated flame location over an acoustic cycle.

problem is formulated for low-Mach number flow and acoustic wavelengths large compared with the characteristic dimension of the stagnation-point region. Under those conditions, the pressure differences from the time-dependent stagnation-point value $p_s^*(t)$ are small and can be correspondingly neglected when writing the equation of state $p_s^* = \rho^*(R/M)T^*$ involving the density ρ^*, temperature T^*, and mean molecular weight M, with R denoting the universal gas constant.

The analysis specifically considers small fluctuations of the pressure $p_s^*(t)$ and of the strain rates $A_O^*(t)$ and $A_F^*(t)$. Mixing of the two streams is confined to a thin layer of characteristic thickness $\delta_m = [\bar{\lambda}_O^*/(\bar{\rho}_O^* c_p^* \bar{A}_O^*)]^{1/2}$, small compared with the natural length scale used in defining the relevant Reynolds number. Here c_p^* is the specific heat at constant pressure, and $\bar{\lambda}_O^*$, $\bar{\rho}_O^*$, and $\bar{A}_O^*$ are the mean values of the thermal conductivity, density, and strain rate in the oxidizer stream. Within this slender layer, the solution takes a self-similar form, with the time t and the distance y to the stagnation plane entering as the only independent variables [20]. In the description, the streamwise component of the velocity $v_x = xA^*(y,t)$, linearly proportional to the streamwise

distance x, is conveniently described in terms of the strain rate $A^*(y,t)$, whose variation accross the mixing layer is determined from momentum conservation. This mixing-layer region exhibits large transverse changes of the density and transport properties, mainly associated with the temperarure increase caused by the heat release at the flame. While these changes have often been handled in the past through introduction of a density-weighted transverse coordinate, recent work [18] suggests that weighting the coordinate with the inverse of the thermal conductivity is beneficial, especially from the viewpoint of providing a compact transport operator, as will be seen below. To this end, the problem is formulated with use made of an inverse-thermal-conductivity-weighted coordinate

$$\eta(y,t) = (\bar{\lambda}^*_{\mathrm{O}}/\delta_m)\int_0^y \frac{\mathrm{d}y}{\lambda^*(y,t)}, \tag{3.1}$$

and a modified nondimensional transverse mass flux

$$F = -\frac{\rho^* v_y + \rho^*\lambda^* \int_0^y \frac{\partial}{\partial t}\left(\frac{1}{\lambda^*}\right)\mathrm{d}y}{\bar{\rho}^*_{\mathrm{O}}\delta_m \bar{A}^*_{\mathrm{O}}}, \tag{3.2}$$

replacing the streamwise velocity in the integration.

In addition, the mean properties of the oxidizer stream are used to define scaled variables $\tau = \bar{A}^*_{\mathrm{O}} t$, $A(\eta,\tau) = A^*/\bar{A}^*_{\mathrm{O}}$, $p_s(\tau) = p^*_s/\bar{p}^*_s$, $T(\eta,\tau) = T/\bar{T}^*_{\mathrm{O}}$, $\rho(\eta,\tau) = \rho^*/\bar{\rho}^*_{\mathrm{O}}$, and $\lambda(\eta,\tau) = \lambda^*/\bar{\lambda}^*_{\mathrm{O}}$. In dimensionless form, the equation of state becomes

$$p_s(\tau) = \rho T \tag{3.3}$$

when changes of molecular weight are neglected, whereas the isentropic equations relating the boundary values of the density and temperature on each side of the mixing layer take the form

$$\left.\begin{aligned} T_{\mathrm{O}}(\tau) = T_{\mathrm{F}}(\tau)/\Theta_{\mathrm{F}} &= p_s^{(\gamma-1)/\gamma} \\ \rho_{\mathrm{O}}(\tau) = \rho_{\mathrm{F}}(\tau)\Theta_{\mathrm{F}} &= p_s^{1/\gamma} \end{aligned}\right\} \tag{3.4}$$

where $\Theta_F = T_F/T_O$ is the constant fuel-to-oxidizer temperature ratio and γ is the ratio of specific-heats. The outer strain rates are related according to

$$\frac{dA_O}{d\tau} + A_O^2 = \frac{1}{\Theta_F}\left(\frac{dA_F}{d\tau} + A_F^2\right), \tag{3.5}$$

as follows from the condition of negligible pressure variation across the separating mixing layer.

The composition will be described in terms of the mass fractions $\mathcal{Y}_i(\eta,\tau)$ of species i. Although our primary interest is in undiluted hydrocarbon-oxygen flames, of interest for liquid-propellant applications, dilution of both streams will be permitted for generality, with $\mathcal{Y}_{F,F}$ and $\mathcal{Y}_{O_2,O}$ denoting the boundary mass fractions of fuel and oxygen, respectively. The oxidation of the fuel will be modeled by the irreversible reaction $F + sO_2 \rightarrow P + Q$, where s represents the mass of oxygen needed to burn the unit mass of fuel and Q is the corresponding total energy released in the process. The mass of fuel consumed per unit volume per unit time will be denoted by w_F with sw_F and Qw_F correspondingly representing the mass of oxygen consumed and the amount of heat released per unit volume per unit time.

The conservation equations, representing mass, momentum, energy, and species balances, written for one-step chemistry in terms of the dimensionless variables defined above become [18]

$$\frac{\partial(\rho\lambda)}{\partial\tau} = \frac{\partial F}{\partial\eta} - \rho\lambda A, \tag{3.6}$$

$$\rho\lambda\frac{\partial A}{\partial\tau} = F\frac{\partial A}{\partial\eta} + Pr\frac{\partial^2 A}{\partial\eta^2} + \lambda\left[\rho_O\left(\frac{dA_O}{d\tau} + A_O^2\right) - \rho A^2\right], \tag{3.7}$$

$$\rho\lambda\frac{\partial T}{\partial\tau} = F\frac{\partial T}{\partial\eta} + \frac{\partial^2 T}{\partial\eta^2} + qkY_F Y_O + \frac{\gamma-1}{\gamma}\lambda\frac{dp_s}{d\tau}, \tag{3.8}$$

$$\rho\lambda\frac{\partial Y_F}{\partial\tau} = F\frac{\partial Y_F}{\partial\eta} + \frac{1}{L_F}\frac{\partial^2 Y_F}{\partial\eta^2} - kY_F Y_O, \tag{3.9}$$

$$\rho\lambda\frac{\partial Y_O}{\partial\tau} = F\frac{\partial Y_O}{\partial\eta} + \frac{\partial^2 Y_O}{\partial\eta^2} - SkY_F Y_O, \tag{3.10}$$

where $kY_{\rm F}Y_{\rm O} = \lambda w_{\rm F}/(\bar{\rho}^*_{\rm O}\bar{A}^*_{\rm O}\mathcal{Y}_{\rm F,F})$ is the dimensionless fuel consumption rate written in terms of the normalized reactant mass fractions $Y_{\rm F} = \mathcal{Y}_{\rm F}/\mathcal{Y}_{\rm F,F}$ and $Y_{\rm O} = \mathcal{Y}_{\rm O}/\mathcal{Y}_{\rm O_2,O}$ and involving an appropriately defined reaction–rate constant k, whose dependence on temperature and pressure need not be specified in our Burke-Schumann analysis. Besides the compact transport operator accounting for local accumulation, convection, and diffusion, unsteady effects introduced by the strain $A_{\rm O}(\tau)$ and stagnation pressure $p_s(\tau)$ are embodied by source terms in (4.10) and (3.8) associated with unsteady pressure gradients imposed on the mixing layer and with compression work, respectively. Although the analysis proceeds with the energy equation (3.8) written in terms of the temperature, alternative forms involving an entropy-related variable $T/p_s^{(\gamma-1)/\gamma}$ have been shown to have advantages in some respects [20, 21], although that selection would not be particulatly helpful here. As can be seen, the reaction terms in (3.8) and (3.10) exhibit the factors

$$q = \frac{Q\mathcal{Y}_{\rm F,F}}{c_p\bar{T}^*_{\rm O}} \quad \text{and} \quad S = \frac{s\mathcal{Y}_{\rm F,F}}{\mathcal{Y}_{\rm O_2,O}}, \tag{3.11}$$

where q is a dimensionless heat of reaction and S is the amount of oxidizer needed to burn completely the unit mass of fuel stream. The ratio $q/S = Q\mathcal{Y}_{\rm O_2,O}/(sc_p\bar{T}^*_{\rm O})$, independent of fuel stream dilution $\mathcal{Y}_{\rm F,F}$, will also play a role in the analysis, with typical value $q/S \simeq 10$ used below. A unity Lewis number has been assumed for the oxidizer, whereas the fuel Lewis number $L_{\rm F}$ is allowed to take general nonunity values. Appearing in momentum conservation (4.10) is the Prandtl number Pr taken to be constant in the analysis.

The conservation equations (3.6)–(3.10) are supplemented with the equation of state (3.3) and with the presumed power law

$$\lambda = T^{\sigma}, \tag{3.12}$$

for the temperature dependence of the thermal conductivity, with the exponent $\sigma = 0.7$ used in the integrations below. Although there are no qualitative changes in any predictions when the formulation is simplified through the removal of two parameters, at the outset setting the Prandtl

number to unity and ignoring the increase in transport properties with increasing temperature by putting $\sigma = 0$, a significant quantitative increase in accuracy for air is achieved with $Pr = 0.7$ and $\sigma = 0.7$, which does not introduce any complications in the numerical computations. Appropriate boundary conditions for integration are $F(0) = 0$, stating that the stagnation plane is located at $\eta = 0$, and

$$\begin{aligned} \eta = +\infty &: A - A_{\mathrm{O}} = T - T_{\mathrm{O}} = Y_{\mathrm{F}} = Y_{\mathrm{O}} - 1 = 0 \\ \eta = -\infty &: A - A_{\mathrm{F}} = T - T_{\mathrm{F}} = Y_{\mathrm{F}} - 1 = Y_{\mathrm{O}} = 0 \end{aligned} \tag{3.13}$$

which follow from matching the mixing-layer solution with that found in the outer inviscid, isentropic regions flanking the mixing layer. The problem is to be solved for given values of the stagnation-point pressure $p_s(\tau)$ and oxidizer-side strain rate $A_{\mathrm{O}}(\tau)$, with (3.4) used to evaluate the boundary temperatures $T_{\mathrm{O}}(\tau)$ and $T_{\mathrm{F}}(\tau)$ and (3.5) used to evaluate $A_{\mathrm{F}}(\tau)$. The reader is referred to [18] for a fuller discussion of the conservation equations.

3.3 Burke-Schumann Flames

The chemical-equilibrium condition

$$Y_{\mathrm{F}} Y_{\mathrm{O}} = 0, \tag{3.14}$$

applies in the the limit of infinitely fast reaction, as can be obtained by taking the limit $k \to \infty$ in any of the three equations (3.8)–(3.10). This condition indicates that the fuel and oxygen appear in different regions, separated by a infinitesimally thin reaction layer located at $\eta = \eta_f(\tau)$. The description of the resulting free-boundary problem is facilitated by introduction of chemistry-free coupling functions, obtained through elimination of the reaction terms in the species and energy conservation equations by appropriate linear combinations [22]. For instance, a combination

of (3.9) and (3.10) leads to

$$\rho\lambda\frac{\partial Z}{\partial\tau}=F\frac{\partial Z}{\partial\eta}+\frac{S/L_{\rm F}+1}{S+1}\frac{\partial^2\mathcal{Z}}{\partial\eta^2} \tag{3.15}$$

involving the classical mixture fraction Z and a diffusion-weighted mixture fraction $\mathcal{Z}$ defined by

$$Z=\frac{SY_{\rm F}-Y_{\rm O}+1}{S+1}\quad\text{and}\quad\mathcal{Z}=\frac{SY_{\rm F}/L_{\rm F}-Y_{\rm O}+1}{S/L_{\rm F}+1}. \tag{3.16}$$

Clearly, the diffusion-weighted mixture fraction reduces to the classical mixture fraction when $L_{\rm F}=1$, so that (3.15) becomes a transport equation for a single scalar, thereby simplifying the solution. On the other hand, since the Lewis number of oxygen is unity, it is convenient to use (3.10) in eliminating the reaction term from (3.8) to yield

$$\begin{aligned}\rho\lambda\frac{\partial\xi}{\partial\tau}&=F\frac{\partial\xi}{\partial\eta}+\frac{\partial^2\xi}{\partial\eta^2}\\&\quad+\left(\frac{\gamma-1}{\gamma}\lambda\frac{{\rm d}p_s}{{\rm d}\tau}\right)\frac{1-(\rho/\rho_{\rm O})[1+\xi(\Theta_{\rm F}-1)]}{T_{\rm O}(\Theta_F-1)-q/S}\end{aligned} \tag{3.17}$$

for the normalized enthalpy

$$\xi=\frac{T-T_O+(q/S)(Y_{\rm O}-1)}{T_{\rm O}(\Theta_F-1)-q/S}. \tag{3.18}$$

The above coupling functions have been normalized to give the convenient boundary values $\xi=Z=\mathcal{Z}=0$ as $\eta\to\infty$ and $\xi=Z=\mathcal{Z}=1$ as $\eta\to-\infty$. When the stagnation point pressure is steady, or if the compression-work term appearing in (3.17) is sufficiently small to be neglected, ξ behaves as a conserved scalar. If, in addition, the fuel Lewis number equals unity, $L_{\rm F}=1$, then ξ becomes equal to the mixture fraction Z, so that $\xi=Z=\mathcal{Z}$, as may be inferred from inspection of their identical transport equations and boundary conditions.

The flame is the iso-surface $Z=Z_S=1/(S+1)$ or $\mathcal{Z}=\mathcal{Z}_S=1/(S/L_{\rm F}+1)$ as follows from use of the condition $Y_{\rm F}=Y_{\rm O}=0$ in the definitions (4.53). On each side of the flame, the non-coexistence condition (3.14) can be used together with the definitions (4.53) and (3.18) to

provide the piecewise-linear relationships

$$\begin{aligned} &Y_{\mathrm{O}} = 0,\ Y_{\mathrm{F}} = \tfrac{(Z-Z_S)}{(1-Z_S)} = \tfrac{(\mathcal{Z}-\mathcal{Z}_S)}{(1-\mathcal{Z}_S)} \\ &T = \tfrac{q}{S}(1-\xi) + T_{\mathrm{O}}[1+\xi(\Theta_{\mathrm{F}}-1)] \end{aligned} \qquad (\eta \le \eta_f) \tag{3.19}$$

$$\begin{aligned} &Y_{\mathrm{O}} = 1 - \tfrac{Z}{Z_S} = 1 - \tfrac{\mathcal{Z}}{\mathcal{Z}_S},\ Y_{\mathrm{F}} = 0 \\ &T = \tfrac{q}{S}(\tfrac{\mathcal{Z}}{\mathcal{Z}_S} - \xi) + T_{\mathrm{O}}[1+\xi(\Theta_{\mathrm{F}}-1)] \end{aligned} \qquad (\eta \ge \eta_f), \tag{3.20}$$

relating the temperature, composition and mixture fraction Z with the coupling functions $\mathcal{Z}$ and ξ. Integration of (3.6), (4.10), (3.15) and (3.17) supplemented with (3.3), (3.12), (3.19), and (3.20) subject to the boundary conditions given above determines the response of the flow to a prescribed temporally varying stagnation point pressure $p_s(\tau)$ and oxidizer-side strain rate $A_{\mathrm{O}}(\tau)$.

The flame location $\eta_f(\tau)$ must be determined as part of the integration. At the flame the normalized enthalpy takes the value $\xi = \xi_f(\tau)$ which in turn determines the flame temperature

$$T_f = \frac{q}{S}(1-\xi_f) + T_{\mathrm{O}}[1+\xi_f(\Theta_{\mathrm{F}}-1)], \tag{3.21}$$

as follows from (3.19) or (3.20), with $T_{\mathrm{O}}(\tau)$ given in (3.4). This value is to be compared with the adiabatic flame temperature

$$T_S = T_{\mathrm{O}} + \frac{q}{S}(1-Z_S) + Z_S(T_{\mathrm{F}} - T_{\mathrm{O}}), \tag{3.22}$$

resulting from the isobaric combustion of a stoichiometric mixture of the fuel and oxidizer gases, each at their corresponding instantaneous temperatures $T_{\mathrm{O}}(\tau)$ and $T_{\mathrm{F}}(\tau)$. Because of differential-diffusion effects associated with the nonunity value of L_{F} and the presence of the compression-work source term in (3.17), the value of ξ_f is in general different from Z_S, with the

result that the flame temperature T_f differs in general from T_S as described by

$$\frac{T_f - T_S}{q/S + T_{\rm F} - T_{\rm O}} = Z_S - \xi_f, \tag{3.23}$$

obtained by substracting (3.22) from (3.21).

In the B-S limit, the reaction terms in (3.8)–(3.10) appear as Dirac delta functions, which are necessarily balanced by jumps in the gradients of the mass fractions and temperature across the flame. The relative jump in the gradients follow from the ratios $q : -1 : -S$ of the reaction terms appearing in these equations, leading to the jump conditions

$$m_{\rm F} = -\frac{1}{L_{\rm F}} \frac{\partial Y_{\rm F}}{\partial \eta}\bigg|_{f-} = \frac{1}{S} \frac{\partial Y_{\rm O}}{\partial \eta}\bigg|_{f+} = \frac{1}{q} \left(\frac{\partial T}{\partial \eta}\bigg|_{f-} - \frac{\partial T}{\partial \eta}\bigg|_{f+} \right), \tag{3.24}$$

where the subscripts $f-$ and $f+$ denote quantities evaluated on the fuel and oxidizer side of the flame sheet. Here, with D_F^* denoting the diffusion coefficient of the fuel,

$$m_{\rm F} = -\frac{[\rho^* D_{\rm F}^* (\partial \mathcal{Y}_{\rm F}/\partial y)]_f}{\mathcal{Y}_{\rm F,F} (\bar{\lambda}_{\rm O}^* \bar{A}_{\rm O}^* \bar{\rho}_{\rm O}^* / c_p^*)^{1/2}} \tag{3.25}$$

is the dimensionless fuel consumption rate per unit flame surface. As can be seen in the first equation of (3.24), in this limit of infinitely fast reaction the fuel consumption rate per unit flame surface is determined exclusively by the fuel mass fraction gradient at the flame sheet since $\rho^* D_{\rm F}^*$ has conveniently been incorporated with use of the coordinate η. Similarly, the oxygen consumption rate $Sm_{\rm F}$ is determined by the oxygen gradient $\partial Y_{\rm O}/\partial \eta|_{f+}$, while the jump in the temperature gradients at the flame sheet determines in this limit the heat-release rate $qm_{\rm F}$. Unlike the gradients of temperature and reactant mass fractions, those of the chemistry-free coupling functions $\mathcal{Z}$ and ξ do not exhibit jumps at the flame. In particular, the gradient of the diffusion-weighted mixture fraction at $\eta = \eta_f$ can be used to evaluate the fuel burning rate according

to

$$m_{\mathrm{F}} = -\frac{1}{L_{\mathrm{F}}(1-\mathcal{Z}_{\mathrm{S}})}\left.\frac{\partial \mathcal{Z}}{\partial \eta}\right|_{f}, \tag{3.26}$$

as follows from the piecewise relation (3.19) .

3.4 Acoustic–perturbation scheme

The analysis below is restricted to harmonic perturbations of small relative amplitude $\varepsilon \ll 1$ and acoustic frequencies ω^* of the order of the local strain rate, corresponding to $\omega = \omega^*/\bar{A}^*_{\mathrm{O}} \sim 1$, a relevant distinguished limit for liquid-propellant rocket engines [15]. As previously mentioned, in the linear limit the flame response to pressure perturbations and velocity perturbations may be studied independently by considering the flame to be located at an acoustic velocity node (i.e. a pressure antinode) with forcing terms

$$p_s(\tau) - 1 = \varepsilon e^{i\omega\tau} \quad \text{and} \quad A_{\mathrm{O}}(\tau) = 1 \tag{3.27}$$

or at a pressure node (i.e. a velocity antinode) with

$$p_s(\tau) = 1 \quad \text{and} \quad A_{\mathrm{O}}(\tau) - 1 = \varepsilon e^{i\omega\tau}. \tag{3.28}$$

The associated unsteady response can be addressed by a linear analysis in which the independent variables are expressed in the form

$$f = \bar{f}(\eta) + \varepsilon e^{i\omega\tau}\hat{f}(\eta) \tag{3.29}$$

(f representing any of the independent variables) where the bar is used to denote unperturbed quantities and the hat is used for the complex functions that describe the acoustic response.

Correspondingly, the expressions

$$\begin{cases} \eta_f = \bar{\eta}_f + \varepsilon e^{i\omega\tau}\hat{\eta}_f \\ T_f = \bar{T}_f + \varepsilon e^{i\omega\tau}\hat{T}_f \\ m_{\mathrm{F}} = \bar{m}_{\mathrm{F}} + \varepsilon e^{i\omega\tau}\hat{m}_{\mathrm{F}} \end{cases}, \tag{3.30}$$

involving the time-averaged values $\bar{\eta}_f$, $\bar{T}_f$, and $\bar{m}_{\mathrm{F}}$, and the complex response components $\hat{\eta}_f$, $\hat{T}_f$, and $\hat{m}_{\mathrm{F}}$, will be employed for the resulting flame location, flame temperature, and fuel burning rate, respectively.

The unperturbed quantities $\bar{F}$, $\bar{A}$, $\bar{\xi}$ and $\bar{\mathcal{Z}}$ are the steady solutions of the governing equations with corresponding steady boundary conditions and whose profiles may be found in [18, 23]. The flame is located at $\bar{\eta}_f$ where $\bar{\mathcal{Z}} = \mathcal{Z}_S$ and where the unperturbed temperature reaches the flame value $\bar{T}_f = 1 + q/S + (\Theta_{\mathrm{F}} - 1 - q/S)\bar{\xi}_f$. For fuels such that $L_{\mathrm{F}} = 1$, $\bar{\xi} = \bar{Z} = \bar{\mathcal{Z}}$, hence the peak temperature becomes $\bar{T}_f = 1 + Z_S(q + \Theta_{\mathrm{F}} - 1)$, equal to the unperturbed value of the adiabatic flame temperature (3.22). As indicated in (3.26), the gradient of $\bar{\mathcal{Z}}$ at the flame $\bar{\mathcal{Z}}'_f = \bar{\mathcal{Z}}'(\bar{\eta}_f)$ determines the unperturbed value of the fuel burning rate per unit surface area $\bar{m}_{\mathrm{F}} = -\bar{\mathcal{Z}}'_f/[L_{\mathrm{F}}(1 - \mathcal{Z}_S)]$.

3.5 Acoustic pressure response

3.5.1 The linearized problem

We now turn our attention to the acoustic pressure response by considering perturbations of the form (3.27). With a prime denoting differentiation with respect to η, introducing the

expressions (3.29) into (3.6), (4.10), (3.15), and (3.17) yields the linear equations

$$\left.\begin{aligned} -\bar{T}\hat{F}' + \bar{T}^{\sigma}\hat{A} + (\sigma-1)\bar{T}^{\sigma-1}(\mathrm{i}\omega+\bar{A})\hat{T} \\ = -(\mathrm{i}\omega+\bar{A})\bar{T}^{\sigma}, \end{aligned}\right\} \tag{3.31}$$

$$\left.\begin{aligned} -\bar{A}'\hat{F} + \bar{T}^{\sigma-1}(\mathrm{i}\omega+2\bar{A})\hat{A} - \bar{F}\hat{A}' - Pr\hat{A}'' \\ +\bar{T}^{\sigma-1}[(\sigma-1)\bar{A}^2/\bar{T} - \sigma]\hat{T} \\ = -\bar{T}^{\sigma-1}[\bar{A}^2 - \bar{T}/\gamma], \end{aligned}\right\} \tag{3.32}$$

$$\left.\begin{aligned} -\bar{\xi}'\hat{F} + \mathrm{i}\omega\bar{T}^{\sigma-1}\hat{\xi} - \bar{F}\hat{\xi}' - \hat{\xi}'' \\ = \tfrac{\gamma-1}{\gamma}\mathrm{i}\omega\bar{T}^{\sigma-1}\tfrac{\bar{T}-[(\Theta_{\mathrm{F}}-1)\bar{\xi}+1]}{\Theta_{\mathrm{F}}-1-q/S}, \end{aligned}\right\} \tag{3.33}$$

$$-\bar{Z}'\hat{F} + \mathrm{i}\omega\bar{T}^{\sigma-1}\hat{Z} - \bar{F}\hat{Z}' - (Z_S/\mathcal{Z}_S)\hat{\mathcal{Z}}'' = 0, \tag{3.34}$$

after collecting terms of order ε. As with base variables, the prime denotes differentiation of the response functions with respect to η. Expressions for $\hat{T}$ and $\hat{Z}$, necessary to close the system, can be obtained by linearizing (3.19) and (3.20) to give

$$\begin{aligned} \hat{T} = {} & \frac{\gamma-1}{\gamma}\left(1+(\Theta_{\mathrm{F}}-1)\bar{\xi}\right) \\ & + (\Theta_{\mathrm{F}}-1-q/S)\hat{\xi} + \begin{cases} 0 & (\eta < \bar{\eta}_f) \\ \frac{qZ}{SZ_S} & (\eta > \bar{\eta}_f) \end{cases} \end{aligned} \tag{3.35}$$

and

$$\hat{Z} = \begin{cases} \frac{1-Z_S}{1-\mathcal{Z}_S}\hat{\mathcal{Z}} & (\eta < \bar{\eta}_f) \\ \frac{Z_S}{\mathcal{Z}_S}\hat{\mathcal{Z}} & (\eta > \bar{\eta}_f). \end{cases} \tag{3.36}$$

The above equations must be integrated with the homogeneous boundary conditions $\hat{F}(0) = 0$ and $\hat{A} = \hat{\xi} = \hat{Z} = 0$ as $\eta \to \pm\infty$ to determine the functions $\hat{F}$, $\hat{A}$, $\hat{\mathcal{Z}}$ and $\hat{\xi}$.

The forcing terms appearing on the right-hand sides of (3.31)–(3.33) are related to the

temporal variation of the pressure $p_s(\tau) = 1 + \varepsilon e^{i\omega\tau}$, which in turn induces density variations as dictated by the equation of state (3.3). Besides forcing terms proportional to ω, emerging from time derivatives $dp_s/d\tau$, there are terms independent of the acoustic frequency in the continuity and momentum equations (3.31) and (3.32), which account for the unsteady variations of the density in the last terms of (3.6) and (4.10). Clearly, the latter perturbations become dominant in the quasisteady limit $\omega \ll 1$.

3.5.2 Quantification of flame-response functions

The perturbation functions $\hat{\mathcal{Z}}$ and $\hat{\bar{\xi}}$ can be used to evaluate the three complex numbers $\hat{\eta}_f$, $\hat{T}_f$, and $\hat{m}_F$ that characterize in (3.30) the acoustic response of the B-S flame to perturbations with a given frequency ω. For instance, the value $\hat{\mathcal{Z}}_f$ of $\hat{\mathcal{Z}}$ at $\eta = \bar{\eta}_f$ can be used to determine the flame displacement $\hat{\eta}_f$ from the condition

$$\hat{\eta}_f \bar{\mathcal{Z}}'_f + \hat{\mathcal{Z}}_f = 0 \tag{3.37}$$

obtained by linearizing $\mathcal{Z}(\eta_f) = \mathcal{Z}_S$. Similarly perturbations to the fuel consumption rate take the form

$$\hat{m}_F = -\frac{1}{L_F(1-\mathcal{Z}_S)}(\hat{\mathcal{Z}}'_f + \hat{\eta}_f \bar{\mathcal{Z}}''_f), \tag{3.38}$$

where $\hat{\mathcal{Z}}'_f$ and $\bar{\mathcal{Z}}''_f$ denote, respectively, the values of $d\hat{\mathcal{Z}}/d\eta$ and $d^2\bar{\mathcal{Z}}/d\eta^2$ evaluated at $\eta = \bar{\eta}_f$. On the other hand, the value $\hat{\bar{\xi}}_f = \hat{\bar{\xi}}(\bar{\eta}_f)$ determines the fluctuations of the flame temperature according to

$$\hat{T}_f = \frac{\gamma-1}{\gamma}[(\Theta_F - 1)\hat{\bar{\xi}}_f + 1] + (\Theta_F - 1 - q/S)\left[\hat{\bar{\xi}}_f - \frac{\bar{\xi}'_f}{\bar{\mathcal{Z}}'_f}\hat{\mathcal{Z}}_f\right], \tag{3.39}$$

as follows from linearizing (3.21). The expression (3.39) contains two distinct contributions; the first term is a result of the variation of the boundary temperatures (3.4) due to isentropic

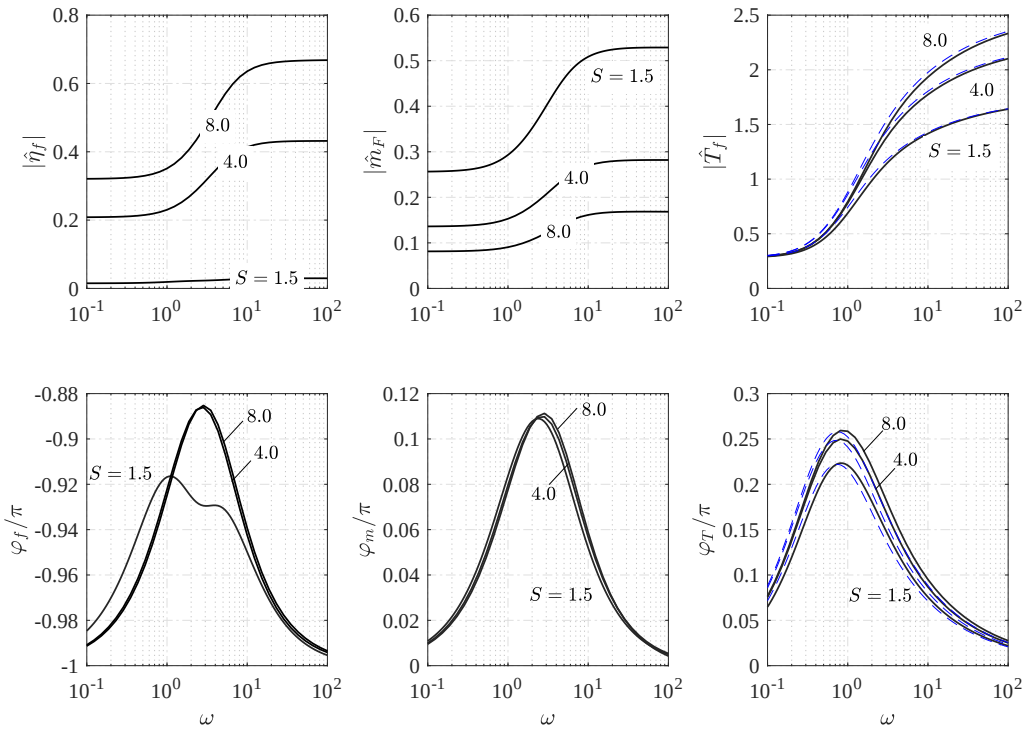

Figure 3.2: Pressure response. For $L_F = 2$, the variation with acoustic frequency of the polar components of perturbations to the (a) flame location $\hat{\eta}_f = |\hat{\eta}_f|e^{i\varphi_f}$, (b) fuel consumption rate $\hat{m}_F = |\hat{m}_F|e^{i\varphi_m}$, and (c) flame temperature $\hat{T}_f = |\hat{T}_f|e^{i\varphi_T}$ obtained from equations (3.37), (3.38), and (3.39) respectively. The phase shift φ is shown in radians, with $|\varphi| \leq \pi/2$ corresponding to perturbations that are in phase with the acoustic forcing, whereas $|\varphi| > \pi/2$ are out of phase. Equal feed-stream conditions ($\Theta_F = 1$) are used in the computation.

compression, whereas the second contribution arises from perturbations to the flame value of the normalized enthalpy, which must be calculated with account taken of the flame displacement according to $\hat{\xi}_f + \hat{\eta}_f \bar{\xi}'_f = \hat{\xi}_f - (\bar{\xi}'_f/\bar{\mathcal{Z}}'_f)\hat{\mathcal{Z}}_f$, so that the resulting value of $\hat{T}_f$ differs from the value of $\hat{T}$ at $\eta = \bar{\eta}_f$.

3.5.3 Representative results

The variation with ω of $\hat{\eta}_f = |\hat{\eta}_f|e^{i\varphi_f}$, $\hat{m}_F = |\hat{m}_F|e^{i\varphi_m}$, and $\hat{T}_f = |\hat{T}_f|e^{i\varphi_T}$ are displayed in Fig. 3.2, with separate plots given for the modulus and phase shift (with respect to the pressure perturbation) of each complex quantity. Results are shown for the case of equal feed temperatures ($\Theta_F = 1$), fuel Lewis number $L_F = 2$, and three different values of $S = (1.5, 4, 8)$, with $S = 4$ being

representative of methane-oxygen combustion and the two flanking cases included to investigate effects of reactant-feed dilution corresponding to either $\mathcal{Y}_{\mathrm{F,F}} < 1$ or $\mathcal{Y}_{\mathrm{O_2,O}} < 1$ as seen in the definition of S given in (3.11). The values $\Theta_{\mathrm{F}} = 1$, $Pr = 0.7$, and $\gamma = 1.4$ are used in generating Fig. 3.2, as well as in all results that follow.

The left plots in Fig. 3.2 show the variation of the flame displacement $\hat{\eta}_f$ with the acoustic frequency. The resulting magnitude $|\hat{\eta}_f| = |\hat{Z}_f|/\bar{Z}'_f$ increases for increasing ω from the quasi-steady values obtained for $\omega \ll 1$. This trend is a consequence of the increase in the value of the perturbed mixture fraction evaluated at the steady flame location, the higher frequencies allowing less time for diffusive relaxation of acoustic-produced oscillations. Larger values of S are seen to give larger displacements, because the resulting flames lie farther from the stagnation plane, where the associated unperturbed gradients $\bar{Z}'_f$ are correspondingly smaller, making the flame location $\hat{\eta}_f = -\hat{Z}_f/\bar{Z}'_f$ very sensitive to perturbations to the mixture-fraction field. The flame displacement is seen to be almost exactly out of phase with the acoustic forcing, in that $\varphi_f - \pi$ remains relatively small for all frequencies. Conversely, the burning-rate amplitude, shown in the middle plots, is almost exactly in phase with the acoustic forcing, a finding that has implications concerning the amplification rate, as discussed later in Section 3.7. Here, as the acoustic frequency increases, instantaneous concentration gradients increase at the flame, leading to a larger reactant supply, an effect that decreases with increasing S, opposite to $|\hat{\eta}_f|$, since the concentration gradients contributing to $|\hat{m}_{\mathrm{F}}|$ are larger closer to the stagnation plane.

The right plots in Fig. 3.2 represent the variation with frequency of the flame-temperature perturbation, revealing trends similar to those of the flame displacement. In particular, the increase in magnitude with frequency is evident. These magnitudes are nearly five times larger than those of $\hat{m}_f$ (and the associated phase variations also are larger), because of the strong temperature gradient in the vicinity of the B-S flame sheet. For acoustic frequencies much smaller than unity, the last term in (3.39) becomes small, so that $\hat{T}_f \simeq [(\gamma-1)/\gamma][(\Theta_F - 1)\bar{\xi}_f + 1]$, where the flame value of the unperturbed normalized enthalpy $\bar{\xi}_f$ depends on the stoichiometry and Lewis number.

When the latter equals unity, however, the value $\hat{T}_f = [(\gamma-1)/\gamma][(\Theta_F-1)Z_s+1]$ corresponding to $\omega \ll 1$ can be obtained from (3.39) by noting that, in this low-frequency limit, equations (3.33) and (3.34) are identical, so that $\hat{\mathcal{Z}} = \hat{Z} = \hat{\xi}$ whereas $\bar{\xi}'_f/\bar{\mathcal{Z}}'_f = 1$. For increasing values of ω the forcing term in the equation for $\hat{\xi}$ enters to give non-zero values of $\hat{\xi}_f - \bar{\xi}'_f/\bar{\mathcal{Z}}'_f\hat{\mathcal{Z}}_f$, resulting in a more pronounced flame-temperature perturbation. The qualitative increase with acoustic frequency described above, especially that exhibited in the burning rate, has been seen in a variety of unsteady non-premixed systems, including the counterflow [15] and droplet burning [13]. These general characteristics depend fundamentally on how close to extinction the flame is, so that distinct qualitative behaviors are expected to arise for flames near extinction, as finite-rate effects, not addressed here, become dominant [15].

The dependence of the flame acoustic response on the fuel Lewis number is investigated in Fig. (3.3). Shown are the perturbation amplitudes of the flame location, burning rate, and peak temperature, for acoustic frequency equal to unity with the same stoichiometric conditions examined in Fig 3.2. Only the amplitudes are shown, with the corresponding phase functions φ_i (not shown) displaying comparatively smaller variations in the range of Lewis numbers $0.3 \leq L_F \leq 2.0$ investigated here. As can be seen from the top plot, Lewis-number effects play a significant role in the flame location, with increased differential diffusion enhancing the amplitudes of the flame-sheet oscillations. Similar trends are evident in the burning rate, shown in the middle plot, although the relative changes are somewhat smaller. Shown in the bottom plot is the variation of the peak-temperature fluctuation amplitude, which reveals different behaviors for near-symmetric flames and flames displaced far from the stagnation plane. In the former, as was the case for the flame location and burning rate, differential diffusion for Lewis numbers less than unity enhances the fluctuating peak-temperature amplitude. By way of comparison however, flames displaced far from the stagnation plane display the opposite behavior, exhibiting smaller amplitudes as the Lewis number decreases.

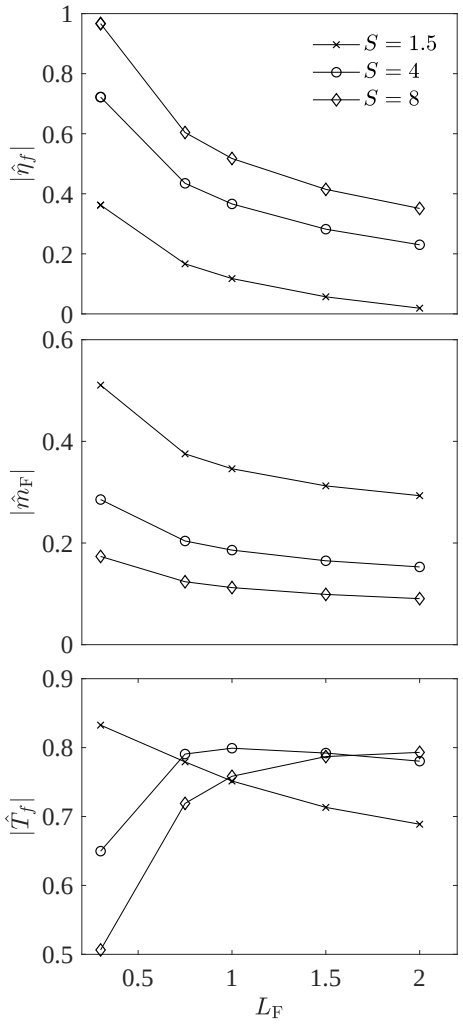

Figure 3.3: Pressure response. The variation with fuel Lewis number of the perturbation amplitudes for acoustic frequency $\omega = 1$. The different curves correspond to the following stoichiometry: $S = 1.5$ (x); $S = 4$ ($\circ$); $S = 8$ ($\diamond$). Results are for the same parametric conditions as Fig 3.2 (i.e. $\Theta_\mathrm{F} = 1, Pr = 0.7, \gamma = 1.4$).

3.5.4 The approximation $F = \eta$

As previously shown [18, 23], under a wide range of conditions the transverse mass flux F in counterflow flames is nearly linear in the thermal-conductivity-weighted coordinate η so that use of the approximation $F = \eta$ in computations provides sufficient accuracy for many purposes. The solution simplifies greatly, in that use of $F = \eta$ uncouples continuity and momentum from species and energy conservation, leading to a problem in η that is nearly identical to that obtained in the natural coordinate y when the assumption of constant density and constant transport properties is employed. In the infinitely fast limit, this simplification is great enough that explicit expressions can be obtained for the mixture fraction $\mathcal{Z}$, composition, flame location and burning rate, and, if the flow is steady, also expressions for the normalized enthalpy and temperature fields.

While these explicit expressions are remarkably accurate for steady flames [18, 23], the predictive capability of the approximation $F = \eta$ is more limited in connection with analyses of acoustic response. Since the perturbations to $\mathcal{Z}$ enter only through modifications to the transverse mass fraction F, use of $F = \eta$ in (3.15) (or equivalently $\hat{F} = 0$ in (3.34)) results in a stationary mixture-fraction profile. As a result, the flame location and the burning rate remain unaffected by the pressure oscillations, so that the associated perturbations are simply $\hat{\eta}_f = \hat{m}_{\mathrm{F}} = 0$. By way of contrast, sufficiently accurate predictions of flame-temperature perturbations can be made on the basis of the approximation $F = \eta$. The associated value of $\hat{T}_f$ can be evaluated from (3.39) with $\hat{\mathcal{Z}}_f = 0$ and with the value $\hat{\xi}_f$ of $\hat{\xi}$ at $\bar{\eta}_f$ determined by integration of the simplified form of (3.33) (i.e with $\hat{F} = 0$). The resulting value of $\hat{T}_f = |\hat{T}_f| e^{\mathrm{i}\varphi_T}$ is compared with the exact results by the dashed curves in Fig. 3.2, giving excellent agreement over the whole range of frequencies considered.

3.6 Acoustic strain response

3.6.1 The linearized problem

When the flame is located at a velocity antinode the pressure remains constant while the oxidizer-side strain rate varies as indicated in (3.28). In the absence of compression work in (3.17), the normalized enthalpy becomes a transported scalar. The solution simplifies to $\xi = Z = \mathcal{Z}$ for $L_{\mathrm{F}} = 1$, and the flame temperature T_f remains equal to the constant adiabatic flame value, independent of the strain-rate variations.

Fluctuations of the oxidizer-side strain rate are accompanied by corresponding fluctuations on the fuel side $A_{\mathrm{F}} = \sqrt{\Theta_{\mathrm{F}}} + \hat{A}_{\mathrm{F}} \varepsilon e^{i\omega\tau}$, where $\hat{A}_{\mathrm{F}}$ is determined from the inviscid momentum equation (3.5) with use of $A_{\mathrm{O}} - 1 = \varepsilon e^{i\omega\tau}$ to give $\hat{A}_{\mathrm{F}} = \Theta_{\mathrm{F}}(2 + \mathrm{i}\omega)/(2\sqrt{\Theta_{\mathrm{F}}} + \mathrm{i}\omega)$. Then perturbing the base state with expressions of the form (3.29) leads to the following system of conservation equations for the complex perturbation functions

$$-\bar{T}\hat{F}' + \bar{T}^{\sigma}\hat{A} + (\sigma - 1)\bar{T}^{\sigma-1}(\mathrm{i}\omega + \bar{A})\hat{T} = 0 \tag{3.40}$$

$$\left.\begin{aligned} &-\bar{A}'\hat{F} + (\mathrm{i}\omega + 2\bar{A})\bar{T}^{\sigma-1}\hat{A} - \bar{F}\hat{A}' - Pr\hat{A}'' \\ &+\bar{T}^{\sigma-1}\left[(\sigma-1)\bar{A}^2/\bar{T} - \sigma\right]\hat{T} = \bar{T}^{\sigma}(\mathrm{i}\omega + 2) \end{aligned}\right\} \tag{3.41}$$

$$-\bar{Z}'\hat{F} + \mathrm{i}\omega\bar{T}^{\sigma-1}\hat{Z} - \bar{F}\hat{Z}' - (Z_S/Z_S)\hat{Z}'' = 0 \tag{3.42}$$

$$-\bar{\xi}'\hat{F} + \mathrm{i}\omega\bar{T}^{\sigma-1}\hat{\xi} - \bar{F}\hat{\xi}' - \hat{\xi}'' = 0 \tag{3.43}$$

with boundary conditions

$$\begin{cases} \eta = -\infty : \hat{A} - \hat{A}_{\mathrm{F}} = \hat{\mathcal{Z}} = \hat{\xi} = 0 \\ \eta = +\infty : \hat{A} - 1 \ \ = \hat{\mathcal{Z}} = \hat{\xi} = 0 \end{cases} \tag{3.44}$$

As before, piecewise relations for $\hat{T}$ and $\hat{Z}$ are necessary to close the system. These are given by (3.35) and (3.36) after dropping the first term in the former. Perturbations to the flame location and burning rate, $\hat{\eta}_f$ and $\hat{m}_{\mathrm{F}}$, are given by (3.37) and (3.38) whereas the peak-temperature perturbation is

$$\hat{T}_f = (\Theta_{\mathrm{F}} - 1 - q/S)(\hat{\xi}_f - \frac{\bar{\xi}'_f}{\bar{Z}'_f}\hat{Z}_f) \tag{3.45}$$

different from (3.39), since boundary temperatures are stationary in the strain response. As is evident, the temperature perturbation $\hat{T}_f$ vanishes when $L_{\mathrm{F}} = 1$, because $\xi = \mathcal{Z}$. Also of interest is that, as seen in (3.42) and (3.43), the perturbations to the mixture fraction and normalized enthalpy, which in turn determine through (3.45) the perturbations to the flame temperature, are a result of the modifications to the transverse mass flux $\hat{F}$, in that if $\hat{F} = 0$ then $\hat{Z} = \hat{\mathcal{Z}} = \hat{\xi} = 0$.

3.6.2 Representative results

The complex perturbations (3.30) to the flame location, burning rate, and peak temperature are displayed in Fig. 3.4 for the parametric conditions investigated earlier in Fig. 3.2. The dependence of the amplitude of the response on frequency in the upper plots of Fig. 3.4 is notably different than that in Fig. 3.2. While both approach their respective quasi-steady values as ω approaches zero, rather than the monotonic increase in the amplitude of the response to pressure oscillations with increasing ω, the amplitude of the response to strain-rate fluctuations increases to a maximum but then decreases to zero as ω approaches infinity. This difference is a consequence of the fact that, while acoustic pressure variations are applied all across the mixing layer, the corresponding strain-rate variations are applied only at the boundaries of the layer. Hence, while only outward-moving diffusive relaxation occurs with pressure excitation, inward diffusive transport, propagating inwards from the boundaries over distances of the order $1/\sqrt{\omega}$ (relative to mixing layer thickness), is an additional phenomenon that is essential to the strain-rate response. As the frequency increases at the lower frequencies in Fig. 3.4, the former of these two

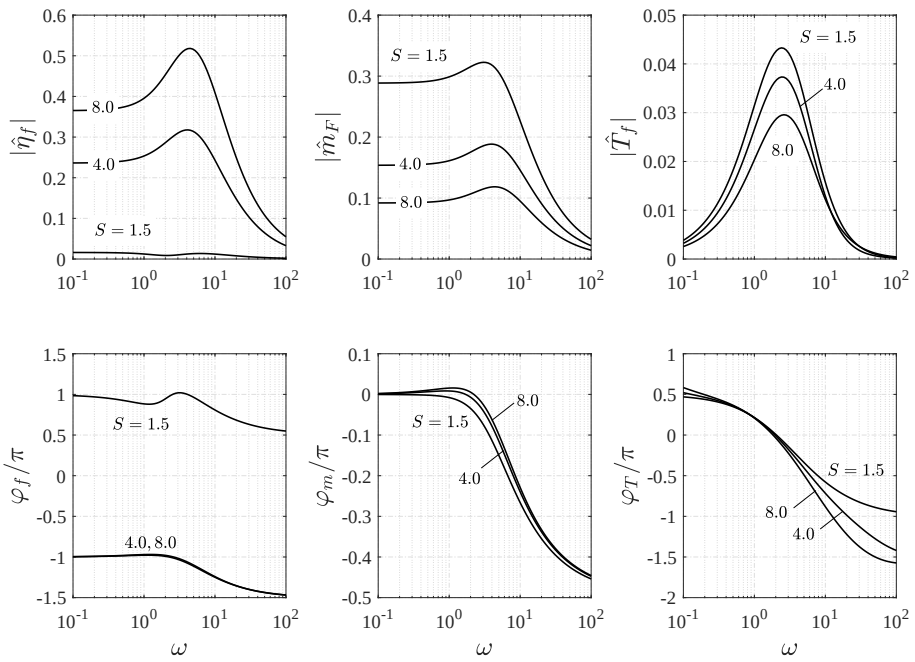

Figure 3.4: Strain response. For $L_F = 2$, the variation with acoustic frequency of the polar components of perturbations to the (a) flame location $\hat{\eta}_f = |\hat{\eta}_f|e^{i\varphi_f}$, (b) fuel consumption rate $\hat{m}_F = |\hat{m}_F|e^{i\varphi_m}$, and (c) flame temperature $\hat{T}_f = |\hat{T}_f|e^{i\varphi_T}$ obtained from equations (3.37), (3.38) and (3.45) respectively. The phase shift φ is shown in radians. Results are for the same parametric conditions as Fig 3.2 (i.e. $\Theta_F = 1, Pr = 0.7, \gamma = 1.4$).

effects produces an increase like that seen in Fig. 3.2, but at higher frequencies the latter effect prevents the mixing layer from sensing the externally imposed strain-rate variations, eventually completely insulating the mixing layer from the acoustic field in the limit of infinite frequency. Thus by the principle of superposition, this aspect of the solution leads to the expectation that the pressure response becomes dominant at sufficiently high frequencies.

The dependences on S of the magnitudes of the flame-location and burning-rate responses in Fig. 4 are in the same direction as in Fig. 2, for the same reason, while, in contrast, the magnitude of the flame-temperature response is much smaller in Fig. 4 and actually exhibits the opposite dependence on S. These differences are attributable to the absence of compression work, which causes the flame temperature in B-S flames to be rather insensitive to temporal variations of the strain rate. The phase of the burning-rate fluctuations φ_m for $S = 4$ and $S = 8$ is seen in Fig. 3.4 to change sign at an intermediate crossover frequency ω_c, whose value increases with

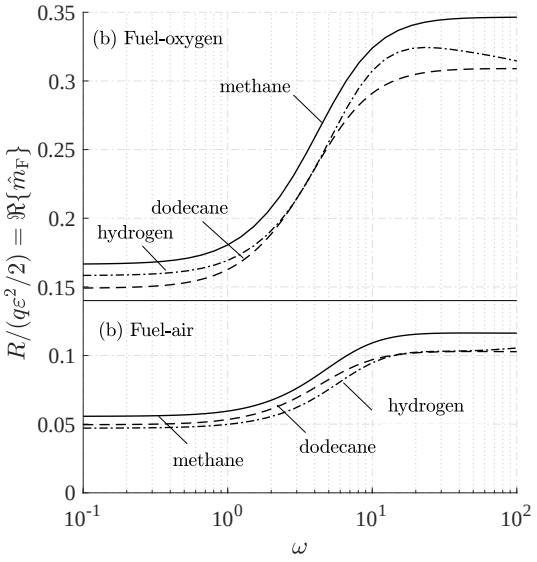

Figure 3.5: Representative scaled Rayleigh index evaluated from (3.47) and (3.38) for (top) methane-oxygen $(S, L_F) = (4.0, 1.0)$, hydrogen-oxygen $(S, L_F) = (8.0, 0.3)$ and heavy hydrocarbon (such as dodecane)-oxygen $(S, L_F) = (3.5, 2.0)$ flames and (bottom) methane-air $(S, L_F) = (17.2, 1.0)$, hydrogen-air $(S, L_F) = (34.5, 0.3)$ and heavy hydrocarbon (such as dodecane)-air $(S, L_F) = (15, 2.0)$ flames. The values $\Theta_F = 1, Pr = 0.7, \gamma = 1.4$ are used in the computation.

increasing S (and decreases with increasing Lewis number for fixed S, as was seen in additional computations). On the other hand, for sufficiently large values of L_F or sufficiently small values of S the phase remains always negative, regardless of the frequency. As discussed below, this crossover behavior has implications with regard to the amplification of acoustic energy within the flamelet. Computations of strain response considering different Lewis numbers, not shown here, provided trends similar to those displayed in Fig. 3.3 for flame location and fuel consumption rates. That similarity does not extend to resulting magnitudes of peak-temperature perturbations $|\hat{T}_f|$; unlike the curves shown in the bottom plot of Fig. 3.3 for the pressure response, the corresponding value of $|\hat{T}_f|$ for the strain-rate response, which is identically zero for $L_F = 1$, increases with increasing $|L_F - 1|$.

3.7 Discussion and implications for acoustic instability

The results of the previous analyses may be readily applied towards computations of acoustic instabilities by application of the Rayleigh criterion, which states that amplification occurs when, on average, heat is added in phase with the pressure increase [12]. Since the heat release rate is qm_{F}, for the counterflow flame amplification occurs when the perturbations $m_{\mathrm{F}} - \bar{m}_{\mathrm{F}}$ are in phase with the pressure oscillations. Consequently, use of the Rayleigh index

$$R(\omega) = \frac{q}{(2\pi/\omega)} \int_0^{2\pi/\omega} (p_s - 1)(m_{\mathrm{F}} - \bar{m}_{\mathrm{F}}) \mathrm{d}\tau \tag{3.46}$$

provides a convenient measure for quantifying the acoustic response [24], with $R > 0$ describing a condition of amplification whereas $R < 0$ corresponds to attenuation, as follows from Rayleigh's criterion. For the B-S flames considered here, the burning rate is equal to the diffusive flux of fuel at the flame as described by $m_{\mathrm{F}} = \bar{m}_{\mathrm{F}} + \varepsilon e^{i\omega\tau} \hat{m}_{\mathrm{F}}$.

For the acoustic pressure response use of $p_s = 1 + \varepsilon \cos(\omega\tau)$ in (3.46) yields

$$R/(q\varepsilon^2/2) = \Re\{\hat{m}_{\mathrm{F}}\}, \tag{3.47}$$

where $\Re\{\hat{m}_{\mathrm{F}}\}$ denotes the real part of the complex function $\hat{m}_{\mathrm{F}}$. Figure 3.5 shows the variation of the scaled Rayleigh index (3.47) quantifying the acoustic pressure response of the outer transport zones for a variety of fuel-oxidizer combinations of practical interest obtained by selecting appropriate values of the stoichiometric mass ratio S and the fuel Lewis number L_{F}. The top plots correspond to fuel-oxygen systems whereas the bottom plot investigates fuel-air configurations. Comparison of the two highlight the role stoichiometry plays on the acoustic response, with larger values of the stoichiometric mass ratio, that being the case for fuel-air combinations for which $\mathcal{Y}_{\mathrm{O}_2,\mathrm{O}} = 0.232$, displaying smaller values of the Rayleigh index. A similar effect is achieved as differential diffusion weakens, as can be seen by comparing the curves representative of methane

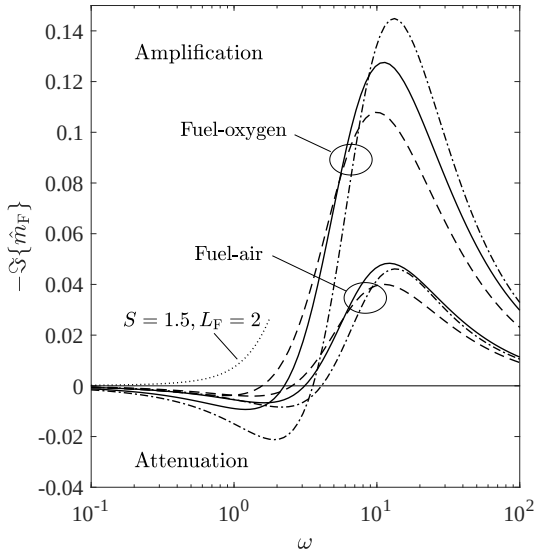

Figure 3.6: The acoustic strain response. The imaginary part of the fuel consumption perturbation $-\Im\{\hat{m}_F\}$, proportional to the amplification of acoustic energy, evaluated using (3.38). Parameters and line styles match those appearing in Fig. 3.5 (e.g $-$ methane; $--$ dodecane; $-.$ hydrogen). The indicated line (for which higher frequencies are not shown, to avoid clutter) corresponds to $(S, L_F) = (1.5, 2)$ for a diluted heavy fuel. The values $\Theta_F = 1, Pr = 0.7, \gamma = 1.4$ are used in the computation.

and dodecane, which posses similar values of S and different values of L_F. As can be seen, the analysis predicts acoustic amplification over all range of frequencies with values of the the scaled index increasing with frequency. The results suggest that fuel-oxygen systems are more susceptible to acoustic pressure instabilities than their fuel-air counterparts.

Acoustic amplification or attenuation through strain-rate variations is more complex than the direct energy addition or removal through pressure-volume work, which is the basis of the Rayleigh criterion. The acoustic velocity variations produce the strain-rate variations that cause thermal-expansion variations through the heat-release variations. The portion of these thermal-expansion variations that is in phase with the pressure variations then contributes to the Rayleigh-criterion pressure-volume-work contribution to acoustic amplification or attenuation. The phase relationship between the pressure and velocity variations associated with the equipartition of energy in the acoustic field external to the heat-release region then completes the feedback of energy that finally produces amplification or attenuation. This cycle is specific to counterflow

flames, which respond differently to pressure and strain-rate variations, although there are other configurations as well, such as droplet burning with non-negligible effects of droplet velocity lags, in which a corresponding duality would appear.

In regard to how this applies to our analysis, since in the acoustic field external to the velocity antinode the pressure variations lag those of the velocity variations by $\pi/2$, the portion of the strain-rate-driven heat release that contributes to amplification or attenuation of acoustic energy is proportional to the imaginary part $-\Im\{\hat{m}_{\mathrm{F}}\} = -|\hat{m}_{\mathrm{F}}|\sin(\varphi_m)$ of the burning rate fluctuation, that being the contribution in phase with pressure variations. This should be contrasted with the real part of the burning-rate fluctuation which determines the portion in phase with velocity variations in the same sense as (3.47). Therefore, in terms of the phase of the complex fuel consumption perturbation amplitude φ_m, amplification occurs for $-\pi < \varphi_m < 0$ whereas attenuation occurs when $0 < \varphi_m < \pi$. Consequently, relevant quantitative information may be obtained from the bottom middle plot in Fig. 3.4, in that $\varphi_m = 0$ (or $\varphi_m = \pi$) delineates the boundary between states of amplification and attenuation.

The variation with acoustic frequency of $-\Im\{\hat{m}_{\mathrm{F}}\}$ is shown in Fig. 3.6 for the same fuel-oxidizer combinations displayed earlier in Fig. 3.5. Of particular interest in Fig. 3.6 is that, while the acoustic-pressure analysis predicts amplification over all frequencies, the results of acoustic-strain analysis exhibit a frequency band of attenuation, eventually undergoing transition to amplification, which occurs for acoustic frequencies of order unity or somewhat larger. This transition frequency, corresponding to the condition $\varphi_m = 0$ mentioned above, depends on the stoichiometry of reactants and on differential diffusion. The extent of the attenuation region decreases as the stoichiometric mass ratio decreases and as the Lewis number increases, and that region disappears completely if S is sufficiently small (as could occur for a diluted-fuel stream reacting with a pure oxygen stream, for example) and if L_F is sufficiently large, corresponding to a sufficiently heavy fuel; see the partial curve for $S = 1.5$ and $L_{\mathrm{F}} = 2$ in the figure. Although the peak amplification rate is appreciably larger than the peak attenuation rate, it occurs at a

higher frequency, where other attenuation effects would tend to be greater, so that the influence of the attenuation range in Fig. 6 may not be negligible. The magnitudes for fuel-oxygen systems are greater than those for fuel-air systems in Fig. 6, just as they are in Fig. 5, which is to be expected, and the peak magnitudes of the real part seem to be about twice the peak magnitudes of the imaginary part, favoring greater practical importance of the pressure response, although the effects of the strain-rate response are not necessarily negligible. The peak in the amplification rate is seen to fall off at high frequencies towards zero as inward acting diffusive transport is no longer able to keep up with strain-rate variations applied at the boundaries of the mixing layer. This behavior is analogous to the high-frequency trends seen in Fig. 3.4 and described in Sec. 3.6.2.

Concerning applications to acoustic instabilities in combustion chambers and to experimental testing of predictions, different approaches may be relevant for different configurations. In chambers that have relatively random distributions of turbulence exhibiting diffusion flamelets, turbulence modeling of the flame-surface density may be employed to determine the spatial distribution of their presence, thereby providing the Rayleigh-criterion amplification rates. Although amplification is absent at pressure nodes, responses in the vicinity of such points may be important if the velocity fluctuations are sufficiently large. In configurations with axial injection, for example, initial amplification estimates may be made directly from the diffusion-flame predictions, for transverse modes, for example, by estimating flame areas. For testing the present predictions, experiments that may achieve steady self-supported oscillations may be considered, analogous to T-burner experiments for solid-propellant acoustic-combustion-instability investigations, with counterflow equipment replacing the solid-propellant surfaces, the length of the chamber connecting the two ends adjusted to produce the frequency of interest, although larger wall losses and flow-turning losses may render such designs impractical. More difficult, direct measurements of acoustic responses with piston-generated imposed pressure waves may be needed, with oscillating optical emissions detected as indicators of burning-rate responses, for example. In general, then, a number of challenging experimental studies may be motivated by the present type of investigation.

3.8 Conclusions

The response of strained diffusion flames in a stagnation-type counterflow subject to harmonic pressure forcing and harmonic strain-rate forcing exhibits a variety of types of behavior even in the limit of infinitely fast reaction. Since the development of acoustic instabilities depends on the interplay of the pressure fluctuations with fluctuations in the heat-release rate, the latter proportional to fluctuations of the fuel burning rate m_{F}, it is important to target quantification of fluctuations of m_{F} for different forcing frequencies and different values of the fuel Lewis number L_{F} and stoichiometric ratio S. Fluctuations of m_{F} are related to direct harmonic modifications of the transport rates in the outer regions surrounding the flame as controlled mainly by perturbations in the transverse mass flux. When fluctuations to the transverse mass flux are neglected, the response is limited, resulting in steady reactant consumption and stationary flames, with temporally fluctuating peak temperatures driven by the compression work introduced into the system by the unsteady background pressure. When this background pressure is also a constant, as applies for the strain-rate response, the peak temperature remains unchanged.

Effects of non-unity fuel Lewis number enhance fuel consumption and flame displacements as differential diffusion becomes significant. Concerning the pressure response, distinct behaviors with regard to effects of fuel Lewis number on the flame-temperature-perturbation amplitude arise for near-unity values of S and for flames with large values of S. The pressure response tends to increase with increasing frequency whereas the strain-rate response drops off at sufficiently high frequencies. For this reason, the pressure response appears to tend to be dominant, especially at higher acoustic frequencies.

When the expressions derived for the fluctuations of m_{F} are used in the evaluation of the relevant Rayleigh index characterizing the amplification/attenuation of acoustic instabilities, it is found that amplification is predicted in the pressure response for all values of the acoustic frequency with fuel-oxygen systems more unstable than their fuel-air counterparts, while, by way

of contrast, the strain-response exhibits attenuation at low frequencies, with a crossover frequency, dependent on stoichiometry and Lewis number, at which a transition to amplification occurs.

Although the present work is restricted to the limit of infinitely fast reaction, the analysis serves as a necessary step in examining the response of flamelets that experience finite-rate effects in the so-called diffusion-flame regime, relevant in hydrocarbon-oxygen systems, and it provides clear indications of one of the two contributions that arise in that type of problem. Analyses of such flames accounting for finite-rate effects, which have been shown to be important near extinction [15, 16], could be carried out on the basis of the present analysis by coupling the results of the outer transport regions discussed here with a thin quasi-steady reactive-diffusive layer, following the rigorous asymptotic approach employed in [17] for steady flames. The present clarifications of parametric dependences on stoichiometry and on fuel Lewis numbers, not previously available, will be helpful in such analyses.

This chapter, in full, has been published in *Combustion and Flame* titled "The acoustic response of Burke-Schumann counterflow flames", by A. D. Weiss, W. Coenen, A. L. Sánchez and F. A. Williams (2018) 192, 25-34. The dissertation author is the primary investigator in this publication.

Bibliography

[1] L Crocco and SI Cheng. *Theory of Combustion Instability in Liquid Propellant Rocket Motors*. Butterworths Scientific, London, U.K., 1956.

[2] David T Harrje. Liquid propellant rocket combustion instability. Technical Report NASA-SP-194, NASA, Washington DC, 1972.

[3] Y. Yu, J. Sisco, S. Rosen, A. Madhav, and W. Anderson. Spontaneous longitudinal combustion instability in a continuously variable resonance combustor. *J. Propul. Power*, 28(5):876–887, 2012.

[4] R. Smith, G. Xia, W. Anderson, and C. L. Merkle. Computational studies of the effects of oxidiser injector length on combustion instability. *Combust. Theor. Model.*, 16(2):341–368, 2012.

[5] M. Harvazinski, W. Anderson, and C. Merkle. Analysis of self-excited combustion in-

stabilities using two-and three-dimensional simulations. *J. Propul. Power*, 29:396–409, 2013.

[6] Romain Garby, Laurent Selle, and Thierry Poinsot. Large-eddy simulation of combustion instabilities in a variable-length combustor. *CR. Mécanique*, 341(1-2):220–229, 2013.

[7] S Srinivasan, R Ranjan, and S Menon. Flame dynamics during combustion instability in a high-pressure, shear-coaxial injector combustor. *Flow Turbul. Combust.*, 94(1):237–262, 2015.

[8] Thierry Poinsot. Prediction and control of combustion instabilities in real engines. *P. Combust. Inst.*, 36(1):1–28, 2017.

[9] Norbert Peters. *Turbulent combustion*. Cambridge University Press, 2000.

[10] Ken Bray. Laminar flamelets in turbulent combustion modeling. *Combust. Sci. Technol.*, 188(9):1372–1375, 2016.

[11] Paul A Libby and Forman A Williams. *Turbulent Reacting Flows*. Springer-Verlag, 1980.

[12] Forman A Williams. Combustion theory, (1985). *Cummings Publ. Co*, 1985.

[13] Warren C Strahle. Periodic solutions to a convective droplet burning problem: the stagnation point. *Symp. (Int.) Combust.*, 10:1315–1325, 1965.

[14] FA Williams. Response of a burning fuel plate to sound vibrations. *AIAA J*, 3(11):2112–2124, 1965.

[15] JS Kim and F A Williams. Contribution of strained diffusion flames to acoustic pressure response. *Combust. Flame*, 98(3):279–299, 1994.

[16] HG Im, CK Law, JS Kim, and F A Williams. Response of counterflow diffusion flames to oscillating strain rates. *Combust. Flame*, 100(1):21–30, 1995.

[17] Amable Liñán. The asymptotic structure of counterflow diffusion flames for large activation energies. *Acta Astronaut.*, 1(7):1007–1039, 1974.

[18] A. D Weiss, M Vera, A Liñán, A. L Sánchez, and F. A Williams. A novel formulation for unsteady counterflow flames using a thermal-conductivity weighted coordinate. *Combust. Theor. Model.*, 2017. (in press).

[19] AD Weiss, W Coenen, and AL Sánchez. Aerodynamics of planar counterflowing jets. *J. Fluid Mech.*, 821:1–30, 2017.

[20] A Liñán and F A Williams. Ignition in an unsteady mixing layer subject to strain and variable pressure. *Combust. Flame*, 95(1-2):31–46, 1993.

[21] WA Sirignano. One-dimensional analysis of combustion in a spark-ignition engine. *Combust.*

Sci. Technol., 7(3):99–108, 1973.

[22] Amable Liñán, Marcos Vera, and Antonio L Sánchez. Ignition, liftoff, and extinction of gaseous diffusion flames. *Annu. Rev. Fluid Mech.*, 47:293–314, 2015.

[23] Amable Liñán, Daniel Martínez-Ruiz, Marcos Vera, and Antonio L Sánchez. The large-activation-energy analysis of extinction of counterflow diffusion flames with non-unity lewis numbers of the fuel. *Combust. Flame*, 175:91–106, 2017.

[24] Thierry J Poinsot, Arnaud C Trouve, Denis P Veynante, Sebastien M Candel, and Emile J Esposito. Vortex-driven acoustically coupled combustion instabilities. *J. Fluid Mech.*, 177:265–292, 1987.

Chapter 4

Acoustic response of near-equilibrium diffusion flames with large activation energies

4.1 Introduction

In a recent effort [1], we investigated the acoustic response of strained non-premixed counterflow flames subject to small harmonic fluctuations of the stagnation-point pressure and strain rate. The reader is referred to that publication for explanations of the background and motivation of these studies, as well as citation and discussion of the previous relevant literature. The model addressed serves as a simplified representation for the interactions of acoustic waves with laminar flamelets of interest, statistical averages of which would apply to computations of acoustic instabilities in liquid-propellant rocket motors. That analysis was restricted to the limit of infinitely fast chemical reactions so that, while the response of the outer transport layers was captured, effects of the finite-rate chemistry present in the thin reaction zones of the flamelets, coupled with the outer transport regions, could not be predicted. The present contribution remedies

that omission by analyzing the acoustic pressure response of counterflow flames including the effects of finite-rate kinetics and their interplay with acoustic forcing, for systems with large activation energies, thereby extending and complementing our previous work [1]. The large activation energy introduces an additional parameter that, along with the small parameter of the acoustic amplitude, gives rise to a distinguished limit that is fully described here, in addition to determining small-amplitude, harmonic growth rates. In contrast to earlier investigations (such as [2]), which addresses the so-called premixed-flame regime of the diffusion flame [3] (in which only one of the two reactants is nearly consumed completely in the thin reaction zone), the present work treats the diffusion-flame regime (in which both reactants are nearly consumed completely) reasoned [1] to be most relevant for acoustic instabilities in liquid-propellant rockets and considered in a recent treatment of diffusion-flame extinction [4].

4.2 Statement of the problem

The relevant problem for acoustic interaction of flamelets in turbulent combustion is the unsteady, reacting, locally planar strained mixing layer situated in the stagnation-point flow generated by opposed streams of fuel and oxidizer. The objective of the analysis is to quantify the interaction of the low-Mach-number flow with acoustic pressure fluctuations of wavelength large compared with the characteristic dimension of the stagnation-point region. Under those conditions, the spatial differences of the pressure p^* from its stagnation-point value p_o^* (a function of time t only) are smaller than p_o^* by a factor of the order of the Mach number squared, so that p^* can be replaced by $p_o^*(t)$ when writing the equation of state as well as the energy equation. The analysis specifically considers small harmonic fluctuations of the pressure from a prescribed steady value $\bar{p}_o^*$ of the form

$$\frac{p_o^*}{\bar{p}_o^*} = 1 + \varepsilon \cos(\omega^* t), \tag{4.1}$$

involving the frequency ω^* and the amplitude $\varepsilon \ll 1$. In the notation employed, the asterisk (*) is used to differentiate dimensional variables from equivalent scaled variables that will be defined later.

Attention is given to the region located around the stagnation point, where the flow is self-similar, both inside and outside the mixing layer [5]. The description uses the cartesian coordinates (s,n), with s measuring the streamwise distance from the stagnation point and n representing the coordinate normal to the stagnation plane, the oxidizer and fuel stream approaching from $n = \pm\infty$, respectively. The temperature $T^*(n,t)$, density $\rho^*(n,t)$, and mass fractions of fuel and oxygen $\mathcal{Y}_F(n,t)$ and $\mathcal{Y}_{O_2}(n,t)$ are independent of s. The streamwise and transverse velocity components are given by $v_s = A^*(n,t)s$ and $v_n(n,t)$, where A^* is the strain rate. In the outer inviscid streams the velocity is given by the potential solutions $(v_s, v_n) = (A^*_O s, -A^*_O n)$ and $(v_s, v_n) = (A^*_F s, -A^*_F n)$, involving the constant strain rates A^*_O and A^*_F on the oxidizer and fuel sides, which are related by

$$\rho^*_O (A^*_O)^2 = \rho^*_F (A^*_F)^2, \tag{4.2}$$

as follows from the condition of negligible pressure jump across the mixing layer. Here, the subscripts F and O denote properties in the fuel and oxidizer feed streams, respectively. Although the boundary values of the strain rate A^*_O and A^*_F are constant, the compression work associated with the fluctuating pressure given in Eq. (4.1) causes the density and temperature in the feed streams to change with time following the familiar isentropic law

$$\frac{T^*_F}{\bar{T}^*_F} = \frac{T^*_O}{\bar{T}^*_O} = \left(\frac{\rho^*_F}{\bar{\rho}^*_F}\right)^{\gamma-1} = \left(\frac{\rho^*_O}{\bar{\rho}^*_O}\right)^{\gamma-1} = \left(\frac{p^*_o}{\bar{p}^*_o}\right)^{(\gamma-1)/\gamma}, \tag{4.3}$$

where γ is the specific-heat ratio, assumed to be constant. In the notation, the bar will be used to denote quantities associated with the steady solution corresponding to unperturbed flames with $p^*_o = \bar{p}^*_o$.

The reaction between the fuel and the oxygen is assumed to occur according to a simple

irreversible step, with ν denoting the mass of oxygen required to burn a unit mass of fuel and q^* the amount of heat released per unit mass of fuel consumed. The reaction rate (i.e. the mass of fuel burnt per unit volume per unit time) is taken to be

$$\dot{w}_{\mathrm{F}} = B^* \rho^* \mathcal{Y}_{\mathrm{F}} \mathcal{Y}_{\mathrm{O}_2} \exp[-E/(RT^*)] \tag{4.4}$$

involving the frequency factor B^* and the activation energy E, which appears divided by the universal gas constant R.

The problem is formulated in dimensionless form following our previous analyses [1, 6], which should be consulted for details of the derivation. A Fickian description with Soret diffusion neglected is adopted for the diffusion velocities, and the specific heat at constant pressure c_p is assumed to be constant. To simplify the expression of the transport operator, the formulation employs a thermal-conductivity-weighted transverse coordinate η and accompanying transverse mass flux F, defined according to

$$\eta = (\bar{\rho}_{\mathrm{O}}^* A_{\mathrm{O}}^* \bar{\lambda}_{\mathrm{O}}^* c_p)^{1/2} \int_0^n \frac{\mathrm{d}n'}{\lambda^*(n',t)} \quad \text{and} \quad F = -\frac{\rho^* v_n + \rho^* \lambda^* \int_0^n \frac{\partial}{\partial t}\left(\frac{1}{\lambda^*}\right) \mathrm{d}n'}{(\bar{\rho}_{\mathrm{O}}^* A_{\mathrm{O}}^* \bar{\lambda}_{\mathrm{O}}^* / c_p)^{1/2}}, \tag{4.5}$$

where λ^* is the thermal conductivity and n' is a dummy variable of integration. Time is scaled using the strain rate of the oxidizer stream to give $\tau = A_{\mathrm{O}}^* t$, and the stagnation-point value of the pressure p_o^* is scaled with its unperturbed value $\bar{p}_o^*$ to give

$$p = 1 + \varepsilon \cos(\omega\tau), \tag{4.6}$$

as follows from Eq. (4.1), with the dimensionless frequency $\omega = \omega^*/A_{\mathrm{O}}^*$ treated as being of order unity. The oxidizer-side properties are used in defining the additional dimensionless variables

$$A = A^*/A_{\mathrm{O}}^*, \quad \rho = \rho^*/\bar{\rho}_{\mathrm{O}}^*, \quad T = T^*/\bar{T}_{\mathrm{O}}^*, \quad \lambda = \lambda^*/\bar{\lambda}_{\mathrm{O}}^*, \tag{4.7}$$

and the reactants mass fractions are normalized with their free-stream values to give

$$Y_{\mathrm{F}} = \mathcal{Y}_{\mathrm{F}}/\mathcal{Y}_{\mathrm{F,F}}, \quad Y_{\mathrm{O}} = \mathcal{Y}_{\mathrm{O}_2}/\mathcal{Y}_{\mathrm{O}_2,\mathrm{O}}. \tag{4.8}$$

The variables defined above lead to a compact description of the conservation equations for mass, momentum, species, and energy.

A complicating aspect of the unsteady problem analyzed below is the motion of the thin flame in response to the pressure fluctuations, which hinders the application of large activation-energy asymptotic techniques, as recognized in previous studies [2, 7]. The analysis is facilitated by introduction of a coordinate $x = \eta - \eta_f(\tau)$, including an apparent instantaneous flame location $\eta_f(\tau)$, whose precise definition, given in the paragraph following Eq. (4.20), is associated with the basic flame structure that arises for large activation energies, to be discussed in the following section. Unnecessary in our previous investigation [1], this further transformation facilitates analysis of the reaction layer. In terms of this alternative coordinate, the conservation equations take the form (see Eqs. 17-22 in [6] and their full derivation therein)

$$\frac{\partial(\rho\lambda)}{\partial\tau} = \frac{\partial}{\partial x}\left(F + \rho\lambda\frac{\mathrm{d}\eta_f}{\mathrm{d}\tau}\right) - \rho\lambda A \tag{4.9}$$

$$\rho\lambda\frac{\partial A}{\partial\tau} = \left(F + \rho\lambda\frac{\mathrm{d}\eta_f}{\mathrm{d}\tau}\right)\frac{\partial A}{\partial x} + Pr\frac{\partial^2 A}{\partial x^2} + \lambda p^{1/\gamma} - \rho\lambda A^2 \tag{4.10}$$

$$\rho\lambda\frac{\partial Y_{\mathrm{F}}}{\partial\tau} = \left(F + \rho\lambda\frac{\mathrm{d}\eta_f}{\mathrm{d}\tau}\right)\frac{\partial Y_{\mathrm{F}}}{\partial x} + \frac{\partial^2 Y_{\mathrm{F}}}{\partial x^2} - \Omega \tag{4.11}$$

$$\rho\lambda\frac{\partial Y_{\mathrm{O}}}{\partial\tau} = \left(F + \rho\lambda\frac{\mathrm{d}\eta_f}{\mathrm{d}\tau}\right)\frac{\partial Y_{\mathrm{O}}}{\partial x} + \frac{\partial^2 Y_{\mathrm{O}}}{\partial x^2} - S\Omega \tag{4.12}$$

$$\rho\lambda\frac{\partial T}{\partial\tau} = \left(F + \rho\lambda\frac{\mathrm{d}\eta_f}{\mathrm{d}\tau}\right)\frac{\partial T}{\partial x} + \frac{\partial^2 T}{\partial x^2} + q\Omega + \lambda\left(\frac{\gamma-1}{\gamma}\right)\frac{\mathrm{d}p}{\mathrm{d}\tau} \tag{4.13}$$

where the flame location $\eta_f(\tau)$ appears (through its derivative) as an eigenvalue of the problem, to be determined from the solution. A constant Prandtl number Pr has been used in writing Eq. (4.10), and Lewis numbers of unity are assumed for both reactants, a good approximation for

methane-oxygen combustion, for instance.

The reaction rate appears in Eqs. (4.11)–(4.13) in the dimensionless form

$$\Omega = \rho\lambda B Y_{\mathrm{O}} Y_{\mathrm{F}} \exp(-T_a/T), \tag{4.14}$$

involving the reduced frequency factor $B = B^* \mathcal{Y}_{\mathrm{O,O}}/A^*_{\mathrm{O}}$ and the dimensionless activation temperature $T_a = E/(R\bar{T}^*_{\mathrm{O}}) \gg 1$. The factors $S = \nu \mathcal{Y}_{\mathrm{F,F}}/\mathcal{Y}_{\mathrm{O,O}}$ and $q = q^* \mathcal{Y}_{\mathrm{F,F}}/(c_p \bar{T}^*_{\mathrm{O}})$ appearing in Eqs. (4.12) and (4.13) are the mass of oxidizer stream needed to completely burn a unit mass of fuel stream and the dimensionless heat release per unit mass of reacted fuel stream, respectively. As will be seen in the following analysis, an important quantity characterizing the flame response to pressure variations is the dimensionless fuel consumption rate per unit flame surface m_{F}, which can be evaluated from

$$m_{\mathrm{F}} = \int_{-\infty}^{+\infty} \Omega \mathrm{d}x = \int_{-\infty}^{+\infty} \rho\lambda B Y_{\mathrm{O}} Y_{\mathrm{F}} \exp(-T_a/T) \mathrm{d}x, \tag{4.15}$$

with the associated rate at which heat is released given simply by $q m_{\mathrm{F}}$.

The above equations are supplemented by the equation of state and an additional expression for the thermal conductivity. These are written in the simplified forms

$$\rho T = p(\tau) \quad \text{and} \quad \lambda = T^{\sigma}, \tag{4.16}$$

neglecting changes of ρ and λ with composition, with a power law having exponent $\sigma = 0.7$ assumed for the temperature variation of the latter.

The condition that the transverse mass flux vanishes at the stagnation plane $\eta = 0$ provides the boundary condition $F = 0$ at $x = -\eta_f$. Additional boundary conditions, associated with the

known streamwise velocity, composition, and temperature in the outer streams, are given by

$$\begin{cases} x = +\infty : A = 1, & Y_{\mathrm{O}} = 1, \quad Y_{\mathrm{F}} = 0, \quad T = T_{\mathrm{O}}(\tau) = p(\tau)^{(\gamma-1)/\gamma} \\ x = -\infty : A = \Theta^{1/2}, & Y_{\mathrm{O}} = 0, \quad Y_{\mathrm{F}} = 1, \quad T = T_{\mathrm{F}}(\tau) = \Theta p(\tau)^{(\gamma-1)/\gamma} \end{cases}, \tag{4.17}$$

which are written with account taken of the relationships given in Eqs. (4.2) and (4.3). Since changes in the molecular weight are neglected, the ratios of feed-stream temperatures and densities are related according to $\Theta = T_{\mathrm{F}}^*/T_{\mathrm{O}}^* = \rho_{\mathrm{O}}^*/\rho_{\mathrm{F}}^*$, an additional parameter that appears in Eq. (4.17).

Our objective is to describe the response of (6.33)–(4.13) under the realistic consideration that the effective activation temperature T_a appearing in the reaction rate is large. Although fully time-dependent computations can be made with detailed chemistry that is not excessively complex, the overall results of such calculations often can be described well by this asymptotic limit of this one-step approximation, which helps to clarify the underlying mechanism of the pressure response.

4.3 Preliminary considerations concerning finite-rate effects

Simplified versions of the above formulation serve to analyze different problems of interest. For example, when $\varepsilon = 0$ the solution becomes steady, that being the case investigated in Liñán's seminal analysis [3] using the nondimensional activation temperature T_a as an asymptotically large parameter. Of relevance to the present work is the diffusion-flame regime, in which the flame structure at leading order is given by the Burke-Schumann (BS) limit of infinitely fast reaction, including two regions of equilibrium flow separated by an infinitesimally thin reaction layer where the peak temperature is given by the adiabatic value

$$T_s = 1 + \frac{\Theta - 1}{S+1} + \frac{q}{S+1}. \tag{4.18}$$

The temperature profile is rounded off due to finite-rate effects in the thin reaction layer. It is seen that small temperature decrements of the order of the Frank-Kamenetskii value T_s^2/T_a are able to reduce the reaction rate by a factor of order unity. The ratio of the characteristic temperature increment produced by the chemical heat release $q/(S+1)$ to this Frank-Kamenetskii temperature T_s^2/T_a defines the Zel'dovich number

$$\beta = \frac{T_a}{T_s^2}\frac{q}{S+1} \tag{4.19}$$

the relevant parameter for the analysis of flame extinction [3]. As explained in [4], consideration of the asymptotic limit $\beta \gg 1$ requires associated asymptotically large values of the preexponential factor B, as needed to ensure that the temperature decrements are of order T_s^2/T_a in the reaction layer. This last requirement results in order-unity values of the relevant Damköhler number $\mathcal{D}$, defined below in Eq. (4.31). In the limit $\beta \gg 1$ with $\mathcal{D} \sim 1$, the flame structure includes two chemistry-free transport region flanking a thin reaction-diffusion layer of characteristic thickness β^{-1} where the reactant mass fractions are of order β^{-1}. The problem can be solved by expressing the different flow variables as expansions in powers of β^{-1}, including small corrections in the outer equilibrium regions due to reactant leakage, with small mass fractions of order β^{-1}, through the reaction layer [4].

Unsteady effects associated with acoustic pressure variations can be investigated by considering nonzero values of the pressure amplitude $\varepsilon \ll 1$. Our previous work [1] specifically considered the BS limit $B \to \infty$ (or equivalently $\mathcal{D} \to \infty$, cf. Eq. (4.31)). The acoustic response was obtained by analyzing the time-dependent perturbations to the base steady solution, including relative displacements of the flame sheet of order ε and associated variations of the peak temperature, resulting from the fluctuations of the reactant diffusion rate into the flame, of order $T_f - T_s \sim \varepsilon q/(S+1)$. This BS analysis of flame acoustic response is extended here, following the recent work [4], by considering finite-rate effects in the limit $\beta \gg 1$. In view of the previous

results, it can be expected that small pressure-induced fluctuations of the flame temperature $T_f - T_s \sim \varepsilon q/(S+1)$ of the order of the Frank-Kamenetskii temperature T_s^2/T_a, corresponding to values of ε of order β^{-1}, may result in order-unity changes of the reaction rate. From the viewpoint of the classical S-shape curve of the peak temperature as a function of the Damköhler number (shown for instance on p. 82 of [8]), the previous analysis [1] applies in the limit of large Damköhler numbers where the curve is nearly flat, while the present analysis extends father towards the turning point. The reaction-rate changes can be described in this new regime by addressing the double distinguished limit

$$\varepsilon \ll 1 \quad \text{and} \quad \beta \gg 1 \qquad \text{with} \quad \beta\varepsilon \sim 1, \tag{4.20}$$

with the accompanying value of $B \gg 1$ selected to yield $\mathcal{D} \sim 1$.

The solution at leading order reduces to the steady chemical-equilibrium flow. Perturbations are described by introducing expansions in powers of β^{-1} both in the outer unsteady transport region, where the corrections satisfy linear unsteady equations, and in the inner reaction layer, whose quasi-steady response to the acoustic perturbations is fully nonlinear for $\beta\varepsilon \sim 1$. As viewed from the outer regions, the flame appears as a sheet oscillating in response to the acoustic forcing. The definition of the coordinate $x = \eta - \eta_f$ used in writing Eqs. (6.33)–(4.13) incorporates the instantaneous flame-sheet location $\eta_f(\tau)$, with η_f defined for definiteness as the apparent fuel-depletion point as seen from the fuel side in the outer solution. This definition implies that, at all orders in the asymptotic expansion for $\beta \gg 1$, the fuel mass fraction in the outer transport region ($x < 0$) vanishes at $x = 0$, a condition to be used in the asymptotic procedure when writing the matching conditions between the outer and inner solutions for the fuel in Eq. (4.26).

4.4 Solution by matched asymptotic expansions

4.4.1 Leading-order description

At leading order in the double distinguished limit defined in Eq. (4.20) the flame is steady and described by the BS limit of infinitely fast reaction, characterized by two regions of chemical equilibrium – one with fuel and no oxidizer, the other vice-versa – separated by a flame sheet at which both the fuel and oxidizer vanish. The subscript 0 will be employed to denote this solution (e.g. $T_0(x)$ for the temperature), which provides the leading terms in the asymptotic expansions introduced below in Eqs. (6.19) and (4.25). The problem and its solution are summarized in Supplement A.

The results of the integration provide a number of quantities characterizing the steady combustion process, including the fuel consumption rate $m_{\mathrm{F}0}$ and the heat liberated at the flame $qm_{\mathrm{F}0}$, given by

$$m_{\mathrm{F}0} = -\left.\frac{\mathrm{d}Y_{\mathrm{F}0}}{\mathrm{d}x}\right|_{0^-} \qquad \text{and} \qquad qm_{\mathrm{F}0} = \left.\frac{\mathrm{d}T_0}{\mathrm{d}x}\right|_{0^-} - \left.\frac{\mathrm{d}T_0}{\mathrm{d}x}\right|_{0^+}, \tag{4.21}$$

respectively. It can be seen that the fractions of the total heat release that are conducted towards the fuel and oxidizer sides,

$$\gamma_{\mathrm{F}} = \left.\frac{1}{qm_{\mathrm{F}0}}\frac{\mathrm{d}T_0}{\mathrm{d}x}\right|_{0^-} \qquad \text{and} \qquad \gamma_{\mathrm{O}} = -\left.\frac{1}{qm_{\mathrm{F}0}}\frac{\mathrm{d}T_0}{\mathrm{d}x}\right|_{0^+}, \tag{4.22}$$

are given by

$$\gamma_{\mathrm{F}} = 1 - \gamma_{\mathrm{O}} = Z_s - (1 - Z_s)(\Theta - 1)/q, \tag{4.23}$$

where $Z_s = 1/(S+1)$ is the stoichiometric value of the mixture fraction. Typical values of γ_{O} and γ_{F} to be expected are $\gamma_{\mathrm{O}} = 1 - \gamma_{\mathrm{F}} = 0.80$, corresponding to methane-oxygen combustion ($S = 4$) when the feed streams have equal temperature.

4.4.2 Perturbation strategy and matching requirements

In the distinguished limit defined in Eq. (4.20) the departures from the BS steady flame, induced by the combined effects of finite-rate kinetics and pressure fluctuations, can be described by introducing expansions in powers of either β^{-1} or ε. The former expansion parameter facilitates the investigation of infinitesimal acoustic perturbations with $\beta\varepsilon \ll 1$. The selected expansions in the outer transport regions take the form

$$\begin{aligned} Y_{\mathrm{O}} &= Y_{\mathrm{O}0}(x) + \beta^{-1} Y_{\mathrm{O}1}(x,\tau) + \cdots \\ Y_{\mathrm{F}} &= Y_{\mathrm{F}0}(x) + \beta^{-1} Y_{\mathrm{F}1}(x,\tau) + \cdots \\ T &= T_0(x) + \beta^{-1} T_1(x,\tau) + \cdots \\ F &= F_0(x) + \beta^{-1} F_1(x,\tau) + \cdots \\ A &= A_0(x) + \beta^{-1} A_1(x,\tau) + \cdots \\ \eta_f &= \eta_0 + \beta^{-1} \eta_1(\tau) + \cdots \end{aligned} \tag{4.24}$$

each beginning at leading order with the steady BS profile described in the previous section. The first-order corrections, denoted by the subscript 1, depend parametrically on $\beta\varepsilon$, which measures the unsteadiness of the flow. Consequently, for $\beta\varepsilon = 0$ the analysis naturally reduces to that of the steady diffusion flame, with associated outer-flow corrections determined in [4]. The equations involved in the computation of the functions $Y_{\mathrm{O}1}, Y_{\mathrm{F}1}, T_1, A_1, F_1$, to be presented below, are obtained by linearizing the governing Eqs. (6.33)–(4.13) with reaction $\Omega = 0$, whereas the value of the flame-sheet location η_f is to be determined from the condition $Y_{\mathrm{F}}(x = 0^-, \tau) = 0$, which follows from the definition of x adopted in the analysis.

The reactants coexist with small mass fractions of order β^{-1} in a thin reaction layer of characteristic thickness β^{-1} centered about $x = 0$, where the temperature departures from T_s are of order $\beta^{-1} q/(S+1)$. This reaction layer can be described by introducing a stretched coordinate

$\zeta = \beta x$ along with expansions in powers of β^{-1} of the form

$$\begin{aligned} Y_{\rm O} &= \beta^{-1} y_{\rm O}(\zeta,\tau) + \cdots \\ Y_{\rm F} &= \beta^{-1} y_{\rm F}(\zeta,\tau) + \cdots \\ T &= T_s + \beta^{-1}\frac{q}{S+1}\theta(\zeta,\tau) + \cdots. \\ F &= F_0(0) + \beta^{-1} f(\zeta,\tau) + \cdots \\ A &= A_0(0) + \beta^{-1} a(\zeta,\tau) + \cdots \end{aligned} \tag{4.25}$$

Matching between Eqs. (6.19) and (4.25) provides the conditions

$$\begin{cases} \zeta \to -\infty: \quad y_{\rm O} = y_{\rm O}^{-}(\tau), & y_{\rm F} = -m_{\rm F0}\zeta, \;\; \theta = \theta^{-}(\tau) + (S+1)m_{\rm F0}\gamma_{\rm F}\zeta, \\ \zeta \to +\infty: \quad y_{\rm O} = y_{\rm O}^{+}(\tau) + S m_{\rm F0}\zeta, \;\; y_{\rm F} = y_{\rm F}^{+}(\tau), & \theta = \theta^{+}(\tau) - (S+1)m_{\rm F0}\gamma_{\rm O}\zeta, \end{cases} \tag{4.26}$$

where

$$y_{\rm O}^{\pm}(\tau) = Y_{\rm O1}(0^{\pm},\tau),\; y_{\rm F}^{+}(\tau) = Y_{\rm F1}(0^{+},\tau) \text{ and } \theta^{\pm}(\tau) = \frac{T_1(0^{\pm},\tau)}{q/(S+1)}, \tag{4.27}$$

and Eqs. (4.21) and (4.22) have been used. The matching condition for $y_{\rm F}$ as $\zeta \to -\infty$ involves a zero displacement, consistent with the definition of the coordinate x, that is, x has been defined to prevent a function $y_{\rm F}^{-}(\tau)$ from appearing in Eq. (4.26). The expressions in Eq. (4.26) imply that the gradients of mass fractions and temperature asymptotically approach the boundary values

$$\begin{cases} \zeta \to -\infty: \quad \frac{\partial y_{\rm O}}{\partial \zeta} = 0, & \frac{\partial y_{\rm F}}{\partial \zeta} = -m_{\rm F0}, \;\; \frac{\partial \theta}{\partial \zeta} = (S+1)m_{\rm F0}\gamma_{\rm F}, \\ \zeta \to +\infty: \quad \frac{\partial y_{\rm O}}{\partial \zeta} = S m_{\rm F0}, & \frac{\partial y_{\rm F}}{\partial \zeta} = 0, \quad \frac{\partial \theta}{\partial \zeta} = -(S+1)m_{\rm F0}\gamma_{\rm O}. \end{cases} \tag{4.28}$$

Similarly, the kinematic variables f and a satisfy the matching conditions

$$\begin{cases} \zeta \to \pm\infty: \quad f = f_o^{\pm}(\tau) + \zeta \frac{\mathrm{d}F_0}{\mathrm{d}x}(0), \quad a = a_o^{\pm}(\tau) + \zeta \frac{\mathrm{d}A_0}{\mathrm{d}x}(0) \\ \zeta \to \pm\infty: \quad \frac{\partial f}{\partial \zeta} = \frac{\mathrm{d}F_0}{\mathrm{d}x}(0), \quad \frac{\partial a}{\partial \zeta} = \frac{\mathrm{d}A_0}{\mathrm{d}x}(0) \end{cases}, \tag{4.29}$$

where $f_o^{\pm}(\tau) = F_1(0^{\pm}, \tau)$ and $a_o^{\pm}(\tau) = A_1(0^{\pm}, \tau)$, respectively.

4.4.3 Summary of the analysis of the reaction layer

The inner layer is found to be quasi-steady, as described in Supplement B. The solution can be reduced to Liñán's canonical problem [4] by introduction of a rescaled fuel mass fraction $y = y_{\mathrm{F}}/Z_s$ along with a reduced Damköhler number

$$\Lambda = \mathcal{D} \exp\left(C_1 + \frac{S+1}{S} \gamma_{\mathrm{F}} C_2 \right), \tag{4.30}$$

involving the classical Damköhler number

$$\mathcal{D} = \frac{S \beta^{-3} B T_s^{\sigma-1}}{(S+1)^3 m_{\mathrm{F}0}^2} e^{-T_a/T_s} \tag{4.31}$$

and the time-dependent functions $C_1(\tau)$ and $C_2(\tau)$, defined in Supplement B, to be obtained as part of the matching procedure. The solution to the canonical problem provides the amounts of fuel and oxygen that leak through the flame, with resulting values $y_{\mathrm{F}}^+ = Z_s y^+$ and $y_{\mathrm{O}}^- = (1 - Z_s) y^-$ shown on the right in Fig. 4.1 for three representative values of γ_{O}.

The curves on the left plot of Fig. 4.1, characterizing the quasi-steady response of the reaction layer, show a turning point at a minimum value $\Lambda = \Lambda_E$ of Λ that defines extinction conditions (e.g. $\Lambda_E = 0.176$ for $\gamma_{\mathrm{O}} = 0.80$). This extinction point is marked with a circle on all three curves. The upper branch of each curve, extending above the circle, corresponds to unstable solutions, so that only solutions along the lower branch are relevant for the analysis.

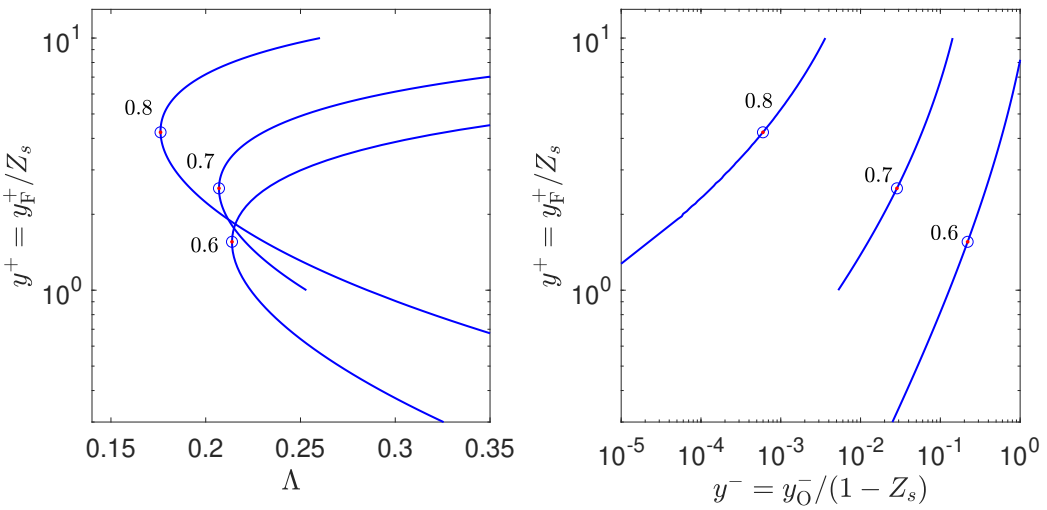

Figure 4.1: The variation of the rescaled reactant leakages with the canonical Damköhler number Λ for selected values of the leading-order oxidizer-side heat-conduction fraction γ_o. The turning points, defining extinction conditions, are labeled by circles.

In the quasi-steady response described here the solution fluctuates about the unperturbed point $\Lambda = \mathcal{D}$ as the reduced Damköhler number varies in response to the pressure pulsation following Eq. (4.30), resulting in fluctuating reactant leakages.

4.4.4 Analysis of the outer transport regions

The order β^{-1} corrections in the transport zone satisfy the system

$$\begin{gathered}
-T_0\frac{\partial F_1}{\partial x}+T_0^{\sigma}A_1+(\sigma-1)T_0^{\sigma-1}\left(\frac{\partial}{\partial\tau}+A_0\right)T_1\\
=-(\beta\varepsilon)T_0^{\sigma}\left[A_0\cos(\omega\tau)-\omega\sin(\omega\tau)\right]+(\sigma-1)T_0^{\sigma-1}\frac{\mathrm{d}T_0}{\mathrm{d}x}\frac{\mathrm{d}\eta_1}{\mathrm{d}\tau},\\
-\frac{\mathrm{d}A_0}{\mathrm{d}x}F_1+T_0^{\sigma-1}\left(\frac{\partial}{\partial\tau}+2A_0\right)A_1-F_0\frac{\partial A_1}{\partial x}-Pr\frac{\partial^2A_1}{\partial x^2}+T_0^{\sigma-1}\left(\frac{(\sigma-1)A_0^2}{T_0}-\sigma\right)T_1\\
=(\beta\varepsilon)T_0^{\sigma-1}\cos(\omega\tau)\left(\frac{T_0}{\gamma}-A_0^2\right)+T_0^{\sigma-1}\frac{\mathrm{d}A_0}{\mathrm{d}x}\frac{\mathrm{d}\eta_1}{\mathrm{d}\tau},\\
-\frac{\mathrm{d}Y_{\mathrm{F}0}}{\mathrm{d}x}F_1+\left(T_0^{\sigma-1}\frac{\partial}{\partial\tau}-F_0\frac{\partial}{\partial x}-\frac{\partial^2}{\partial x^2}\right)Y_{\mathrm{F}1}=T_0^{\sigma-1}\frac{\mathrm{d}Y_{\mathrm{F}0}}{\mathrm{d}x}\frac{\mathrm{d}\eta_1}{\mathrm{d}\tau},\\
-\frac{\mathrm{d}Y_{\mathrm{O}0}}{\mathrm{d}x}F_1+\left(T_0^{\sigma-1}\frac{\partial}{\partial\tau}-F_0\frac{\partial}{\partial x}-\frac{\partial^2}{\partial x^2}\right)Y_{\mathrm{O}1}=T_0^{\sigma-1}\frac{\mathrm{d}Y_{\mathrm{O}0}}{\mathrm{d}x}\frac{\mathrm{d}\eta_1}{\mathrm{d}\tau},\\
-\frac{\mathrm{d}T_0}{\mathrm{d}x}F_1+\left(T_0^{\sigma-1}\frac{\partial}{\partial\tau}-F_0\frac{\partial}{\partial x}-\frac{\partial^2}{\partial x^2}\right)T_1=T_0^{\sigma-1}\frac{\mathrm{d}T_0}{\mathrm{d}x}\frac{\mathrm{d}\eta_1}{\mathrm{d}\tau}-(\beta\varepsilon)T_0^{\sigma}\left(\frac{\gamma-1}{\gamma}\right)\omega\sin(\omega\tau),
\end{gathered}\tag{4.32}$$

involving the parameter $\beta\varepsilon$ and the flame displacement $\eta_1(\tau)$, to be determined in the integration. For a given frequency ω, these equations must be integrated on each side of the flame. When solving on the fuel side ($x<0$) the corresponding boundary conditions are

$$\begin{cases}
x=-\infty: \quad A_1=Y_{\mathrm{F}1}=Y_{\mathrm{O}1}=T_1-(\beta\varepsilon)\Theta\frac{\gamma-1}{\gamma}\cos\omega\tau=0,\\
x=0^-: \quad F_1-f_o(\tau)=A_1-a_o(\tau)=Y_{\mathrm{F}1}=Y_{\mathrm{O}1}-y_{\mathrm{O}}^-(\tau)=T_1-\frac{q}{S+1}\theta^-(\tau)=0.
\end{cases}\tag{4.33}$$

Similarly, appropriate boundary conditions on the oxidizer side ($x>0$) are

$$\begin{cases}
x=0^+: \quad F_1-f_o(\tau)=A_1-a_o(\tau)=Y_{\mathrm{F}1}-y_{\mathrm{F}}^+(\tau)=Y_{\mathrm{O}1}-y_{\mathrm{O}}^+(\tau)=T_1-\frac{q}{S+1}\theta^+(\tau)=0,\\
x=+\infty: \quad A_1=Y_{\mathrm{F}1}=Y_{\mathrm{O}1}=T_1-(\beta\varepsilon)\frac{\gamma-1}{\gamma}\cos\omega\tau=0.
\end{cases}\tag{4.34}$$

In writing Eqs. (4.33) and (4.34) continuity of A_1 and F_1 across the flame has been used, a result that follows from the inner-layer analysis, as shown in Supplement B.

4.4.5 Closure and solution procedure

Integration of the outer problem Eq. (4.32) for given ω and $\mathcal{D}$ requires knowledge of the values of various variables at each side of the flame, measured by the quantities $y_{\mathrm{F}}^{+}(\tau)$, $y_{\mathrm{O}}^{\pm}(\tau)$, $\theta^{\pm}(\tau)$, $a_o(\tau)$, and $f_o(\tau)$ appearing in the boundary conditions given in Eqs. (4.33) and (4.34), along with information regarding the flame shift $\eta_1(\tau)$. The values of $y_{\mathrm{F}}^{+}(\tau)$, $y_{\mathrm{O}}^{\pm}(\tau)$, and $\theta^{\pm}(\tau)$ can be expressed in terms of the reduced reactant leakages y^{+} and y^{-} according to

$$y_{\mathrm{F}}^{+}=\frac{y^{+}}{S+1},\quad \begin{cases} y_{\mathrm{O}}^{-}=\frac{S}{S+1}y^{-} \\ y_{\mathrm{O}}^{+}=\frac{S}{S+1}(y^{+}+y^{-}) \end{cases},\quad \begin{cases} \theta^{-}=\ln(\Lambda/\mathcal{D})-\bar{\gamma}_{\mathrm{O}}y^{-} \\ \theta^{+}=\theta^{-}-y^{+} \end{cases}, \tag{4.35}$$

obtained from Eqs. (4.62) and (4.65) supplemented with the relations $C_2=-(S/[S+1])y^{-}$ (from Supplement B) and $C_1=\ln(\Lambda/\mathcal{D})+\bar{\gamma}_{\mathrm{F}}y^{-}$, the latter following from Eq. (4.30). The canonical curves in Fig. 4.1 can be used to evaluate y^{-} and y^{+} in terms of Λ, thereby reducing the set of unknowns to $\Lambda(\tau), a_o(\tau)$, $f_o(\tau)$, and $\eta_1(\tau)$. Closure of the solution then requires four additional equations. The condition of zero mass flux at the stagnation plane yields

$$F_1=\eta_1\frac{\mathrm{d}F_0}{\mathrm{d}x}\quad\text{at}\quad x=-\eta_0. \tag{4.36}$$

Three additional conditions relating the gradients of A_1, $Y_{\mathrm{F}1}$, $Y_{\mathrm{O}1}$, and T_1 at $x=0^{\pm}$ can be obtained by integrating the conservation equations across the flame, with the limits of integration $x=-\delta$ and $x=+\delta$ lying in the intermediate matching region between the inner and outer expansions, i.e. $\beta^{-1}\ll\delta\ll 1$. The integration procedure is applied to the momentum Eq. (4.10) and to two reaction-free linear combinations of Eqs. (4.11)–(4.13). Using the outer expansions shown in Eq. (6.19) to evaluate the resulting expressions provides at order β^{-1} the three jump conditions

$$\left[\frac{\partial A_1}{\partial x}\right]=\left[S\frac{\partial Y_{\mathrm{F}1}}{\partial x}-\frac{\partial Y_{\mathrm{O}1}}{\partial x}\right]=\left[\frac{\partial T_1}{\partial x}+\frac{q}{S}\frac{\partial Y_{\mathrm{O}1}}{\partial x}\right]=0, \tag{4.37}$$

thereby effectively closing the problem. Here, the bracket is employed to denote the jump of a given quantity across the flame, i.e. $[(\,)] = (\,)_{0^+} - (\,)_{0^-}$. The one-dimensional, unsteady problem defined by Eqs. (4.32)–(4.34) may be integrated on each side of the flame using the method of lines after discretization of the spatial derivatives with the boundary conditions at the flame $x = 0^{\pm}$ determined in an iterative (e.g. Newton Raphson) fashion at each time step when use is made of the conditions (4.36) and (4.37), as explained above.

4.4.6 Characteristics of the solution

The asymptotic procedure presented above provides the general framework for the analysis of the periodic flame response to harmonic pressure fluctuations in the distinguished limit defined in Eq. (4.20). The problem reduces to the integration of Eq. (4.32) subject to Eqs. (4.33) and (4.34) and supplemented with Eqs. (4.35)–(4.37) and the additional relations $y^-(\Lambda)$ and $y^+(\Lambda)$ given by the canonical curves of Fig. 4.1. An important outcome of the analysis is the departure of the burning rate m_{F} from its steady Burke-Schumann value $m_{\mathrm{F}0}$, which can be obtained, following the procedure used to derive Eq. (4.37), by integrating Eq. (4.11) across the flame to yield

$$m_{\mathrm{F}} - m_{\mathrm{F}0} = \beta^{-1}\left(\left[\frac{\partial Y_{\mathrm{F}1}}{\partial x}\right] + F_0(0)\, y_{\mathrm{F}}^{+}(\tau)\right). \tag{4.38}$$

This result shows that the variation of m_{F} is partly due to the modification of the fuel diffusion flux into the reaction layer and partly due to the unburnt fuel leaking through the flame.

The solution delineated above simplifies for steady counterflow flames with constant pressure, which can be investigated from the present formulation by considering the steady counterpart of Eq. (4.32) and setting $\beta\varepsilon = 0$ in Eqs. (4.32)–(4.34). With both reactants having unity Lewis numbers, it can be shown that the resulting steady value of the rescaled Damköhler number reduces to $\bar{\Lambda} = \mathcal{D}$ [4], so that the critical conditions at extinction, defined in this case by the equation $\mathcal{D} = \Lambda_E$, are independent of the finite-rate perturbations in the outer near-

equilibrium regions, as first demonstrated in [3]. These perturbations need to be calculated, however, to determine the corrections to the burning rate resulting from finite-rate effects, given by

$$\bar{m}_{\mathrm{F}} - m_{\mathrm{F}0} = \beta^{-1} \left(\left[\frac{\mathrm{d}\bar{Y}_{\mathrm{F}1}}{\mathrm{d}x} \right] + F_0(0) \bar{y}_{\mathrm{F}}^{+}(\tau) \right), \tag{4.39}$$

with all variables corresponding to the steady solution denoted by a bar.

The response to unsteady pressure fluctuations is investigated by considering non-zero values of $\beta\varepsilon$. In the distinguished limit given in Eq. (4.20) the departures from the steady Burke-Schumann solution, described by the functions $Y_{\mathrm{O}1}(x,\tau)$, $Y_{\mathrm{F}1}(x,\tau)$, ... in the outer regions and by the functions $y_{\mathrm{O}}(\zeta,\tau)$, $y_{\mathrm{F}}(\zeta,\tau)$ ... in the reaction layer, exhibit relative temporal changes of order unity, larger for larger $\beta\varepsilon$, associated with order-unity fluctuations of the Damköhler number Λ about its unperturbed value $\mathcal{D}$. These variations of Λ are accompanied by periodic variations in the reactant leaking across the flame as the system oscillates back and forth along the lower branch of the canonical curves of Fig. 4.1. Although periodic, these leakages are inharmonic, as a consequence of the nonlinear character of the reaction-layer problem in Supplement B, reflected in the exponential time dependence present in the definition of Λ and in the varying slope of the canonical curves, especially pronounced close to extinction conditions.

The existence of the solution requires that the values of $\mathcal{D}$ and $\beta\varepsilon$ are such that the minimum value $\Lambda_{\min}$ of Λ during the fluctuating cycle remains above Λ_E. Clearly, the analysis given here can be expected to fail near the turning point, because the associated rapid variation of the fuel leakage is incompatible with the assumption of quasi-steadiness in the inner reaction layer. Therefore, while the condition $\Lambda_{\min} = \Lambda_E$ can be used to predict critical extinction conditions, the detailed description of transient extinction events requires consideration of unsteady effects in the reaction layer, not considered here.

The expression given in Eq. (4.38) simplifies in the Burke-Schumann limit $\mathcal{D} \to \infty$, corresponding to solutions with negligibly small reactant leakages lying far below the extinction points of Fig. 4.1. As shown in our previous analysis [1], the fluctuations of the burning rate

$m_F - m_{F0}$ for $\mathcal{D} \to \infty$ are proportional to ε, a result that can be recovered from the present formulation by noting that, with negligible reactant leakage, the first-order corrections to the outer flow, to be obtained from Eqs. (4.32)–(4.34), are driven only by the pressure forcing term, proportional to $\beta\varepsilon$, so that $\partial Y_{F1}/\partial x \propto \beta\varepsilon$, thereby yielding the expected dependence $m_F - m_{F0} \propto \varepsilon$ from Eq. (4.38).

Thus far we have presented the asymptotic description of the flame response to harmonic pressure fluctuations of amplitude $\varepsilon \sim \beta^{-1}$, sufficient in driving order-unity changes of the reaction rate in the distinguished limit (4.20). Interest is now directed to the examination of acoustic phenomena, formally described by infinitesimal acoustic amplitudes ε smaller than all other perturbations including those due to finite-rate effects $\sim \beta^{-1}$. The resulting problem, to be described below, may be treated by considering flames with $\mathcal{D} \sim 1$ subject to pressure fluctuations of small amplitude $\varepsilon \ll \beta^{-1}$, such that both the leading-order BS solution and its first-order corrections of order β^{-1} are steady in the first approximation. The resulting problem for the acoustic perturbations is linear both in the outer transport regions and also in the reaction layer, so that the flame response is harmonic and can be described in terms of separable variables, thereby simplifying the solution.

4.5 Flame response for acoustic-pressure amplitudes $\varepsilon \ll \beta^{-1}$

In the asymptotic formulation presented above the acoustic-pressure amplitude ε enters in the expansions shown in Eqs. (6.19) and (4.25) through the implicit dependence of the first-order corrections on $\beta\varepsilon$. Small departures from the steady solution of order $\beta\varepsilon$ can be expected for $\beta\varepsilon \ll 1$. These can be described by expanding the first-order corrections in powers of $\beta\varepsilon$, with

the first two terms in the expansions taking the form

$$\begin{aligned} Y_{\mathrm{O}1}(x,\tau) &= \bar{Y}_{\mathrm{O}1}(x) + \beta\varepsilon e^{i\omega\tau}\tilde{Y}_{\mathrm{O}1}(x) \\ Y_{\mathrm{F}1}(x,\tau) &= \bar{Y}_{\mathrm{F}1}(x) + \beta\varepsilon e^{i\omega\tau}\tilde{Y}_{\mathrm{F}1}(x) \\ T_1(x,\tau) &= \bar{T}_1(x) + \beta\varepsilon e^{i\omega\tau}\tilde{T}_1(x) \\ F_1(x,\tau) &= \bar{F}_1(x) + \beta\varepsilon e^{i\omega\tau}\tilde{F}_1(x) \\ A_1(x,\tau) &= \bar{A}_1(x) + \beta\varepsilon e^{i\omega\tau}\tilde{A}_1(x) \\ \eta_1(\tau) &= \bar{\eta}_1 + \beta\varepsilon e^{i\omega\tau}\tilde{\eta}_1 \end{aligned} \tag{4.40}$$

for the outer variables and

$$\begin{aligned} y_{\mathrm{O}}(\zeta,\tau) &= \bar{y}_{\mathrm{O}}(\zeta) + \beta\varepsilon e^{i\omega\tau}\tilde{y}_{\mathrm{O}}(\zeta) \\ y_{\mathrm{F}}(\zeta,\tau) &= \bar{y}_{\mathrm{F}}(\zeta) + \beta\varepsilon e^{i\omega\tau}\tilde{y}_{\mathrm{F}}(\zeta) \\ \theta(\zeta,\tau) &= \bar{\theta}(\zeta) + \beta\varepsilon e^{i\omega\tau}\tilde{\theta}(\zeta) \\ f(\zeta,\tau) &= \bar{f}(\zeta) + \beta\varepsilon e^{i\omega\tau}\tilde{f}_o \\ a(\zeta,\tau) &= \bar{a}(\zeta) + \beta\varepsilon e^{i\omega\tau}\tilde{a}_o \end{aligned} \tag{4.41}$$

for the inner variables. Both sets of expansions begin with the steady solutions corresponding to $\beta\varepsilon = 0$. The second terms, separable and with a harmonic time dependence, amount to perturbations of order ε to the original flow variables, as may be made clear by introducing Eq. (4.40) into Eq. (6.19) (or Eq. (4.41) into Eq. (4.25)). A tilde is used to denote the response functions, carrying the spatial dependence of the acoustic perturbations, with the velocity functions $\tilde{f}_o$ and $\tilde{a}_o$ anticipated to be uniform across the reaction layer, as follows from Eq. (4.59). Matching between the two expansions in Eqs. (4.40) and (4.41) at $O(\beta\varepsilon)$ requires that $\tilde{F}_1(0) - \tilde{f}_o = \tilde{A}_1(0) - \tilde{a}_o = 0$ and that the complex functions $\tilde{y}_{\mathrm{O}}$, $\tilde{y}_{\mathrm{F}}$, and $\tilde{\theta}$ approach the complex limiting values

$$\tilde{y}_{\mathrm{O}} = \tilde{y}_{\mathrm{O}}^{\pm},\ \tilde{y}_{\mathrm{F}} = \{\tilde{y}_{\mathrm{F}}^{+}, 0\},\ \tilde{\theta} = \tilde{\theta}^{\pm} \quad \text{as} \quad \zeta \to \pm\infty \tag{4.42}$$

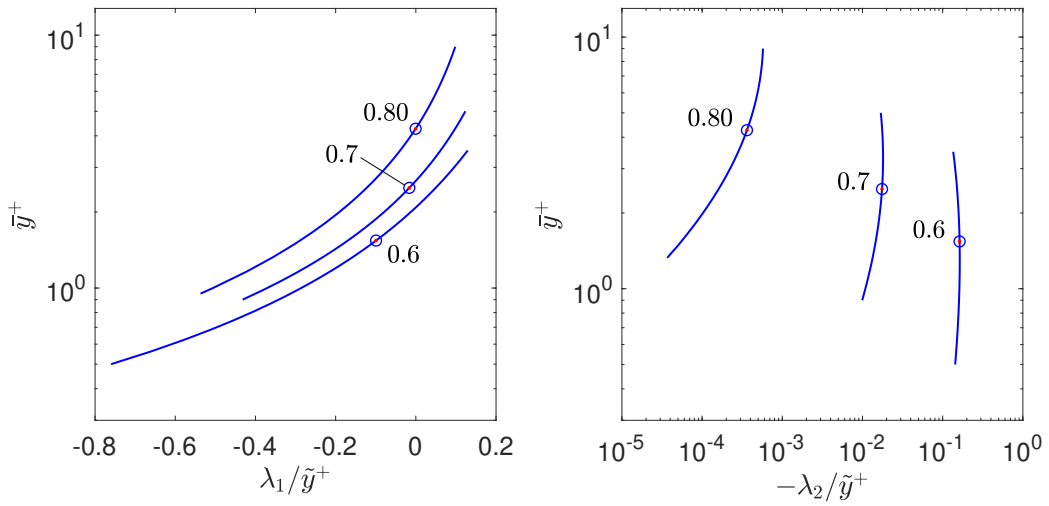

Figure 4.2: The variation of the canonical eigenvalue-to-leakage ratios $\lambda_1/\tilde{y}^+$ and $\lambda_2/\tilde{y}^+$ with the steady rescaled fuel leakage $\bar{y}^+$ for several values of the leading-order oxidizer-side heat-conduction fraction γ_o. The circles identify the turning points indicated in Fig. 4.1

where

$$\tilde{y}_O^{\pm} = \tilde{Y}_{O1}(0^{\pm}),\ \tilde{y}_F^{+} = \tilde{Y}_{F1}(0^{+}),\ \frac{q}{S+1}\tilde{\theta}^{\pm} = \tilde{T}_1(0^{\pm}). \tag{4.43}$$

The analysis of the acoustic response of the inner layer, presented in Supplement C, provides in particular the expressions

$$\tilde{y}_F^{+} = \frac{\tilde{y}^{+}}{S+1},\quad \begin{cases} \tilde{y}_O^{-} = -\frac{S}{S+1}\lambda_2 \\ \tilde{y}_O^{+} = \frac{S}{S+1}(\tilde{y}^{+} - \lambda_2) \end{cases},\quad \begin{cases} \theta^{-} = \lambda_1 \\ \theta^{+} = \lambda_1 - \tilde{y}^{+} \end{cases}, \tag{4.44}$$

for the boundary values appearing in Eqs. (4.42)–(4.43). The values of λ_1 and λ_2, which determine the variation of the Damköhler number according to $\Lambda/\bar{\Lambda} = 1 + \beta\varepsilon e^{i\omega\tau}(\lambda_1 - \gamma_O\lambda_2)$, are proportional to the complex amplitude of the fuel leakage $\tilde{y}_F^{+} = Z_s\tilde{y}^{+}$, with a proportionality constant that depends on the steady fuel leakage $\bar{y}_F^{+} = Z_s\bar{y}^{+}$, as shown in Fig. 4.2.

Analysis of the acoustic response of the outer layers is presented in Supplement D. That analysis requires jump conditions across the inner layer, which can be shown from Eq. (4.37) to

be

$$\left[\frac{\mathrm{d}\tilde{A}_1}{\mathrm{d}x}\right] = \left[S\frac{\mathrm{d}\tilde{Y}_{\mathrm{F}1}}{\mathrm{d}x} - \frac{\mathrm{d}\tilde{Y}_{\mathrm{O}1}}{\mathrm{d}x}\right] = \left[\frac{\mathrm{d}\tilde{T}_1}{\mathrm{d}x} + \frac{q}{S}\frac{\mathrm{d}\tilde{Y}_{\mathrm{O}1}}{\mathrm{d}x}\right] = 0. \tag{4.45}$$

For given values of ω and $\mathcal{D}$ integration of the problem delineated in Supplement D provides in particular $\tilde{y}^+$, representing the complex amplitude of the harmonic oscillation of the fuel leakage about its mean value $\bar{y}^+$. The resulting fluctuations in the fuel leakage lead to oscillations in the burning rate from its unperturbed value $\bar{m}_{\mathrm{F}}$ (defined in Eq. (4.39)) taking the form

$$m_{\mathrm{F}} - \bar{m}_{\mathrm{F}} = \varepsilon e^{i\omega\tau}\tilde{m}_{\mathrm{F}}, \quad \text{where} \quad \tilde{m}_{\mathrm{F}} = \left[\frac{\mathrm{d}\tilde{Y}_{\mathrm{F},1}}{\mathrm{d}x}\right] + \frac{F_0(0)}{S+1}\tilde{y}^+. \tag{4.46}$$

The resulting solution may also be employed in quantifying perturbations to the peak temperature. For a steady flame, the peak temperature is related to the rescaled fuel mass fraction $\bar{y}$ by means of the coupling Eq. (4.63) relating $\bar{\theta}$ with $\bar{y}$, with the latter determined by integration of the canonical problem defined in Eq. (4.64). This implies that the order β^{-1} decrement to the adiabatic value T_s of the BS peak temperature is determined by the maximum value $\bar{\theta}_{\max} = \bar{\theta}(\bar{r}_m)$ of $\bar{\theta}$ with the location $\bar{r}_m$ determined from the condition $\mathrm{d}\bar{y}/\mathrm{d}\bar{r} + \gamma_{\mathrm{O}} = 0$ following from Eq. (4.63). Fluctuations of order ε about this steady peak temperature are described by the function $\tilde{\theta}$, leading to harmonic oscillations with complex amplitudes $\tilde{T}_{\max} = [q/(S+1)]\tilde{\theta}_{\max}$ with $\tilde{\theta}_{\max}$ taking the form $\tilde{\theta}_{\max} = \mathcal{F}\tilde{y}^+$, including a real factor

$$\mathcal{F}(\mathcal{D}) = \frac{\lambda_1}{\tilde{y}^+} - \frac{\tilde{y}(\bar{r}_m)}{\tilde{y}^+}, \tag{4.47}$$

that depends only of the unperturbed Damköhler number $\mathcal{D}$ through the values of $\tilde{y}/\tilde{y}^+$ and $\lambda_1/\tilde{y}^+$. These can be obtained for $\gamma_{\mathrm{O}} = 0.8$ from Figs. 4.8 and 4.2, respectively, yielding, for instance, $\mathcal{F} = -(0.35, 0.65, 2.03)$ for $\mathcal{D} = (0.19, 0.25, 0.50)$. The associated fluctuations of peak temperature take the form

$$\tilde{T}_{\max} = \frac{q}{S+1}\mathcal{F}(\mathcal{D})\,\tilde{y}^+, \tag{4.48}$$

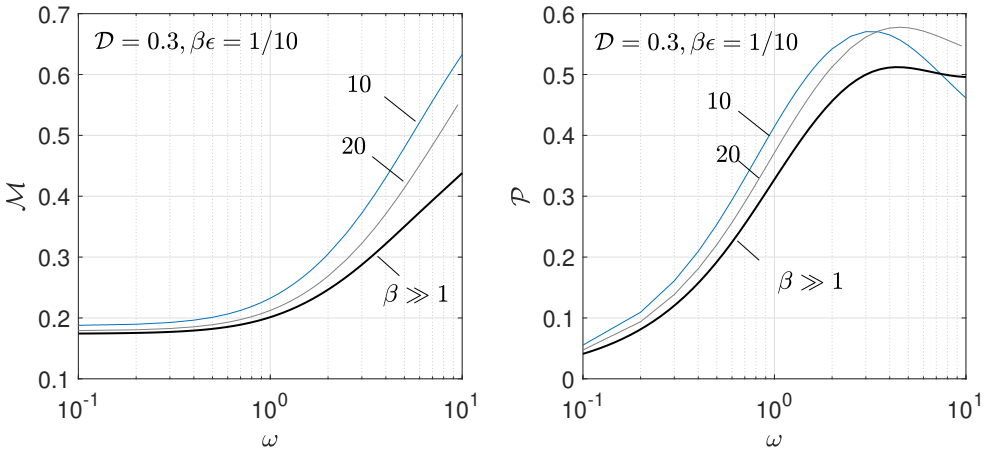

Figure 4.3: Variation of the relative amplitude $\mathcal{M}$ and phase lag $\mathcal{P}$ of the burning rate, defined in Eq. (4.50), obtained from full numeric integration of the governing Eqs. (6.33)–(4.17) when written in terms of the original coordinate η with $\mathcal{D} = 0.3$ and $\beta\varepsilon = 1/10$ for increasing values of the Zel'dovich number β. The asymptotic prediction given in Eq. (4.46) is also shown with the amplitude and phase lag given by $|\tilde{m}_{\rm F}|$ and φ_m, respectively, corresponding to the polar components of $\tilde{m}_{\rm F} = |\tilde{m}_{\rm F}|e^{i\varphi_m}$.

where the complex leakage $\tilde{y}^+$ carries the dependence on ω, along with an additional dependence on $\mathcal{D}$.

4.6 Sample results in the acoustic limit $\beta\varepsilon \ll 1$

The results in Sec. 4.5 can be used to evaluate the acoustic response of near-equilibrium diffusion flames for acoustic amplitudes $\varepsilon \ll \beta^{-1} \ll 1$. Illustrative results will be given below for $S = 4$, $q/S = 10$, $Pr = \sigma = 0.7$, and $\Theta = 1$, selected as representative of methane-oxygen diffusion flames with equal feed-stream temperatures. The corresponding unperturbed solution is characterized by $T_s = 9$ and $\gamma_{\rm O} = 0.8$, determined from Eqs. (4.18) and (4.23), with accompanying values of the flame location and burning rate given by $\eta_0 = 0.77$ and $m_{\rm F0} = 0.38$, obtained from integration of the steady Burke-Schumann problem. Fixing these values allows us to quantify the response in terms of the frequency ω and the unperturbed Damköhler number $\mathcal{D}$.

4.6.1 Comparison with numerical integrations for finite values of β

Before presenting results that quantify the response to acoustic forcing, it is of interest to investigate the accuracy of the large-activation-energy results by comparing the burning-rate prediction given in Eq. (4.46) for $\beta \to \infty$ with the value obtained from the integral in Eq. (4.15) with the temperature and composition determined by numerical integrations of the initial problem defined in Eqs. (6.33)–(4.17) for finite values of $\beta \gg 1$. In the computations, the conservation equations were written in terms of the original coordinate η. To facilitate comparisons with the asymptotic results, the activation temperature T_a and the preexponential factor B appearing in Eq. (4.14) were expressed in terms of β and $\mathcal{D}$ with use made of Eqs. (4.19) and (4.31) to give

$$Be^{-T_a/T} = \mathcal{D}\frac{(S+1)^3 m_{\mathrm{F}0}^2}{S} T_s^{\sigma-1}\beta^3 \exp\left(\beta\frac{T-T_s}{T}\frac{T_s}{q/(S+1)}\right). \tag{4.49}$$

The computations considered a fixed value of $\mathcal{D}$ and increasing values of β, with accompanying acoustic amplitudes ε selected such that $\beta\varepsilon \ll 1$. The latter limit ensures that the full numerical response is nearly harmonic. Correspondingly, Eq. (4.15) takes the approximate form

$$m_{\mathrm{F}}(\tau) - \bar{m}_{\mathrm{F}} \simeq \varepsilon\mathcal{M}\cos(\omega\tau + \mathcal{P}), \tag{4.50}$$

where the amplitude $\mathcal{M}$ (relative to the acoustic amplitude) and the phase lag $\mathcal{P}$ of the burning-rate fluctuations can be evaluted from the appropriate Fourier coefficients of the time series $m_{\mathrm{F}}(\tau)$ obtained in the full integration, thereby enabling comparisons with the asymptotic result in Eq. (4.46) to be made.

Results are shown in Fig. 4.3, where the thin curves represent the variation with the acoustic frequency ω of the values of $\mathcal{M}$ and $\mathcal{P}$ obtained from the numerical integrations for $\beta = 10$ and $\beta = 20$ and fixed values $\mathcal{D} = 0.3$ and $\beta\varepsilon = 1/10$. Also shown as thick curves are the asymptotic results, characterized by the complex value $\tilde{m}_{\mathrm{F}} = |\tilde{m}_{\mathrm{F}}|e^{i\varphi_m}$ defined in Eq. (4.46). The

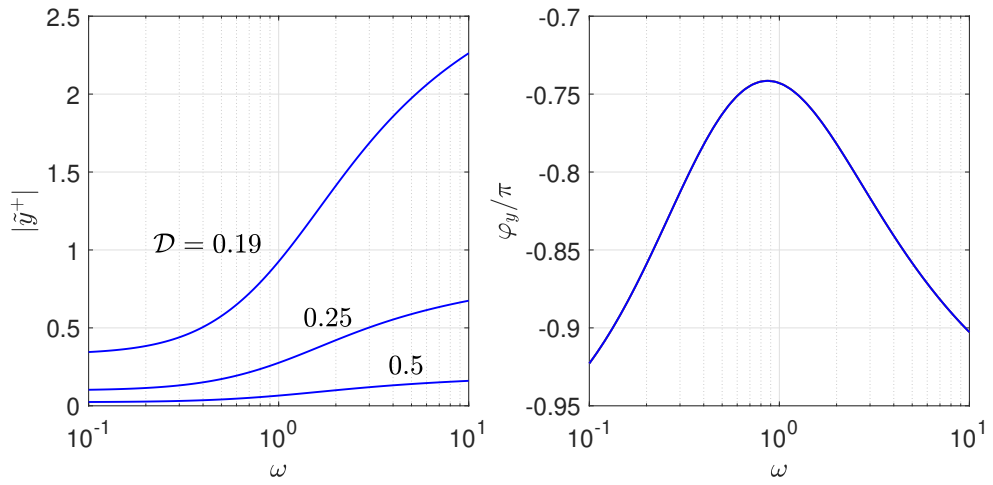

Figure 4.4: The variation of the complex fuel leakage $\tilde{y}^+ = |\tilde{y}^+|e^{i\varphi_y}$ with the acoustic frequency for increasing values of the Damkhöhler number $\mathcal{D} = (0.19, 0.25, 0.5)$; the corresponding points have been labeled on the turning-point curve in the inset of Fig. 4.6.

agreement between the asymptotic predictions ($|\tilde{m}_F|$ and φ_m) and the numerical results ($\mathcal{M}$ and $\mathcal{P}$) is seen to be satisfactory for frequencies of order unity, with observed relative errors $\sim \beta^{-1}$, consistent with the order of the asymptotic analysis. The larger relative errors encountered at high frequencies can be attributable to the quasi-steady structure of the inner reaction layer, which applies in the asymptotic analysis for $\omega \sim 1$, becoming increasing inaccurate for $\omega \gg 1$.

4.6.2 Quantification of flame response: variation with Damköhler and acoustic frequency

Integration of the equations governing the outer transport regions, described by Eqs. (4.73)–(4.76), provide the response functions $\tilde{Y}_{F,1}$, $\tilde{Y}_{O,1}$, and $\tilde{T}_1$, along with the flame shift $\tilde{\eta}_1$ and the fluctuating fuel leakage $\tilde{y}^+$. The latter, a complex quantity expressible as $\tilde{y}^+ = |\tilde{y}^+|e^{i\varphi_y}$ in terms of its modulus $|\tilde{y}^+|$ and phase shift φ_y with respect to the imposed pressure perturbation, represents an appropriate measure of the extent of finite-rate effects. The variation of $|\tilde{y}^+|$ and φ_y with frequency is shown in Fig. 4.4 for selected values of the unperturbed Damköhler number $\mathcal{D} = (0.19, 0.25.0.5)$, with the lowest value $\mathcal{D} = 0.19$ placing the flame near extinction

($\mathcal{D}_E = 0.176$ for $\gamma_O = 0.8$). For these near-extinction conditions, the solution lies near the turning point of the C-shape curve, where small perturbations lead to large variations of the reactant leakage, reflected in the large value of $|\tilde{y}^+|$ shown for $\mathcal{D} = 0.19$ in Fig. 4.4. The amplitude of the fluctuating leakage is seen to increase monotonically with the frequency and to decrease with increasing $\mathcal{D}$, the latter consistent with the approach to the Burke-Schumann limit $\mathcal{D} \gg 1$ of vanishing reactant leakage. The phase, on the other hand, is independent of $\mathcal{D}$ and shows a non-monotonic dependence on the frequency, including a peak value at an intermediate value of $\omega \simeq 0.9$.

The value of the flame shift $\tilde{\eta}_1 = |\tilde{\eta}_1| e^{i\varphi_f}$, together with the fluctuation of the peak temperature $\tilde{T}_{\max} = |\tilde{T}_{\max}| e^{i\varphi_T}$, computed using Eq. (4.48), and the burning-rate fluctuation $\tilde{m}_F = |\tilde{m}_F| e^{i\varphi_m}$, evaluated from Eq. (4.46), are used in Fig 4.5 to evaluate the response of diffusion flames to acoustic perturbations of frequency ω. To better illustrate the extent of finite-rate effects, besides results obtained for $\mathcal{D} = (0.19, 0.25.0.5)$, represented with thin curves, the plots include results corresponding to the Burke-Schumann limit $\mathcal{D} \to \infty$, obtained in our previous analysis [1]. As expected, all finite-rate curves approach the Burke-Schumann results for increasing values of $\mathcal{D}$. An important first observation from the plots is that the influence of finite-rate effects in weakly strained flames is very limited, as measured by the small differences between the curves for $\mathcal{D} = 0.5$ and the BS results, consistent with the small reactant leakages shown in Fig. 4.4 for $\mathcal{D} = 0.5$.

The plots in the left column of Fig 4.5 show the variation of the flame shift $\tilde{\eta}_1 = |\tilde{\eta}_1| e^{i\varphi_f}$. As can be seen, its magnitude $|\tilde{\eta}_1|$ increases with increasing ω from the quasi-steady value obtained for $\omega \ll 1$. Interestingly, the resulting $|\tilde{\eta}_1|$ is seen to be rather insensitive to changes in the Damköhler number, revealing that the flame location is governed mainly by the unsteady modifications to the outer transport regions, largely independent of the finite-rate chemistry. Also of interest is that the phase of the flame displacement, shown in the bottom left corner of the figure, is characterized by values $|\varphi_f - \pi|$ that are relatively small, revealing that the flame displacement

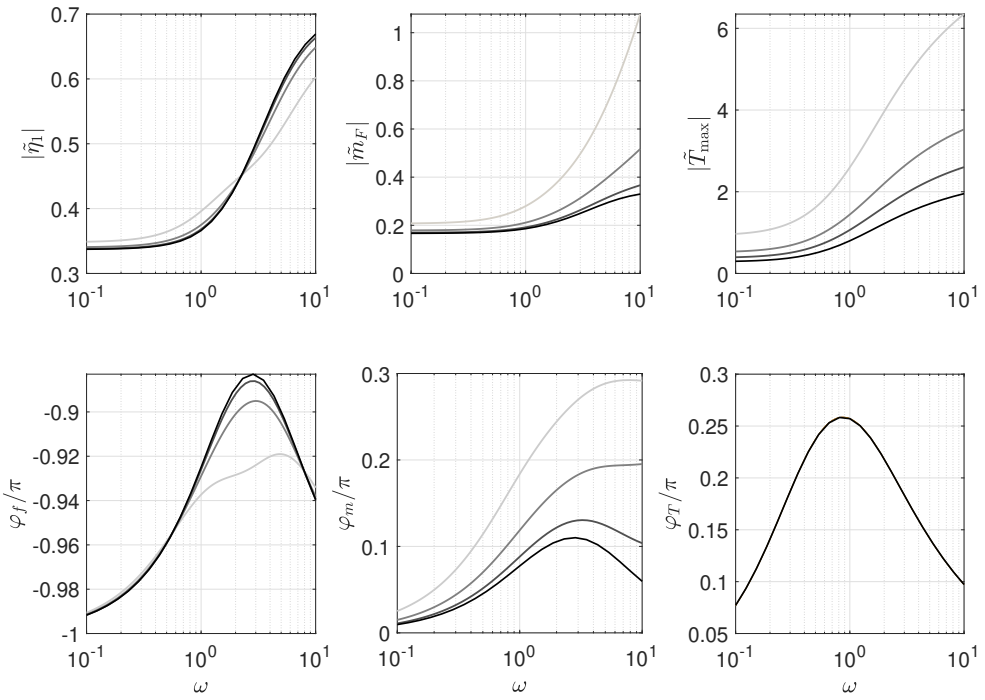

Figure 4.5: The variation with acoustic frequency of the polar components of perturbations to the flame location $\tilde{\eta}_1 = |\tilde{\eta}_1|e^{i\varphi_f}$ (left), the burning rate $\tilde{m}_F = |\tilde{m}_F|e^{i\varphi_m}$ (middle), and to the maximum temperature $\tilde{T}_{\max} = |\tilde{T}_{\max}|e^{i\varphi_T}$ (right). Each curve (in order from light to dark) is for increasing values of the Damköhler number $\mathcal{D} = (0.19, 0.25, 0.5)$; the corresponding points have been labeled on the turning-point curve in the inset of Fig. 4.6. The black line corresponds to data taken from the $\mathcal{D} = \infty$ analysis in [1].

is almost exactly out of phase with the acoustic forcing for all frequencies.

The perturbations to the burning rate $\tilde{m}_F = |\tilde{m}_F|e^{i\varphi_m}$, proportional to fluctuations in the rate of heat release, are also shown in Fig 4.5. The expression for $\tilde{m}_F$ in Eq. (4.46) includes two contributions, one involving the jump of fuel-mass-fraction gradient at the flame $[d\tilde{Y}_{F,1}/dx]$ and the other being proportional to the leakage $\tilde{y}^+$. The departures of $|\tilde{m}_F|$ from the Burke-Schumann value shown in the upper middle plot of Fig 4.5, larger for higher frequencies and smaller Damköhler numbers, are largely attributable to the direct dependence of the burning rate on reactant leakage $\tilde{y}^+$, whose variation with $\mathcal{D}$ and ω is given in Fig. 4.4. The phase shift φ_m, shown in the bottom middle plot of Fig 4.5, reveals that the perturbations to the burning rate remain nearly in phase with the acoustic pressure for all frequencies regardless of the Damköhler number. This fact has implications concerning the amplification of acoustic energy, to be discussed below,

and this result may be anticipated from the fact that the reaction term Ω is proportional to the pressure through the factor $\rho\lambda$ present in its definition.

Shown in the right column of Fig. 4.5 are the variations of the peak temperature $\tilde{T}_{\max} = |\tilde{T}_{\max}|e^{i\varphi_T}$, which are linearly proportional to $\tilde{y}^+$. Since the constant of proportionality $[q/(S+1)]\mathcal{F}(\mathcal{D})$ is a negative real number, the values of $\tilde{T}_{\max}$ and $\tilde{y}^+$ are exactly out of phase, as can be seen by comparing the values of φ_y and φ_T shown in Figs. 4.4 and 4.5, respectively. Also of interest is that, although $\tilde{y}^+$ approaches zero as the Damköhler number increases, the accompanying value of $|\mathcal{F}|$ increases, with the product approaching a finite value, corresponding to the peak temperature fluctuation of the Burke-Schumann flame.

4.6.3 Implications for acoustic instability

The use of the counterflow flame subject to harmonic acoustic forcing serves as a simplified model for the interaction of a sound wave with a laminar flamelet. The amplification or attenuation of the pressure oscillations in the combustion chamber is a global result of these local interactions. According to Rayleigh's criterion, amplification occurs when, on average, heat is added in phase with the pressure increase. This criterion, based on the fact that the rate of change of the mean acoustic energy is proportional to the average of the product of the pressure perturbations with the unsteady heat release [8], may be conveniently characterized through use of the Rayleigh index,

$$R(\omega) = \frac{q}{2\pi/\omega}\int_0^{2\pi/\omega}(p_s-1)(m_{\mathrm{F}}-\bar{m}_{\mathrm{F}})\mathrm{d}\tau \tag{4.51}$$

with $q(m_{\mathrm{F}}-\bar{m}_{\mathrm{F}})$ representing the unsteady heat release. In this sense, the Rayleigh index R provides a local criterion for amplification of a flamelet, with $R>0$ and $R<0$ describing amplification or attenuation, respectively, as follows from Rayleigh's criterion.

Substituting into Eq. (4.51) the expression $m_{\mathrm{F}}-\bar{m}_{\mathrm{F}} = \varepsilon e^{i\omega\tau}\tilde{m}_{\mathrm{F}}$, given in Eq. (4.46) for the

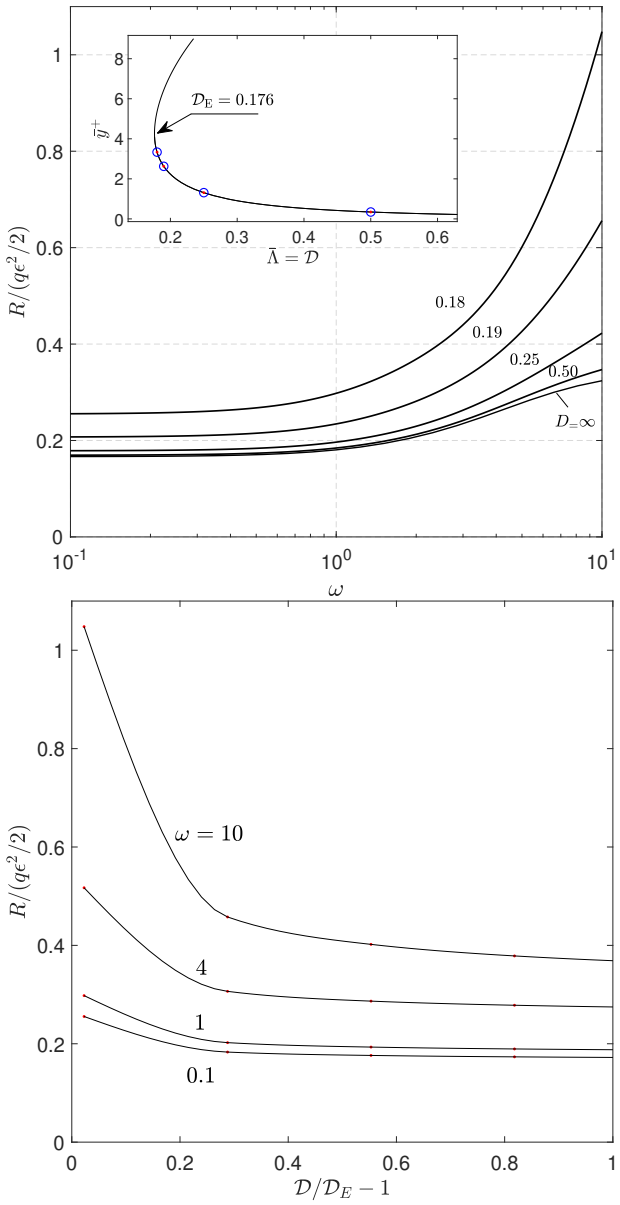

Figure 4.6: For the representative system defined in the first paragraph of this section, the variation of the scaled Rayleigh index with acoustic frequency for increasing values of the Damköhler number $\mathcal{D} = (0.18, 0.19, 0.25, 0.50)$ corresponding to the points labeled on the turning-point curve in the inset. The curve $\mathcal{D} = \infty$ is taken from an earlier analysis [1].

burning rate, along with the imposed pressure variation $p_s - 1 = \varepsilon\cos(\omega\tau)$ leads to

$$R/(q\varepsilon^2/2) = \mathbb{R}\{\tilde{m}_{\mathrm{F}}\}, \tag{4.52}$$

with the symbol $\mathbb{R}$ introduced to denote the real part of a complex quantity. Equation (4.52) is used to evaluate the Rayleigh index, with results shown in Fig. 4.6. The left-hand plot gives the variation of the Rayleigh index with the frequency of the acoustic pressure oscillations for selected values of the Damkhöhler number $\mathcal{D}$, marked with a circle along the C-shape curve shown in the inset. As is evident from the curves, the analysis predicts amplification over all ranges of the acoustic frequency ω regardless of the Damkhöhler number, a result that may be anticipated from Fig. 4.5 since the phase φ_m of the burning-rate perturbation lies within the range $|\varphi_m| < \pi/2$, ensuring that $\mathbb{R}\{\tilde{m}_{\mathrm{F}}\} = |\tilde{m}_{\mathrm{F}}|\cos(\varphi_m)$ is positive.

The variation of the Rayleigh index with the Damkhöler number is examined in the right-hand plot of Fig. 4.6. The results indicate that finite-rate effects dominate the acoustic pressure response of strained flamelets near extinction. For robust, diffusion-controlled flames unsteady modifications to the outer chemical-equilibrium transport regions produce only moderate effects. This result is tied closely to the diminishing value of the leakage as the Damkhöler number increases, shown in Fig. 4.4. For the typical flow conditions found in the combustion chamber of a liquid-propellant rocket engine, the strain rate exerted on the flamelets can be expected to decrease with increasing axial distance from the injectors, leading to an increase in the resulting local Damköhler number. Therefore, the present results indicate that the acoustic interactions with the flamelets produce larger rates of amplification in the highly strained near-injector region, whereas the contribution of the near-equilibrium flamelets found farther downstream will be of lesser importance. This same result has been found earlier in the context of the premixed-flame regime of diffusion flames [2].

The extent to which the above amplification results may be applied to realistic rocket

motors depends also on the relevant damping mechanisms present, including nozzle and/or wall damping [8], for example, which are not considered in the local analysis presented here. The inclusion of these effects, as well as addressing self-sustained pressure oscillations through closed-loop interactions, treated for example in [9, 10], warrants further investigation.

4.7 Concluding remarks

This investigation has served to determine the local response of diffusion flamelets to imposed harmonic pressure oscillations of wavelength large compared with local mixing-layer thicknesses, focusing on counterflows, with effects of amplification or attenuation of acoustic combustion instabilities in liquid-propellant rocket motors identified. The different physical contributions to the response have been identified and explained, showing that the response for typical propellant combinations of interest leads to acoustic amplification, not attenuation, the amplification being larger at higher strain rates (closer to flamelet extinction). These conclusions are drawn on the basis of one-step Arrhenius chemical kinetics, of first order with respect to both the fuel and oxidizer, the temperature dependence of the heat-release rate being strong, so that methods of activation-energy asymptotics can be applied. The extent to which the results of this chemical-kinetic approximation would apply to the chemistry of bipropellant pairs of methane-oxygen or hydrogen-oxygen systems would be worthy of future study along these lines, the first of these being described reasonably employing the equal-diffusivity (Lewis-number-unity) approximation of the present study, but the second motivating further consideration of Lewis-number effects. While for hydrogen-oxygen systems detailed chemistry can be used in one-dimensional pressure response computations [11, 12], for hydrocarbon-oxygen systems reduced mechanisms might be needed to reduce computational cost, and comparison to the asymptotic predictions presented here would be worthwhile.

Supplement A: Steady Burke-Schumann solution

The temperature and composition is described in terms of the mixture fraction

$$Z_0 = \frac{SY_{F0} - Y_{O0} - 1}{S+1} = \frac{T_0 - 1 + (q/S)(Y_{O0} - 1)}{\Theta - 1 - q/S}, \tag{4.53}$$

which satisfies the chemistry-free problem

$$\frac{d^2 Z_0}{dx^2} + F_0 \frac{dZ_0}{dx} = 0; \quad Z_0(-\infty) = 1, Z_0(+\infty) = 0. \tag{4.54}$$

At the flame $x = 0$ both $Y_{F0} = Y_{O0} = 0$ so that $Z_0 = Z_s = 1/(S+1)$ and the temperature reaches the peak value $T_0(0) = T_s$, where T_s is the adiabatic flame temperature defined in Eq. (4.18). Since $Y_{O0} = 0$ on the fuel side of the flame while $Y_{F0} = 0$ on the oxidizer side of the flame, the definition given in Eq. (4.53) yields the piecewise linear relations

$$\begin{cases} Y_{F0} = \frac{Z_0 - Z_s}{1 - Z_s}, & Y_{O0} = 0, & T_0 = (\Theta - 1 - \frac{q}{S}) Z_0 + 1 + \frac{q}{S}, & \text{for} \quad x < 0 \\ Y_{F0} = 0, & Y_{O0} = 1 - \frac{Z_0}{Z_s}, & T_0 = (\Theta - 1 - \frac{q}{S}) Z_0 + 1 + \frac{qZ_0}{SZ_s}, & \text{for} \quad x > 0 \end{cases} . \tag{4.55}$$

The problem reduces to the integration of Eq. (4.54) along with the steady forms of the continuity and momentum Eqs. (6.33) and (4.10)

$$\frac{dF_0}{dx} - \rho_0 \lambda_0 A_0 = F_0 \frac{dA_0}{dx} + Pr \frac{d^2 A_0}{dx^2} + \lambda_0 (1 - \rho_0 A_0^2) = 0 \tag{4.56}$$

subject to the boundary conditions $A_0(+\infty) - 1 = A_0(-\infty) - \Theta^{1/2} = F_0(-\eta_0) = 0$, with the density ρ_0 and thermal conductivity λ_0 evaluated in terms of Z_0 with use made of Eqs. (4.16) and (4.55). The unperturbed flame location η_0 is to be determined as part of the computation from the condition that the derivative of Z_0 is continuous across the flame at $x = 0$. For values of $S > 1$ the flame tends to be on the oxidizer side of the mixing layer (i.e. positive values of η_0),

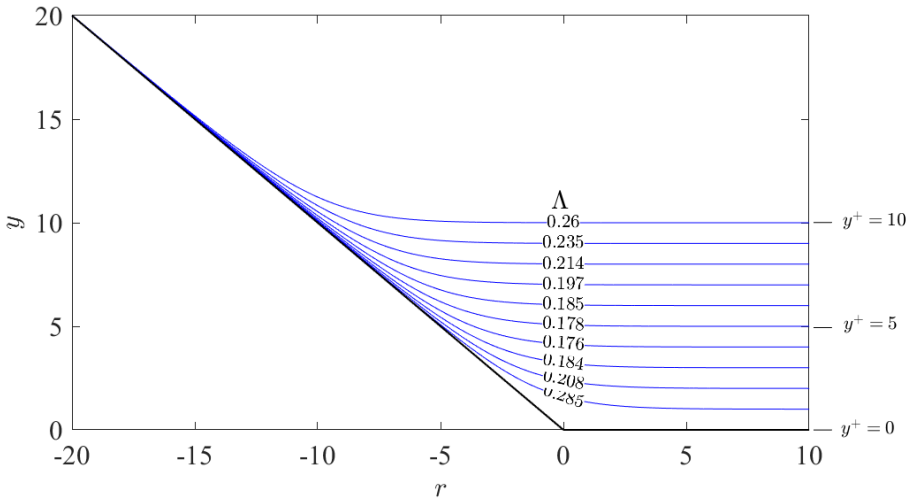

Figure 4.7: Internal structure of the reactive-diffusive layer as given by integration of the canonical problem defined in Eq. (4.64) for $\gamma_o = 0.80$ with fuel-leakages y^+ between 1 and 10 in increments of one.

so that at leading order the stagnation plane is located at $x = -\eta_0 < 0$. As can be inferred from Eq. (4.55), the derivative of Z_0 at the flame is related to those of the temperature and reactant mass fractions according to

$$\left.\frac{\mathrm{d}Z_0}{\mathrm{d}x}\right|_0 = (1-Z_s)\left.\frac{\mathrm{d}Y_{F0}}{\mathrm{d}x}\right|_{0^-} = -Z_s\left.\frac{\mathrm{d}Y_{O0}}{\mathrm{d}x}\right|_{0^+} = -\frac{(1-Z_s)}{q}\left(\left.\frac{\mathrm{d}T_0}{\mathrm{d}x}\right|_{0^-} - \left.\frac{\mathrm{d}T_0}{\mathrm{d}x}\right|_{0^+}\right), \tag{4.57}$$

which can be used to evaluate the rates of fuel consumption and heat release, as indicated in the main text in Eq. (4.21).

Supplement B: Analysis of the reaction layer

Introduction of the rescaled coordinate $\zeta = \beta x$ and inner expansions of Eq. (4.25) into Eqs. (6.33)–(4.13) leads to a set of reduced equations for the structure of the inner layer. For

example, the continuity and momentum equations reduce to

$$\frac{\partial f}{\partial \zeta} - \frac{\mathrm{d}F_0}{\mathrm{d}x}(0) = \frac{\partial^2 a}{\partial \zeta^2} = 0, \tag{4.58}$$

which yield

$$f = f_o(\tau) + \frac{\mathrm{d}F_0}{\mathrm{d}x}(0)\zeta \quad \text{and} \quad a = a_o(\tau) + \frac{\mathrm{d}A_0}{\mathrm{d}x}(0)\zeta \tag{4.59}$$

upon integration with the boundary conditions given in Eq. (4.29), with $f_o = f_o^+ = f_o^-$ and $a_o = a_o^+ = a_o^-$. The above result indicates in particular that the corrections F_1 and A_1 in the outer solution are continuous at $x = 0$, a result to be used in writing Eqs. (4.33) and (4.34) in the main text.

The equations for reactants and energy take the form

$$-\frac{S}{S+1}\frac{\partial^2 \theta}{\partial \zeta^2} = S\frac{\partial^2 y_{\mathrm{F}}}{\partial \zeta^2} = \frac{\partial^2 y_{\mathrm{O}}}{\partial \zeta^2} = \frac{S\beta^{-3}B}{T_s^{1-\sigma}} e^{-T_a/T_s} y_{\mathrm{F}} y_{\mathrm{O}} e^{\theta}. \tag{4.60}$$

The first two equations can be integrated twice with use of the matching conditions in Eqs. (4.26) and (4.28) to yield

$$\begin{aligned} y_{\mathrm{O}} &= S y_{\mathrm{F}} + S m_{\mathrm{F0}} \zeta - C_2(\tau), \\ \theta &= -(S+1) y_{\mathrm{F}} - (S+1) m_{\mathrm{F0}} \gamma_{\mathrm{O}} \zeta + \frac{S+1}{S} C_2(\tau) + C_1(\tau), \end{aligned} \tag{4.61}$$

involving the time-dependent functions

$$\begin{aligned} C_1(\tau) &= \frac{S+1}{S} y_{\mathrm{O}}^+(\tau) + \theta^+(\tau) = \frac{S+1}{S} y_{\mathrm{O}}^-(\tau) + \theta^-(\tau), \\ C_2(\tau) &= S y_{\mathrm{F}}^+(\tau) - y_{\mathrm{O}}^+(\tau) = -y_{\mathrm{O}}^-(\tau). \end{aligned} \tag{4.62}$$

Rewriting Eq. (4.60) in terms of the shifted coordinate $r = (S+1)m_{\mathrm{F0}}\zeta - (S+1)C_2/S$ and the

rescaled fuel mass fraction $y = (S+1)y_F$, defined such that

$$y_O = \frac{S}{S+1}(y+r) \quad \text{and} \quad \theta = -y - \gamma_O r + \frac{S+1}{S}\gamma_F C_2 + C_1, \tag{4.63}$$

produces the canonical problem [4]

$$\frac{\partial^2 y}{\partial r^2} = \Lambda y(y+r)\exp\left[-\gamma_O r - y\right] \quad \begin{cases} r \to -\infty: & y + r = y^-(\tau) \quad \Leftrightarrow \ \frac{\partial y}{\partial r} = -1, \\ r \to +\infty: & y = y^+(\tau) \qquad \Leftrightarrow \ \frac{\partial y}{\partial r} = 0, \end{cases} \tag{4.64}$$

where the boundary conditions are expressed in terms of the rescaled reactant leakages

$$y^- = \frac{S+1}{S} y_O^- \quad \text{and} \quad y^+ = (S+1)y_F^+. \tag{4.65}$$

The relative importance of reaction and diffusion is measured in Eq. (4.64) by the canonical Damköhler number $\Lambda = \mathcal{D}\exp\left[C_1 + \gamma_F C_2(S+1)/S\right]$, involving the unknown functions $C_1(\tau)$ and $C_2(\tau)$ and the unperturbed Damköhler defined in Eq. (4.31). For a given γ_O the integration of Eq. (4.64) begins by selecting y^+ and marching from $r = \infty$ with an initial zero slope, with the associated value of Λ obtained by enforcing the condition $\partial y/\partial r = -1$ at $r = -\infty$. Sample profiles of $y(r)$ obtained for methane-oxygen combustion ($\gamma_O = 0.80$) are shown in Fig. 4.7, including values of the fuel leakage y^+ increasing from $y^+ = 1$ to $y^+ = 10$ in unity increments. The resulting values of Λ, indicated in the figure, display a non-monotonic variation, a distinctive feature of the solution associated with the existence of a critical value of Λ characterizing flame extinction [3]. For the case $\gamma_O = 0.80$ considered in Fig. 4.7, oxygen leakage is negligibly small, with associated values of y^- given in the main text in Fig. 4.1. Increased oxygen leakage is seen to occur for smaller values of γ_O, corresponding to configurations with fuel-feed dilution (i.e. smaller values of S).

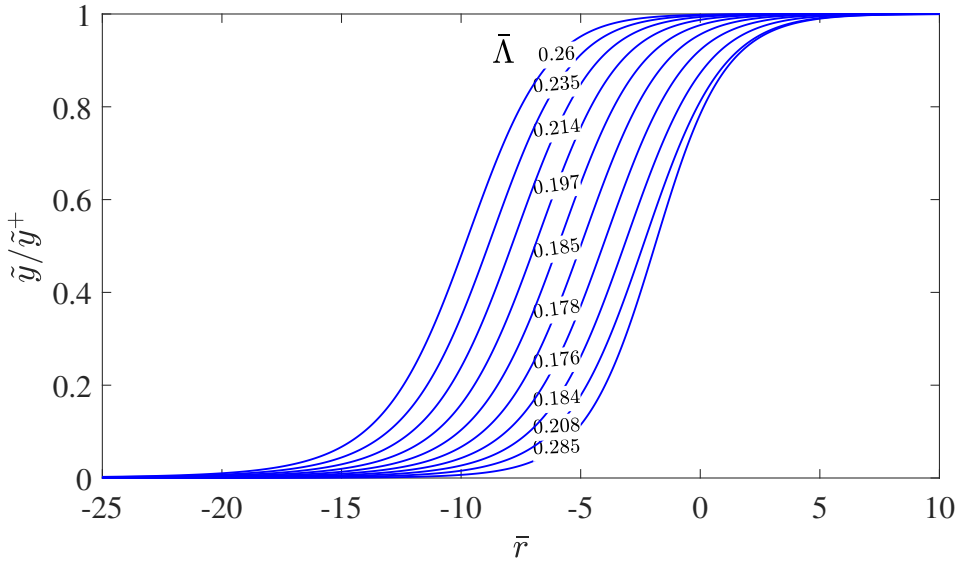

Figure 4.8: The internal structure of reactive-diffusive layer at $O(\beta\varepsilon)$ as obtained for $\gamma_o = 0.8$ by integration of the linearized canonical problem given in Eq. (4.66).

Supplement C: Acoustic response of inner region for $\beta\varepsilon \ll 1$

For the analysis of the reaction layer, the time-dependent functions in Eq. (4.62) are expressed following Eq. (4.41) as $C_1 = \bar{C}_1 + \beta\varepsilon e^{i\omega\tau}\tilde{C}_1$ and $C_2 = \bar{C}_2 + \beta\varepsilon e^{i\omega\tau}\tilde{C}_2$. For the case of unity Lewis numbers considered here $\bar{\Lambda} = \mathcal{D}$ [4] implying that the unperturbed values $\bar{C}_1$ and $\bar{C}_2$ satisfy $\bar{C}_1 + \bar{C}_2\gamma_F(S+1)/S = 0$ as follows from Eq. (4.30). Correspondingly, the rescaled variables in Eq. (4.63) for the canonical problem given in Eq. (4.64) take the form $r = \bar{r} - \beta\varepsilon e^{i\omega\tau}(S+1)\tilde{C}_2/S$ and $y = \bar{y} + \beta\varepsilon e^{i\omega\tau}(S+1)\tilde{y}_F$, including the unperturbed variables $\bar{r} = (S+1)m_{F0}\zeta - (S+1)\bar{C}_2/S$ and $\bar{y} = (S+1)\bar{y}_F$, equivalent to previous results [4]. Linearizing the canonical problem given in Eq. (4.64) about the unperturbed solution $\bar{y}(\bar{r})$ yields

$$\frac{d^2\tilde{y}}{d\bar{r}^2} - k(\bar{r})\tilde{y} = \lambda_1 g(\bar{r}) + \lambda_2 h(\bar{r}) \tag{4.66}$$

for the complex rescaled fuel mass fraction $\tilde{y} = (S+1)\tilde{y}_F$. The corresponding boundary conditions, written in terms of the rescaled complex amplitude of the fuel leakage $\tilde{y}^+ = (S+1)\tilde{y}_F^+$, become

$$\bar{r} = -\infty : \tilde{y} = \frac{d\tilde{y}}{d\bar{r}} = 0; \quad \text{and} \quad \bar{r} = +\infty : \tilde{y} - \tilde{y}^+ = \frac{d\tilde{y}}{d\bar{r}} = 0. \tag{4.67}$$

The real coefficient functions

$$\begin{aligned} k(\bar{r}) &= \bar{\Lambda} \exp(-\bar{y} - \bar{\gamma}_O \bar{r})(2\bar{y} + \bar{r} - \bar{y}^2 - \bar{y}\bar{r}), \\ g(\bar{r}) &= \bar{\Lambda}\bar{y}(\bar{y} + \bar{r}) \exp(-\bar{y} - \bar{\gamma}_O \bar{r}), \\ h(\bar{r}) &= -\bar{\Lambda}\bar{y} \exp(-\bar{y} - \bar{\gamma}_O \bar{r}), \end{aligned} \tag{4.68}$$

can be evaluated in terms of the unperturbed solution $\bar{\Lambda} = \mathcal{D}$ and $\bar{y}(\bar{r})$, which in turn depends on the steady fuel leakage $\bar{y}^+$.

The complex eigenvalues $\lambda_1 = \tilde{C}_1 + \lambda_2$ and $\lambda_2 = (S+1)\tilde{C}_2/S$ appearing in Eq. (4.66), which determine from Eq. (4.30) the variations of the canonical Damköhler number

$$\Lambda/\bar{\Lambda} = 1 + \beta\varepsilon e^{i\omega\tau}(\lambda_1 - \gamma_O \lambda_2), \tag{4.69}$$

may be evaluated through

$$\frac{\lambda_1}{\tilde{y}^+} = \frac{\frac{d\tilde{y}_2}{d\bar{r}}(\infty) J_1 - \frac{d\tilde{y}_1}{d\bar{r}}(\infty) J_2}{I_1 J_2 - I_2 J_1} \quad \text{and} \quad \frac{\lambda_2}{\tilde{y}^+} = -\frac{\frac{d\tilde{y}_2}{d\bar{r}}(\infty) I_1 - \frac{d\tilde{y}_1}{d\bar{r}}(\infty) I_2}{I_1 J_2 - I_2 J_1}, \tag{4.70}$$

in terms of any two linearly independent homogeneous solutions $\tilde{y}_{1,2}$ of Eq. (4.66), with

$$I_{1,2} = \int_{-\infty}^{\infty} \tilde{y}_{1,2}(t) g(t) dt \quad \text{and} \quad J_{1,2} = \int_{-\infty}^{\infty} \tilde{y}_{1,2}(t) h(t) dt, \tag{4.71}$$

as obtained from an integration of Eq. (4.66) with application of the appropriate boundary conditions. It may be shown from Eq. (4.66) and its boundary conditions that the ratios in

Eq. (4.70) are real. The values of λ_1 and λ_2 computed in this manner may be used to evaluate the oxygen mass fraction $\tilde{y}_{\rm O}$ and temperature $\tilde{\theta}$ in terms of $\tilde{y}$ from

$$\tilde{y}_{\rm O} = \frac{S}{S+1}\,(\tilde{y}-\lambda_2) \quad \text{and} \quad \tilde{\theta} = \lambda_1 - \tilde{y}, \tag{4.72}$$

obtained from Eq. (4.63). It follows immediately that the boundary values appearing in Eqs. (4.42)–(4.43) take the form shown in Eq. (4.44), needed in integrating the linear equations for the acoustic response of the outer layers. The resulting variation of $\lambda_1/\tilde{y}^+$ and $\lambda_2/\tilde{y}^+$ with the steady fuel leakage $\bar{y}^+$ are shown in Fig. 4.2. The corresponding structure of the inner reactive-diffusive layer is shown in Fig. 4.8 where $\tilde{y}/\tilde{y}^+$ is shown as a function of $\bar{r}$ for the values of $\bar{\Lambda}$ used previously in Fig. 4.7.

Supplement D: Acoustic response of the outer layers for $\beta\varepsilon \ll 1$

Linearization of the conservation equations for the outer problem leads to

$$\begin{aligned}
-T_0\frac{d\tilde{F}_1}{dx} + T_0^{\sigma}\tilde{A}_1 + (\sigma-1)T_0^{\sigma-1}(i\omega+A_0)\tilde{T}_1 &= B_1,\\
-\frac{dA_0}{dx}\tilde{F}_1 + T_0^{\sigma-1}(i\omega+2A_0)\tilde{A}_1 - F_0\frac{d\tilde{A}_1}{dx} - Pr\frac{d^2\tilde{A}_1}{dx^2} + T_0^{\sigma-1}\left([\sigma-1]\frac{A_0^2}{T_0}-\sigma\right)\tilde{T}_1 &= B_2,\\
-\frac{dY_{\rm O0}}{dx}\tilde{F}_1 + i\omega T_0^{\sigma-1}\tilde{Y}_{\rm O1} - F_0\frac{d\tilde{Y}_{\rm O1}}{dx} - \frac{d^2\tilde{Y}_{\rm O1}}{dx^2} &= B_3,\\
-\frac{dY_{\rm F0}}{dx}\tilde{F}_1 + i\omega T_0^{\sigma-1}\tilde{Y}_{\rm F1} - F_0\frac{d\tilde{Y}_{\rm F1}}{dx} - \frac{d^2\tilde{Y}_{\rm F1}}{dx^2} &= B_4,\\
-\frac{dT_0}{dx}\tilde{F}_1 + i\omega T_0^{\sigma-1}\tilde{T}_1 - F_0\frac{d\tilde{T}_1}{dx} - \frac{d^2\tilde{T}_1}{dx^2} &= B_5.
\end{aligned} \tag{4.73}$$

The forcing terms $\boldsymbol{B} = [B_1; B_2; B_3; B_4; B_5]$ on the right-hand side of the above equations are given by

$$\begin{aligned}\boldsymbol{B} = &\left[-T_0^{\sigma}(\mathrm{i}\omega + A_0); T_0^{\sigma-1}\left(\frac{T_0}{\gamma} - A_0^2\right); 0\,; 0\,; \mathrm{i}\omega T_0^{\sigma}\left(\frac{\gamma-1}{\gamma}\right)\right] \\ &+ \left[(\sigma-1)\frac{\mathrm{d}T_0}{\mathrm{d}x}; \frac{\mathrm{d}A_0}{\mathrm{d}x}; \frac{\mathrm{d}Y_{\mathrm{O}0}}{\mathrm{d}x}; \frac{\mathrm{d}Y_{\mathrm{F}0}}{\mathrm{d}x}; \frac{\mathrm{d}T_0}{\mathrm{d}x}\right] T_0^{\sigma-1}\mathrm{i}\omega\tilde{\eta}_1,\end{aligned} \tag{4.74}$$

where the first contribution arises directly through unsteady forcing, whereas the second is due to the motion of the reaction layer, proportional to $\tilde{\eta}_1$. Equations (4.73) are to be integrated with boundary conditions

$$\begin{cases} x = -\infty: \quad \tilde{A}_1 = \tilde{Y}_{\mathrm{F}1} = \tilde{Y}_{\mathrm{O}1} = \tilde{T}_1 - \Theta\frac{\gamma-1}{\gamma} = 0 \\ x = 0^-: \quad \tilde{F}_1 - \tilde{f}_o = \tilde{A}_1 - \tilde{a}_o = \tilde{Y}_{\mathrm{F}1} = \tilde{Y}_{\mathrm{O}1} - \tilde{y}_{\mathrm{O}}^- = \tilde{T}_1 - \frac{q}{S+1}\tilde{\theta}^- = 0 \end{cases} \tag{4.75}$$

on the fuel side and

$$\begin{cases} x = 0^+: \quad \tilde{F}_1 - \tilde{f}_o = \tilde{A}_1 - \tilde{a}_o = \tilde{Y}_{\mathrm{F}1} - \tilde{y}_{\mathrm{F}}^+ = \tilde{Y}_{\mathrm{O}1} - \tilde{y}_{\mathrm{O}}^+ = \tilde{T}_1 - \frac{q}{S+1}\tilde{\theta}^+ = 0 \\ x = +\infty: \quad \tilde{A}_1 = \tilde{Y}_{\mathrm{F}1} = \tilde{Y}_{\mathrm{O}1} = \tilde{T}_1 - \frac{\gamma-1}{\gamma} = 0 \end{cases} \tag{4.76}$$

on the oxidizer side. The relationship $\tilde{F}_1 = \tilde{\eta}_1(\mathrm{d}F_0/\mathrm{d}x)$ at $x = -\eta_0$, obtained from Eq. (4.36), together with the jump conditions given in Eq. (4.45), close the problem by providing four equations for determining $\tilde{f}_o$, $\tilde{a}_o$, $\tilde{\eta}_1$ and $\tilde{y}^+$, with the latter used in Eq. (4.44) together with the two values $\lambda_1/\tilde{y}^+$ and $\lambda_2/\tilde{y}^+$ obtained from the curves in Fig. 4.2, needed to evaluate the flame values appearing in the boundary conditions in Eqs. (4.75) and (4.76). In this way, numerical integration of the linear system served to determine the ten unknown real functions involved.

This chapter, in full, has been published in *AIAA Journal* titled "Acoustic response of near-equilibrium diffusion flames with large activation energies", by A. D. Weiss, A. L. Sánchez and F. A. Williams (2019) 57, 2933-2945. The dissertation author is the primary investigator

in this publication. The input of Professor Amable Liñán on different aspects of this research, especially the suggestion of an attached-flame coordinate x, are gratefully acknowledged.

Bibliography

[1] Adam D Weiss, Wilfried Coenen, Antonio L Sanchez, and Forman A Williams. The acoustic response of burke-schumann counterflow flames. *Combustion and Flame*, 192:25–34, 2018.

[2] JS Kim and F A Williams. Contribution of strained diffusion flames to acoustic pressure response. *Combustion and Flame*, 98(3):279–299, 1994.

[3] Amable Liñán. The asymptotic structure of counterflow diffusion flames for large activation energies. *Acta Astronautica*, 1(7):1007–1039, 1974.

[4] Amable Liñán, Daniel Martínez-Ruiz, Marcos Vera, and Antonio L Sánchez. The large-activation-energy analysis of extinction of counterflow diffusion flames with non-unity lewis numbers of the fuel. *Combustion and Flame*, 175:91–106, 2017.

[5] A D Weiss, W Coenen, and A L Sánchez. Aerodynamics of planar counterflowing jets. *Journal of Fluid Mechanics*, 821:1–30, 2017.

[6] A. D Weiss, M Vera, A Liñán, A. L Sánchez, and F. A Williams. A novel formulation for unsteady counterflow flames using a thermal-conductivity weighted coordinate. *Combustion Theory and Modelling.*, 22(1):185 – 201, 2018.

[7] Paul A Libby, Amable Liñán, and Forman A Williams. Strained premixed laminar flames with nonunity lewis numbers. *Combustion Science and Technology*, 34(1-6):257–293, 1983.

[8] Forman A Williams. Combustion theory, (1985). *Cummings Publ. Co*, 1985.

[9] AC Zambon and HK Chelliah. Self-sustained acoustic-wave interactions with counterflow flames. *Journal of Fluid Mechanics*, 560:249–278, 2006.

[10] M Tyagi, SR Chakravarthy, and RI Sujith. Unsteady combustion response of a ducted non-premixed flame and acoustic coupling. *Combustion Theory and Modelling*, 11(2):205–226, 2007.

[11] CH Sohn and SH Chung. Effect of pressure on the extinction, acoustic pressure response, and no formation in diluted hydrogen–air diffusion flames. *Combustion and Flame*, 121(1-2):288–300, 2000.

[12] Chae-Hoon Sohn. Unsteady analysis of acoustic pressure response in n2 diluted h2 and air diffusion flames. *Combustion and Flame*, 128(1-2):111–120, 2002.

Chapter 5

Accuracies of reduced mechanisms for predicting acoustic combustion instabilities

There is continuing interest in developing methods for computationally predicting combustion instabilities in liquid-propellant rockets and other engines [1]. One relevant aspect of such investigations is to consider acoustic amplification rates through use of the Rayleigh index [2, 3]

$$R = \frac{1}{\tau} \int_0^{\tau} \tilde{p} Q \, \mathrm{d}t \tag{5.1}$$

where $\tilde{p}$ is the oscillatory component of the pressure, Q is the oscillatory component of the chemical heat-release rate, and τ is the period of oscillation. The present chapter employs R as a vehicle for addressing inaccuracies that result from introducing reduced chemical-kinetic mechanisms in such computations, as often is done because of the excessive computer time required with detailed chemistry. This can be accomplished in the context of a non-premixed counterflow configuration, which often has been selected in studying combustion instabilities, with model one-step Arrhenius chemistry [4–6], with one-step [7] and two-step [8] approximations for methane-oxygen systems, and with detailed chemistry for hydrogen-oxygen systems [9, 10], the propellant combination considered here. For realistic combustion chambers DNS is impractical,

necessitating LES, often performed with flamelet subgrids, following suggestions of Peters [11], and when that is done the counterflow strain rates A that enter the analysis are larger near injectors than farther downstream, consistent with stability-diagram correlations [12]. The reciprocal of the product of A and a chemical heat-release time is a Damköhler number, Da, which becomes small, tending to lead to extinction, as A increases, which motivates calculations of how R changes as Da is decreased.

Since counterflow flamelet response calculations with detailed chemistry become increasingly time-consuming as the size of the chemical mechanism increases, there is interest in introducing systematic reductions through application of chemical-kinetic steady-state approximations to appropriate reaction intermediaries. That could be especially helpful for hydrocarbon-oxygen systems, for example, for which four-step approximations are available [13, 14]. To obtain an indication of magnitudes of resulting errors in R and of how they depend on Da, computations for hydrogen-air flames with equal feed-stream temperatures $T = 298\,K$ were made with a 12-step detailed mechanism and a 2-step systematically reduced mechanism. This 12-step mechanism, shown in Table 2 of [15], involves 8 chemical species H_2, O_2, H_2O, H, HO_2, H_2O_2, OH, and O, and it has been reasoned to accurately predict structures of a wide range of premixed and nonpremixed hydrogen flames. Imposing the steady-state assumption for the last four cited radical species leads to a two-step mechanism, derived and applied in [16, 17], represented by the overall chain-branching and termination reactions $3H_2 + O_2 \rightleftharpoons 2H_2O + 2H$ and $H + H + M \rightleftharpoons H_2 + M$, respectively. The two steps proceed with global rates written explicitly in Eqs. (9)–(11), (14) and (16) of [15].

The asymptotic analyses [4–6], drawn on the basis of one-step model chemistry, described the dependence of the Rayleigh index R on the Damköhler number Da, revealing in particular a stronger dependence near extinction as compared to the moderate response seen for robust flames near equilibrium. Since the amplification rate is highest near extinction (where the strain is large) and decreases towards equilibrium (where the strain is low), two strain rates are selected here in

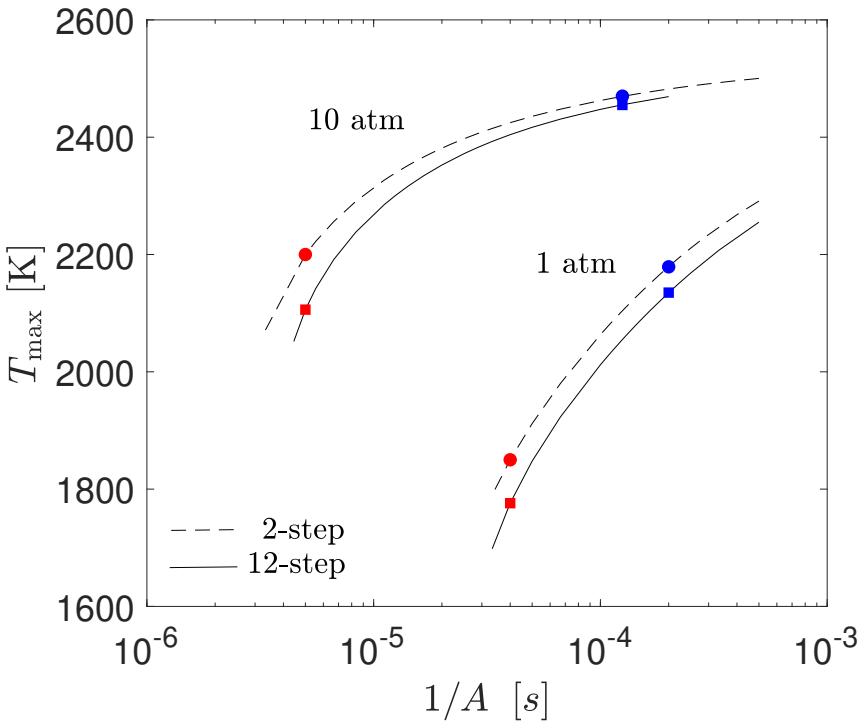

Figure 5.1: The variation with the reciprocal of the strain rate $1/A$ of the maximum temperature in a hydrogen-air planar counterflow diffusion flame with equal feed-stream temperatures $T = 298\,\mathrm{K}$ as obtained from detailed chemistry (Table 2. of [15]) (solid curves) and with the 2-step mechanism [16, 17] (dashed curves), at 1 atm and 10 atm. Red and blue markers on each curve represent near-extinction and near-equilibrium conditions, respectively, to be used in unsteady computations for the production of Fig. 5.2.

presenting results for R, other values of A providing values that lie in between these two limiting cases. The specific choice employed is based on the extinction curves presented in Fig. 5.1 shown dimensionally as the maximum temperature as a function of the reciprocal of the strain rate, computed for steady hydrogen-air diffusion flames in the planar counterflow configuration with equal feed-stream temperatures $T = 298$ K. The pressure in a steady counterflow diffusion flame is known to affect the extinction strain rate since it plays a fundamental role in determining the chemical rates, notably influencing radical recombination taking place through three-body reactions [9]. Because of this, and because typical combustors operate at pressures above atmospheric, results in Fig. 5.1 are presented for both $p = 1\,\mathrm{atm}$ and $p = 10\,\mathrm{atm}$. In each case, the solid curve denotes the results of computations employing the detailed mechanism whereas

the dashed curve corresponds to those using the 2-step systematically reduced mechanism.

As can be seen from the figure, the 2-step mechanism overestimates the maximum temperature, with errors on the order of 50 K (a few percent) for $p = 1\,\text{atm}$ and 100 K near extinction at $p = 10\,\text{atm}$, although, because of the increase in the maximum temperature with pressure, the relative errors remain comparable, on the order of a few percent. These trends have been identified previously [16]. For $p = 1\,\text{atm}$, the values $A = 5,000\,s^{-1}$ and $A = 25,000\,s^{-1}$, labeled with markers, were selected as representative of near-equilibrium and near-extinction conditions, respectively, to be used below in presenting unsteady results. Similarly, the values $A = 8,000\,s^{-1}$ and $A = 200,000\,s^{-1}$ were selected as representative near-equilibrium and near-extinction conditions, respectively, for $p = 10\,\text{atm}$. These near-extinction values were chosen to be approximately 70% of the extinction strain rate computed with the detailed mechanism.

The compact formulation [18], developed for unsteady planar mixing layers in the counterflow configuration subject to unsteady pressure variations, was used for the calculation of R. These computations were performed for each of the strain conditions listed above with the amplitude of the oscillatory component of the pressure set to 1% of the steady value, that is $|\tilde{p}| = 0.01 \times 1\,\text{atm}$ or $|\tilde{p}| = 0.01 \times 10\,\text{atm}$. A wide range of oscillatory frequencies $\omega = 2\pi/\tau$ were used in the computations. For a given frequency, the integration provides the heat-release rate $Q(t)$, with time-average Q_m, allowing for the computation of R with aid of Eq. (5.1). By varying the frequency between integrations, the curves in Fig. 5.2, expressed in a normalized form, were produced. It should be noted that, with typical acoustic frequencies ω on the order of 10^3 to 10^4 Hz for practical combustors, different portions of the curves shown in Fig. 5.2 become relevant when comparing different strain rates. For example, for the near-equilibrium cases ($A = 5,000\,s^{-1}$ and $A = 8,000\,s^{-1}$ for $p = 1\,\text{atm}$ and $p = 10\,\text{atm}$, respectively) results with $\omega/A \sim 1$ are encountered in practice, but for the larger strain rates of the near-extinction cases, quasisteady results obtained for $\omega/A \ll 1$ become more relevant.

As is apparent from the blue curves in Fig. 5.2 (a), for diffusion-controlled flames near

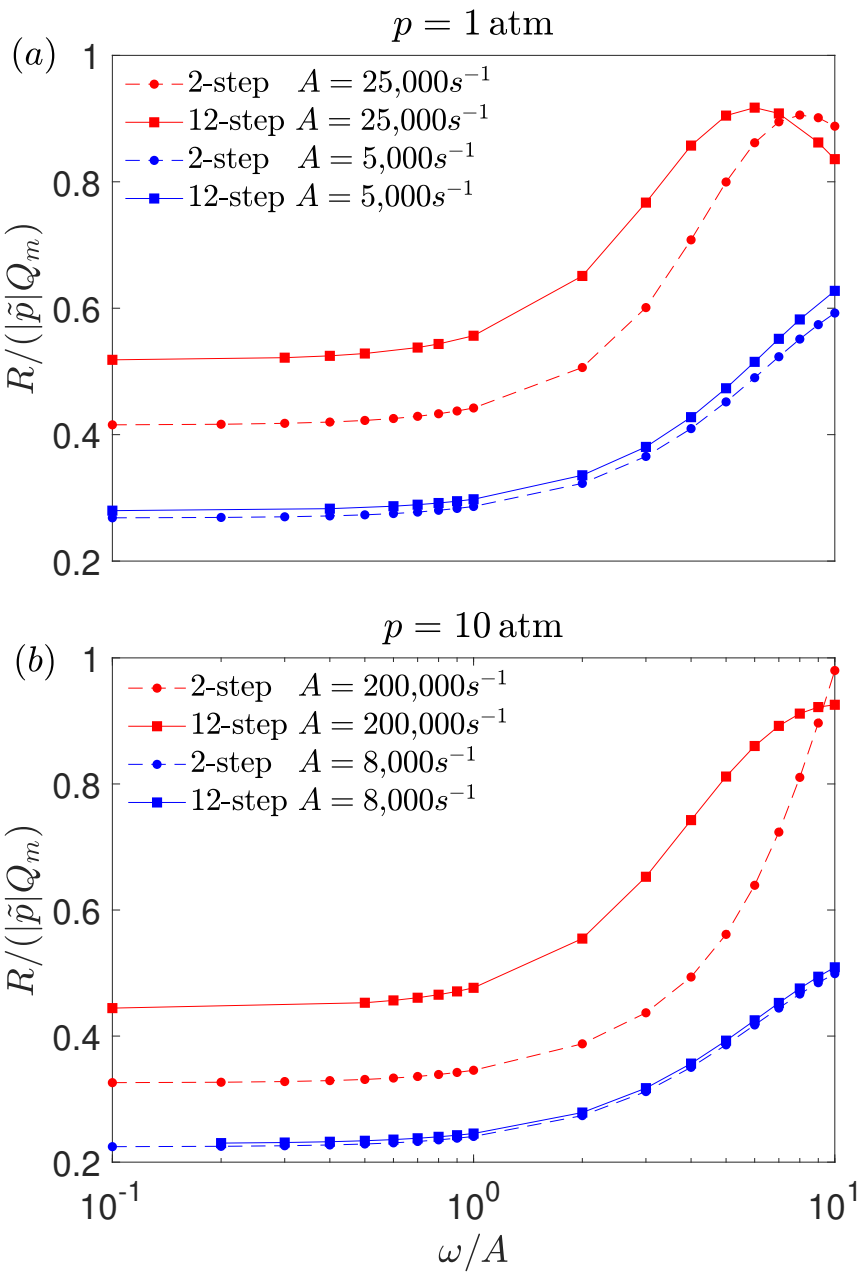

Figure 5.2: The variation with reduced acoustic frequency ω/A of the Rayleigh index R (scaled with the amplitude of the pressure variation $|\tilde{p}| = 0.01 \times p$ and the mean heat-release rate Q_m) for strained hydrogen-air flames at $T = 298\,K$ as computed from (5.1) using the 12-step mechanism (solid curves) and the 2-step mechanism (dashed curves) for different strain and pressure conditions.

equilibrium and at normal atmospheric pressure, the reduced mechanism is able to accurately predict the Rayleigh index with errors that do not exceed more than 4% over the range of frequencies of interest. The error is seen to increase (slightly) as ω/A increases. The increase in the Rayleigh index R for increasing strain A, predicted by [4–6], is also captured by the two-step mechanism, although the increase is underpredicted over the majority of frequencies considered, as is evident from comparison of the red curves in Fig. 5.2 (a). These errors are on the order of 20% for the near-extinction case considered here. Fig. 5.2 (b), for $p = 10\,\text{atm}$ demonstrates that similar conclusions hold at elevated pressures. Here the reduced mechanism reproduces near-equilibrium results with excellent accuracy throughout the range shown, exhibiting errors around 1% over these frequencies. For near-extinction conditions, the reduced mechanism again substantially underpredicts the Rayleigh index, here with errors on the order of 25%, larger than those at normal atmospheric conditions.

The conservation equations for chemical species have accumulation, convective-diffusive transport, and chemical consumption and production terms. For the non-premixed counterflow configuration under consideration here, these rates are characterized by the reciprocal times ω, A, $1/t_c$ and $1/t_p$, respectively, where t_c and t_p are the characteristic chemical consumption and production times. The steady-state approximation is strictly valid for radicals when $\omega, A \ll 1/t_c \sim 1/t_p$, ensuring that accumulation and convective-diffusive transport can be neglected in comparison with chemical production/consumption in the radical-species balance. For the lower strain rates in Fig. 5.2, there is a hint of the first of these effects in the curves for $p = 1\,\text{atm}$, where discrepancies tend to increase towards the right-hand edge of the plot; for all strain rates selected, this disagreement occurs mainly to the right of the range of conditions shown. The second effect, on the other hand, is evident at both pressures in Fig. 5.2, the differences being appreciably larger at the higher strain rates. It is curious, in a sense, that the steady-state approximation deteriorates as extinction is approached, since, for steadily propagating unstrained premixed flames, the smaller radical concentrations near flammability limits (at which extinction

occurs) favor improved accuracy of chemical-kinetic steady states there, as some of our previous publications have shown [19–21], leading to useful predictions of extinction limits, there being no externally imposed time scale independent of the chemistry. The reason for this difference is the strong variation of temperature and radical concentration with the strain rate near strain-induced extinction, as occurs in the counterflow configuration, an effect absent in unstrained flames.

In general, then, while systematically reduced mechanisms reduce computation times, to increasing extents as detailed mechanisms become larger, if applying them for acoustic-response estimates they may be expected to become increasingly inaccurate as near-extinction conditions are approached and amplification rates increase, corresponding to near-injector locations where strain rates are high.

This chapter, in full, has been published in *Combustion and Flame* titled "Accuracies of reduced mechanisms for predicting acoustic combustion instabilities", by A. D. Weiss, A. L. Sánchez and F. A. Williams (2019) 209, 405-407. The dissertation author is the primary investigator in this publication.

Bibliography

[1] William A Sirignano. Driving mechanisms for combustion instability. *Combust Sci Technol*, 187:162–205, 2015.

[2] Abbott Allen Putnam. *Combustion-driven oscillations in industry*. Elsevier Publishing Company, 1971.

[3] KR McManus, Thierry Poinsot, and Sébastien M Candel. A review of active control of combustion instabilities. *Prog Energ Combust*, 19:1–29, 1993.

[4] JS Kim and F A Williams. Contribution of strained diffusion flames to acoustic pressure response. *Combust Flame*, 98:279–299, 1994.

[5] Adam D Weiss, Wilfried Coenen, Antonio L Sanchez, and Forman A Williams. The acoustic response of burke-schumann counterflow flames. *Combust Flame*, 192:25–34, 2018.

[6] Adam D Weiss, Antonio L Sánchez, and Forman A Williams. Acoustic response of near-equilibrium diffusion flames with large activation energies. *AIAA J*, 57:, 2019.

[7] AC Zambon and HK Chelliah. Self-sustained acoustic-wave interactions with counterflow flames. *J Fluid Mech*, 560:249–278, 2006.

[8] AC Zambon and HK Chelliah. Acoustic-wave interactions with counterflow single-and twin-premixed flames: Finite-rate kinetics, heat release and phase effects. *Proc Combust Inst*, 31:1247–1255, 2007.

[9] CH Sohn and SH Chung. Effect of pressure on the extinction, acoustic pressure response, and NO formation in diluted hydrogen–air diffusion flames. *Combust Flame*, 121:288–300, 2000.

[10] Chae-Hoon Sohn. Unsteady analysis of acoustic pressure response in N2 diluted H2 and air diffusion flames. *Combust Flame*, 128:111–120, 2002.

[11] Norbert Peters. *Turbulent combustion*. Cambridge university press, 2000.

[12] JS Kim and FA Williams. Acoustic-instability boundaries in liquid-propellant rockets-theoretical explanation of empirical correlation. *J Propul Power*, 12:621–624, 1996.

[13] Mitchell D Smooke. *Reduced kinetic mechanisms and asymptotic approximations for methane-air flames: a topical volume*. Springer, 1991.

[14] M Bui-Pham and K Seshadri. Comparison between experimental measurements and numerical calculations of the structure of heptane-air diffusion flames. *Combust Sci Technol*, 79:293–310, 1991.

[15] Antonio L Sánchez and Forman A Williams. Recent advances in understanding of flammability characteristics of hydrogen. *Prog Energ Combust*, 41:1–55, 2014.

[16] Pierre Boivin, Carmen Jiménez, Antonio L Sánchez, and Forman A Williams. An explicit reduced mechanism for H2–air combustion. *Proc Combust Inst*, 33:517–523, 2011.

[17] Pierre Boivin, Antonio L Sánchez, and Forman A Williams. Explicit analytic prediction for hydrogen–oxygen ignition times at temperatures below crossover. *Combust Flame*, 159:748–752, 2012.

[18] Adam D Weiss, Marcos Vera, Amable Liñán, Antonio L Sánchez, and Forman A Williams. A novel formulation for unsteady counterflow flames using a thermal-conductivity-weighted coordinate. *Combust Theor Model*, 22:185–201, 2018.

[19] Daniel Fernández-Galisteo, A L Sánchez, A Liñán, and F A Williams. One-step reduced kinetics for lean hydrogen–air deflagration. *Combust Flame*, 156:985–996, 2009.

[20] Daniel Fernández-Galisteo, A L Sánchez, A Liñán, and F A Williams. The hydrogen–air burning rate near the lean flammability limit. *Combust Theor Model*, 13:741–761, 2009.

[21] Daniel Fernández-Galisteo, Adam D Weiss, Antonio L Sánchez, and Forman A Williams. A

one-step reduced mechanism for near-limit hydrogen combustion with general stoichiometry. *Combust Flame*, 208:1–4, 2019.

Part II

Swirling flows induced by buoyancy

Brief overview of Part II

Part II investigates the steady axisymmetric structure of the cold boundary-layer flow surrounding fire whirls developing over localized fuel sources lying on a horizontal surface. The inviscid swirling motion found outside the boundary layer, driven by the entrainment of the buoyant turbulent plume of hot combustion products that develops above the fire, is described by an irrotational solution, obtained by combining Taylor's self-similar solution for the motion in the axial plane with the azimuthal motion induced by a line vortex of circulation $2\pi\Gamma$. The development of the boundary layer from a prescribed radial location is determined by numerical integration for different swirl levels, measured by the value of the radial-to-azimuthal velocity ratio σ at the initial radial location. As in the case $\sigma = 0$, treated in the seminal boundary-layer analysis of Burggraf *et. al* (1971), the pressure gradient associated with the centripetal acceleration of the inviscid flow is seen to generate a pronounced radial inflow. Specific attention is given to the terminal shape of the boundary-layer velocity near the axis, which displays a three-layered structure that is described by matched asymptotic expansions. The resulting composite expansion, dependent on the level of ambient swirl through the parameter σ, is employed as boundary condition to describe the deflection of the boundary-layer flow near the axis to form a vertical swirl jet. Numerical solutions of the resulting non-slender collision region for different values of σ are presented both for inviscid flow and for viscous flow with moderately large values of the controlling Reynolds number Γ/ν. The velocity description provided is useful in mathematical formulations of localized fire-whirl flows, providing consistent boundary conditions accounting for the ambient swirl level.

Chapter 6

A model for the boundary layer surrounding fire whirls

6.1 Introduction

Fire whirls are vortical columns with a concentrated burning core. Observed lengths vary from about 0.1 m in small experiments to tens of meters in wildland fires. As stated in the recent review paper by [1], despite significant research efforts, the current understanding of the flow structure and dynamics of fire whirls, including the reasons for their dramatic flame-lengthening effect and increased burning rate, is far from complete. The present paper contributes to the needed understanding by investigating the steady axisymmetric structure of the cold outer flow surrounding fire whirls developing over localized fuel sources lying on a horizontal surface, a configuration shown schematically in figure 6.1. Attention will be directed to the development of the important near-wall boundary layer and the collision consequent to its radially inward flow component in the vicinity of the fire whirl. The structures of the plume and of the interior of the fire whirl depicted in the figure are not analyzed here.

The flow of cold air surrounding the fire whirl, at distances much larger than the size of

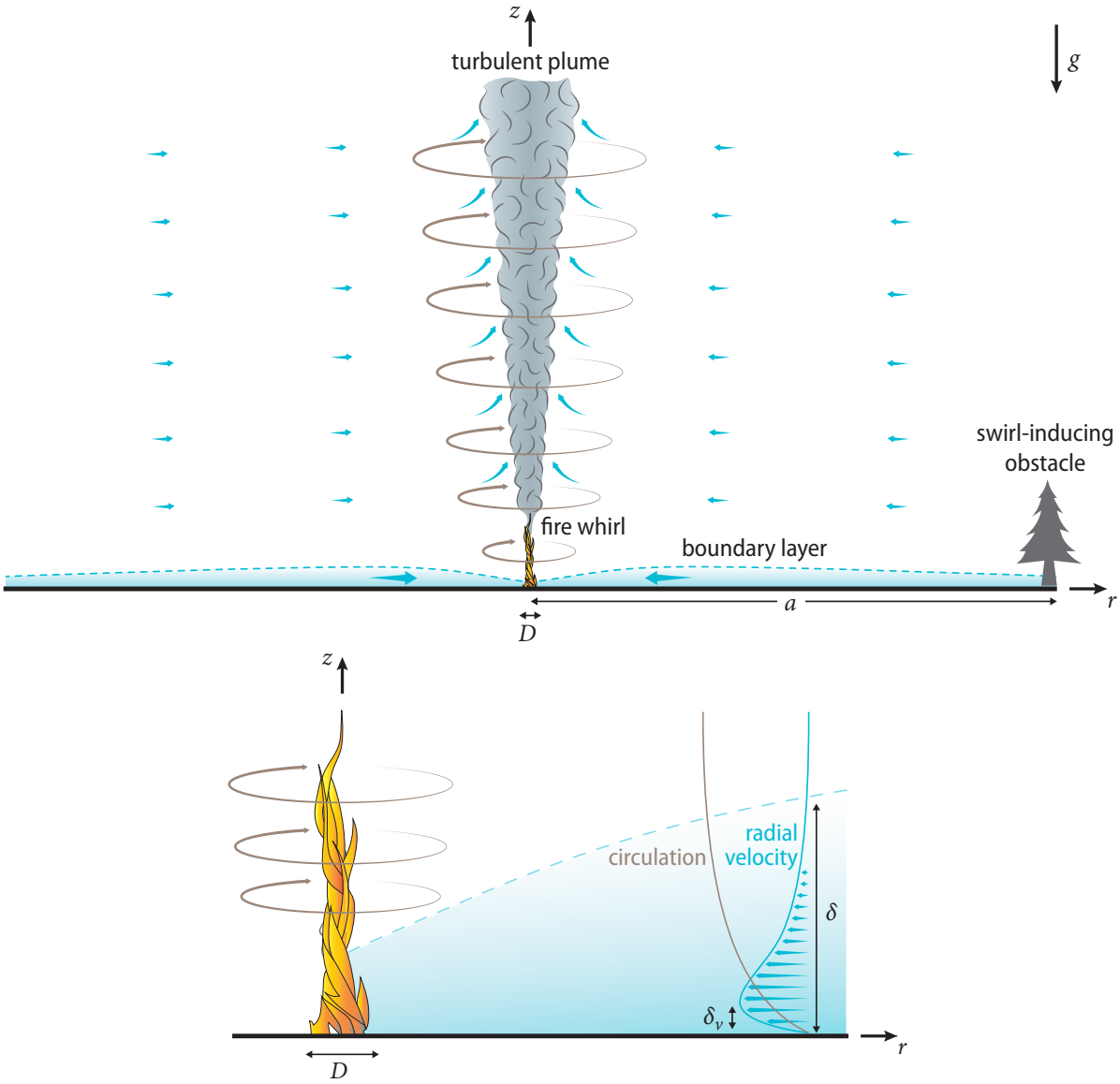

Figure 6.1: General overview.

the fuel source (e.g. the diameter D of the fuel pool in liquid-pool fires), ultimately is driven by the buoyant turbulent plume of hot combustion products that develops above the fire. As revealed by detailed experimental measurements [2], the temperature in fire-whirl plumes decays exponentially with radial distance from the axis towards the ambient value, so that density variations are only encountered near the axis, while the flow induced outside by the entrainment of the turbulent plume has constant density. Since the volumetric entrainment rate per unit length increases with the two thirds power of the vertical distance [3], the effect of the slender plume on the outer flow is that of a semi-infinite line sink of varying strength, resulting in a self-similar potential solution described by [4]. In the presence of obstacles, this meridional flow may be deflected, introducing an azimuthal velocity component, a fundamental ingredient in the development of fire whirls [1] and other naturally occurring vortex phenomena, such as tornadoes [5] and dust devils [6]. In wildland fires, for example, flow deflections beyond those associated with the circulation in weather patterns may be the result of flow interactions with topological features or tall vegetation, while in laboratory experiments on fire whirls and dust devils the deflection is achieved by surrounding the experimental setup with rotating circular screens [7], thin vertical flow vanes placed at a nonzero angle with respect to the radial direction [8, 9], or offset cylindrical or planar walls that leave small vertical slits for the tangential inflow of the incoming air [10].

The specific characteristics of the resulting inviscid swirling flow depend on the flow-deflection mechanism. For example, while the flow deflection by vertical vanes can be expected to be largely irrotational, the use of rotating circular screens may introduce a significant amount of azimuthal vorticity, which is not considered in the present analysis. In the present investigation, as in some laboratory experiments [9], the distance a at which the circulation is induced is large compared with the flame height enhanced by whirl augmentation, so that the Taylor solution, applicable for turbulent plumes with sufficiently weak swirl, can be employed. Strong-swirl solutions that would generate different inviscid external flow fields at lower altitudes, which then

would require a different analysis if a were smaller, are not available. The production of swirl by deflection of the flow entrained by the turbulent plume is a distinctive characteristic of fire whirls, not present in swirl combustors, for instance, where the swirl is imparted prior to injection into the combustion chamber [11, 12], leading to flow structures that are markedly different from those analyzed here.

The presence of swirl in the flow surrounding the fire whirl is accompanied by an increased radial pressure gradient, needed to balance the centripetal acceleration. Viscous forces decelerate the swirling motion in a near-wall boundary layer, where the imposed pressure gradient generates an overshoot of the radial inflow, which becomes more pronounced on approaching the axis. This flow feature was investigated in the seminal work [13] for the specific case of a boundary layer on a fixed, non-rotating circular disk of radius a whose axis is concentric with a potential vortex with circulation $2\pi\Gamma$. Their analysis clarified in particular the structure of the terminal velocity profile found at small radial distances $r^* \ll a$, including a near-wall viscous sublayer of shrinking thickness $(\nu/\Gamma)^{1/2} r^*$ and a nearly inviscid layer of finite thickness $\delta = (\nu/\Gamma)^{1/2} a$, with ν representing the kinematic viscosity.

The boundary layer surrounding a fire whirl depends on the outer inviscid flow through its near-wall radial distributions of both azimuthal and radial velocity. To clarify the effect of the latter on the boundary-layer development, the previous potential-vortex analysis [13], in which the flow outside the boundary layer was purely azimuthal, is extended here by using as a model for the inviscid outer flow the potential solution obtained by combining linearly Taylor's potential solution [4] for the flow in the axial plane with a potential vortex for the azimuthal motion. Numerical integrations of the boundary-layer equations are used to describe the development of the boundary layer for selected radial-to-azimuthal velocity ratios. A consistent asymptotic description is given for the terminal velocity profiles at the axis, whose structure includes a thick external layer, additional to the two layers identified earlier by [13], which is needed to describe the transition to Taylor's radial flow. A composite expansion combining the results of the

three layers in a single expression is developed for the profiles of radial and azimuthal velocity, providing an accurate description for the flow approaching the base of the fire whirl.

As in the potential-vortex analysis [13], the radial mass flux carried by the wall boundary layer tends to a finite value on approaching the axis. The subsequent boundary-layer collision leads to the upward deflection of the flow in a nonslender region scaling with the characteristic near-axis boundary-layer thickness $\delta = (\nu/\Gamma)^{1/2}a$. Similar nonslender collision regions have been found in other buoyancy-driven flows, for instance in free convection from a heated sphere, where the eruption of the fluid into the plume above the sphere is the result of the collision of the boundary layer at the upper stagnation point, as described by [14]. Because of its relevance in connection with tornados, its inviscid structure has been investigated in the past, using as lateral boundary condition the velocity profile induced by a potential vortex [15]. Additional results are presented below for fire whirls, with results given for different values of the ambient swirl, including profiles of vertical velocity for the deflected stream, which are ultimately responsible for the locally observed lengthening of fire-whirl flames. Furthermore, the validity of the inviscid description is critically assessed by investigating the accompanying boundary layer that develops near the wall in the collision region. Although boundary-layer separation is found to occur in all cases at a finite distance from the axis, additional integrations of the Navier-Stokes equations for moderately large values of the relevant Reynolds number Γ/ν reveal that the boundary layer reattaches before reaching the axis to form a slender recirculating bubble, so that the inviscid description remains largely valid.

6.2 Boundary-layer development

6.2.1 Preliminary considerations

The cold flow surrounding fire whirls, to be described using cylindrical polar coordinates (r^*, θ, z^*) and associated velocity components (u^*, v^*, w^*), is induced by the entrainment of

the turbulent plume that extends vertically above the flame along the axis of symmetry. The volumetric entrainment rate per unit length, taken from investigations free from fire-whirl swirl, increases with the two thirds power of the vertical distance z^* according to $\Phi = 2\pi C B^{1/3} z^{*2/3}$, where B is the specific buoyancy flux [3] and C is a dimensionless factor, which approximately assumes the value $C = 0.041$, as suggested by experimental results [16, 17]. Correspondingly, the flow induced in the axial plane has velocities decaying with the radial distance according to $C(B/r^*)^{1/3}$. For $r^* \gg [\nu/(CB^{1/3})]^{3/2}$ the associated Reynolds number $CB^{1/3} r^{*2/3}/\nu$ is large, resulting in nearly inviscid motion, which, in the absence of swirl, is described by a self-similar potential solution that is due to [4]. The corresponding slip velocity at the wall is given by

$$u_w^* = -A_T C (B/r^*)^{1/3}, \tag{6.1}$$

involving the numerical factor

$$A_T = \frac{4(2)^{1/3}\pi^2}{3\Gamma^3(1/3)} \simeq 0.8624, \tag{6.2}$$

where Γ denotes the Gamma function. The potential solution fails in the boundary layer, where the radial velocity, also self-similar, is given by $u^*/u_w^* = f_{\mathrm{T}}'$ in terms of the derivative of the reduced stream function $f_{\mathrm{T}}(\varsigma)$, a function of the rescaled vertical distance $\varsigma = (A_T C B^{1/3}/\nu)^{1/2} r^{*-2/3} z^*$ determined from the boundary-value problem

$$f_{\mathrm{T}}''' - \frac{4}{3} f_{\mathrm{T}} f_{\mathrm{T}}'' + \frac{1}{3}(1 - f_{\mathrm{T}}'^2) = 0; \quad f_{\mathrm{T}}(0) = f_{\mathrm{T}}'(0) = f_{\mathrm{T}}'(\infty) - 1 = 0, \tag{6.3}$$

the subscript T referring to the boundary layer accompanying Taylor's potential flow. In the notation employed throughout the paper the prime denotes differentiation of functions of one variable (e.g. in the above description, it represents differentiation with respect to the self-similar coordinate ς). It is worth mentioning that the flow structure surrounding turbulent plumes, relevant

to fire whirls, is fundamentally different from that surrounding laminar plumes, characterized by small entrainment rates $\Phi \sim \nu$ and associated flow Reynolds numbers of order unity, the case analyzed by [18], who found an exact self-similar solution of the first kind for the swirl-free flow in the axial plane. As shown recently by [19], the accompanying circulation in this viscous case is described by a self-similar solution of the second kind.

As previously mentioned, the three-dimensional inviscid motion surrounding fire whirls is affected by the manner in which swirl is imparted to the flow. Instead of focusing on a specific configuration, for generality in the following analysis the inviscid flow outside the boundary layer will be described using as a canonical model the exact axisymmetric solution of the Euler equations resulting from combining Taylor's potential solution for the meridional flow and a line vortex of circulation $2\pi\Gamma$ for the azimuthal flow. Correspondingly, at the outer edge of the boundary layer the radial velocity approaches the value given in (6.1) while the azimuthal component approaches the value

$$v_w^* = \Gamma / r^*. \tag{6.4}$$

The presence of swirl alters the flow across the boundary layer, so that, even for this model problem, a self-similar description, which is available in the absence of swirl, as described above in (6.3), does not exist when $v_w^* \neq 0$. The fundamental lack of flow similarity can be illustrated by considering the flow at large radial distances, where the radial motion becomes dominant, as can be inferred from the different decay rates present in (6.1) and (6.4). Correspondingly, as $r^* \to \infty$ the self-similar function $u^*/u_w^* = f_{\mathrm{T}}'(\varsigma)$ appears to be the appropriate leading-order representation for the radial velocity across the boundary layer, while the azimuthal velocity $v^* = \Gamma g_{\mathrm{T}}(\varsigma)/r^*$ should be determined by the accompanying problem

$$g_{\mathrm{T}}'' - \frac{4}{3} f_{\mathrm{T}} g_{\mathrm{T}}' = 0; \quad g_{\mathrm{T}}(0) = g_{\mathrm{T}}(\infty) - 1 = 0, \tag{6.5}$$

obtained at leading order from the axisymmetric boundary-layer form of the azimuthal momentum

equation. This presumed self-similar structure fails, however, because the last problem has no solution, which can be seen by investigating the behavior as $\varsigma \to \infty$ of the first integral $g_{\mathrm{T}}' = g_{\mathrm{T}}'(0)\exp\left[\frac{4}{3}\int_0^{\varsigma} f_{\mathrm{T}}\mathrm{d}\tilde{\varsigma}\right]$ to show that $g_{\mathrm{T}}'(0) = 0$ to avoid divergence, so that the only possible solution is $g_{\mathrm{T}} =$ constant, which cannot satisfy simultaneously both boundary conditions $g_{\mathrm{T}}(0) = g_{\mathrm{T}}(\infty) - 1 = 0$; this lack of similarity is also encountered when the outer flow is driven solely by a potential vortex [20] (see also [21] for a discussion of boundary-layer selfsimilarity when the outer azimuthal velocity varies with a general power of the radial distance).

Progress in understanding can be achieved by investigating the development of the boundary layer from a given radial location, as was done in the previous analysis of the boundary layer on a disk of radius a [13]. The same approach is to be considered below, with the ratio of the radial-to-azimuthal velocity

$$\sigma = \frac{u_w^*(a)}{v_w^*(a)} \tag{6.6}$$

at the disk edge arising as the only controlling parameter in the resulting description. This idealized disk problem may, for example, be considered to provide an approximate description of the main features of the boundary-layer flow in the region between the fire and swirl-producing vanes at radius a in laboratory fire-whirl experiments, with the velocity ratio σ being directly related to the angle of inclination of the vanes. In particular, the terminal velocity profile at $r^* \ll a$ can be anticipated to provide a realistic representation for the flow surrounding localized fire whirls, with the parameter σ measuring the level of swirl introduced by the collective effect of the flow-deflecting obstacles, located at radial distances much larger than the characteristic size of the fuel source feeding the fire.

6.2.2 Problem formulation

Following [13], the problem is scaled using a and

$$\delta = \frac{a}{\sqrt{Re}} \tag{6.7}$$

for the radial and axial coordinates, with

$$Re = \frac{\Gamma}{\nu} \tag{6.8}$$

representing the relevant Reynolds number. Correspondingly, the azimuthal and radial velocity components u^* and v^* are scaled with Γ/a, corresponding to a radial pressure gradient scaling with $\rho\Gamma^2/a^3$ (ρ representing the density), while the axial component w^* is scaled with $(\Gamma/a)/\sqrt{Re}$, resulting in the dimensionless variables

$$r = \frac{r^*}{a}, \quad z = \frac{z^*}{\delta}, \quad u = \frac{u^*}{\Gamma/a}, \quad v = \frac{v^*}{\Gamma/a}, \quad w = \frac{w^*}{\Gamma/(a\sqrt{Re})}. \tag{6.9}$$

Neglecting terms of order $Re^{-2} \ll 1$ reduces the conservation equations, written in their steady axisymmetric form for a constant-density fluid, to their boundary-layer form

$$u\frac{\partial u}{\partial r} + w\frac{\partial u}{\partial z} - \frac{v^2}{r} = -\frac{\sigma^2}{3r^{5/3}} - \frac{1}{r^3} + \frac{\partial^2 u}{\partial z^2}, \tag{6.10}$$

$$u\frac{\partial}{\partial r}(rv) + w\frac{\partial}{\partial z}(rv) = \frac{\partial^2}{\partial z^2}(rv), \tag{6.11}$$

$$\frac{\partial}{\partial r}(ru) + \frac{\partial}{\partial z}(rw) = 0. \tag{6.12}$$

The first two terms on the right-hand side of (6.10) arise from the radial pressure gradients imposed by the external Taylor and potential-vortex flows, respectively. These equations are to be

integrated for decreasing values of r with the boundary conditions

$$u \to -\sigma r^{-1/3}, \quad v \to \frac{1}{r} \quad \text{as} \quad z \to \infty \tag{6.13}$$

and

$$u = v = w = 0 \quad \text{at} \quad z = 0 \tag{6.14}$$

for $r < 1$ and the initial velocity profiles $u = -\sigma$ and $v = 1$ at $r = 1$, consistent with (6.13). The only parameter in the description is the initial flow inclination σ. As expected, for $\sigma = 0$ the problem reduces exactly to that addressed by [13].

6.2.3 Sample numerical results

The problem (6.10)–(6.14) was integrated numerically by marching from $r = 1$ with decreasing values of r for selected values of σ. Sample results are shown in figure 6.2 for $\sigma = 1$. The radial and azimuthal velocities are uncoupled for $1 - r \ll 1$, when the effects of the centripetal acceleration $-v^2/r$ and pressure gradient $-\sigma^2 r^{-3/5}/3 - r^{-3}$ can be neglected in (6.10) at leading order, reducing the solution with $\sigma \neq 0$ to $-u/(\sigma r^{-1/3}) = rv = f_{\mathrm{B}}'(\zeta)$, where f_{B} is Blasius stream function, obtained by integration of $f_{\mathrm{B}}''' + f_{\mathrm{B}} f_{\mathrm{B}}''/2 = 0$ with boundary conditions $f_{\mathrm{B}}(0) = f_{\mathrm{B}}'(0) = f_{\mathrm{B}}'(\infty) - 1 = 0$, with the prime denoting here differentiation with respect to the local self-similar coordinate $\zeta = z/(1-r)^{1/2}$. The asymptotic predictions for $1 - r \ll 1$ are compared in figure 6.2 with the profiles obtained numerically at $r = 0.9$.

The effect of the azimuthal motion on the radial flow is no longer negligible as $1 - r$ increases to values of order unity, leading to an overshoot in the radial velocity, as is already evident in the results of figure 6.2 for $r = 0.5$. This overshoot becomes more prominent as $r \to 0$, with the peak value of ru reaching a near-unity value at small distances $z \sim r$. A detailed view of this near-wall region is shown in figure 6.3, where the dashed curves represent analytic results, to be developed below.

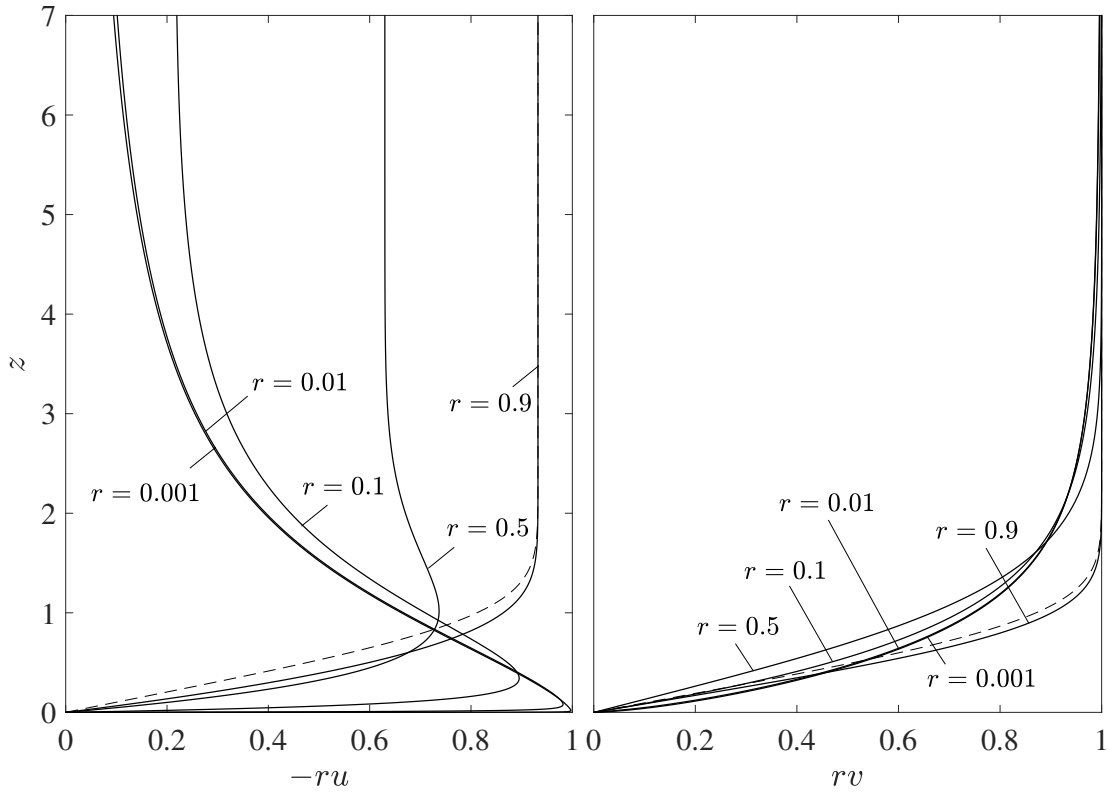

Figure 6.2: Boundary-layer profiles of radial and azimuthal velocity at various radial locations for $\sigma = 1$. The dashed curves represent the asymptotic predictions $-u/(\sigma r^{-1/3}) = rv = f'_{\mathrm{B}}(\zeta)$ for $1 - r \ll 1$ evaluated at $r = 0.9$.

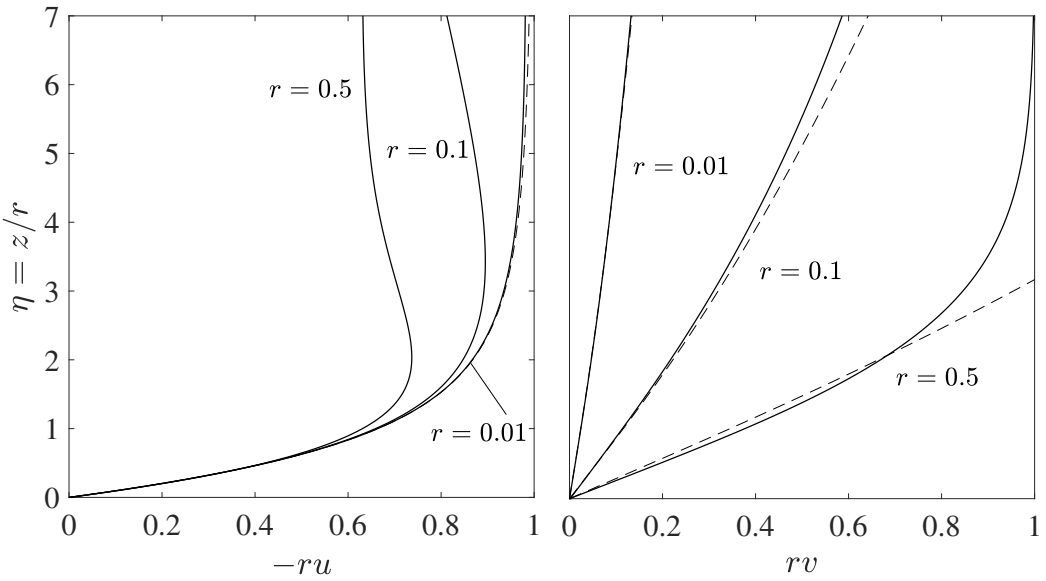

Figure 6.3: Comparison of the near-wall boundary-layer profiles obtained from the asymptotic predictions $ru = -\psi_0'(\eta)$ and $rv = C_1 r^{\lambda}\gamma_1(\eta)$ (dashed curves) with those determined numerically at various radial locations by integration of (6.10)–(6.12) for $\sigma = 1$ (solid curves).

The profiles of ru and rv shown in figure 6.2 are seen to approach a terminal shape as $r \to 0$. Although the specific shape of these terminal profiles depends on the value of σ, all solutions show a common multi-layered asymptotic structure, which, with the exception of the outermost layer, is fundamentally similar to that described in [13] for the potential vortex ($\sigma = 0$). A detailed analysis of the different layers is given below, and the associated asymptotic solutions are combined to generate composite expansions for the radial and azimuthal velocity components, providing an accurate boundary-layer description for $r \ll 1$ (i.e. dimensional distances $r^* \ll a$).

6.3 The structure of the terminal velocity profile

We consider now the solution to (6.10)–(6.12) with boundary conditions (6.13) and (6.14) in the asymptotic limit $r \ll 1$ for $\sigma \sim 1$. As noted by [13], at leading order viscous effects are confined to a thin layer $z \sim r$, outside of which the flow is inviscid, with values of $-ru \sim 1$ and $1 - rv \sim 1$ at distances $z \sim 1$. Unlike the potential-vortex solution $\sigma = 0$, which exhibits velocity

profiles with a rapid exponential decay away from the wall, in fire whirls the transition to the outer solution $ru = -\sigma r^{2/3}$ and $rv = 1$ occurs in a fairly large external layer, which necessitates a separate analysis, as shown below, exercising the full formalism of matched asymptotic expansions [22].

6.3.1 The lower viscous sub-layer

At leading order, the solution in the viscous sub-layer, where $rv \ll -ru$ (as is apparent from figure 6.3), is independent of σ and corresponds to that described by [13]. With circulation neglected, the boundary–layer equation (6.10) can be expressed in terms of the self-similar coordinate $\eta = z/r$ and accompanying stream function $\psi = r\psi_0(\eta)$, defined such that $ru = -\psi_0'$ and $rw = \psi_0 - \eta\psi_0'$, to give at leading order the problem

$$\psi_0''' - \psi_0\psi_0'' - \psi_0'^2 + 1 = 0; \qquad \psi_0(0) = \psi_0'(0) = \psi_0'(\infty) - 1 = 0. \tag{6.15}$$

The solution, expressible in terms of the parabolic cylinder functions [23], provides the asymptotic behaviour $\psi_0 \simeq \eta - 1.0864$ and

$$rw \to -1.0864 \tag{6.16}$$

for $\eta \gg 1$. The accompanying weak azimuthal motion is described by a self-similar solution of the second kind of the form $rv \propto r^{\lambda}\gamma_1(\eta)$, where the eigenfunction $\gamma_1(\eta)$ obeys the linear equation

$$\gamma_1'' - \psi_0\gamma_1' + \lambda\psi_0'\gamma_1 = 0 \tag{6.17}$$

stemming from (6.11). A nontrivial solution satisfying the non-slip condition $\gamma_1 = 0$ at $\eta = 0$ and exhibiting algebraic growth $\gamma_1 \propto \eta^{\lambda}$ (as opposed to exponential growth) as $\eta \to \infty$, as needed to enable matching with the outer profile, exists only for a discrete set of values of the eigenvalue λ, with the smallest eigenvalue, corresponding to the dominant eigenfunction for small r, found to

be $\lambda = 0.6797$.

The solution to the above eigenvalue problem determines the near-wall azimuthal velocity $rv = C_1 r^\lambda \gamma_1(\eta)$, aside from a multiplicative factor C_1, a function of σ to be determined by matching with the outer inviscid solution. For definiteness, it is convenient to use $\gamma_1 = \eta^\lambda$ as $\eta \gg 1$ as the normalization condition for the eigenfunction γ_1, resulting in the asymptotic behaviour

$$rv \to C_1 z^\lambda \quad \text{as} \quad \eta \to \infty, \tag{6.18}$$

to be employed below in the matching procedure. The near-wall asymptotic predictions $ru = -\psi_0'(\eta)$ and $rv = C_1 r^\lambda \gamma_1(\eta)$ for $r \ll 1$ are compared in figure 6.3 with the results of numerical integration for $\sigma = 1$. The predictions for $rv = C_1 r^\lambda \gamma_1(\eta)$ are computed with $C_1 = 0.5496$, the value obtained below by matching with the outer inviscid results when $\sigma = 1$. The asymptotic predictions and the numerical results are seen to be virtually indistinguishable for $r = 0.01$ in figure 6.3.

6.3.2 The main inviscid layer

In the intermediate layer $z \sim 1$, the expansions for the velocity components at $r \ll 1$ take the form

$$ru = F_0(z) + rF_1(z) + \cdots, \quad rv = G_0(z) + rG_1(z) + \cdots, \quad rw = H_1(z) + \cdots. \tag{6.19}$$

The leading-order functions $F_0(z)$ and $G_0(z)$ must satisfy $F_0 \to -1$ and $z^{-\lambda} G_0 \to C_1$ as $z \to 0$, corresponding to matching with the viscous sublayer, and as $z \to \infty$ they must approach the outer values $F_0 = G_0 - 1 = 0$, consistent at this order with the velocity found outside the boundary layer. The two functions F_0 and G_0 are related by the equation

$$F_0^2 + G_0^2 = 1, \tag{6.20}$$

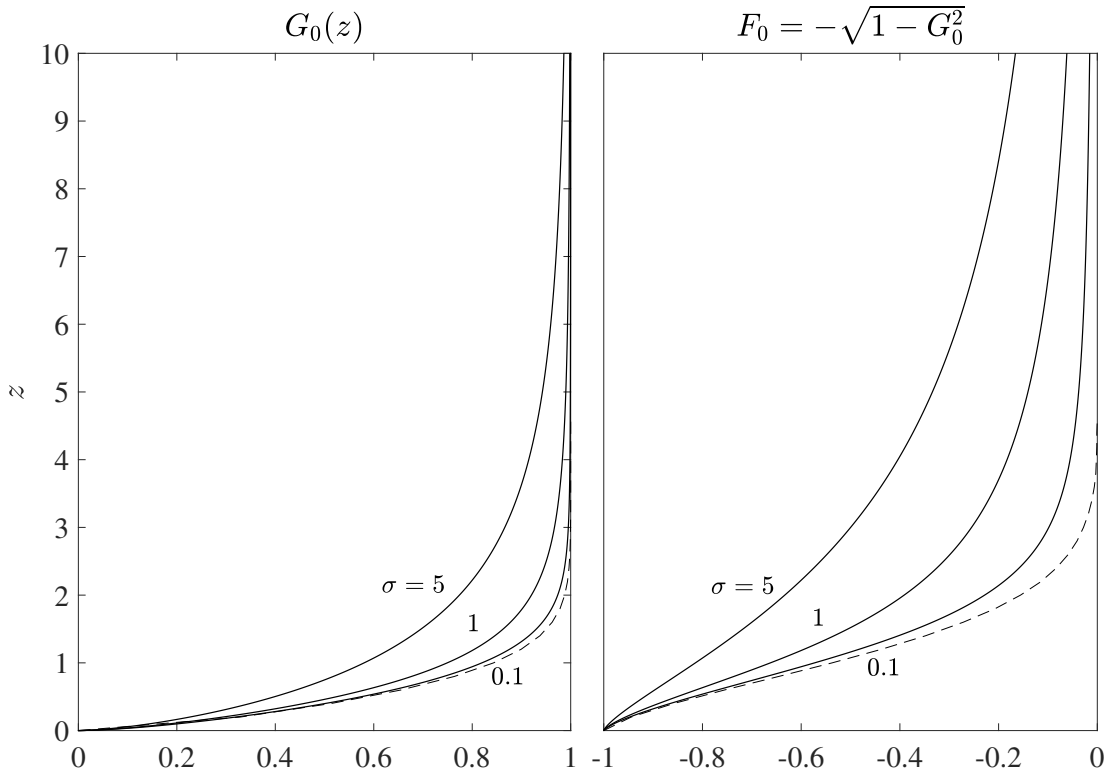

Figure 6.4: Profiles of G_0 and F_0 for various σ. Shown as dashed line are the profiles of [13] for $\sigma = 0$.

which follows from the leading-order $1/r^3$ terms in (6.10), but, other than that, their specific shape depends on the development of the boundary layer for $0 < r < 1$, yielding different profiles for different values of σ. The additional functions F_1, G_1, and H_1 appearing in (6.19) are related to the leading-order functions by

$$H_1 = 1.0864F_0,\ F_1 = -1.0864F_0',\ G_1 = -1.0864G_0' \tag{6.21}$$

as can be seen by carrying the asymptotic solution to a higher order, with the numerical factor 1.0864 selected to ensure inner matching with the vertical velocity (6.16).

To determine G_0 and $F_0 = -\sqrt{1-G_0^2}$, the numerical integration of (6.10)–(6.12) was extended to extremely small radial distances $r \sim 10^{-4}$, and the asymptotic predictions $ru = F_0(z) - 1.0864rF_0'(z)$ and $rv = G_0(z) - 1.0864rG_0'(z)$ were used to extrapolate the result to $r = 0$. The solution was further corrected to remove the viscous sublayer by replacing the solution at $z \ll 1$ with the near-wall behavior

$$F_0 = -1 + \frac{1}{2}C_1^2 z^{2\lambda}, \quad G_0 = C_1 z^{\lambda}, \tag{6.22}$$

arising from matching with (6.18), with the constant C_1 obtained from the numerical integrations by evaluating $z^{-\lambda}rv$ at small distances $z \sim r$ from the wall, yielding for instance $C_1 = (0.7125, 0.8275, 0.9065, 0.9596, 1.0181, 1.6187)$ for $\sigma = (5, 2, 1, 0.5, 0.2, 0.1)$. The observed evolution for decreasing values of σ appears to be in agreement with the limiting value $C_1 = 1.6518$ reported by [13] for $\sigma = 0$.

While the asymptotic behaviour $G_0 = \sqrt{1-F_0^2} \propto z^{\lambda}$ as $z \to 0$ shown in (6.22) applies for both $\sigma = 0$ and $\sigma \neq 0$, the solution as $z \to \infty$ is qualitatively different in these two cases, with the exponential decay found by [13] for $\sigma = 0$ being replaced for $\sigma \neq 0$ by an algebraic decay of the form

$$F_0 = -C_2 z^{-\mu} + \cdots, \quad G_0 = 1 - \frac{1}{2}C_2^2 z^{-2\mu} + \cdots, \tag{6.23}$$

where the factor C_2 and the exponent μ depend on σ. Their values were obtained from the numerical results by examining the decay with vertical distance of the near-axis terminal profiles of ru and rv, yielding for instance $C_2 = (2.85, 1.50, 0.88, 0.47)$ and $\mu = (1.21, 1.19, 1.16, 1.11)$ for $\sigma = (5, 2, 1, 0.5)$. At a given $r \ll 1$, the range of z over which (6.23) applies decreases for decreasing σ, thereby hindering the precise evaluation of C_2 and μ for $\sigma < 0.5$. The observed evolution of the approximate values, computed with use of the velocity profiles at the smallest radial distance reached in the boundary-layer computations (i.e. $r \simeq 10^{-4}$), indicates that the exponent μ decreases with decreasing σ to approach unity as $\sigma \to 0$, with the accompanying value of C_2 vanishing in this limit.

6.3.3 The upper transition region

The asymptotic expansion (6.19) fails in a transition region corresponding to $z \sim r^{-2/(3\mu)} \gg 1$ where, according to (6.23), the value of F_0 becomes of order $F_0 \sim r^{2/3}$, comparable to the limiting value $ru = -\sigma r^{2/3}$ found at $z = \infty$. This transition region can be described in terms of the order-unity similarity coordinate $\xi = (\sigma/C_2)^{1/\mu} r^{\frac{2}{3\mu}} z$ and associated rescaled velocity variables

$$ru = \sigma r^{2/3} f(\xi),\ rv = 1 + \sigma^2 r^{4/3} g(\xi),\ rw = C_2^{1/\mu} \sigma^{\frac{\mu-1}{\mu}} r^{-\frac{2+\mu}{3\mu}} h(\xi). \tag{6.24}$$

At leading order, the boundary-layer equations (6.10)–(6.12) in this inviscid outer transition region simplify to

$$\left(\frac{2\xi}{3\mu} f + h\right) f' = \frac{f^2 - 1}{3} + 2g, \tag{6.25}$$

$$\left(\frac{2\xi}{3\mu} f + h\right) g' = -\frac{4fg}{3}, \tag{6.26}$$

$$\left(f + \frac{\xi}{\mu} f'\right) + \frac{3h'}{2} = 0. \tag{6.27}$$

The solution can be reduced to a quadrature as follows. Dividing (6.25) by (6.26) and integrating the resulting equation using the boundary conditions $f(\infty) \to -1$ and $g(\infty) \to 0$, which follow from matching with the outer potential solution, provides

$$g = \frac{1}{2}(1 - f^2). \tag{6.28}$$

Substitution of this result into (6.25) and elimination of h with use of (6.27) leads to the autonomous equation

$$(f^2 - 1)f'' - \frac{\mu + 1}{\mu} f f'^2 = 0, \tag{6.29}$$

which can be integrated once using the boundary condition $f \to -\xi^{-\mu}$ as $\xi \to 0$, obtained by matching with (6.23), to give $f' = \mu(f^2 - 1)^{(\mu+1)/(2\mu)}$, finally yielding

$$\mu\xi = \int_{-\infty}^{f} \frac{\mathrm{d}\tilde{f}}{(\tilde{f}^2 - 1)^{\frac{\mu+1}{2\mu}}}, \tag{6.30}$$

with $\tilde{f}$ being a dummy integration variable. The above integral, which is expressible in terms of incomplete beta function, provides, together with the previous equation (6.28), the radial and azimuthal velocity distributions $f(\xi)$ and $g(\xi)$.

Inspection of (6.30) reveals that, for the values $\mu > 1$ that apply in our description, the function f is a front solution that reaches the boundary value $f = -1$ at a finite location $\xi = \xi_o$ given by

$$\xi_o = \frac{1}{2\mu} \mathrm{B}\left(\frac{1}{2\mu}, \frac{\mu - 1}{2\mu}\right), \tag{6.31}$$

as follows directly from (6.30), with B representing here the beta function. Note that, since the value of $\mu - 1$ remains relatively small for $\sigma \sim 1$, the front is always located at large distances $\xi_o \simeq 1/(\mu - 1)$.

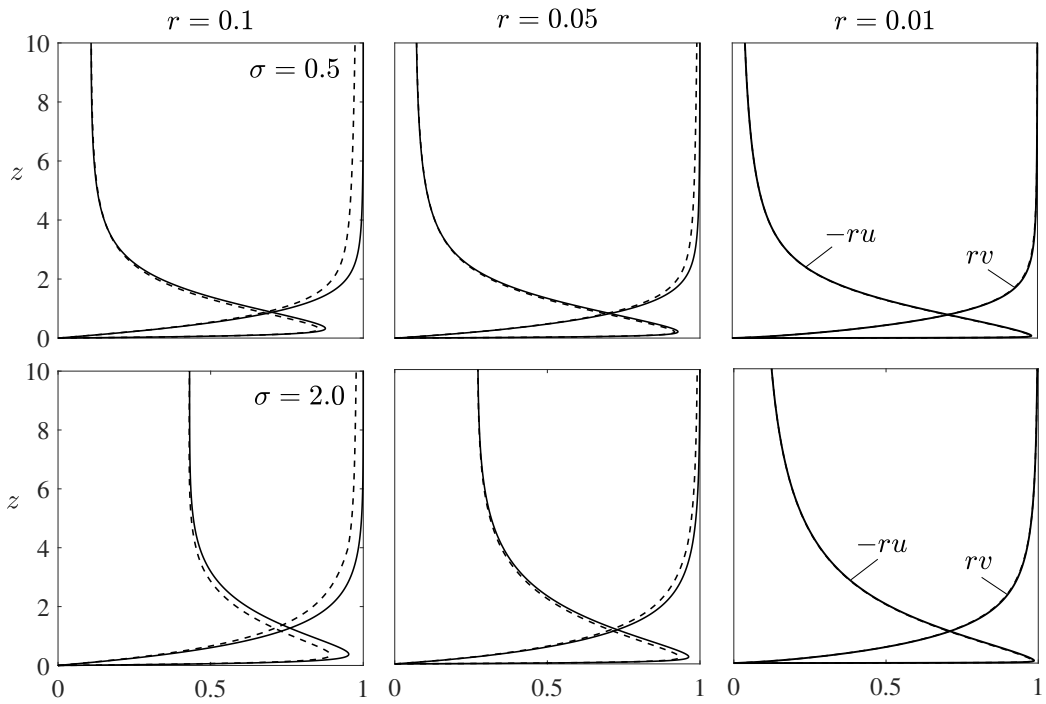

Figure 6.5: Profiles of radial and azimuthal velocity for $\sigma = 0.5$ (top row) and $\sigma = 2.0$ (bottom row) obtained at different radial locations $r \ll 1$ by numerical integration of (6.10)–(6.12) (solid curves) and by evaluation of the composite expansion (6.32) (dashed curves).

6.3.4 The composite expansion

The separate solutions found in the different regions can be used to generate the composite expansions

$$\begin{aligned} ru &= -\psi_0'(z/r) + 1 + F_0(z) + \sigma r^{2/3} f[(\sigma/C_2)^{1/\mu} r^{\frac{2}{3\mu}} z] + C_2 z^{-\mu}, \\ rv &= C_1 r^{\lambda} \gamma_1(z/r) - C_1 z^{\lambda} + G_0(z) + \sigma^2 r^{4/3} g[(\sigma/C_2)^{1/\mu} r^{\frac{2}{3\mu}} z] + \tfrac{1}{2} C_2^2 z^{-2\mu}, \end{aligned} \tag{6.32}$$

which describe the radial and azimuthal velocity profiles as $r \to 0$ with small errors of order r. The accuracy of these expansions is tested in figure 6.5 by comparing the asymptotic predictions with the results of numerical integrations of the boundary-layer equations (6.10)–(6.12). The degree of agreement displayed in the figure is clearly satisfactory, with the composite expansion being virtually indistinguishable from the numerical results at $r = 0.01$.

6.4 The collision region

The boundary-layer flow, approaching the axis with a velocity nearly parallel to the wall, undergoes a rapid upward deflection in a non-slender collision region of characteristic size $\delta = a/\sqrt{Re}$. This region is illustrated in figure 6.6, where the three-level flow outside that region also is shown. The thickness of the viscous sublayer decreases linearly with decreasing radius, the rotational inviscid layer occupying an increasing fraction of the initially non-similar boundary layer that emerges at the outer edge of the disk. For the incoming flow, described by the previous composite expansion, the viscous sublayer, the main inviscid layer, and the region of transition to potential flow at radial distances of order $r^* \sim \delta$ have associated thicknesses of increasing magnitude, given by $\delta/\sqrt{Re} \ll \delta$, δ, and $Re^{1/(3\mu)}\delta \gg \delta$, respectively. Since the thickness of the outer transition layer is much larger than the size of the collision region, a two-level composite expansion could in principle provide the inlet boundary conditions needed for computation of the structure of the stagnation-flow-like collision region. Nevertheless, the three-level expansion can serve the same purpose with higher accuracy and was used in the computations instead.

The collision region has been described earlier for vortex flows relevant to tornado phenomena. The early control-volume analysis of [24] employed the velocity profiles of [13] for the lateral incoming-flow boundary condition along with a prescribed form of the outlet velocity profile of the rising core to generate an approximate description. Inviscid solutions were determined by [25] using simple presumed functional forms for the radial and azimuthal velocity distributions across the incoming near-wall boundary layer. Additional inviscid results were obtained by [15] employing instead tabulated values of the terminal velocity profiles obtained by [13]. The latter analysis, pertaining to the case $\sigma = 0$, focused on computation of the velocity profile approached by the deflected stream above the collision region, which was used to assess the occurrence of vortex breakdown by application of Benjamin's criterion [26]. Also of interest is the numerical work of [27], who employed as boundary conditions the velocity profiles measured

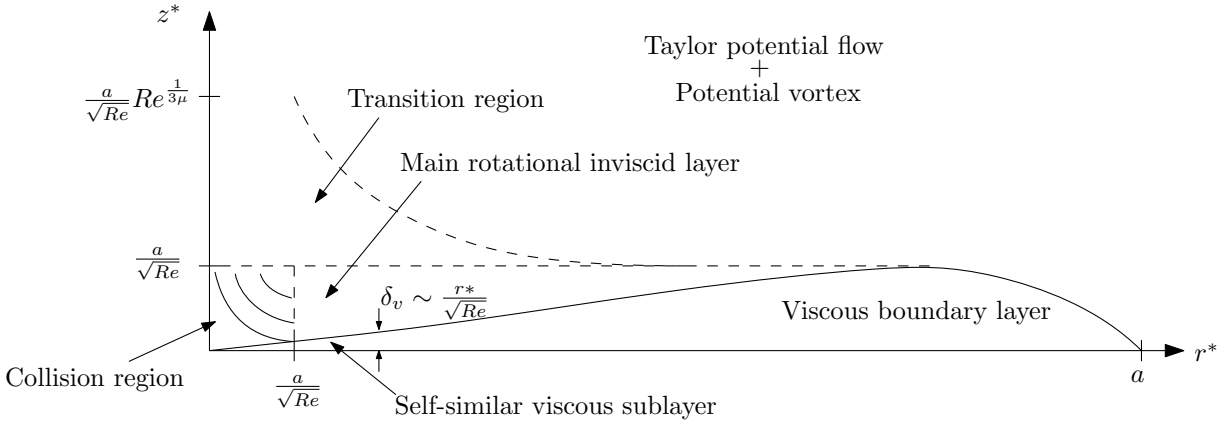

Figure 6.6: A schematic view of the boundary-layer flow with indication of the different scales.

experimentally in a vortex chamber [28]. For the moderately large Reynolds number of the experiments, good agreement was found between the inviscid description and the results of numerical integrations of the full Navier-Stokes equations, thereby supporting the idea that the structure of the collision region is fundamentally inviscid.

6.4.1 The rescaled problem

In the non-slender collision region, of characteristic size $\delta = a/\sqrt{Re}$, all three velocity components have comparable magnitudes $u^* \sim v^* \sim w^* \sim \Gamma/\delta$. Correspondingly, the analysis of this region necessitates introduction of rescaled velocity components $\tilde{u} = u^*/(\Gamma/\delta)$, $\tilde{v} = v^*/(\Gamma/\delta)$, and $\tilde{w} = w^*/(\Gamma/\delta)$ along with a rescaled radial coordinate $\tilde{r} = r^*/\delta$, while the accompanying vertical coordinate $\tilde{z} = z^*/\delta = z$ is that used in the boundary-layer analysis. With these scales, the

steady, axisymmetric continuity and momentum equations take the dimensionless form

$$\frac{1}{\tilde{r}}\frac{\partial}{\partial\tilde{r}}(\tilde{r}\tilde{u})+\frac{\partial\tilde{w}}{\partial\tilde{z}}=0, \tag{6.33}$$

$$\tilde{u}\frac{\partial\tilde{u}}{\partial\tilde{r}}-\frac{\tilde{v}^2}{\tilde{r}}+\tilde{w}\frac{\partial\tilde{u}}{\partial\tilde{z}}=-\frac{\partial\tilde{p}}{\partial\tilde{r}}+\frac{1}{Re}\left[\frac{\partial}{\partial\tilde{r}}\left(\frac{1}{\tilde{r}}\frac{\partial}{\partial\tilde{r}}(\tilde{r}\tilde{u})\right)+\frac{\partial^2\tilde{u}}{\partial\tilde{z}^2}\right], \tag{6.34}$$

$$\tilde{u}\frac{\partial}{\partial\tilde{r}}(\tilde{r}\tilde{v})+\tilde{w}\frac{\partial}{\partial\tilde{z}}(\tilde{r}\tilde{v})=\frac{1}{Re}\left[\tilde{r}\frac{\partial}{\partial\tilde{r}}\left(\frac{1}{\tilde{r}}\frac{\partial}{\partial\tilde{r}}(\tilde{r}\tilde{v})\right)+\frac{\partial^2}{\partial\tilde{z}^2}(\tilde{r}\tilde{v})\right], \tag{6.35}$$

$$\tilde{u}\frac{\partial\tilde{w}}{\partial\tilde{r}}+\tilde{w}\frac{\partial\tilde{w}}{\partial\tilde{z}}=-\frac{\partial\tilde{p}}{\partial\tilde{z}}+\frac{1}{Re}\left[\frac{1}{\tilde{r}}\frac{\partial}{\partial\tilde{r}}\left(\tilde{r}\frac{\partial\tilde{w}}{\partial\tilde{r}}\right)+\frac{\partial^2\tilde{w}}{\partial\tilde{z}^2}\right], \tag{6.36}$$

where $\tilde{p}$ denotes the spatial pressure variations scaled with the characteristic dynamic pressure $\rho(\Gamma/\delta)^2$. The distribution of radial and azimuthal velocity at large radial distances is given by the terminal profiles (6.32) written in terms of the rescaled variables. The solution depends on the Reynolds number $Re=\Gamma/\nu$, which appears explicitly in the equations, and on the ambient swirl level, through the parameter σ present in the boundary velocity profiles (6.32).

For the large values $Re\gg 1$ considered here, the flow can be expected to be nearly inviscid, although rotational, with viscous effects largely confined to a near-wall layer and to a near-axis core region, both of characteristic size $\delta_v=\delta/\sqrt{Re}\ll\delta$. The inviscid solution is to be investigated in detail below for different values of σ. To check for consistency of the large-Reynolds-number structure, additional attention is given to the accompanying near-wall boundary layer. The computations reveal that boundary-layer separation occurs at a finite distance $r^*\sim\delta$ regardless of the value of σ, indicating that the description of the corner region should, in principle, account for viscous effects. This finding motivates additional Navier-Stokes computations for moderately large values of Re, which allow us to investigate the extent of the separation region and its dependence on the Reynolds number.

The results to be presented below, extending the previous studies by using boundary velocity profiles that are directly relevant to fire-whirl applications, pertain to cold flow only. Before proceeding with the analysis, it is worth discussing the relevance of the results in connection with

localized fire whirls. If one considers, for definiteness, the case of fire whirls developing above liquid-fuel pools, then the fuel-pool diameter D emerges as relevant characteristic length, to be compared with the size of the collision region δ. In the relevant distinguished limit $D \sim \delta$ the fire whirl develops in the collision region, driven by the approaching boundary-layer profile described in (6.32). Since $Re \gg 1$, the flame, developing from the liquid-pool rim, would be confined initially to the viscous layer $z^* \sim \delta_v = \delta/\sqrt{Re}$ found in the immediate vicinity of the pool surface and, upon flow deflection near the origin, to the near-axis viscous core found at $r^* \sim \delta/\sqrt{Re}$. The inviscid results given below provide in this case the velocity profile found outside the thin reactive regions as well as the associated imposed pressure gradient, both along the liquid-pool surface and along the vertical axis. The fire whirl, driven by the fast upward flow resulting from the deflection, would continue to develop vertically over distances larger than δ, eventually transitioning to a turbulent plume. Depending on the flow conditions, buoyancy effects, which eventually drive the turbulent plume, can become important already in the reactive boundary layer developing near the liquid-pool surface, possibly helping to prevent boundary-layer separation. A recent attempt to describe this layer [29] has employed a constant-density model along with the self-similar velocity profile computed from (6.15). Clearly, more accurate numerical computations, accounting for variable-density and buoyancy effects and using as boundary condition the wall-velocity distribution obtained in the inviscid analysis of the collision region, are worth pursuing in future work.

6.4.2 The reduced inviscid formulation

As first shown by [30], the inviscid equations that follow from removing the viscous terms involving the factor Re^{-1} from the momentum equations (6.33)–(6.36) can be combined into a single equation for the stream function $\tilde{\psi}$. As explained by [31], the development uses the condition that the circulation per unit azimuthal angle $\tilde{C} = \tilde{r}\tilde{v}$ and the total head $\tilde{H} = \tilde{p} + (\tilde{u}^2 + \tilde{v}^2 + \tilde{w}^2)/2$ remain constant along any given streamline, allowing the azimuthal component of the

vorticity to be written in the form

$$\frac{\partial \tilde{u}}{\partial \tilde{z}} - \frac{\partial \tilde{w}}{\partial \tilde{r}} = \frac{\tilde{C}}{\tilde{r}} \frac{\mathrm{d}\tilde{C}}{\mathrm{d}\tilde{\psi}} - \tilde{r} \frac{\mathrm{d}\tilde{H}}{\mathrm{d}\tilde{\psi}}, \tag{6.37}$$

finally yielding

$$\frac{\partial^2 \tilde{\psi}}{\partial \tilde{r}^2} - \frac{1}{\tilde{r}} \frac{\partial \tilde{\psi}}{\partial \tilde{r}} + \frac{\partial^2 \tilde{\psi}}{\partial \tilde{z}^2} = -\tilde{C} \frac{\mathrm{d}\tilde{C}}{\mathrm{d}\tilde{\psi}} + \tilde{r}^2 \frac{\mathrm{d}\tilde{H}}{\mathrm{d}\tilde{\psi}}, \tag{6.38}$$

upon substitution of the expressions $\tilde{r}\tilde{w} = \partial\tilde{\psi}/\partial\tilde{r}$ and $\tilde{r}\tilde{u} = -\partial\tilde{\psi}/\partial\tilde{z}$. As shown below, the functions $\tilde{C}(\tilde{\psi})$ and $\tilde{H}(\tilde{\psi})$ are to be evaluated using the terminal velocity profiles (6.32) written in the simplified form $\tilde{r}\tilde{u} = F_0(\tilde{z})$ and $\tilde{r}\tilde{v} = G_0(\tilde{z})$, corresponding to $Re \to \infty$, with the functions F_0 and G_0 carrying the dependence on σ, as shown in figure 6.4.

Since the streamlines lie parallel to the wall as $\tilde{r} \to \infty$, the equation $\tilde{r}\tilde{u} = -\partial\tilde{\psi}/\partial\tilde{z}$ provides $\tilde{\psi} = -\int_0^{\tilde{z}} F_0 \mathrm{d}\tilde{z}$, which can be used to determine the boundary distribution

$$\tilde{\psi} = \tilde{\psi}_\infty(\tilde{z}) = -\int_0^{\tilde{z}} F_0 \mathrm{d}\tilde{z} \quad \text{as } \tilde{r} \to \infty, \tag{6.39}$$

and, implicitly through

$$\tilde{\psi} = -\int_0^{\tilde{z}_\infty} F_0 \mathrm{d}\tilde{z}, \tag{6.40}$$

the height $\tilde{z}_\infty(\tilde{\psi})$ at which a given streamline originates. While the head tends to a uniform value as the velocity decays far from the axis, so that $\mathrm{d}\tilde{H}/\mathrm{d}\tilde{\psi} = 0$ in (6.38), the circulation $\tilde{C}$ varies between streamlines, yielding a contribution to (6.38) that can be evaluated by using $\tilde{C}\mathrm{d}\tilde{C}/\mathrm{d}\tilde{\psi} = F_0'[\tilde{z}_\infty(\tilde{\psi})]$, derived with use of (6.20). The problem then reduces to that of integrating the nonlinear equation

$$\frac{\partial^2 \tilde{\psi}}{\partial \tilde{r}^2} - \frac{1}{\tilde{r}} \frac{\partial \tilde{\psi}}{\partial \tilde{r}} + \frac{\partial^2 \tilde{\psi}}{\partial \tilde{z}^2} = m(\tilde{\psi}), \tag{6.41}$$

where $m(\tilde{\psi}) = -F_0'[\tilde{z}_\infty(\tilde{\psi})]$, with boundary conditions

$$\tilde{\psi}(0,\tilde{z}) = \tilde{\psi}(\tilde{r},0) = \tilde{\psi}(\infty,\tilde{z}) - \tilde{\psi}_\infty(\tilde{z}) = 0 \quad \text{and} \quad \frac{\partial\tilde{\psi}}{\partial\tilde{z}} = 0 \quad \text{as} \quad \tilde{z}\to\infty. \tag{6.42}$$

The solution depends on σ through the derivative and antiderivative of the function F_0, which appear on the right-hand side of (6.41) and in the boundary distribution $\tilde{\psi}_\infty$ given in (6.39), respectively. Note that, despite the slow algebraic decay $F_0 \simeq -C_2\tilde{z}^{-\mu}$ indicated in (6.23), the condition $\mu > 1$ guarantees that the antiderivative $\int_0^{\tilde{z}} F_0 \mathrm{d}\tilde{z}$ approaches a finite value as $\tilde{z}\to\infty$ for all values of σ. Once $\tilde{\psi}(\tilde{r},\tilde{z})$ has been determined, the distribution of azimuthal velocity can be evaluated with use of $\tilde{r}\tilde{v} = \tilde{C}(\tilde{\psi}) = G_0[\tilde{z}_\infty(\tilde{\psi})]$ supplemented by (6.40), as follows in the inviscid limit from conservation of circulation along streamlines. This reduced description is the basis of many of the early vortex-core studies [15, 25, 27].

6.4.3 Sample results

Numerical solutions to the problem defined in (6.41) and (6.42) were obtained using a finite-element method [32]. No convergence problems were encountered for any value of σ. The streamlines and circulation distribution corresponding to $\sigma = 1$ are shown in figure 6.7(a). The integration provides in particular the slip velocity along the wall $\tilde{u}_w = -(1/\tilde{r})\partial\tilde{\psi}/\partial\tilde{z}|_{\tilde{z}=0}$ and the associated radial pressure gradient $-\partial\tilde{p}/\partial\tilde{r} = \tilde{u}_w \mathrm{d}\tilde{u}_w/\mathrm{d}\tilde{r}$, with the latter shown in figure 6.7(b) for selected values of σ. In all cases, the pressure gradient, whose magnitude increases with decreasing σ, is favorable far from the axis and adverse near the axis. The value of $\tilde{u}_w \mathrm{d}\tilde{u}_w/\mathrm{d}\tilde{r}$ is seen to decrease linearly with the radial distance on approaching the origin, a behavior that is consistent with the local stagnation-point solution $\tilde{\psi} \sim \tilde{r}^2\tilde{z}$ that prevails at $\tilde{r}^2 + \tilde{z}^2 \ll 1$, as follows from a local analysis of (6.41).

The deflected streamlines become aligned with the axis for $\tilde{z} \gg 1$, when the stream function approaches the limiting distribution $\Psi(\tilde{r}) = \tilde{\psi}(\tilde{r},\infty)$, to be determined from integration

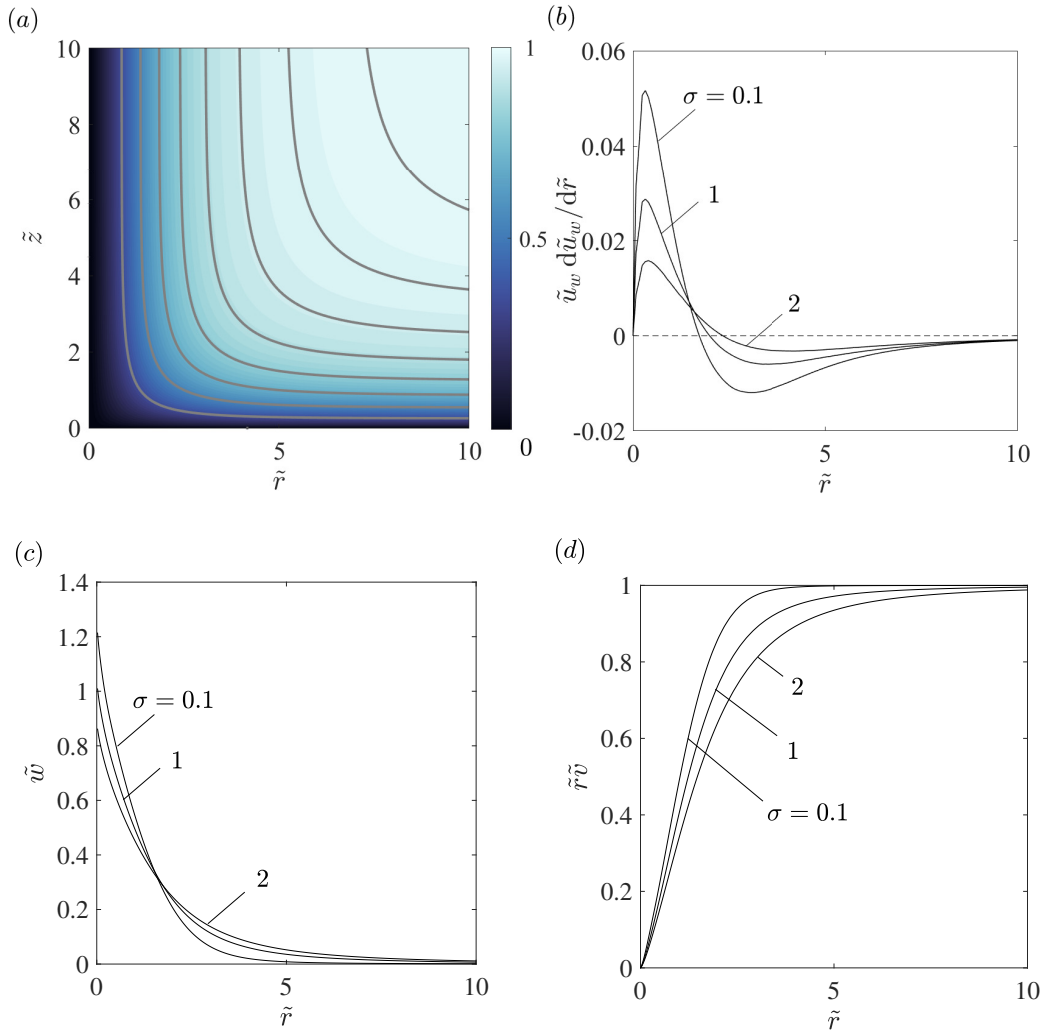

Figure 6.7: The inviscid structure of the collision region calculated from (6.41), including the streamlines $\tilde{\psi} = (0.25, 0.5, 0.75, 1.0, 1.25, 1.5, 1.75, 2.0)$ (solid curves) and circulation $\tilde{r}\tilde{v}$ (color map) for $\sigma = 1$ (a), the negative radial pressure gradient on the wall obtained from $\tilde{u}_w(\tilde{r}) = -(1/\tilde{r})\partial\tilde{\psi}/\partial\tilde{z}|_{\tilde{z}=0}$ for $\sigma = (0.1, 1.0, 2.0)$ (b), and the corresponding profiles of axial velocity $\tilde{w}$ (c) and circulation $\tilde{r}\tilde{v}$ (d) approached as $\tilde{z} \to \infty$.

of

$$\Psi'' - \Psi'/\tilde{r} = m(\Psi), \quad \Psi(0) = \Psi(\infty) + \int_0^\infty F_0 \mathrm{d}\tilde{z} = 0, \tag{6.43}$$

the one-dimensional counterpart of (6.41). The corresponding distributions of axial velocity $\tilde{w} = \Psi'/\tilde{r}$ and circulation $\tilde{r}\tilde{v} = \tilde{C}[\Psi(\tilde{r})]$, which provide the initial conditions for studying the development of the flow above the collision region, are shown in figures 6.7(c) and 6.7(d) for the three representative flow inclinations $\sigma = (0.1, 1, 2)$, for which the boundary values of the stream function are $\Psi(\infty) = (1.62, 4.16, 5.57)$, respectively. As can be seen, the rising jet is found to be wider for increasing σ, a consequence of the shape of the boundary velocity distributions F_0 and G_0. The integration provides, in particular, the peak axial velocity $\tilde{w}_0 = \tilde{w}(0)$, given by $\tilde{w}_0 = (1.22, 1.01, 0.86)$ for $\sigma = (0.1, 1, 2)$. Near the axis, where $m = -C_1^2 \lambda \Psi^{2\lambda-1}$ and $\tilde{C} = C_1 \Psi^\lambda$ with $\lambda = 0.6797$, as follows from (6.22), the solution takes the form

$$\tilde{w} = \tilde{w}_0 - \frac{C_1^2 \lambda \tilde{w}_0^{2\lambda-1} \tilde{r}^{4\lambda-2}}{2^{2\lambda}(2\lambda - 1)} \quad \text{and} \quad \tilde{r}\tilde{v} = C_1 \left(\tilde{w}_0 \tilde{r}^2/2\right)^\lambda. \tag{6.44}$$

Since $\lambda < 3/4$, the axial velocity of the inviscid solution displays an infinite slope at the axis. This characteristic of the velocity distribution, which would disappear in the presence of viscous forces, is not revealed in the early results of [15] because the tabulated representations of F_0 and G_0 employed in their description, taken from [13], did not contain enough points to reproduce the near-wall behavior (6.22).

6.4.4 The boundary layer in the collision region

The inviscid flow described above is accompanied by a near-wall viscous boundary layer with characteristic thickness $z^* \sim \delta_v = \delta/\sqrt{Re}$ at radial distances $r^* \sim \delta$. As seen in figure 6.7(b) this boundary layer develops under the action of a pressure gradient $-\partial\tilde{p}/\partial\tilde{r} = \tilde{u}_w \mathrm{d}\tilde{u}_w/\mathrm{d}\tilde{r}$ that is negative (favorable) at large radial distances but becomes positive (adverse) on approaching the axis. Clearly, the validity of the inviscid solution as a representation of the flow for $Re \gg 1$

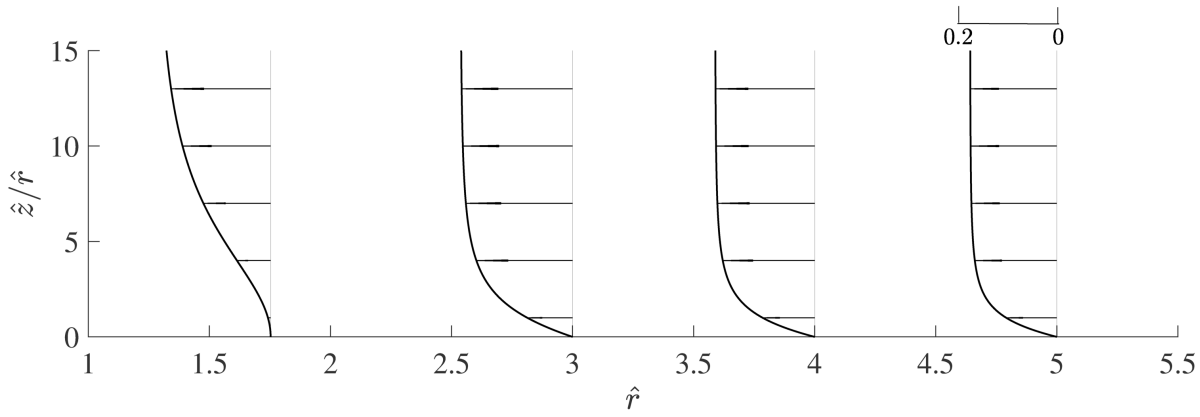

Figure 6.8: Boundary-layer profiles of radial velocity at selected locations obtained by integration of (6.46) for $\sigma = 1$.

requires that the boundary layer remains attached, that being the assumption underlying previous descriptions [5, 15, 27]. Examination of this aspect of the problem requires introduction of the rescaled variables

$$\hat{r} = \frac{r^*}{\delta} = \tilde{r}, \quad \hat{z} = \frac{z^*}{\delta_v} = \sqrt{Re}\tilde{z}, \quad \hat{u} = \frac{u^*}{\Gamma/\delta} = \tilde{u}, \quad \hat{w} = \frac{\sqrt{Re}w^*}{\Gamma/\delta} = \sqrt{Re}\tilde{w} \tag{6.45}$$

to write the boundary-layer equations

$$\hat{u}\frac{\partial \hat{u}}{\partial \hat{r}} + \hat{w}\frac{\partial \hat{u}}{\partial \hat{z}} = \tilde{u}_w\frac{\mathrm{d}\tilde{u}_w}{\mathrm{d}\hat{r}} + \frac{\partial^2 \hat{u}}{\partial \hat{z}^2}, \tag{6.46}$$

$$\frac{\partial}{\partial \hat{r}}(\hat{r}\hat{u}) + \frac{\partial}{\partial \hat{z}}(\hat{r}\hat{w}) = 0, \tag{6.47}$$

and associated initial and boundary conditions

$$\begin{aligned} &\hat{r} \to \infty : \quad \hat{r}\hat{u} = -\psi_0'(\hat{z}/\hat{r}), \\ &\hat{z} = 0 : \quad \hat{u} = \hat{w} = 0, \quad \hat{z} \to \infty : \quad \hat{u} \to \tilde{u}_w(\hat{r}), \end{aligned} \tag{6.48}$$

involving the apparent slip velocity $\tilde{u}_w$ of the inviscid collision region, which carries the dependence on σ, and on the rescaled stream function ψ_0 across the viscous sublayer, determined

from (6.15).

Numerical integration of (6.46)–(6.48) for decreasing values of $\hat{r}$ reveals that for all σ the boundary layer separates at a radial location $\hat{r} \sim 1$, where the velocity profile develops an inflection point at the wall, preventing integration beyond that point. Illustrative results are shown in figure 6.8 for $\sigma = 1$, for which separation is predicted to occur at $\hat{r} \simeq 1.76$.

6.4.5 The viscous structure of the collision region

The predicted separation of the boundary layer, questioning the validity of the inviscid description, was further investigated numerically by integrating the complete Navier-Stokes equations (6.33)–(6.36) with a Newton-Raphson method in combination with the finite-element solver FreeFem++ [32] for increasing values of *Re* and different values of σ. A cylindrical computational domain with outer radius $\tilde{r}_{\max} \gg 1$ and height $\tilde{z}_{\max} \gg 1$ was employed in the integrations. The three-level composite expansions of (6.32), written in terms of the collision-region variables, were used to provide the inlet boundary conditions at $\tilde{r} = \tilde{r}_{\max}$. Additional boundary conditions include $\tilde{u} = \tilde{v} = \tilde{w} = 0$ at $\tilde{z} = 0$, $\tilde{u} = \tilde{v} = \partial\tilde{w}/\partial\tilde{r} = 0$ at $\tilde{r} = 0$, and the outflow condition $\partial p/\partial z = 0$ at $\tilde{z} = \tilde{z}_{\max}$. The results for the flow in the collision region $\tilde{r} \sim \tilde{z} \sim 1$ were found to be independent of the size of the computational domain provided that the boundaries were selected in the ranges $5 \lesssim \tilde{r}_{\max} \lesssim 10$ and $10 \lesssim \tilde{z}_{\max} \lesssim 20$. Illustrative results using $\tilde{r}_{\max} = 8$ and $\tilde{z}_{\max} = 16$ are shown in figure 6.9(a), (b) and (c) for $\sigma = 1$ and three different values of the relevant Reynolds number *Re*. It should be noted that previous experimental results [33] suggest that, for the two largest Reynolds numbers considered, namely, $Re = 10^5$ and $Re = 4 \times 10^5$, the boundary layer of the steady-flow solutions considered here is probably unstable and would experience transition to a turbulent state, but that aspect of the problem is not investigated in our numerical computations, which are focused instead on the emergence of boundary-layer separation.

It can be seen in figure 6.9(a) that the structure of the flow for $Re = 10^4$ is very similar to

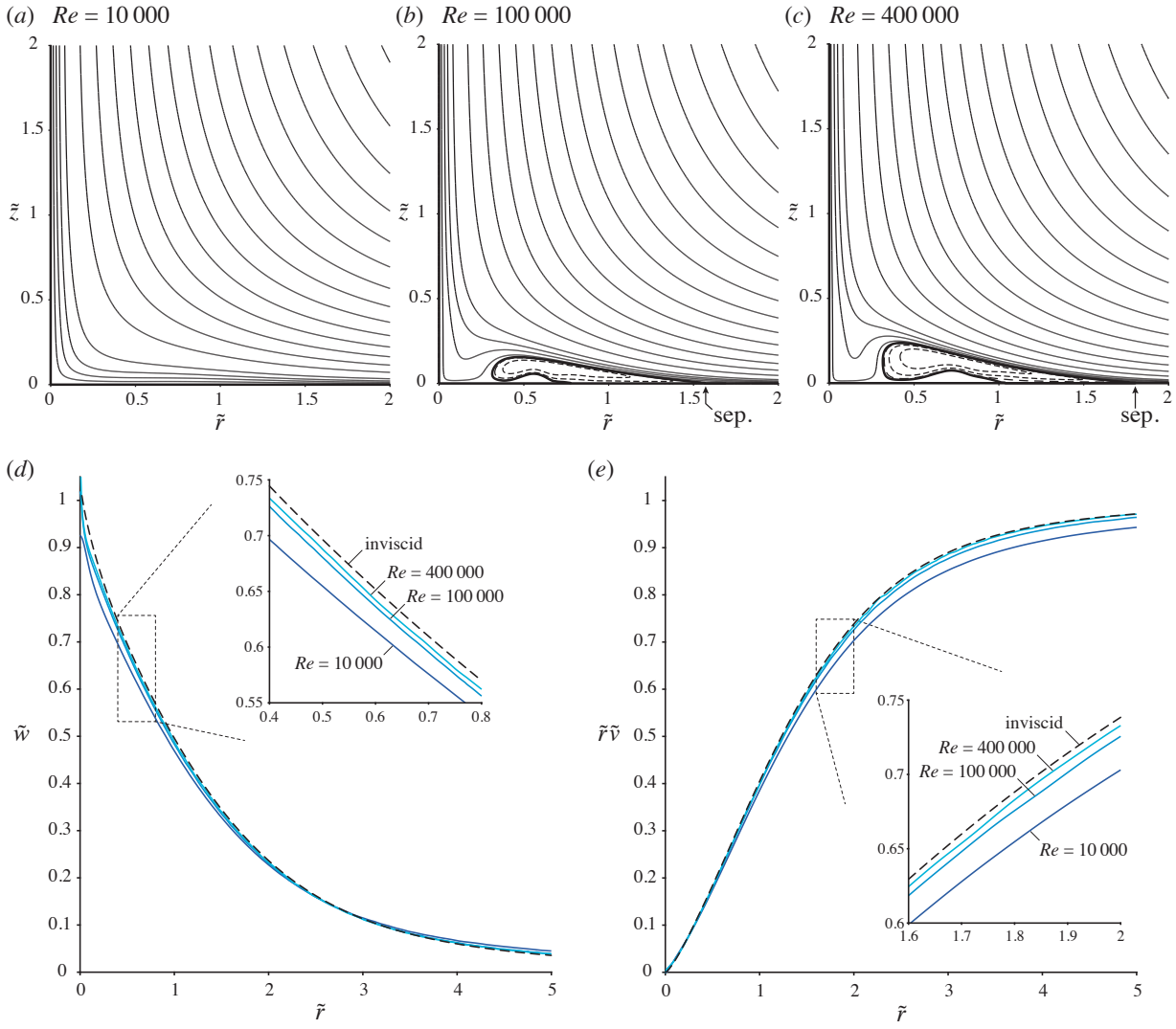

Figure 6.9: The viscous structure of the collision region for $\sigma = 1$, including streamlines obtained by integration of (6.33)–(6.36) for (a) $Re = 10^4$, (b) $Re = 10^5$, and (c) $Re = 4 \times 10^5$, together with a comparison of radial profiles of (d) axial velocity $\tilde{w}$ and (e) circulation $\tilde{r}\tilde{v}$ at $\tilde{z} = 5$ with the inviscid results shown in figure 6.7(c) and 6.7(d). Streamlines in (a)–(c) are not equispaced. The arrows in (b) and (c) indicate the location where the boundary layer separates.

the inviscid structure, in that the boundary layer remains attached and the resulting streamlines are similar to those shown in figure (6.7)(a). By way of contrast, the flow structure found when the Reynolds number is increased to $Re = 10^5$ is markedly different (figure 6.9(b)). The streamline pattern reveals the presence of a slender recirculating bubble adjacent to the wall, generated by the separation of the boundary layer at $\tilde{r} \simeq 1.55$, and subsequent reattachment at $\tilde{r} \simeq 0.3$. Further increasing the Reynolds number to $Re = 4 \times 10^5$ causes the recirculation bubble to enlarge, and this also moves the location of the point at which the boundary layer separates to $\tilde{r} = 1.75$, approaching the value $\tilde{r} = 1.76$ predicted by the boundary-layer computations.

The closed recirculating bubble has a limited effect on the vertical jet issuing from the collision region. This is quantified in figures 6.9(d) and (e), where profiles of axial velocity and circulation at $\tilde{z} = 5$ for the three values of the Reynolds number considered before are compared with the inviscid results shown in figure 6.7(c) and (d). A noticeable difference is found near the axis, where the sharp peak of the inviscid axial velocity is smoothed by the viscous forces. The resulting near-axis boundary layer is thicker for smaller Reynolds numbers, resulting in a smaller peak velocity. The quantitative agreement everywhere else is quite satisfactory, with the viscous results approaching the inviscid profile for increasing values of the Reynolds number.

It is worth pointing out that closed recirculating bubbles, similar to those shown in figures 6.9(b) and 6.9(c), were observed near the end wall in early flow simulations of Ward-type vortex chambers with Reynolds number 10^3 (based on the flow rate and on the vortex-chamber radius) when the swirl level was sufficiently low [34]. The separation bubble disappears for increasing swirl level [34] and is not present in subsequent computations of the same flow at Reynolds number 10^4 [27], for which the flow was shown to be fundamentally inviscid. No indication of boundary-layer separation was found in recent tornado simulations at much higher Reynolds numbers [35] employing a prescribed forcing term in the vertical momentum equation to generate the motion. The differences between the results of these previous simulations [27, 34, 35] and the predictions reported above are attributable to the differences in the associated flow field,

suggesting that the detailed distribution of near-wall velocity plays a critical role in the occurrence of boundary-layer separation on approaching the axis.

6.5 Conclusions

This investigation clarifies a number of aspects of the structure of the boundary layer that will develop between an axisymmetric fire and swirl-producing obstacles located at a large but finite radius from its center, by analyzing situations in which the external inviscid flow can be described as a superposition of a potential vortex and the Taylor potential flow generated by a turbulent plume. A one-parameter family of solutions was developed, that parameter being the ratio of the inward radial component of velocity to the azimuthal (swirl) component at the cylindrical swirl-generation boundary, thereby extending an earlier, tornado-motivated analysis (for which that parameter vanishes) to conditions of interest for fire whirls. The initially non-similar boundary layer evolves, at radii small compared with the radius of the obstacle location, into a three-level structure composed of an inner self-similar viscous sublayer, below a thicker, self-similar, rotational, inviscid layer which, in turn, lies below an even thicker, self-similar, still rotational, inviscid layer of transition to the external potential flow. A composite expansion is given that describes the structure of this three-level boundary layer, which helps in addressing computationally the flow near the axis of symmetry, needing study for accurate and complete descriptions of fire-whirl structures, including their stability and the onset of vortex breakdown.For instance, the composite expansion has been used recently [36] as boundary condition for the numerical description of the structure of fire whirls lifted over liquid-fuel pools, stabilized by vortex breakdown when the level of ambient swirl becomes sufficiently large [37]. Similar numerical investigations can be useful in addressing unsteady fire-whirl dynamics, including transitions between attached and lifted flames and intermittent vortex breakdown, which have been observed in controlled laboratory experiments [9].

With decreasing radius, the thickness of the viscous sublayer decreases, and the azimuthal velocity decreases, while the inward radial velocity increases, leading to a collision region near the axis, of a size proportional to the square root of the ratio of the kinematic viscosity to the circulation (the reciprocal of a Reynolds number), in which the flow experiences transition from predominantly radially inward to predominantly upward motion. This collision region is described, in general, by the full Navier-Stokes equations, but it develops a dominantly inviscid structure for large enough Reynolds numbers, with boundary layers at the base and on the axis. The colliding inward motion produces a stagnation-flow type of behavior, which results in an unfavorable pressure gradient acting on the viscous base flow, leading to its separation at high enough Reynolds numbers, but which apparently turns out to be followed by re-attachment, at least at Reynolds numbers accessible computationally, so that the upward outflow can be estimated reasonably. These rather complex constant-density boundary-layer structures in fire whirls underlie the combustion effects which, by decreasing the gas density, give rise to the tall fire whirls that generally are seen. Proper complete analyses of these fire whirls and of the vortex-breakdown phenomena that occur in them at sufficiently small values of the ratio of radial to azimuthal incoming velocity need to take into account the flow characteristics uncovered in the present work.

This chapter, in full, has been submitted for publication in the *Journal of Fluid Mechanics*, "A model for the boundary layer surrounding fire whirls", by A. D. Weiss, P. Rajamanickam, W. Coenen, A. L. Sánchez, and F. A. Williams. The dissertation author is the primary investigator in this publication.

Bibliography

[1] A. Tohidi, M. J. Gollner, and H. Xiao. Fire whirls. *Annu. Rev. Fluid Mech.*, 50:187–213, 2018.

[2] J. Lei, N. Liu, L. Zhang, and K. Satoh. Temperature, velocity and air entrainment of

fire whirl plume: A comprehensive experimental investigation. *Combustion and Flame*, 162(3):745–758, 2015.

[3] G. K. Batchelor. Heat convection and buoyancy effects in fluids. *Q. J. R. Meteorol. Soc.*, 80(345):339–358, 1954.

[4] G. I. Taylor. Flow induced by jets. *J. Aerosp. Sci.*, 25(7):464–465, 1958.

[5] R. Rotunno. The fluid dynamics of tornadoes. *Annu. Rev. Fluid Mech.*, 45:59–84, 2013.

[6] T. Maxworthy. A vorticity source for large-scale dust devils and other comments on naturally occurring columnar vortices. *J. Atmos. Sci.*, 30(8):1717–1722, 1973.

[7] H. W. Emmons and S.-J. Ying. The fire whirl. *Proc. Combust. Inst.*, 11:475–488, 1967.

[8] J. B. Mullen and T. Maxworthy. A laboratory model of dust devil vortices. *Dyn. Atmos. Oceans*, 1(3):181–214, 1977.

[9] W. Coenen, E. J. Kolb, A. L. Sánchez, and F. A. Williams. Observed dependence of characteristics of liquid-pool fires on swirl magnitude. *Combust. Flame*, 205:1–6, 2019.

[10] G. M. Byram and R. E. Martin. Fire whirlwinds in the laboratory. *Fire Control Notes*, 33(1):13–17, 1962.

[11] A. K. Gupta, D. G. Lilley, and N. Syred. *Swirl flows*. Abacus Press, 1984.

[12] S. Candel, D. Durox, T. Schuller, J.-F. Bourgouin, and J. P. Moeck. Dynamics of swirling flames. *Annu. Rev. Fluid Mech.*, 46:147–173, 2014.

[13] O. R. Burggraf, K. Stewartson, and R. Belcher. Boundary layer induced by a potential vortex. *Phys. Fluids*, 14(9):1821–1833, 1971.

[14] J. M. Potter and N. Riley. Free convection from a heated sphere at large grashof number. *J. Fluid Mech.*, 100(4):769–783, 1980.

[15] B. H. Fiedler and R. Rotunno. A theory for the maximum windspeeds in tornado-like vortices. *J. Atmos. Sci.*, 43(21):2328–2340, 1986.

[16] H. Rouse, C. S. Yih, and H. W. Humphreys. Gravitational convection from a boundary source. *Tellus*, 4(3):201–210, 1952.

[17] E. J. List. Turbulent jets and plumes. *Annu. Rev. Fluid Mech.*, 14(1):189–212, 1982.

[18] W. Schneider. Flow induced by jets and plumes. *J. Fluid Mech.*, 108:55–65, 1981.

[19] W. Coenen, P. Rajamanickam, A. D. Weiss, A. L. Sánchez, and F. A. Williams. Swirling flow induced by jets and plumes. *Acta Mech.*, 230(6):2221–2231, 2019.

[20] M. A. Gol'dshtik. A paradoxical solution of the navier-stokes equations. *Appl. Mat. Mech. (Sov.)*, 24(4):913–929, 1960.

[21] W. S. King and W. S. Lewellen. Boundary-layer similarity solutions for rotating flows with and without magnetic interaction. *Phys. Fluids*, 7(10):1674–1680, 1964.

[22] P. A. Lagerstrom. *Matched asymptotic expansions: ideas and techniques*. Springer-Verlag, 1988.

[23] R. H. Mills. *The boundary layer for some axial symmetric flows*. PhD thesis, California Institute of Technology, 1935.

[24] M. R. Head, T. S. Prahlad, and W. R. C. Phillips. Transition to a rising core at the centre of a vortex. simplified analysis for laminar flow. *Aeronaut. Quart.*, 28(3):197–210, 1977.

[25] R. Rotunno. Vorticity dynamics of a convective swirling boundary layer. *J. Fluid Mech.*, 97(3):623–640, 1980.

[26] T. B. Benjamin. Theory of the vortex breakdown phenomenon. *J. Fluid Mech.*, 14(4):593–629, 1962.

[27] T. Wilson and R. Rotunno. Numerical simulation of a laminar end-wall vortex and boundary layer. *Phys. Fluids*, 29(12):3993–4005, 1986.

[28] G. L. Baker. *Boundary Layers in Laminar Vortex Flows*. PhD thesis, PURDUE UNIVERSITY, 1981.

[29] S. Li, Q. Yao, and C. K. Law. The bottom boundary-layer structure of fire whirls. *Proc. Combust. Inst.*, 37(3):4277–4284, 2019.

[30] W. M. Hicks. Ii. researches in vortex motion.—part iii. on spiral or gyrostatic vortex aggregates. *Philos. Trans. Royal Soc. A*, 192:33–99, 1899.

[31] G. K. Batchelor. *An introduction to fluid dynamics*. Cambridge University Press, 1967.

[32] F. Hecht. New development in FreeFem++. *J. Numer. Math.*, 20(3-4), 2012.

[33] W. R. C. Phillips. On vortex boundary layers. *Proceedings of the Royal Society of London. A. Mathematical and Physical Sciences*, 400(1819):253–261, 1985.

[34] R. Rotunno. A study in tornado-like vortex dynamics. *J. Atmos. Sci.*, 36(1):140–155, 1979.

[35] R. Rotunno, G. H. Bryan, D. S. Nolan, and N. A. Dahl. Axisymmetric tornado simulations at high reynolds number. *J. Atmos. Sci.*, 73(10):3843–3854, 2016.

[36] J. Carpio, W. Coenen, A. L. Sánchez, E. Oran, and F. A. Williams. Numerical description of axisymmetric blue whirls over liquid-fuel pools. *P. Combust. Inst.*, 35:submitted, 2020.

[37] H. Xiao, M. J. Gollner, and E. S. Oran. From fire whirls to blue whirls and combustion with reduced pollution. *Proc. Nat. Acad. Sci.*, 113(34):9457–9462, 2016.